UNIVERSITY OF CALIFORNIA, SAN DIEGO

Determinations of $|V_{ub}|$ from Inclusive Semileptonic B Decays with Reduced Model Dependency

A dissertation submitted in partial satisfaction of the
requirements for the degree Doctor of Philosophy

in

Physics

by

Edward J. Hill

Committee in charge:

Professor David MacFarlane, Chair
Professor James Branson
Professor Bruce Driver
Professor Douglas Magde
Professor Aneesh Manohar

2005

The dissertation of Edward J. Hill is approved, and
it is acceptable in quality and form for publication on
microfilm:

_____

_____

_____

_____

_____

Chair

University of California, San Diego

2005

DEDICATION

For Judy,
Let our adventures begin.

TABLE OF CONTENTS

LIST OF FIGURES

LIST OF TABLES

Acknowledgments

The work in this thesis would not be possible if not for the instruction and support I have received from my colleagues along the way. There are many people to thank, and I will attempt to list them below. I apologize to anyone who I may have forgotten.

Rolf Dubitzky and Urs Langenegger. Thanks for working with me on this analysis. It was a pleasure working with both of you.

Adam Leibovich, Ian Low, and Ira Rothstein. Thanks for consistently and patiently answering my questions.

The members of the Semileptonic AWG, in particular Daniele Del Re, Riccardo Faccini, Virginia Azzolini, Concezio Bozzi, Kerstin Tackmann, and Dominique Fortin. The work in this thesis has benefited greatly from your work.

The members of *BABAR* who devoted time to reviewing this analysis and helping prepare it for publication.

The UC San Diego *BABAR* group of past and present. In particular, I would like to thank my advisor, David MacFarlane, for his support.

Lastly, I would like to offer a special thank you to Urs Langenegger. This analysis would not have been possible without you. Thanks for being limitlessly patient and always finding time to speak with me from the other side of the Atlantic, regardless of the time. You've been a true mentor and friend.

VITA

1999	Bachelor of Arts, University of Chicago
1999–2005	Research Assistant, University of California, San Diego
2000	Masters of Science, University of California, San Diego
2001	Teaching Assistant, University of California, San Diego
2005	Ph.D., University of California, San Diego

ABSTRACT OF THE DISSERTATION

Determinations of $|V_{ub}|$ from Inclusive Semileptonic B Decays with Reduced Model Dependency

by

Edward J. Hill

Doctor of Philosophy in Physics

University of California, San Diego, 2005

Professor David MacFarlane, Chair

This thesis presents several measurements of the CKM quark mixing matrix element $|V_{ub}|$ with reduced theoretical model dependency. The data sample for these results consists of about 90 million $\Upsilon(4S) \rightarrow B\bar{B}$ decays collected between 1999 and 2002 with the *BABAR* detector at the PEP-II asymmetric-energy e^+e^- collider, located at the Stanford Linear Accelerator Center. The determinations of $|V_{ub}|$ are performed by measuring the invariant hadronic mass spectrum from inclusive semileptonic B meson decays recoiling from a fully reconstructed B meson decaying hadronically. In one method, the partial rate extracted from the charmless semileptonic hadronic mass spectrum below $1.67\,\mathrm{GeV}/c^2$ is combined with a weighted integral over the endpoint of the photon energy spectrum from $b \rightarrow s\gamma$ decays and the result $|V_{ub}| = (4.43 \pm 0.38_{stat} \pm 0.25_{syst} \pm 0.29_{theo}) \times 10^{-3}$ is obtained. In a second method, the charmless hadronic mass spectrum is measured up to $2.50\,\mathrm{GeV}/c^2$, corresponding to 96.5% of the simulated hadronic mass spectrum. The charmless semileptonic branching fraction is deduced from this measurement and results in $\mathcal{B}(\overline{B} \rightarrow X_u\ell\bar{\nu}) = (1.64 \pm 0.60_{stat} \pm 0.25_{syst}) \times 10^{-3}$ which yields $|V_{ub}| = (3.84 \pm 0.70_{stat} \pm 0.30_{syst} \pm 0.19_{theo}) \times 10^{-3}$.

Chapter 1

Introduction

Given the inelegance of the Standard Model, in particular the large number of elementary constituents and parameters, particle physics experiments seek to make ever more precise tests of its predictions with the aim of revealing evidence for a more fundamental underlying theory. As a part of this program, understanding the nature of flavor changing processes of electroweak interactions is a central component. Currently, in the Cabibbo-Kobayashi-Maskawa (CKM) matrix that describes how quarks can change flavor in hadron decays through the electroweak interaction, the element $|V_{ub}|$ is not precisely determined and arguably represents one of the largest gaps in our knowledge of the CKM description of electroweak interactions.

Measuring $|V_{ub}|$ has proved to be a challenge for both theory and experiment. Experimentally, we can only use a restricted region of the available phase space to measure $b \to u\ell\bar{\nu}$ decays because of the overwhelming background from $b \to c\ell\bar{\nu}$ decays. Theoretically, providing the necessary calculations for extracting $|V_{ub}|$ from a measurement performed in a small region of the phase space is challenging. Since $|V_{ub}|^2$ is proportional to the total $b \to u\ell\bar{\nu}$ decay width, theorists must introduce ad-hoc models to extrapolate the measurement performed in a small region of phase space to the full phase space. These models are responsible for describing the dynamics of the motion of the b quark inside the B meson. This motion, called Fermi motion, is not calculable by theorists.

While it is not possible to calculate from first principles the momentum distribution of the b quark inside the B meson, there are other approaches that sidestep the problem. Since the dependence on the dynamics of the motion of the b quark is common to other decay processes of the B meson, a method exists to combine the measurable regions of two experimentally difficult decays, $b \to u\ell\bar{\nu}$ and $b \to s\gamma$, and cancel the common dependence on the ad-hoc model to leading order. Also, measuring the full spectrum of $b \to u\ell\bar{\nu}$ decays leaves very little theoretical uncertainty in

the determination of $|V_{ub}|$ because the model dependency enters only when performing a measurement in a restricted region of phase space. However, this method will incur larger uncertainties from the large amount of background present and also from imperfect knowledge of the shape and normalization of the background.

In this dissertation, two determinations of $|V_{ub}|$ with reduced model dependencies are presented. The first determination will measure the inclusive charmless semileptonic hadronic mass spectrum in the measurable region below the D meson mass and combine it with the partial $b \to s\gamma$ photon energy spectrum. The second uses the full inclusive charmless semileptonic hadronic mass spectrum past the folkloric cut-off at the D meson mass.

Given the theoretical and experimental difficulties in measuring $|V_{ub}|$, it is clear that we will greatly benefit from several different approaches with correspondingly different techniques and assumptions. The measurement techniques developed here are novel approaches that offer reduced model dependency unmatched by previous methods. Although still statistically limited, these techniques offer a promise of more precise measurements in the future as additional data becomes available.

1.1 Outline of Dissertation

The determinations of $|V_{ub}|$ presented in this dissertation use the charmless semileptonic B decay rate from the hadronic mass spectrum. The first method to extract $|V_{ub}|$ makes use of the $b \to u\ell\bar{\nu}$ events below a hadronic mass cut-off near the D meson mass and combines this with a measurement of the photon energy spectrum from $b \to s\gamma$ decays. The $b \to s\gamma$ photon energy spectrum is taken from a recently published analysis by *BABAR* [69]. The second method uses the full charmless semileptonic decay B rate which allows for a straight-forward determination of $|V_{ub}|$.

The measurement is performed with a sample of $\Upsilon(4S) \to B\overline{B}$ events recorded at the *BABAR* detector at the Stanford Linear Accelerator Center. In order to reduce backgrounds, we fully reconstruct one B meson, called a B_{reco}, in the event through its decays to an hadronic final state. The other charged and neutral particles in the event are then ascribed to the decay of the second or recoiling B meson, called a B_{recoil}. Requiring a fully reconstructed B meson, with an efficiency of only about 0.5%, results in a relatively small signal sample. However, there are great advantages to using this approach as the reconstruction provides a clean environment to study semileptonic B decays and makes simple the neutrino reconstruction that is necessary for studying the hadronic mass of a semileptonic decay.

The analysis is performed by studying the decays of the recoil B mesons. A sample of semileptonic decays is identified by the presence of a high momentum lepton with charge properly correlated to the flavor of the B_{recoil}. The hadron that the B_{recoil} eventually decays to is comprised of the remaining detected charged and neutral particles in the event not belonging to the B_{reco}. The 4-momenta of these charged and neutral particles is summed which yields the 4-momentum of the hadron. Since the 4-momenta of the B_{reco}, the lepton, the hadron, and the colliding beams are known, the 4-momentum of the undetected neutrino is deduced by applying conservation laws.

The signal $b \to u\ell\bar{\nu}$ decays are enhanced and the large background from $b \to c\ell\bar{\nu}$ decays is reduced by applying a selection procedure that exploits fundamental differences in the two types of decays. For example, $b \to u\ell\bar{\nu}$ decay processes rarely involve kaons whereas they are abundant in $b \to c\ell\bar{\nu}$ decays. Thus, rejecting events with kaons will reduce background and enhance signal. The selection procedure also exploits differences in the distributions of various kinematic variables that describe the event. By making restrictions on the mass and momentum of the undetected neutrino and the total charge of the event, the signal sample is further enhanced.

After the event selection is applied, the signal yield is determined from the hadronic mass spectrum. This spectrum is made up of signal $b \to u\ell\bar{\nu}$ decays, background $b \to c\ell\bar{\nu}$ decays, and a small amount of other backgrounds including events with misidentified leptons or leptons from secondary τ or charm decays. To determine the signal yield, the contributions from $b \to c\ell\bar{\nu}$ and other backgrounds are simulated and subtracted from the measured mass spectrum.

For the first method to extract $|V_{ub}|$, the partial $b \to u\ell\bar{\nu}$ decay rate below a cut-off near the D meson mass is determined from the signal hadronic mass spectrum. This partial rate is combined with a weighted integral over the partial $b \to s\gamma$ photon energy spectrum to determine $|V_{ub}|$. For the second method to extract $|V_{ub}|$, the total $b \to u\ell\bar{\nu}$ decay rate is determined from the full signal hadronic mass spectrum. $|V_{ub}|$ is then determined from a simple expression relating the decay rate to $|V_{ub}|$.

The following outlines the chapters in this dissertation and the information they aim to provide:

- Chapter 2 introduces the Standard Model of fundamental particles and provides the background for the electroweak interaction and the CKM description of quark mixing. Also in this chapter, the theory to relate the charmless semileptonic B decay rate to the CKM matrix element $|V_{ub}|$ is presented.

- Chapter 3 describes SLAC and the *BABAR* detector and how they combine to record the decays of B mesons.

- Chapter 4 describes how various types of charged and neutral particles are reconstructed from the information provided by the detector systems.
- Chapter 5 describes the full reconstruction method for the B_{reco}, which defines the sample used for selecting the charmless semileptonic decays in the final signal sample.
- Chapter 6 describes the selection procedures and analysis applied to the recoil B meson.
- Chapter 7 describes the signal extraction technique from the measured semileptonic hadronic mass spectrum, as well as the calculation of the weighted integrals over the $b \to s\gamma$ photon energy spectrum and the results for the extraction of $|V_{ub}|$.
- Chapter 8 discusses the uncertainties on the values extracted for $|V_{ub}|$.
- Chapter 9 summarizes and discusses the results obtained for $|V_{ub}|$ from the various methods described in this dissertation.

Chapter 2

The Theory of Weak Interactions and the Extraction of $|V_{ub}|$

In this chapter, a summary of the theory describing the extraction of $|V_{ub}|$ is presented. To do so, a brief introduction to the Standard Model of fundamental particle interactions is presented, along with a formulation of the Cabibbo-Kobayashi-Maskawa description of the weak interaction. A detailed description of charmless inclusive semileptonic decays of the B meson and the relation of the decay rate to $|V_{ub}|$ is then provided. In this description, the problem of having reliable model-independent theoretical calculations in an experimentally feasible framework is highlighted. Concluding the chapter, the model-independent $|V_{ub}|$ extraction method of Leibovich, Low, and Rothstein is presented in detail.

2.1 The Standard Model

Fundamental particle properties and interactions are described by the Standard Model (SM). In the SM, all matter is comprised from the six quarks and six leptons. The quarks and leptons are classified as fermions, which are particles with half-integer spin $J^P = n + \frac{1}{2}$. The quarks and leptons are separated into three generations with the third generation having the largest masses and the first generation having the smallest masses. Matter made up of second and third generation particles is not stable and ultimately decays to first generation matter. Table 2.1 summarizes the matter constituent of the SM and their properties.

In the SM, quarks and leptons can interact through the fundamental forces of nature via the

Table 2.1: The six quarks and six leptons and their properties are presented in this table. They are split into three generations. u is the "up" quark, d is the "down" quark, c is the "charm" quark, s is the "strange" quark, t is the "top" quark, b is the "bottom" quark, e is the electron, μ is the muon, τ is the tau lepton, and ν_X are the corresponding neutrinos.

Quark	Q (e)	Mass (GeV/c^2)	Lepton	Q (e)	Mass (MeV/c^2)
u	$+\frac{2}{3}$	~ 0.003	e	-1	0.511
d	$-\frac{1}{3}$	~ 0.006	ν_e	0	~ 0
c	$+\frac{2}{3}$	~ 1.25	μ	-1	105.7
s	$-\frac{1}{3}$	~ 0.10	ν_μ	0	~ 0
t	$+\frac{2}{3}$	~ 175	τ	-1	1777.0
b	$-\frac{1}{3}$	~ 4.5	ν_τ	0	~ 0

exchange of gauge bosons. These gauge bosons are force carrying particles that carry spin of integer value $J^P = n$. There are four fundamental forces found in nature: gravity, electromagnetic (EM), weak, and strong. These forces and their associated properties and gauge bosons are described in Table 2.2

The gravitational force is a long-range force, mediated by the exchange of a massless boson called the graviton. The source of the interaction is the coupling of the energy-momentum tensor in two particles. Gravitational interactions are negligible in the study of particle interactions because the force is many orders of magnitude weaker than the other forces. The coupling constant in the classical formulation is

$$\frac{G_N M_1 M_2}{4\pi\hbar} \sim 10^{-40}$$

where M_1 and M_2 are the masses of the interacting particles, $\hbar$ is Planck's constant, and G_N is the gravitational constant.

The EM force is also a long-range force because it is mediated by the exchange of a massless boson, the photon. The theory of quantum electrodynamics (QED) describes EM interactions between particles in the SM. The source of the interaction is the electric charge of the particles. The coupling constant between two particles of unit charge e is

$$\frac{e^2}{4\pi\hbar} \sim \frac{1}{137}$$

The strong force governs interaction between quarks. Quarks are not known to exist as free par-

ticles, they are only observed as constituents of hadrons. The theory of quantum chromo-dynamics (QCD) describes the strong force in the SM. The source of the interaction is the color charge of the quark and it is mediated by the exchange of the massless gluon. Quarks can either have a color of red, blue, or green. Despite the gluon being massless, the strong force is a short-ranged force because the coupling between quarks is not constant. The force confining quarks into hadrons is very large at large distances, but vanishes at short distances. This principle is referred to as asymptotic freedom. The coupling constant for the strong force is

$$\alpha_s(m_b) \sim 0.22$$

The weak force is a short-range force between quarks and leptons. It is short-ranged because the gauge bosons that mediate the force are massive. The source of the force is the weak charge of particles. The theory of weak interactions is grouped together with EM theory in electroweak theory. All processes where a quark or lepton changes flavor are mediated through the electroweak interaction. The coupling for the weak force is

$$\frac{e^2}{8M_W^2 \sin^2(\Theta_W)} \sim 10^{-5}$$

where M_W is the mass of the W boson and Θ_W is the weak mixing angle.

Table 2.2: The fundamental forces of nature and their associated force carrying gauge bosons, spins, masses, effective range, sources and couplings.

		ElectroWeak		
	Gravity	EM	Weak	Strong
Gauge Boson	graviton	photon	W,Z	gluon
J^P	2^+	1^-	$1^\pm$	1^-
Mass (GeV/c^2)	0	0	80.4, 91.2	0
Range (m)	∞	∞	10^{-18}	10^{-15}
Source	mass	electric charge	weak charge	color charge
Coupling Constant	10^{-40}	10^{-2}	10^{-5}	1

While the SM of fundamental particle interaction is known to be consistent with all experimental results, it is considered to be incomplete. For example, the SM does not incorporate gravitation as a self-consistent quantum field theory. This particular example is not a problem per se because the effect of gravity between particles is negligible in comparison to the other forces. Rather, the complexity of the theory, such as the existence of three generations of quarks and leptons, and the

large number of parameters suggest that it cannot be the complete description of nature's particles and their interactions. As a result, there is an expectation that a more fundamental theory underlies the SM, which can be revealed either directly by experiments at higher energy or indirectly by inconsistencies in measurements at lower energy. Pursuing this latter approach, we attempt to test SM predictions with every increasing precision for such evidence.

2.2 The CKM Picture of Weak Interactions

In the SM, flavor changing processes involving quarks are mediated by the weak interaction. Take, for example, the neutron decay process $n \to p\, e\, \overline{\nu}_e$. The quark content of the neutron is udd and the quark content of the proton is uud. This a weak process because the decay clearly involves a transition of $d \to u$. That is to say, the d quark is changing flavor to a u quark.

In the formalism of quantum field theory[1], we can write a Lagrangian to describe the mechanics of the interaction of quarks with the $SU(2)_L$ gauge bosons that mediate the weak interaction as

$$\mathcal{L}_W = -\frac{1}{2} g \overline{Q^I_{Li}} \gamma^\mu \tau^a \mathbf{1}_{ij} Q^I_{Lj} W^a_\mu. \tag{2.1}$$

Here, Q^I_L are quark fields of the left-handed quark generations, W^a_μ are the gauge boson fields of the weak interaction, $\mathbf{1}_{ij}$ is the unit matrix, g is the weak coupling constant, τ^a are Pauli matrices operating in $SU(2)$ space, and γ^μ are Dirac matrices operating in Lorentz space.

In the SM, the Higgs field, which is a single complex scalar doublet $\phi = \binom{\phi^+}{\phi^0}$, is the postulated mechanism by which the fundamental particles of the SM acquire mass through spontaneous symmetry breaking. Spontaneous symmetry breaking occurs when a system that obeys a given symmetry loses its symmetry when it goes into a vacuum state (the lowest energy state). In particle dynamics, this spontaneous symmetry breaking is realized from the non-zero vacuum expectation value of the Higgs field. The expectation value of the field at vacuum can be expressed as

$$E_0^{vac} = \frac{1}{\sqrt{2}} \begin{pmatrix} 0 \\ v \end{pmatrix} \tag{2.2}$$

which is not symmetric in $SU(2)$ gauge theory because a global $SU(2)$ transformation

$$E_0^{vac'} = e^{i \overrightarrow{\alpha}\, \overrightarrow{\tau}} \frac{1}{\sqrt{2}} \begin{pmatrix} 0 \\ v \end{pmatrix} \tag{2.3}$$

[1]Quantum field theory is necessary to describe the theory of electro-weak interactions. As a reference, "An Introduction to Quantum Field Theory", by Michael Peskin and Daniel Schroeder is suggested

yields a distinct state that has the same energy.

The Lagrangian for the interaction of quarks with the Higgs field is

$$\mathcal{L}_Y = -G_{ij}\overline{Q^I_{Li}}\phi d^I_{Rj} - F_{ij}\overline{Q^I_{Li}}\tilde{\phi}u^I_{Rj} + \text{hermitian conjugate}, \tag{2.4}$$

where d^I_R and u^I_R are multiplets of the quark generations and G and F are general complex 3×3 matrices. The fact that they are complex is directly responsible for the existence of CP violation, as we will see. The charge conjugation C and parity P symmetries are discrete symmetries of particle dynamics. Charge conjugation reverses the quantum numbers describing the particle and the particle is changed into its antiparticle. Parity reflects the particle coordinates through the origin $P(ct, \overrightarrow{r}) \rightarrow (ct, -\overrightarrow{r})$. Both C and P are found to be violated in the weak interaction, and also the combination of C and P (CP) is known to be violated in the weak interaction.

The charged current from the flavor changing weak process in Eq. 2.1 can be written as

$$\mathcal{L}_{cc} = -\sqrt{\frac{1}{2}}g\overline{u^I_{Li}}\gamma^\mu \mathbf{1}_{ij} d^I_{Lj} W^+_\mu + \text{hermitian conjugate}, \tag{2.5}$$

and the mass terms for the quarks can be written from Eq. 2.4 as

$$\mathcal{L}_M = -\sqrt{\frac{1}{2}}vG_{ij}\overline{d^I_{Li}}d^I_{Rj} - \sqrt{\frac{1}{2}}vF_{ij}\overline{u^I_{Li}}u^I_{Rj} + \text{hermitian conjugate}. \tag{2.6}$$

The actual mass matrices for the quarks from Eq. 2.6 are then simply

$$M_d = Gv, \quad M_u = Fv. \tag{2.7}$$

The quark eigenstates are different from the mass eigenstates, therefore, to obtain physical mass eigenstates, the mass matrices must be diagonalized so

$$V_{dL}M_d{V^\dagger}_{dR} = M_d^{diag}, \quad V_{uL}M_u{V^\dagger}_{uR} = M_u^{diag}, \tag{2.8}$$

where the diagonalized matrices M_X^{diag} are real and unitary and the matrices V_{XL} and V_{XR} are complex and unitary since any complex matrix can be diagonalized by two unitary matrices. Equation 2.5 can now be rewritten in terms of the basis defined by the mass eigenstates as

$$\mathcal{L}_{cc} = -\sqrt{\frac{1}{2}}g\overline{u_{Li}}\gamma^\mu \overline{V}_{ij} d_{Lj} W^+_\mu + \text{hermitian conjugate}, \tag{2.9}$$

where the removal of the superscript I on the quark fields u and d indicates that the basis defined

by mass eigenstates is being used, and $\overline{V}_{ij} = V_{uL}V_{dL}$ is the Cabibbo-Kobayashi-Maskawa (CKM) matrix [1, 2].

The CKM matrix, $\overline{V}_{ij}$, is the complex and unitary mixing matrix for the three quark generations which describes the flavor changing processes of quarks.

$$\begin{pmatrix} d' \\ s' \\ b' \end{pmatrix} = V \begin{pmatrix} d \\ s \\ b \end{pmatrix} \tag{2.10}$$

where we express the CKM matrix as

$$V_{CKM} = \begin{pmatrix} V_{d'd} & V_{d's} & V_{d'b} \\ V_{s'd} & V_{s's} & V_{s'b} \\ V_{b'd} & V_{b's} & V_{b'b} \end{pmatrix} = \begin{pmatrix} V_{ud} & V_{us} & V_{ub} \\ V_{cd} & V_{cs} & V_{cb} \\ V_{td} & V_{ts} & V_{tb} \end{pmatrix} \tag{2.11}$$

The CKM matrix has nine parameters, three are real and six are complex phases. The matrix can be re-phased, however, so as to be described by only one complex phase. Such a re-phasing is permissible in this framework because re-phasing by a transformation

$$\overline{V} \quad \rightarrow \quad \overline{V} = P_u \overline{V} P_d^* \tag{2.12}$$

only redefines the phases of the mass eigenstates q_L and q_R $(q = u, d)$, which doesn't change the diagonalized mass matrices M_X^{diag}. It is this one remaining non-trivial phase in the CKM matrix that is thought to be responsible for the phenomenon of CP violation in the weak interaction. If there were only two generations of quarks, the CKM matrix would not permit CP violation because there would be no complex phase. It was this realization that led Kobayashi and Maskawa to predict the existence of a third generation of quarks [2].

Remembering that the CKM matrix is unitary ($VV^\dagger = 1$), several relations can be derived (see for example Ref. [3]). The three that are especially helpful in testing the predictions of the SM are:

$$V_{ud}V_{us}^* + V_{cd}V_{cs}^* + V_{td}V_{ts}^* = 0 \tag{2.13}$$

$$V_{us}V_{ub}^* + V_{cs}V_{cb}^* + V_{ts}V_{tb}^* = 0 \tag{2.14}$$

$$V_{ud}V_{ub}^* + V_{cd}V_{cb}^* + V_{td}V_{tb}^* = 0 \tag{2.15}$$

These three unitarity relations can be geometrically represented as triangles in the complex plane. They are called the "unitarity triangles". Pictures of the unitarity triangles are shown in Fig. 2.1. The triangles all have the same area, yet greatly different angles and leg lengths.

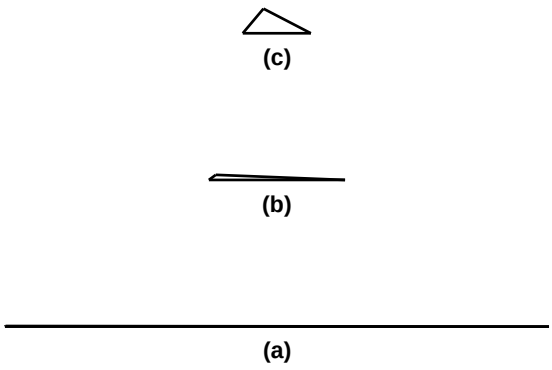

Figure 2.1: The three unitary triangles detailed in Eq. 2.13 (a), 2.14 (b), and 2.15 (c).

You can see from Fig. 2.1 that the first two triangles resulting from the unitarity relations almost appear to be a line. That is because the amount of CP violation in K decays and leading B_s decays is small, where as physics of the B meson, represented by the third triangle, predicts larger CP violation. Figure 2.2 depicts the unitarity triangle defined by Eq. 2.15.

The CKM matrix is commonly expressed in an expansion using four parameters (λ, A, ρ, η) where λ is the expansion parameter and η is the CP-violating phase. This is referred to as the Wolfenstein parameterization [4] and its form is

$$V_{CKM} = \begin{pmatrix} 1-\frac{\lambda^2}{2} & \lambda & A\lambda^3(\rho - i\eta) \\ -\lambda & 1-\frac{\lambda^2}{2} & A\lambda^2 \\ A\lambda^3(1-\rho-i\eta) & -A\lambda^2 & 1 \end{pmatrix} + \mathcal{O}(\lambda^4) \tag{2.16}$$

At a higher order ($\mathcal{O}(\lambda^6)$) in the expansion, the Wolfenstein parameters can be related to the matrix elements of the CKM matrix as

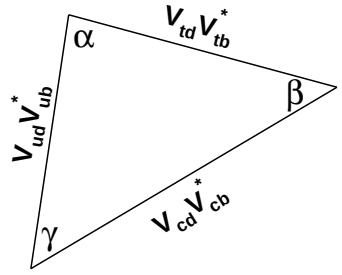

Figure 2.2: The unitary triangle.

$$V_{us} = \lambda, \quad V_{cb} = A\lambda^2, \quad V_{ub} = A\lambda^3(\rho - i\eta) \tag{2.17}$$

$$V_{td} = A\lambda^3(1 - \overline{\rho} - i\overline{\eta}) \tag{2.18}$$

$$Im(V_{cd}) = -A^2\lambda^5\eta, \quad Im(V_{ts}) = -A\lambda^4\eta \tag{2.19}$$

where

$$\overline{\rho} = \rho(1 - \frac{\lambda^2}{2}), \quad \overline{\eta} = \eta(1 - \frac{\lambda^2}{2}) \tag{2.20}$$

The Wolfenstein representation of the CKM matrix elements is a very good approximation to the full matrix. With these approximations, the unitarity triangle from Fig. 2.2 can be redrawn in the complex plane whose coordinate axes are $\overline{\rho}$ and $\overline{\eta}$. Figure 2.3 depicts this normalized triangle, where the length of the sides have all been divided by $|V_{cd}V_{cb}^*|$.

The lengths of the non-unit sides of the triangle in Fig. 2.3 are

$$R_b \equiv \sqrt{\overline{\rho}^2 + \overline{\eta}^2} = \frac{1 - \lambda^2/2}{\lambda}|\frac{V_{ub}}{V_{cb}}|, \quad R_t \equiv \sqrt{(1 - \overline{\rho})^2 + \overline{\eta}^2} = \frac{1}{\lambda}|\frac{V_{td}}{V_{cb}}| \tag{2.21}$$

and the angles of the triangle α, β, and γ are [5]

$$\alpha \equiv arg[-\frac{V_{td}V_{tb}^*}{V_{ud}V_{ub}^*}], \quad \beta \equiv arg[-\frac{V_{cd}V_{cb}^*}{V_{td}V_{tb}^*}], \quad \gamma \equiv arg[-\frac{V_{ud}V_{ub}^*}{V_{cd}V_{cb}^*}] = \pi - \alpha - \beta. \tag{2.22}$$

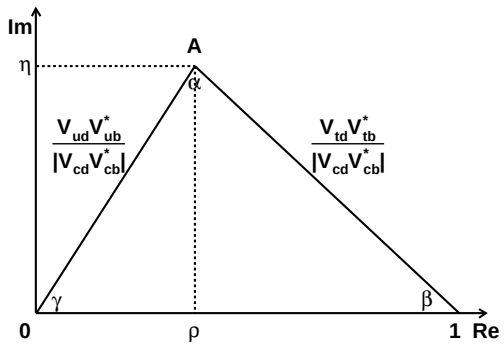

Figure 2.3: The rescaled unitary triangle, drawn in the (ρ, η) plane.

Making precise measurements of all of the elements of the CKM matrix, determining the sides (R_b, R_t) and angles (α, β, γ) of the unitarity triangles, and even determining whether they are in fact triangles is essential to testing and validating the predictions of the SM. Any deviation from the predictions of the SM could hint at physics existing outside the realm of the SM. Current measurements of $|V_{CKM}|$ are listed in Eq. 2.23 [6]. Figure 2.4 [7] displays fitted results for the sides and angles of the unitary triangle. The existing measurements of the off-diagonal elements, $|V_{td}|$ and $|V_{ub}|$, are the least well known. As can be seen from Fig. 2.4, the resulting constraint on the unitarity triangle will be substantially improved by new measurements. The various measurements of $|V_{ub}|$ tend to be dominated by large theoretical uncertainties, which will be discussed in greater depth in section 2.7.

$$|V_{CKM}| = \begin{pmatrix} 0.9739 - 0.9751 & 0.221 - 0.227 & 0.0029 - 0.0045 \\ 0.221 - 0.227 & 0.9730 - 0.9744 & 0.039 - 0.044 \\ 0.0048 - 0.014 & 0.037 - 0.043 & 0.9990 - 0.9992 \end{pmatrix} \tag{2.23}$$

2.3 Semileptonic Decays

Semileptonic decays of the B meson provide the ideal platform for the extraction of the CKM matrix elements $|V_{ub}|$ and $|V_{cb}|$. As one might expect, $b \to c\ell\bar{\nu}$ transitions are used to extract $|V_{cb}|$ and $b \to u\ell\bar{\nu}$ transitions are used to extract $|V_{ub}|$. Using these decays, the usually theoretically

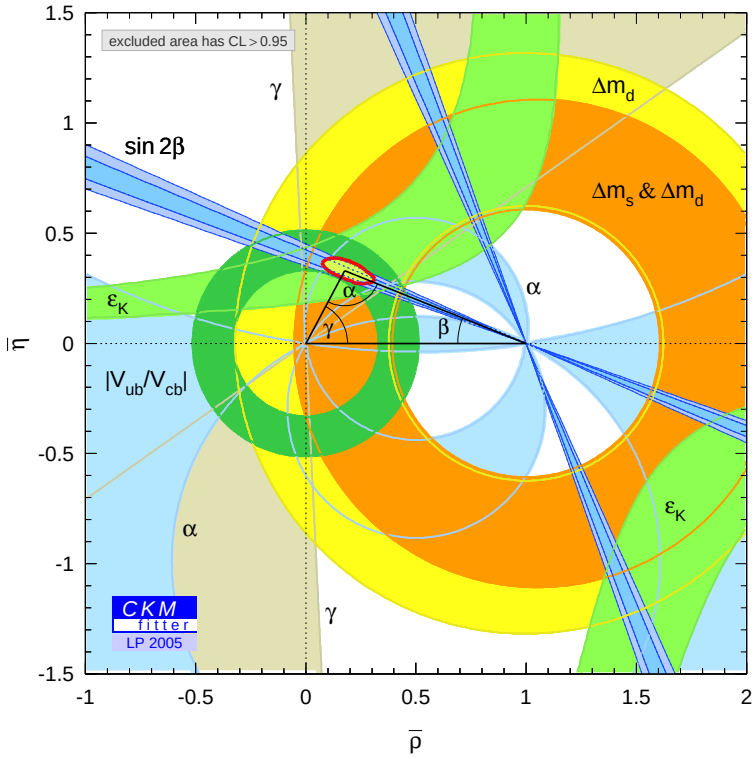

Figure 2.4: The experimental constraints for the sides and angles of the unitary triangle in the $(\overline{\rho}, \overline{\eta})$ plane.

complicated effects of non-perturbative QCD interactions in the weak decay processes are manageable because these QCD effects are solely present in the hadronic current, since the leptons do not interact via the strong force. The diagram in Fig. 2.5 clearly illustrates the localization of the QCD effects to the hadronic current in the decay process.

There are two basic ways to study the semileptonic decays of the B meson, both relating the semileptonic decay rates to the relevant CKM matrix elements. The first method is using *exclusive* decays. This means studying one or a handful of particular decay resonances. For example, of the possible $b \to c\ell\bar{\nu}$ decays, one could examine solely the decays of the B meson to the D^* in the process $B \to D^*\ell\nu$. The second method in studying semileptonic B decays is to study *inclusive* decays. This means that the sum of all of the possible final state hadrons are studied, with no specification made on the hadronic state accompanying the lepton and neutrino.

In the case of the $b \to c\ell\bar{\nu}$ decays, both the b and c quarks are very heavy which simplifies the theoretical calculations. For exclusive decays, the techniques of heavy quark effective theory (HQET) and heavy quark expansions (HQE) relate the decay rate to the matrix element $|V_{cb}|$ [8]-

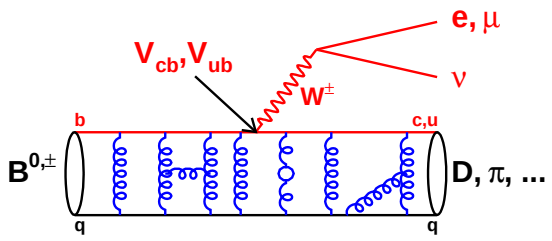

Figure 2.5: The semileptonic decay of a B meson. The complicated QCD effects carried by the gluons (depicted by the curly lines) are located entirely within the hadronic current.

[13]. These calculations proceed by using the heavy quark symmetry limit which holds in the limit of infinite mass for the b, and c quarks. In this limit, the b quark does not recoil when it changes flavor to the c quark. This allows the calculation of the form factors which describe the overlap of the wave functions for the initial and final state mesons. Corrections for the finite mass of the b and c quark are calculable. These corrections have been determined for $b \rightarrow c\ell\bar{\nu}$ decays, allowing the extraction of $|V_{cb}|$ with relatively small theoretical uncertainty. The situation is not quite as manageable in the case of exclusive $b \rightarrow u\ell\bar{\nu}$ decays due to the much smaller mass of the u quark. The form factors can be calculated using lattice gauge theory, QCD sum rules, perturbative QCD, or quark models. Unfortunately, with the light u quark in the final state, heavy quark symmetry is no longer directly applicable. Also, the light mass of the final state hadron provides more q^2 phase space for the final state hadron, making the form factor calculations less reliable.

For inclusive $b \rightarrow c\ell\bar{\nu}$ and $b \rightarrow u\ell\bar{\nu}$ decays it is possible to use operator product expansion (OPE) techniques [14] to relate the decay rates to the matrix elements $|V_{cb}|$ and $|V_{ub}|$. Theoretically, the inclusive approach is more desirable for two main reasons, leading to a less model-dependent determination of the CKM matrix elements. First, effects of the initial bound quark state, such as the Fermi motion of the b quark inside the hadron, can be dealt with using the heavy quark expansion. Second, there are no bound-state effects to be considered for the final state hadronic system as there are for exclusive decays. This is due to the fact that the energy released to the final state hadron in a b to light quark transition is large compared with the QCD energy scale ($\Lambda_{\rm QCD}$). The result is that the short-distance part of the decay (the disappearance of the b quark) and the long-distance part (appearance of the hadronic decay product) are factorized. The hadronization to the final decay product can be assumed to occur with unit probability, allowing only the short-distance part of the decay to be considered. The factorization of the long-distance and short-distance parts of the decay is known as parton-hadron duality.

2.4 Inclusive Decays of the B Meson

The starting point to describe the decay of hadron is the optical theorem [15, 16, 17], which describes the decay width of a hadron as

$$\Gamma(H_b \to X) = \frac{1}{m_{H_b}} \text{Im} \langle H_b | \mathbf{T} | H_b \rangle, \tag{2.24}$$

where H_b is a hadron containing a b quark, and T is the transition operator defined as

$$\mathbf{T} = i \int d^4x T\{\mathcal{L}_{\text{eff}}(x), \mathcal{L}_{\text{eff}}(0)\}, \tag{2.25}$$

where $\mathcal{L}_{\text{eff}}(x)$ is the effective weak Lagrangian. The relevant contributions to **T** are shown in the Feynman diagrams of Fig. 2.6. Due to the large mass of the b quark, an OPE can be applied in calculating **T**. In such an expansion, **T** can be expressed as a series of local operators containing b-quark fields (see Fig. 2.6). The result of the OPE is that any inclusive decay width of the B meson can be written as [15]-[20]

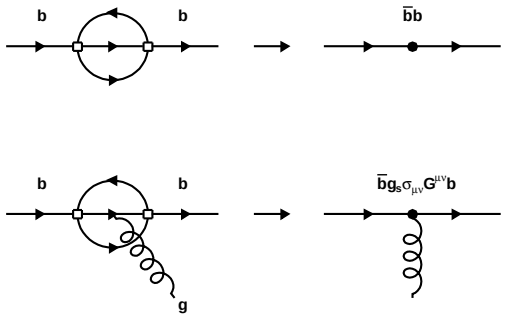

Figure 2.6: The contributing terms to the transition operator **T** (left), and the corresponding operators in the OPE (right). The open squares represent the four-fermion interaction in the weak Lagrangian $\mathcal{L}_{\text{eff}}$ and the black dots represent local operators of the $1/m_b$ expansion

$$\Gamma(\overline{B} \to X_f) = \frac{G_F^2 m_b^5}{192\pi^3} \left\{ c_3^f \langle \overline{b} b \rangle_B + c_5^f \frac{\langle \overline{b} g_s \sigma_{\mu\nu} G^{\mu\nu} b \rangle_B}{m_b^2} + ... \right\}, \tag{2.26}$$

where c_x^f are short-distance coefficients that are functions of the quantum numbers f of the final states and $\langle O \rangle_H$ is shorthand notation for normalized matrix elements of local operators that contain all of the long-distance information defined as

$$\langle O \rangle_B = \frac{1}{2m_B} \langle B|O|B\rangle. \tag{2.27}$$

where B is the B meson. These matrix elements can then be expanded in powers of $1/m_b$ using HQET. The expansion results in [15],[17]-[19], [21, 22]

$$\langle \overline{b}b \rangle = 1 + \frac{\lambda_1 + 3\lambda_2}{2m_b^2} + \mathcal{O}(1/m_b^3), \tag{2.28}$$

$$\frac{\langle \overline{b} g_s \sigma_{\mu\nu} G^{\mu\nu} b \rangle}{m_b^2} = \frac{6\lambda_2}{m_b^2} + \mathcal{O}(1/m_b^3), \tag{2.29}$$

where λ_1 describes the kinetic energy of the b quark inside the B meson and λ_2 describes the chromo-magnetic interaction among the quarks in the B meson. Plugging Eqs. 2.28 and 2.29 into Eq. 2.26 provides the expression describing the decay width of a B meson

$$\Gamma(\overline{B} \to X_f) = \frac{G_F^2 m_b^5}{192\pi^3} \left\{ c_3^f \left(1 + \frac{\lambda_1 + 3\lambda_2}{2m_b^2} \right) + c_5^f \frac{6\lambda_2}{m_b^2} + ... \right\}. \tag{2.30}$$

The first term in Eq. 2.30, proportional to m_b^5, is the result at the parton level for a free quark decay [23, 24]. The terms containing λ_1 and λ_2 are proportional to m_b^3 and are non-perturbative corrections to the free quark decay. They account for bound state affects inside the B meson. Given the large mass of the b quark, the free quark decay model is quite accurate [25]-[28].

2.5 Extracting $|V_{ub}|$ from Charmless Inclusive Semileptonic Decays

The charmless inclusive semileptonic decay width of the B meson $\Gamma(B \to X_u \ell \nu)$ provides a way to extract the CKM matrix element $|V_{ub}|$. To adapt the generic expression of Eq. 2.30 to describe semileptonic decay rates, the proper values of the short-distance coefficients c_3^f and c_5^f need to be inserted. These coefficients are proportional to the square of the CKM matrix element, which allows us to relate the decay width to the CKM matrix element. For $b \to u \ell \bar{\nu}$ transitions, these coefficients are

$$c_3^{\text{SL}} = |V_{ub}|^2 \{1 + \mathcal{O}(\alpha_s)\}, \tag{2.31}$$

$$c_5^{\text{SL}} = -|V_{ub}|^2. \tag{2.32}$$

Inserting the short-distance coefficients into Eq. 2.30 yields

$$\Gamma(\overline{B} \to X_u \ell \overline{\nu}) = \frac{G_F^2 |V_{ub}|^2 m_b^5}{192\pi^3} \left\{ 1 + \frac{\lambda_1 - 9\lambda_2}{2m_b^2} + \mathcal{O}(\alpha_s) + ... \right\} \tag{2.33}$$

Calculations in reference [29] provide the $\mathcal{O}(\alpha_s)$ corrections to the expression which yields the following expression

$$\Gamma(\overline{B} \to X_u \ell \overline{\nu}) = \frac{G_F^2 |V_{ub}|^2 m_b^5}{192\pi^3} \left\{ 1 - 2.41\frac{\alpha_s}{\pi} + \frac{\lambda_1 - 9\lambda_2}{2m_b^2} + ... \right\} \tag{2.34}$$

The theoretical errors in Eq. 2.34 come from the non-perturbative parameters (λ_1 and λ_2) and uncertainty in the mass of the b quark m_b. The non-perturbative errors are small, whereas the error from the b quark mass is larger and dominates the uncertainty. Nevertheless, the theoretical errors are manageable and have been calculated and yield the following expression to relate the charmless semileptonic branching fraction $\mathcal{B}(\overline{B} \to X_u \ell \overline{\nu})$ to $|V_{ub}|$ [30, 31]

$$|V_{ub}| = 0.00424 \left(\frac{\mathcal{B}(\overline{B} \to X_u \ell \overline{\nu})}{0.002} \frac{1.61ps}{\tau_b} \right)^{1/2} \times (1 \pm 0.028_{OPE} \pm 0.039_{m_b}). \tag{2.35}$$

Here, τ_b is the lifetime of the B meson, and the charmless semileptonic branching fraction $\mathcal{B}(\overline{B} \to X_u \ell \overline{\nu})$ is related to the decay width $\Gamma(\overline{B} \to X_u \ell \overline{\nu})$ as

$$\Gamma(\overline{B} \to X_u \ell \overline{\nu}) = \frac{\mathcal{B}(\overline{B} \to X_u \ell \overline{\nu})}{\tau_b} \tag{2.36}$$

In Eq. 2.35, the b quark mass is assumed to be $m_b = 4.61 \pm 0.07\,\mathrm{GeV}/c^2$ [32]. The subscripts in the last two terms of Eq. 2.35 refer to the errors in the OPE calculation and the error due to uncertainty in the b quark mass, respectively.

2.6 Extracting $|V_{ub}|$ in the Real World

With the expression in Eq. 2.35, a simple method exists for the extraction of $|V_{ub}|$ from the total charmless decay rate with a small theoretical uncertainty ($\sim 5\%$ [30, 31]). Unfortunately, until this point, the measurement of the total charmless decay rate has been considered impossible because the B meson favors decaying via a charm channel by two orders of magnitude, i.e. $\mathcal{B}(b \to c\ell\bar{\nu}) \sim 100 \times \mathcal{B}(b \to u\ell\bar{\nu})$ or $|V_{cb}| \sim 10 \times |V_{ub}|$ and the decays are not distinguishable over the entire phase space.

How do we work around this problem and separate the charmless from the charm decays? As it turns out, the heavy mass of the c quark and the light mass of the u quark are what allow us to experimentally separate the decays. Because of this mass difference, the energy of the lepton E_ℓ in the decay and the mass of the decay product hadron m_X are distributed differently for $b \to c\ell\bar{\nu}$ and $b \to u\ell\bar{\nu}$ decays. The high energy endpoint of the lepton energy spectra for the $b \to c\ell\bar{\nu}$ decays tails off above $2.3\,\mathrm{GeV}$ and the remaining phase space contains mostly $b \to u\ell\bar{\nu}$ decays. Similarly, the low mass region of the hadronic mass spectrum of semileptonic decays is dominated by $b \to u\ell\bar{\nu}$ decays, with the $b \to c\ell\bar{\nu}$ decays clustering at higher masses $m_X > m_D$. These examples are illustrated in Figs. 2.7 and 2.8.

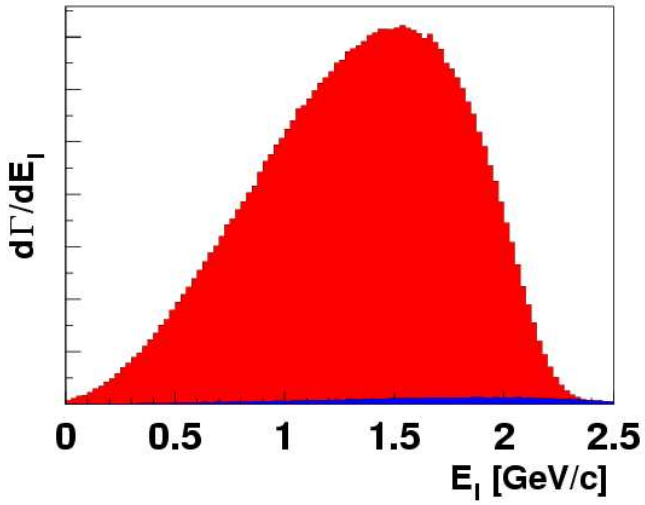

Figure 2.7: The lepton energy spectra of semileptonic decays. The charmless $b \to u\ell\bar{\nu}$ decays are shown in blue while the $b \to c\ell\bar{\nu}$ decays are shown in red. The high momentum region above $2.3\,\mathrm{GeV}/c$ is dominated by $b \to u\ell\bar{\nu}$ decays.

This means that, experimentally, we can measure a part of the charmless semileptonic rate in a favorable region of phase space. Of course, to extract $|V_{ub}|$ in Eq. 2.35, the total rate is required. To reconcile the situation and provide a framework to translate the phase space restricted measurement of the charmless semileptonic decay rate to $|V_{ub}|$, the semileptonic decay width OPE must be re-computed as a differential distribution of the relevant kinematic variables such as the lepton energy or hadronic mass. In the case of the lepton energy, to order $1/m_b^2$, the OPE results in [19, 20]

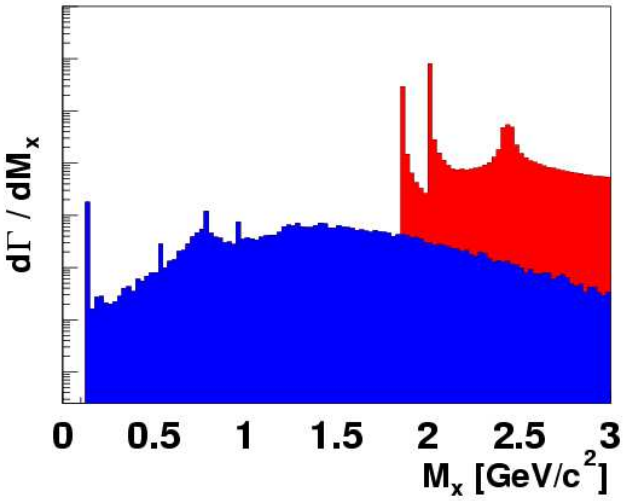

Figure 2.8: The hadronic mass spectra from semileptonic decays before the effects of detector resolution. The charmless $b \to u\ell\bar{\nu}$ decays are shown in blue while the $b \to c\ell\bar{\nu}$ decays are shown in red. Note the logarithmic scale for the vertical axis. The low mass region is dominated by $b \to u\ell\bar{\nu}$ decays and the region above m_D is dominated by $b \to u\ell\bar{\nu}$ decays.

$$\begin{aligned}\frac{1}{\Gamma_0}\frac{d\Gamma}{dx} = \Theta(1-x)\Bigg[&\frac{5x^3}{3}\frac{2\lambda_1}{m_b^2} + (6+5x)x^2\frac{2\lambda_2}{m_b^2}\Bigg] \\ &-\frac{\lambda_1+33\lambda_2}{3m_b^2}\delta(1-x) - \frac{\lambda_1}{3m_b^2}\delta'(1-x) \\ &+\Theta(1-x)2x^2(3-2x)[1-\frac{2\alpha_s}{3\pi}G(x)],\end{aligned} \tag{2.37}$$

where δ' is the derivative of the delta function, $x = 2E_\ell/m_b$ is the scaled lepton energy, and

$$\begin{aligned}G(x) &= \log^2(1-x) + 2\mathrm{Li}_2(x) + \frac{2\pi^2}{3} + \frac{82-153x+86x^2}{12x(3-2x)} \\ &+ \frac{41-36x+42x^2-16x^3}{6x^2(3-2x)}\log(1-x) \qquad (2.38)\end{aligned}$$

$$\Gamma_0 = |V_{ub}|^2\frac{G_F^2 m_b^5}{192\pi^3} \tag{2.39}$$

The first two lines in Eq. 2.37 contain the non-perturbative corrections and the last line contains the perturbative corrections. The differential decay width given in Eq. 2.37 can be understood as a double expansion in powers of $\Lambda_{\mathrm{QCD}}/m_b$ and $\Lambda_{\mathrm{QCD}}/m_b(1-x)$. This expansion is well behaved in

most of phase space except near the endpoint. At the endpoint (as $x \rightarrow 1$), the expansion becomes singular. To solve the singularity problem, the terms can be re-summed in a twist expansion. In doing so, it is useful to define a non-perturbative shape function $f(k_+)$ [33]. The shape function describes the distribution of the light-cone residual momentum k_+ of the heavy quark 4-momentum $\overrightarrow{k}$ inside the B meson (*i.e.* $k_+ \sim k^0 + k^3$) and is defined as [33]-[37]

$$f(k_+) = \frac{1}{2m_B}\langle B(v)|\overline{b}_v \delta(k_+ - iD_+) b_v|B(v)\rangle \tag{2.40}$$

where D is the QCD covariant derivative operator and $D_+ = D^0 + D^3$. The domain of the shape function is $\infty \leq \ k_+ \leq \overline{\Lambda}$ where $\overline{\Lambda} = m_B - m_b$ is the mass splitting between the B meson and b quark. The decay distribution can now be expressed in terms of this shape function as

$$\frac{d\Gamma}{dX} = \int dk_+ \, f(k_+) \frac{d\Gamma_p}{dX}(m_b^*). \tag{2.41}$$

where X is any kinematic variable describing the charmless semileptonic decay, $\frac{d\Gamma_p}{dX}$ is the decay distribution from the parton level calculations, and m_b^* is the effective mass $m_b^* = m_b + k_+$. In the case of the lepton energy the form is

$$\frac{d\Gamma}{dE_\ell} = \int_{2E_\ell - m_b}^{\overline{\Lambda}} dk_+ \, f(k_+) \frac{d\Gamma_p}{dE_\ell}(m_b^*), \tag{2.42}$$

Thus, we have the decay distribution expressed as a function of x_B since

$$x \equiv \frac{2E_\ell}{m_b^*} = \frac{m_B x_B}{m_b^*}, \quad x_B = \frac{2E_\ell}{m_B}. \tag{2.43}$$

With Eq. 2.41, we have a way to extract $|V_{ub}|$ from measuring the branching fraction of $b \rightarrow u\ell\bar{\nu}$ decays in an experimentally favorable region of the phase space. But, what of the uncertainties in this formulation? Unfortunately, the shape function $f(k_+)$ describing the decay width is not theoretically calculable and introduces model dependence through assumptions about its functional form. In principle, the first few moments of the shape function can be measured, but this is a difficult enterprise experimentally. Also, the shape function is sensitive to higher moments, and we are still left with large uncertainties.

2.7 Extracting $|V_{ub}|$ with Reduced Model Dependency

In section 2.6 we have finally understood a way that theory and experiment can come together and extract $|V_{ub}|$ from the decay rate of $b \to u\ell\bar{\nu}$ decays. It is understood, though, that the method has large uncertainty due to ad-hoc model dependence. The uncertainty is not only from the choice of how to parameterize the shape function, but also the parameters themselves. Beyond this, it is even difficult to find a way to quantify the uncertainties. Clearly, a better solution is needed to extract $|V_{ub}|$ with reduced model dependence and uncertainty.

A key observation is that the shape function is universal appearing as well in the inclusive radiative decays $b \to s\gamma$ [34]. Thus, similar to the expression in Eq. 2.42, the differential decay distribution of the $b \to s\gamma$ photon energy spectrum can be described in terms of the energy of the photon E_γ as

$$\frac{d\Gamma}{dE_\gamma} = \int_{2E_\gamma - m_b}^{\overline{\Lambda}} dk_+ \, f(k_+) \frac{d\Gamma_p}{dE_\gamma}(m_b^*). \tag{2.44}$$

In addition, it has been observed that if one takes the ratio of moments of these differential distributions for $b \to s\gamma$ and $b \to u\ell\bar{\nu}$, the dependence on the shape function is removed [34]. The necessary calculations were made and a closed form for the extraction of $|V_{ub}|$ from the the lepton energy endpoint was presented by Leibovich, Low, and Rothstein (LLR) in reference [38]. Later, they provided the corresponding method to extract $|V_{ub}|$ from the hadronic mass spectrum [39].

To explain this method [38]-[40], let us define the following kinematic variables:

$$y_0 = \frac{2v \cdot q}{m_b}, \quad y = \frac{q^2}{m_b^2}, \quad x = \frac{2v \cdot p_\ell}{m_b}, \quad h = \frac{2v \cdot p_h}{m_b}, \tag{2.45}$$

where $v = (1, \overrightarrow{0})$, p_h is the momentum of the hadron, and $q = (p_\ell + p_\nu)$ describes the momentum of the lepton and neutrino pair. In this basis, the charmless semileptonic decay width can be expressed as a triple differential decay width, which conveniently factorizes into hard (H), jet (J), and soft (S) processes [41],

$$\frac{1}{\Gamma_0}\frac{d^3\Gamma}{dy_0 dy dx} = 12(y_0 - x)(x - y) \int_\xi^{m_B/m_b} dz \, S(z) m_b^2 J[m_b^2 h(z - \xi), \mu] H(m_b h/\mu) \tag{2.46}$$

where the factorization scale μ is introduced to delineate the contributing parts into different momentum regions, Γ_0 is defined in Eq. 2.39, $\xi = (1-y)/(2-y_0)$, and $z = 1 + k_+/m_b$. If we change

variables from y to ξ and integrate over x, we obtain

$$\frac{1}{\Gamma_0}\frac{d^2\Gamma}{dy_0 d\xi} = 2(2-y_0)(2y_0-1)\int_{\xi}^{m_B/m_b} dz\, S(z) m_b^2 J[m_b^2(2-y_0)(z-\xi)] H[m_b(2-y_0)]. \quad (2.47)$$

As $p_h \sim 0$ and $z \sim \xi \sim 1$, the jet part $J[m_b^2(2-y_0)(z-\xi)]$ can be replaced with $J[m_b^2(2-y_0)(1-\xi/z)]$. The moments M_N of Eq. 2.47 are then expressed as

$$\begin{aligned} M_N &= \int_0^{m_B/m_b} d\xi\, \xi^{N-1} \frac{1}{\Gamma_0}\frac{d^2\Gamma}{d\xi dy_0} \\ &= 2(2-y_0)^2(2y_0-1) S_N J_N [m_b^2(2-y_0)/\mu^2] H[m_b(2-y_0)/\mu] + \mathcal{O}(\frac{1}{N}) \quad (2.48) \end{aligned}$$

where the moments of the jet and soft parts J_N and S_N are

$$J_N(m_b^2/\mu^2) = m_b^2 \int_0^1 dy\, y^{N-1} J[m_b^2(1-y), \mu] \quad (2.49)$$

$$S_N = \int_0^{m_B/m_b} dz\, z^N S(z). \quad (2.50)$$

The soft part can be separated into a perturbative piece $\sigma(z/s)$ and non-perturbative piece $f(s)$

$$S(z) = \int_z^{m_B/m_b} \frac{ds}{s} f[m_b(s-1)]\sigma(z/s). \quad (2.51)$$

Note that f is the same shape function from Eq. 2.40. Equation 2.51 yields moments that can also be separated into perturbative and non-perturbative parts

$$S_N = f_N \sigma_N. \quad (2.52)$$

The corresponding analysis of $b \to s\gamma$ decays yields very similar results [41]. These calculations provide the moments of the differential $b \to s\gamma$ decay width in terms of the photon energy E_γ

$$M_N^\gamma = \frac{1}{\Gamma_0^\gamma}\int_0^{m_B/m_b} dx_\gamma\, x_\gamma^{N-1}\frac{d\Gamma^\gamma}{dx_\gamma} = S_N J_N^\gamma H^\gamma \tag{2.53}$$

$$\Gamma_0^\gamma = \frac{G_F^2|V_{ts}^*V_{tb}|\alpha_{\rm QED}C_7^{(0)}(m_b)^2(1+H_{\rm mix}^\gamma)m_b^5}{32\pi^4} \tag{2.54}$$

$$H_{\rm mix}^\gamma = \frac{\alpha_s}{2\pi C_7^{(0)}}\left[C_7^{(1)} + C_2^{(0)}\mathcal{R}(r_2) + C_8^{(0)}\left(\frac{44}{9}-\frac{8\pi^2}{27}\right)\right], \tag{2.55}$$

where $x_\gamma = 2E_\gamma/m_b$, $\mathcal{R}(r_2) \approx -4.092 + 12.78(m_c/m_b - 0.29)$ [42, 43], and $C_j^{(i)}$ are Wilson coefficients [44]-[47]. The term $H_{\rm mix}^\gamma$ accounts for interference between the electromagnetic penguin operator O_7 with O_2 and O_8 [42, 43]. As can be seen in Eq. 2.53, the moments are factorized (like the $b \to u\ell\bar{\nu}$ moments) into soft, hard, and jet processes. The superscripts on the hard and jet processes indicate that the moments are different than the $b \to u\ell\bar{\nu}$ moments, but the soft moments S_N are the same moments that appear in the $b \to u\ell\bar{\nu}$ analysis.

The calculations for the soft and jet function moments have been performed at next-to-leading (NLL) logarithmic order [48] and they yield

$$\sigma_N J_N = e^{\log(N)g_1(\chi)+g_2^\gamma(\chi)+g_{sl}(\chi,y_0)} \tag{2.56}$$

$$\sigma_N J_N^\gamma = e^{\log(N)g_1(\chi)+g_2^\gamma(\chi)}, \tag{2.57}$$

where $\chi = \alpha_s(m_b^2)\beta_0\log N$ and g_1, g_2^γ, and g_{sl} are defined in [38]. The hard parts for the two types of decays are given by

$$H(y_0) = 1 - \frac{2\alpha_s}{3\pi}\left[4\log^2(2-y_0) + \frac{8-10y_0}{2y_0-1}\log(2-y_0) + 2{\rm Li}_2(y_0-1) + \frac{5}{2} + \frac{2\pi^2}{3}\right] \tag{2.58}$$

$$H^\gamma = 1 - \frac{2\alpha_s}{3\pi}\left(\frac{13}{2}+\frac{2\pi^2}{3}\right). \tag{2.59}$$

It is now time to return to the physical space from the detour into moment space. To do this, an inverse Mellin transformation must be performed at NLL. The transformation is long and complicated, the details of which can be found in the appendix of reference [38]. The result of an inverse Mellin transformation on Eq. 2.48 is

$$\frac{1}{\Gamma_0}\frac{d^2\Gamma}{dy_0 d\xi} = 2(2-y_0)^2(2y_0-1)H(y_0) \times\frac{d}{d\xi}\left\{\Theta(1-\xi-\eta)\frac{e^{lg_1(\alpha_s\beta_0 l)+g_2(\alpha_s\beta_0 l)}}{\Gamma[1-g_1(\alpha_s\beta_0 l)-\alpha_s\beta_0 l g_1'(\alpha_s\beta_0 l)]}\right\}, \quad (2.60)$$

where $l = -\log(-\log\xi) \approx -\log(1-\xi)$ and $g_2 = g_2^{\gamma} + g_{sl}$. The function Θ serves to make the differential rates a distribution, as $\eta \to 0$.

The fact that the soft function in Eq. 2.51 is universal to inclusive B decays, allows for the extraction of $|V_{ub}|$. Using equations 2.53-2.57 in Eq. 2.48 to substitute for the soft function, the following result is obtained

$$M_N = 2(2-y_0)^2(2y_0-1)\frac{H(y_0)}{H^{\gamma}}e^{g_{sl}(\chi,y_0)}M_N^{\gamma}. \quad (2.61)$$

Once again, applying an inverse Mellin transform, the following relation is derived

$$\frac{\Gamma_0^{\gamma}}{\Gamma_0}\frac{d^2\Gamma}{dy_0 d\xi} = 2(2-y_0)^2(2y_0-1) \times\int_{\xi}^{1}\tilde{H}(y_0)du\frac{d\Gamma^{\gamma}}{du}\left(-z\frac{d}{dz}\right)[\Theta(1-z-\eta)e^{g_{sl}(\chi_z,y_0)}], \quad (2.62)$$

where $\chi_z = -\alpha_s\beta_0\log(1-z)$, $u = 2E_{\gamma}/m_B$, $z = \xi/u$, and

$$\tilde{H}(y_0) = \frac{H(y_0)}{H^{\gamma}} = 1-\frac{2\alpha_s}{3\pi}\left[4\log^2(2-y_0)+\frac{8-10y_0}{2y_0-1}\log(2-y_0)+2\mathrm{Li}_2(y_0-1)-4\right] \quad (2.63)$$

$$g_{sl}(\chi,y_0) = \frac{4}{3\pi\beta_0}\log(2-y_0)\log(1-\chi). \quad (2.64)$$

where the variables are now defined at a physical scale, $i.e.$ they are normalized to the mass m_B of the B meson instead of the mass m_b of the b quark. Integrating over the double differential distribution from Eq. 2.62 to get the cut integrated rate $\delta\Gamma(c)$, where $c = (m_X^{\max}/m_B)^2$ is the hadronic mass cut, yields the following expression

$$d\Gamma(c) = \left(\int_{1-\frac{\sqrt{c}}{2}}^{\frac{1}{1+c}} du \int_{\frac{1-\sqrt{c}/2}{u}}^{1} dz \int_{2-\frac{c}{1-uz}}^{4uz-2} dy_0 + \int_{\frac{1}{1+c}}^{1} du \int_{\frac{1-\sqrt{c}/2}{u}}^{\frac{1}{u(1+c)}} dz \int_{2-\frac{c}{1-uz}}^{4uz-2} dy_0 \right.$$
$$\left. + \int_{\frac{1}{1+c}}^{1} du \int_{\frac{1}{u(1+c)}}^{1} dz \int_{2-\frac{1}{uz}}^{4uz-2} dy_0 \right) \frac{\Gamma_0}{\Gamma_0^\gamma} I(u, y_0, z) \quad (2.65)$$

$$I(y, y_0, z) = 2(2-y_0)^2(2y_0-1)\tilde{H}(y_0)\frac{d\Gamma^\gamma}{du}\left(- z\frac{d}{dz}\right)\left[\Theta(1-z-\eta)e^{g_{sl}(\chi_z, y_0)}\right]. \quad (2.66)$$

If we expand g_{sl} to order α_s, we are left with a closed expression for $|V_{ub}|$ in terms of the partial radiative decay rate and the partial charmless semileptonic decay rate. Using the following approximation

$$-\frac{d}{dz}(\Theta(1-z)e^{g_{sl}}) \approx \delta(1-z) + \frac{4\alpha_s}{3\pi}\left(\frac{\log(2-y_0)}{1-z}\right)_+ \quad (2.67)$$

where the plus distribution is defined as

$$\int_a^1 dx\, \frac{f(x)}{(1-x)_+} = \int_a^1 dx\, \frac{f(x)-f(1)}{1-x} - \int_0^a dx\, \frac{f(1)}{1-x} \quad (2.68)$$

we conclude that

$$\delta\Gamma(c) = \frac{\Gamma_0}{\Gamma_0^\gamma}[I_0(c) + I_+(c)] \quad (2.69)$$

where $I_0(c)$ and $I_+(c)$ are defined as

$$I_0(c) = \left(\int_{1-\frac{\sqrt{c}}{2}}^{\frac{1}{1+c}} du \int_{2-\frac{c}{1-u}}^{4u-2} dy_0 + \int_{\frac{1}{1+c}}^{1} du \int_{2-\frac{1}{u}}^{4u-2} dy_0 \right) 2(2-y_0)^2(2y_0-1)\frac{d\Gamma^\gamma}{du}\tilde{H}(y_0) \quad (2.70)$$

$$I_+(c) = \int du \int dz \int dy_0 2(2-y_0)^2(2y_0-1)z\frac{d\Gamma^\gamma}{du}\frac{4\alpha_s}{3\pi}\left(\frac{\log(2-y_0)}{1-z}\right)_+ \quad (2.71)$$

and the limits of the integrals in Eq. 2.71 are the same as those that appear in Eq. 2.65.

The functions $I_0(c)$ and $I_+(c)$ are simply weighted integrals over the partial photon energy spectrum from $b \to s\gamma$ decays, and $\delta\Gamma(c)$ is simply the partial decay rate of charmless semileptonic decays from the measurable low mass region of the hadronic mass spectrum. Plugging equations 2.39 and 2.54 into Eq. 2.69 yields the following simple expression for the extraction of $|V_{ub}|$ (with no dependence on ad-hoc models) in terms of these two measurable quantities

$$\frac{|V_{ub}|}{|V_{ts}|} = \left\{ \frac{6\alpha(1 + H^{\gamma}_{mix})C_7(m_b)^2\delta\Gamma(c)}{\pi[I_0(c) + I_+(c)]} \right\}^{\frac{1}{2}}. \tag{2.72}$$

Upon reflection, Eq. 2.72 is quite remarkable. Previously, to extract $|V_{ub}|$ from a measurement of the decay rate of inclusive charmless semileptonic decays in a measurable region of the phase space (*i.e.* low hadronic mass region), we had to rely on an ad-hoc model for the shape function and extract parameters by measuring the first few moments of the photon energy spectrum from $b \to s\gamma$ decays to describe the chosen model. With Eq. 2.72, the leading dependence on the shape function has been eliminated and $|V_{ub}|$ is related to the measurable region of the hadronic $b \to u\ell\bar{\nu}$ mass spectrum and the measurable $b \to s\gamma$ photon energy spectrum.

Chapter 3

The *BABAR* Experiment

The measurements presented in this dissertation were performed using data collected by the *BABAR* detector at the PEP-II asymmetric-energy electron-positron (e^+e^-) storage ring which is located at the Stanford Linear Accelerator Center (SLAC) in Menlo Park, California. In this chapter, the design and performance of PEP-II and *BABAR* will be described.

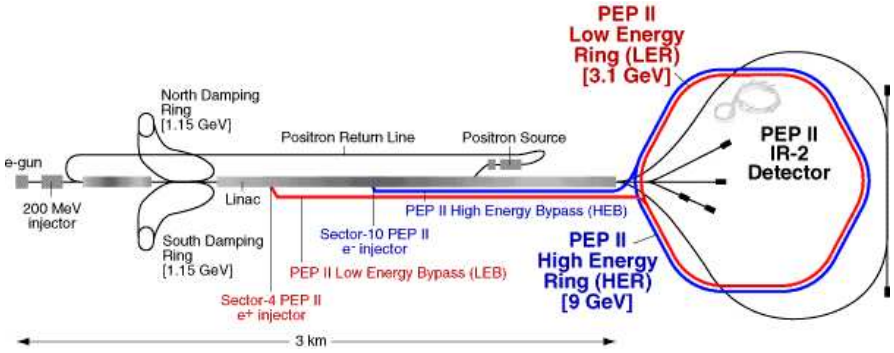

Figure 3.1: The Stanford Linear Accelerator Center.

3.1 PEP-II B Factory

The PEP-II B Factory [49] is an asymmetric energy e^+e^- collider operating at a high luminosity, upward of $\sim 10^{33}\text{cm}^{-2}\text{s}^{-1}$. The electrons and positrons are delivered in bunches and they collide head-on inside the *BABAR* detector. The luminosity $\mathcal{L}$ of the colliding beams is defined as

$$\mathcal{L} = \frac{nfN_1N_2}{A} \tag{3.1}$$

where n is the number of bunches, f is the frequency at which the bunches are colliding, $N_1(N_2)$ is the number of electrons (positrons) in each bunch, and A is the area of the bunches at the collision point.

An e^+e^- collider is preferred over a hadronic collider because the e^+e^- collisions provide an excellent signal-to-background ratio $\sigma_{\overline{b}}/\sigma_{\mathrm{TOT}} \sim 0.28$ (see Table 3.2), clean events characterized by low charged track multiplicities $N_{\mathrm{trk}} \sim 11$, low interaction rates $\sim 10\,\mathrm{Hz}$, and the ability to reconstruct decays containing photons and π^0s [50]. The center-of-mass (CM) energy for the e^+e^- bunch collisions is $\sqrt{s} = 10.58\,\mathrm{GeV}$, which coincides with the mass of the $\Upsilon(4S)$ $b\overline{b}$ resonance. The $\Upsilon(4S)$ is chosen as the operating point because of its relatively large cross section ($1\,\mathrm{nb}$) and the fact that it decays exclusively to $B^0\overline{B}^0$ and B^+B^- pairs, with nearly equal probability [51]. This makes it an ideal source for the study of the properties associated with decays of the B meson. PEP-II is designed to operate with an electron beam (HER) at $9.0\,\mathrm{GeV}$ and a positron beam (LER) at $3.1\,\mathrm{GeV}$, resulting in a Lorentz boost for the $\Upsilon(4S)$ events of $\beta\gamma = 0.56$ in the laboratory frame. The purpose of this boosted collision is to allow for the reconstruction of the decay vertexes of the B meson pair, which is important for measuring time dependent decay rates in $\mathcal{CP}$ analyses. The effect of the boost on the polar angle is shown in Fig. 3.2. The PEP-II design parameters and the achieved values for these parameters are presented in Table 3.1.

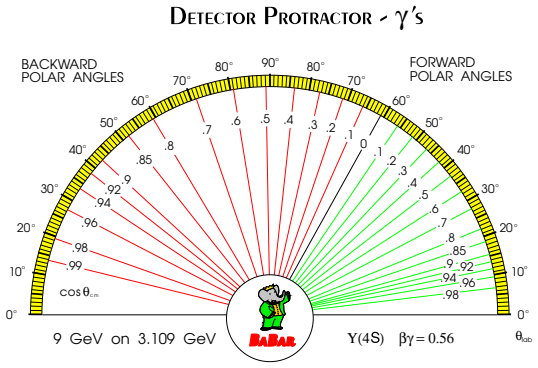

Figure 3.2: The polar angle relationship between the CM frame (expressed as the inscribed $\cos\theta_{\mathrm{CM}}$ lines) and the laboratory frame (outer markings on the protractor). The detector active region lies between $350\,\mathrm{mrad}$ in the forward direction and $400\,\mathrm{mrad}$ in the backward direction.

As previously mentioned, data collection occurs mostly with CM energy of the $\Upsilon(4S)$ resonance. This data is referred to as *on-resonance data*. A summary of the production cross-sections for

Table 3.1: The PEP-II beam design parameters and the corresponding achieved values as of July 2004. σ_{Lx}, σ_{Ly}, σ_{Lz} refer to the size of the interaction region of the collision.

Parameter	Design	Achieved
Energy HER(LER) (GeV)	9.0 (3.1)	9.0 (3.1)
Current HER(LER) (A)	0.75 (2.15)	1.55 (2.45)
# of Bunches	1658	1588
Bunch Spacing (ns)	4.2	$6.3 - 10.5$
σ_{Lx} (μm)	110	120
σ_{Ly} (μm)	3.3	5.6
σ_{Lz} (μm)	9000	9000
Peak Luminosity ($10^{33}\,\mathrm{cm}^{-2}\,\mathrm{s}^{-1}$)	3	9.213
Daily Luminosity (pb^{-1}/day)	135	710.5

collisions at the $\Upsilon(4S)$ is found in Table 3.2. The decays to light quarks (u,d,s) and charm quarks are referred to as *continuum production*. The continuum background events and backgrounds from $\Upsilon(4S)$ decays to states not of interest is referred to as *combinatoric background*. QED production $e^+e^- \rightarrow e^+e^-$ (Bhabha), $\mu^+\mu^-, \tau^+\tau^-$ is used to determine the luminosity. Data collection also occurs at CM energies below than the $\Upsilon(4S)$ resonance. A fraction ($\sim 10\%$) of data is collected at an energy $40\,\mathrm{MeV}$ lower than the $\Upsilon(4S)$ resonance. This data is referred to as *off-resonance data*, and it allows for the study of continuum production, which is a common background for many studies conducted with *BABAR* data. Figure 3.3 displays the total integrated luminosity for runs $1-4$, corresponding to $\sim 245\,\mathrm{fb}^{-1}$ of data taken on the $\Upsilon(4S)$ resonance. Figure 3.4 shows the daily luminosities for runs $1-4$.

Table 3.2: The cross-sections for the production of various states at the $\Upsilon(4S)$ mass $\sqrt{s} = M(\Upsilon(4S))$.

$e^+e^- \rightarrow$	Cross-section (nb)
$b\overline{b}$	1.05
$s\overline{s}$	1.30
$c\overline{c}$	0.35
$u\overline{u}$	1.39
$d\overline{d}$	0.35
$\tau^+\tau^-$	0.94
$\mu^+\mu^-$	1.16
e^+e^-	~ 40

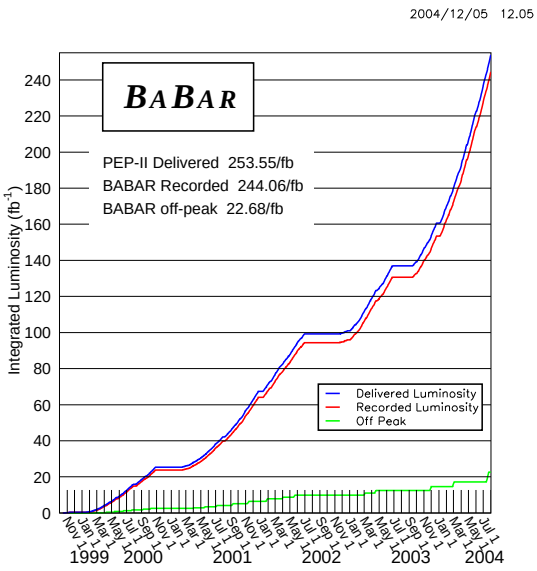

Figure 3.3: The total integrated luminosity delivered by PEP-II (blue) and recorded by *BABAR* (red). The delivered off-peak data is shown in green.

The high beam current, asymmetric energy, head-on collision design of PEP-II produces significant backgrounds whose impact must be carefully controlled. The backgrounds generated by off-axis or off-energy electrons and positrons can cause with high counting rates, dead times in data acquisition, high currents, and radiation damage. These problems will lower the quality of the data recorded by *BABAR* and also shorten the lifetime of the detector systems. The primary sources of background and the strategies for controlling them are as follows:

- *Synchrotron radiation* in the interaction region. This has the potential to be the largest background. The source is beam deflection near the interaction region. This is controlled by channeling most of the radiation out of the interaction region. Careful design of masking near the interaction point, which shadows the central beam pipe, has reduced this source of background to a negligible level;

- *Beam interactions with residual gas* in the accelerator vacuum systems. The beams can undergo bremsstrahlung and Coulomb scattering, which cause the beam particles to stray outside of the nominal orbit. This effect depends on the residual pressure of the background inducing gases in the rings and the beam current. This radiation can only be controlled by keeping the pressure low in the rings;

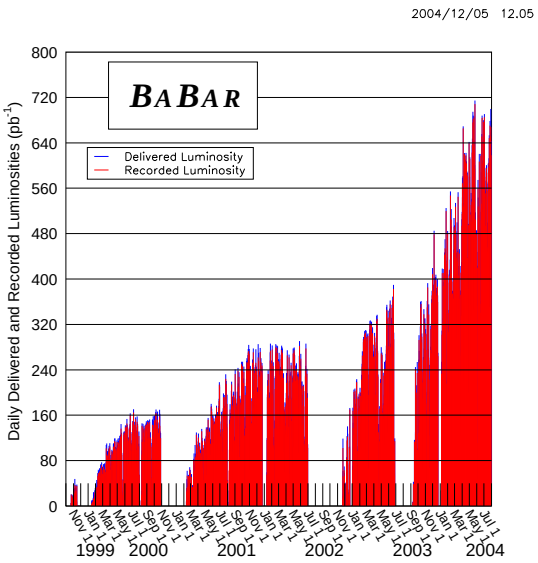

Figure 3.4: The daily recorded luminosity delivered by PEP-II (blue) and recorded by *BABAR* (red).

- *Electromagnetic showers from beam collisions.* This background is caused by Bhabha electrons or positrons near the interaction region, which causes electromagnetic showers to spray the detector. This background is proportional to the beam luminosity.

3.2 *BABAR* Overview

The *BABAR* detector [52] was designed to provide the optimal basis for the study of $\mathcal{CP}$ violating decay processes. Secondary in the design were the goals of making precision measurements of the flavor changing processes involving bottom or charm quarks, and searches for rare decays. Due to the small branching ratios of B mesons to $\mathcal{CP}$ eigenstates (10^{-4}), the need to fully reconstruct final states with high track and charge multiplicities, and the need to tag the second neutral B meson in a $B\overline{B}$ decay, the *BABAR* detector was designed to meet the following criteria:

- A large and uniform geometrical acceptance down to small polar angles relative to the boost direction
- Excellent charged particle reconstruction efficiency down to $60\,\mathrm{MeV}/c$
- Excellent neutral particle reconstruction efficiency down to $20\,\mathrm{MeV}/c$

- Excellent momentum resolution
- Excellent energy and angular resolution for the detection of photons from π^0 and η^0 decays, and from radiative decays in the range from $20\,\mathrm{MeV}$ to $4\,\mathrm{GeV}$
- Very good vertex resolution, both transverse and parallel to the beam direction
- Efficient electron and muon identification, with low misidentification probabilities for hadrons. This feature is crucial for tagging the B flavor, for the reconstruction of charmonium states, and also important for the study of decays involving leptons
- Efficient and accurate identification of hadrons over a wide range of momenta for B flavor-tagging, and for the reconstruction of exclusive states; modes such as $B^0 \to K^{\pm}\pi^{\mp}$ or $B^0 \to \pi^+\pi^-$, as well as in charm meson and τ decays
- A flexible, redundant, and selective trigger system
- Low-noise electronics and a reliable, high bandwidth data-acquisition and control system of high flexibility and operational stability
- Detailed monitoring and automated calibration
- An online computing and network system that can control, process, and store the expected high volume of data
- Detector components that can tolerate significant radiation doses and operate reliably under high-background conditions

Figures 3.5 displays longitudinal and end cutaway views of the *BABAR* detector, respectively. The coordinate system of *BABAR* is a conventional right-handed system. The positive z-axis is defined by the principal axis of the Drift Chamber, which coincides with the direction of the electron beam flight path, while the y-axis points upward.

BABAR is comprised of several separate detector systems, each responsible for different tasks in data taking and event reconstruction. In addition, there is a super-conducting solenoid which provides a $1.5\,\mathrm{T}$ magnetic field in the tracking detector components. The detector systems that comprise *BABAR* are as follows, in order of location from interaction region outward radially:

- *Silicon Vertex Tracker* (SVT). The SVT is once of the two principal detectors used in charged particle tracking. It serves to precisely measure the positions and angles of charged particles

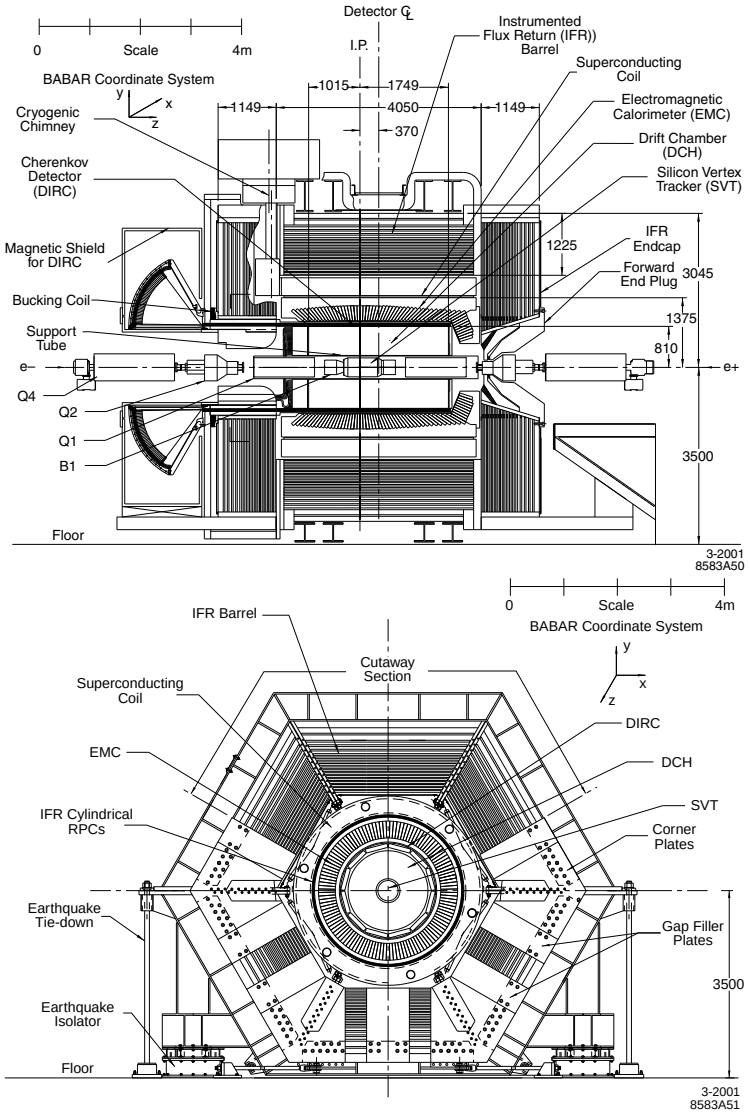

Figure 3.5: A longitudinal cutaway (top) and a horizontal cutaway (bottom) view of the *BABAR* detector.

close to the interaction point. For low transverse momentum particles, the SVT is the sole tracking detector.

- *Drift Chamber* (DCH). The DCH is the other principal detector in charged particle tracking. The DCH provides momentum measurements for charged particles and also contributes to particle identification (PID) through the measurement of gas ionization in the DCH. Apart from tracking, the DCH contributes information to the trigger system.

- *Detector of Internally Reflected Cherenkov Light* (DRC). The DRC serves to identify charged hadrons by separating pions from kaons.
- *Electromagnetic Calorimeter* (EMC). The EMC measures the energy and angular position of electromagnetic showers from charged and neutral particles. The EMC is key to particle identification through measurement of deposited energy, and the information it provides on neutral particles is vital to the measurements presented in this dissertation.
- *Instrumented Flux Return* (IFR). The IFR is used for the identification of muons and neutral hadrons.

The coverage, segmentation, and performance of the aforementioned detector systems is summarized in Table 3.3. The details of the detector systems will be discussed in the following sections.

3.3 Charged Particle Tracking System

Charged particle tracking is the performed by the SVT and the DCH. The goal of the tracking system is high efficiency detection and measurement of the momentum and angles of charged particles. While this endeavor is important to many studies at *BABAR* , it is especially critical in the full reconstruction of B meson decays (and thus the work presented in this dissertation) at high resolution and with limited background. The tracking information is also an input for the functions of the DRC, EMC, and IFR.

For tracks below $1\,\mathrm{GeV}/c$, the majority of those produced in $\Upsilon(4S)$ decays, the precision of the momentum determination is limited by multiple Coulomb scattering in the detector material. As a result, the amount of material in the SVT and DCH has been minimized and is well documented and modeled. As previously mentioned, the *BABAR* coordinate system is defined by the principal axis of the DCH. Because the tracking system is comprised of two detectors, the alignment of the two systems needs to be carefully monitored and continuously updated. This is done on a run-by-run basis as the relative positions of the SVT and DCH can vary significantly due to temperature changes.

3.3.1 Silicon Vertex Tracker

The SVT, pictured in Fig. 3.6, provides *BABAR* with very precise measurements of decay vertexes and charged track trajectories near the interaction region. The design of the SVT was driven

Table 3.3: Overview of the coverage, segmentation, and performance of the *BABAR* detector systems. The notation (C), (F), and (B) refers to the central barrel, forward and backward components of the system, respectively. The detector coverage in the laboratory frame is specified in terms of the polar angles θ_1 (forward) and θ_2 (backward). The number of readout channels is listed. Performance numbers are quoted for $1\,\mathrm{GeV}/c$ particles, except where noted. The performances for the SVT and DCH are quoted for a combined Kalman fit (for the definition of the track parameters, see section 3.3)

System	θ_1 (θ_2)	No. Channels	No. Layers	Segmentation	Performance
SVT	20.1° (-29.8°)	150K	5	50-100 μm $r-\phi$ 100-200 μm z	$\sigma_{d_0} = 55\,\mu\mathrm{m}$ $\sigma_{z_0} = 65\,\mu\mathrm{m}$
DCH	17.2° (-27.4°)	7,104	40	6-8 mm drift distance	$\sigma_\phi = 1$ mrad $\sigma_{tan\lambda} = 0.001$ $\sigma_{p_T}/p_T = 0.47\%$ $\sigma(dE/dx) = 7.5\%$
DIRC	25.5° (-38.6°)	10,752		$35 \times 17\,\mathrm{mm}^2$ ($r\Delta\phi \times \Delta r$) 144 bars	$\sigma_{\theta_C} = 2.5\,\mathrm{mrad}$ per track
EMC(C)	27.1° (-39.2°)	2×5760		$47 \times 47\,\mathrm{mm}^2$ 5760 crystals	$\sigma_E/E = 3.0\%$ $\sigma_\phi = 3.9\,\mathrm{mrad}$
EMC(F)	15.8° (27.1°)	2×820		820 crystals	$\sigma_\theta = 3.9\,\mathrm{mrad}$
IFR(C)	47° (-57°)	22K+2K	19+2	20-38 mm	90% $\mu^\pm$ eff. 6-8% $\pi^\pm$ mis-id (loose selection, 1.5–3.0 GeV/c)
IFR(F)	20° (47°)	14.5K	18	28-38 mm	
IFR(B)	-57° (-26°)	14.5K	18	28-38 mm	

primarily by the need to precisely determine the B decay vertexes for $\mathcal{CP}$ studies, which requires a resolution of $\sim 80\,\mu\mathrm{m}$ along the z-axis. Sufficient resolution is required in the $x-y$ plane to be able to reconstruct final states in B decays, charm decays, and τ decays. This corresponds to a resolution of $\sim 100\,\mu\mathrm{m}$ in the $x-y$ plane.

The SVT serves as the sole provider of tracking information for charged tracks with low transverse momenta $p_T < 120\,\mathrm{MeV}/c$, as such tracks do not penetrate far enough into the DCH for reliable pattern recognition. The tracking of low transverse momentum tracks is critical for the identification of slow pions associated with semileptonic D^* decays, which is important to the work presented in this dissertation. The SVT also provides critical track angle information which is used

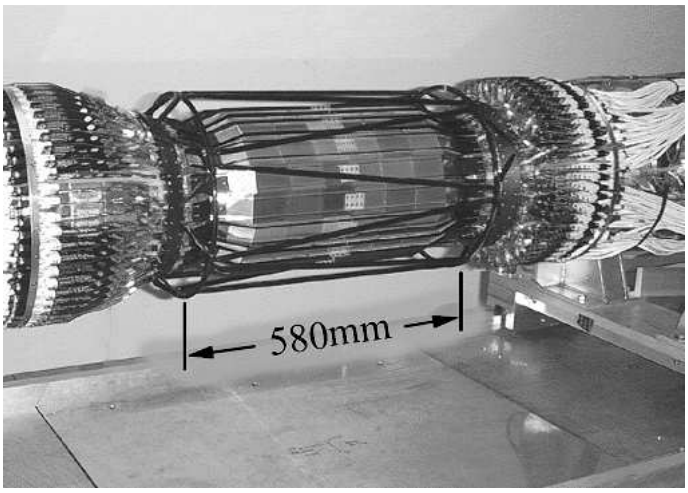

Figure 3.6: The Silicon Vertex Tracker (SVT).

in identifying tracks and determining the Cherenkov angles of high momentum tracks.

The SVT is located inside the beam support tube and is the innermost detector. Because of this and the necessary presence of magnets near the interaction point (IP) that bring the beams into head-on collision at the IP, the angular acceptance of the SVT is $350\,\mathrm{mrad}$ in the forward direction and $520\,\mathrm{mrad}$ in the backward direction. Figure 3.7 depicts the SVT, its dimensions, and angular acceptance.

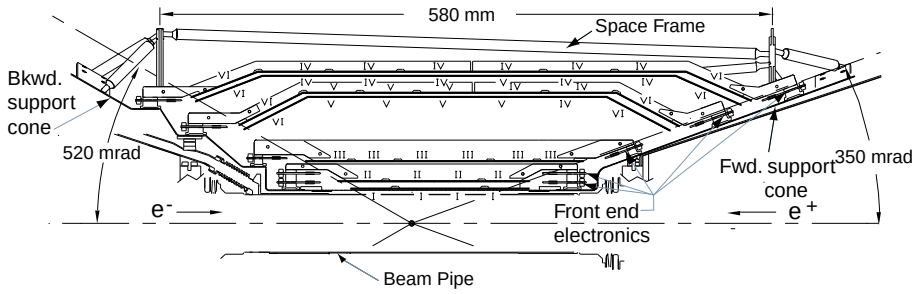

Figure 3.7: A longitudinal view of the SVT. The roman numerals indicate the six different types of sensor modules.

The SVT is made up of five concentric layers of double-sided silicon strip sensors. As seen

in Fig. 3.8, the innermost three layers contain six sensor modules, the fourth layer contains sixteen, and the fifth layer contains eighteen. The two sides of a given module contain silicon strips arranged orthogonally to each other. The strips to measure in the ϕ direction (ϕ-strips) run along the z-axis while the strips to measure in the z direction (z-strips) run transverse to the z-axis. The modules of the inner three layers are flat while the modules in the outer two layers are arch-shaped to allow maximal angular coverage with a minimal amount of silicon material and to yield a larger crossing angle for particles that traverse the module near the outer edge. The inner three layers are responsible for the vertex measurements and the outer two layers are responsible for tracking. The resolution achieved by the SVT is $10 - 15\,\mu\mathrm{m}$ for perpendicular tracks in the inner three layers and $40\,\mu\mathrm{m}$ in the outer two layers.

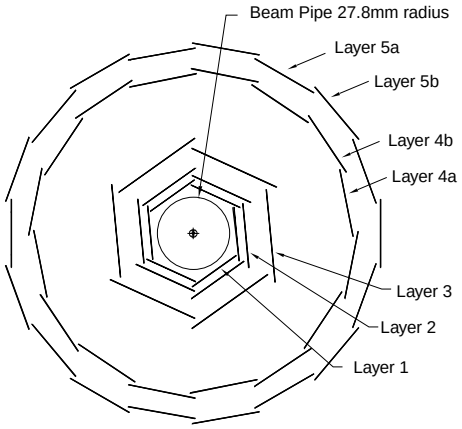

Figure 3.8: A cross-sectional view of the SVT. The orientation of the five layers and the individual strip sensors is shown.

The inner three layers of the SVT are all tilted in the ϕ direction by 5° so adjacent modules will overlap which assures that the entire azimuthal space is covered. The outer two modules cannot be tilted in ϕ because of the arch geometry. Instead, they are arranged in sub-layers, one with a smaller radius than the other. These geometrical nuances can be seen in Fig. 3.8.

The double-sided silicon strip sensors [53] are $300\,\mu\mathrm{m}$ thick. The p^+ and n^+ sensing strips are built on a high-resistivity ($6 - 15\,\mathrm{k}\Omega\ \mathrm{cm}$) n-type substrate. There are six different types of sensor modules, labeled with roman numerals in Fig. 3.7, which have different dimensions, number of strips, and electronic readout pitches. The modules vary in size from $43 \times 42\,\mathrm{mm}^2$ ($z \times \phi$) to $68 \times 53\,\mathrm{mm}^2$. There are a total of 340 silicon sensors which cover a total area of $0.96\,\mathrm{m}^2$, and particles will typically only traverse $\sim 4\%$ of a radiation length of material.

The ϕ-strips on a module are all connected to make one single readout strip. The resulting strip is up to $140\,\mathrm{mm}$ ($240\,\mathrm{mm}$) long in the inner (outer) layers. The z-strips connect to the readout electronics by way of fanout circuits. In the three inner layers, every z-strip has its own readout, but in the outer layers, there are two z-strips per readout. The single z-strips are $\sim 50\,\mathrm{mm}$ long and the paired strips are $\sim 100\,\mathrm{mm}$ long. There are around $150,000$ readout channels and the readout electronics are located well outside of the detector volume so as not to introduce any unnecessary material into the acceptance region of the detector.

Signals are read from the strips, amplified, shaped, and compared to a threshold. The time interval exceeding the threshold (ToT) is related logarithmically to the charge accumulated on the strips. The output is sampled at $\sim 15\,\mathrm{kHz}$ and in the case of a Level 1 trigger accept, the time stamp, ToT, and strip address are sent to the data acquisition system.

3.3.2 Drift Chamber

The purpose of the DCH is to efficiently detect charged tracks with $p_T > 100\,\mathrm{MeV}/c$ and measure their momenta, positions, and angles through measurement of the track curvature in the magnetic field as charged particles ionize the Helium based gas in the DCH. The DCH track information works in conjunction with the information provided by the SVT to reconstruct tracks. The DCH is responsible for the reconstruction of decay vertexes that occur outside of the SVT, like K_S^0 decays. Since it has to provide this vertex information, the DCH also determines longitudinal position of tracks at $\sim 1\,\mathrm{mm}$ resolution.

The DCH also contributes to particle identification of low momentum particles that the DRC cannot provide information for. Particle identification is achieved by measuring the average ionization loss per unit track length in the gas volume (dE/dx). The dE/dx measurement provides π/K separation up to $700\,\mathrm{MeV}/c$ with a resolution of 7%. For higher momentum tracks $p_T > 1\,\mathrm{GeV}/c$ the transverse momentum resolution is given by $\sigma_{p_T} \approx 0.3\% \times p_T$. Apart from tracking and PID, the DCH provides information for the trigger system.

The DCH is $280\,\mathrm{cm}$ long and has an inner (outer) radius of $23.6\,\mathrm{cm}$ ($80.9\,\mathrm{cm}$). Because the collisions are boosted with respect to the laboratory frame, the center of the DCH is off-set by $37\,\mathrm{cm}$ from the interaction region to permit forward and backward traveling particles at the edge of the DCH acceptance region to traverse at least half of the DCH layers. The geometry of the DCH is depicted in Fig. 3.9. Scattering of particles in the material of the chamber is a potential performance limitation and has been minimized in the DCH. The endplates are made from aluminum and thin

with the forward (backward) endplate measuring $12\,\mathrm{mm}$ ($24\,\mathrm{mm}$) thick. The inner cylinder is made of Beryllium and is $1\,\mathrm{mm}$ thick which corresponds to a radiation length of $\sim 0.3\%$. The outer cylinder is made of two carbon fiber layers and has a radiation length of 1.5%.

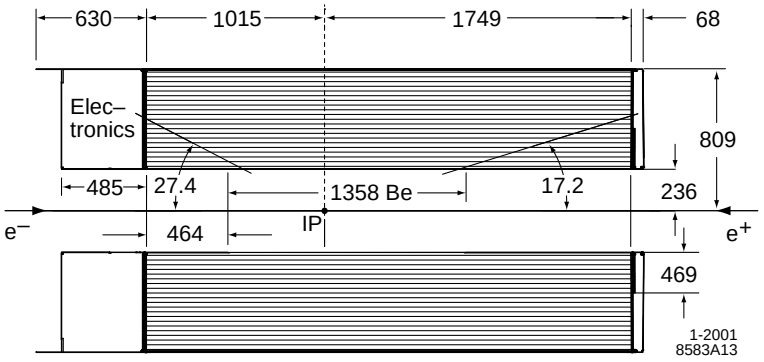

Figure 3.9: A longitudinal cutaway view of the DCH. The dimensions shown are in units of mm. Note that the interaction point, labeled IP, is offset $370\,\mathrm{mm}$ from the center of the DCH.

The DCH consists of a total of 7104 hexagonal drift cells arranged in 40 layers. To provide the necessary resolution both radially and longitudinally, 16 of the layers are oriented parallel to the z-axis (axial layers) and the remaining 24 layers are rotated from the z-axis orientation (stereo layers). The layers are further subdivided into ten superlayers. The superlayers are either axial (A) layers or one of two different types of stereo layers (U,V) and are arranged from the inside of the detector out in an AUVAUVAUVA pattern as depicted in Fig. 3.10 (left). The angles that the stereo layers are rotated from the z-axis (stereo angles) vary from $\pm 45\,\mathrm{mrad}$ at the innermost stereo superlayer to $\pm 76\,\mathrm{mrad}$ at the outermost stereo superlayer.

The drift cell design is shown in Fig. 3.10 (right). They are hexagonal with a length of $11.9\,\mathrm{mm}$ in the radial direction and $19.0\,\mathrm{mm}$ in the direction of the z-axis. A cell consists of a sense wire in the center of the cell and six field wires along the outside. The field wires are grounded, while the sense wires are held at positive electric potential (typically 1930V), which creates an electric field in the drift cell that attracts negatively charged ions (drift electrons) towards the sense wire.

The DCH is filled with a 4:1 mixture of helium and isobutane. The mixture is optimized to minimize drift times and provide sufficient resolution while minimizing the amount of material presented by the gas itself. As charged particles traverse the chamber, they ionize the gas. The free electrons drift along field lines to the sense wire. Two pieces of information are recorded in each drift cell traversed by a charged particle. The first is the drift time, which is defined by the difference from the time the ionization is created in the cell to the time the electronics receives the

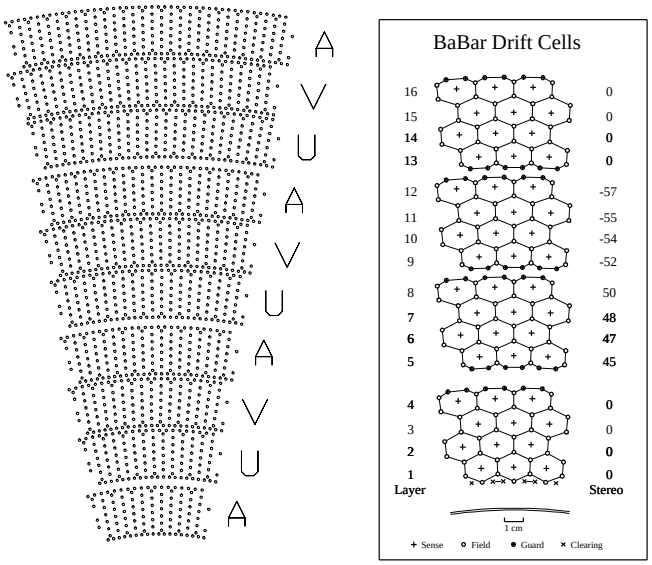

Figure 3.10: The ten DCH superlayers (left) and the layout of the drift cells for the first four superlayers (right). The numbers on the right side of the right plot give the stereo angle of the layer in units of mrad and the lines drawn between field wires illustrate the boundaries of the drift cells.

leading edge of the wire signal. The drift time, after being converted to a distance by an algorithm that uses the distance of closest approach between the track and sense wire, provides the tracking system with the position of the charged track. Figure 3.11 shows $100\,\mathrm{ns}$ isochrones (contours of equal drift times) for an example cell. The second piece of recorded information is the integrated charge deposited in the cell. The signal is first shaped and digitized so it can be integrated to yield a charge measurement. The combination of drift cell charge measurements are used to make the dE/dx measurement.

3.3.3 Tracking Summary

Using the SVT and DCH information, charged tracks are assembled and characterized by five parameters, measured at the track's point of closest approach to the z-axis:

- Distance from the origin in the x-y plane (d_0)
- Distance from the origin in the z plane (z_0)
- Azimuthal angle (ϕ_0)

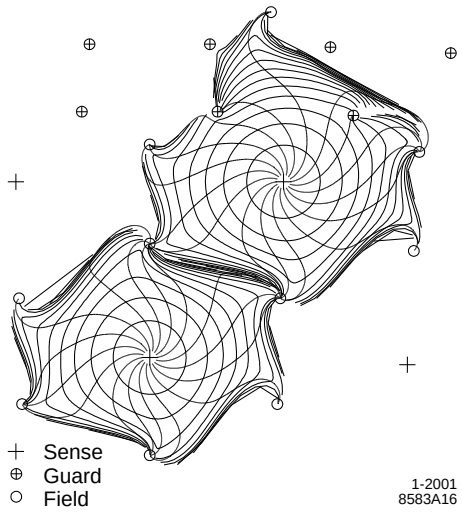

Figure 3.11: Drift cell $100\,\mathrm{ns}$ isochrones in the third and fourth layer of an axial superlayer. The isochrones are quite circular near the sense wires but become non-circular near the edges of a cell.

- Dip angle with respect to the transverse plane (λ)
- Track curvature ($\omega = 1/p_T$)

The variables ω and d_0 are signed quantities indicating the charge associated with the track.

The tracking system efficiency is determined from the ratio of the number of tracks found in the DCH to the number found in the SVT with the requirement that they fall within the DCH's tighter geometrical acceptance. Figure 3.12 displays the efficiency as a function of p_T and polar angle. The efficiency is found to average $98.1 \pm 1\%$ per track at momenta larger than $200\,\mathrm{MeV}/c$ and polar angle larger than $500\,\mathrm{mrad}$.

A cosmic ray muon traversing the full chamber can be divided into a separately reconstructed upper and lower track segment. The difference between the two track halves can then be used to compute track parameter resolutions. The resulting distributions are shown in Fig. 3.13 for tracks with $p_T > 3\,\mathrm{GeV}/c$. The shifts in the z_0 and $\tan\lambda$ plots are a residual affect of a problem with the alignment of the SVT with the DCH. Based on these plots, the single track parameter resolutions are

$$\begin{aligned} \sigma_{d_0} &= 23\,\mu\mathrm{m} \quad \sigma_{\phi_0} = 0.43\,\mathrm{mrad} \\ \sigma_{z_0} &= 29\,\mu\mathrm{m} \quad \sigma_{\tan\lambda} = 0.53 \times 10^{-3}. \end{aligned}$$

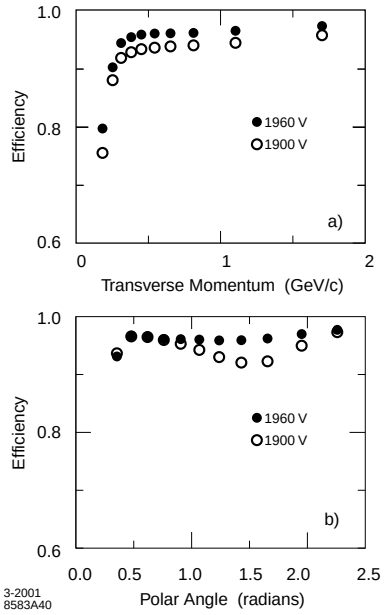

Figure 3.12: The track reconstruction efficiency in the DCH at operating voltages of 1900 V and 1960 V, as a function of transverse momentum (top), and polar angle (bottom). The efficiency is measured using multi-hadron events.

The transverse momenta of charged tracks are primarily determined by the DCH. The resolution on p_T, determined from cosmic ray muons, can be seen in Fig. 3.14. The resolution is well described by a linear function as

$$\sigma_{p_T}/p_T = (0.13 \pm 0.01)\% \cdot p_T + (0.45 \pm 0.03)\% \tag{3.2}$$

where p_T is measured in units of GeV/c. The results of the dE/dx measurement, displaying the π/K separation at low momenta, for a generic data sample including many background triggers can be seen in Fig. 3.15.

3.4 Detector of Internally Reflected Cherenkov Light

The work presented in this dissertation and the various studies conducted using the *BABAR* detector require the ability to separate pions and kaons sufficiently over a broad range of momenta and angular trajectories. At low momenta ($< 700\,\mathrm{MeV}/c$), the DCH is responsible for PID using the dE/dx measurement. Above this threshold, the DRC is the sole PID detector. The DRC can

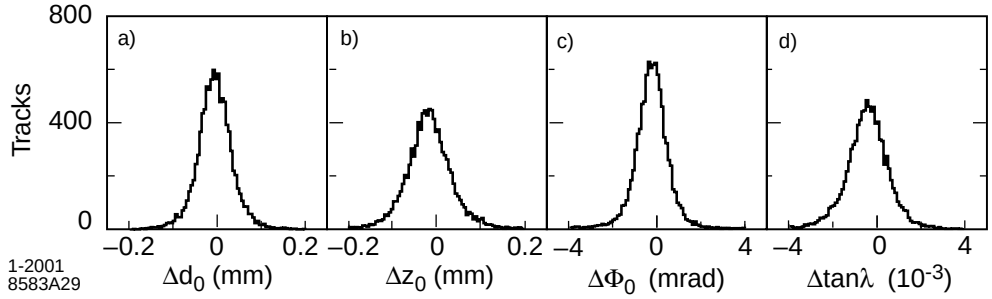

Figure 3.13: Track parameter differences between upper and lower tracks for tracks with $p_T > 3\,\mathrm{GeV}/c$ as determined from cosmic ray muons.

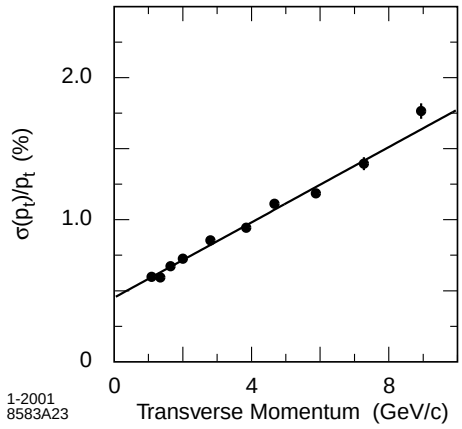

Figure 3.14: The p_T resolution as a function of p_T as determined from cosmic ray muons. The resolution is well described by a linear function.

provide pion/kaon separation of 4σ or greater over a broad range of momenta ($\sim 0.7 - 4.2\,\mathrm{GeV}/c$).

The DRC is a novel PID detector, using the identification of Cherenkov photons that are emitted as a hadron interacts with the radiator material in the DRC [54]-[56]. The photons are trapped due to total internal reflection in such a way that the angles of reflection are maintained. Figure 3.16 provides a schematic drawing for the DRC. The DRC consists of 144 long and narrow ($1.7\,\mathrm{cm} \times 3.5\,\mathrm{cm} \times 4.9\,\mathrm{m}$) radiator bars of rectangular cross-section, made from synthetic fused silica, which have a mean index of refraction $n = 1.473$. The bars are arranged in a 12-sided polygonal barrel and are located just outside the DCH. In all, the DRC uses $80\,\mathrm{mm}$ of space radially which corresponds to about $\sim 17\%$ of a radiation length for the average particle at normal incidence. The radiator bars cover 94% of the azimuthal angle and 83% of the polar angle.

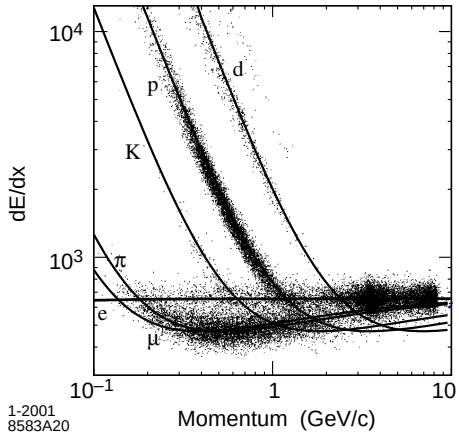

Figure 3.15: The DCH dE/dx measurement vs. the track momentum. The lines display the Bethe-Bloch predictions for the dE/dx measurement.

The detection of Cherenkov light and imaging is handled by an array of photomultiplier tubes (PMTs). The areas between tubes are filled with light catcher cones [57], which capture and deliver light to the PMT that would otherwise not be detected. Particles tend to be distributed in the forward region of the detector due to the asymmetric energy of the beams. Thus, to reduce interference with the other detector systems, the PMT array is placed at the backward end and the radiator bars have mirrors at the forward end to reflect light back towards the PMT array.

When a hadron traverses the DRC radiator bars, Cherenkov photons are emitted with a characteristic incidence angle called the Cherenkov angle θ_C which is given by

$$\cos\theta_C = \frac{1}{n\beta} \tag{3.3}$$

where n is the index of refraction of the silica radiator material and $\beta = v/c$ is the velocity of the particle. The Cherenkov light is reflected along the narrow bar and enters the wedge which is made from fused silica and reflects the Cherenkov light at a large angle. The Cherenkov angle is preserved throughout all of the internal reflections because reflection surfaces are aligned to be parallel. The photons are then detected by the PMTs. The concept is illustrated in Fig. 3.17.

The Cherenkov angle θ_C, the angle of the photon in the azimuthal direction about the particle's momentum vector ϕ_C, and the time of arrival of the photon t are used as a basis to perform a fit to the track Cherenkov angle. Likelihoods are assigned for the various particle hypotheses (e,μ,π,K,p) using an unbinned maximum likelihood technique with the sample of Cherenkov photons emitted by a track, which is typically ~ 30 photons. Figure 3.18 shows the fitted Cherenkov angle for tracks

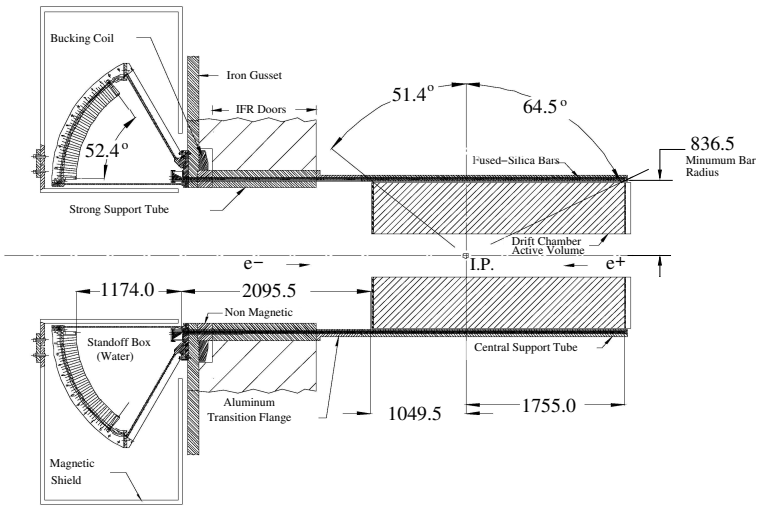

Figure 3.16: A longitudinal cutaway view of the DRC.

from multi-hadron events. Below $3\,\mathrm{GeV}/c$ the pions, kaons, and protons are well separated, which illustrates the particle identification ability of the DRC. Also, the excellent π-K separation achieved with the DRC are shown for $B^0 \to \pi^+\pi^-$ events in Fig. 3.19.

3.5 Electromagnetic Calorimeter

The EMC is designed to provide the excellent electromagnetic calorimetry that studies at *BABAR* require. The EMC measures electromagnetic showers with high angular and energy resolution over a broad range of energies. This includes the detection of low energy photons down to $20\,\mathrm{MeV}$ from π^0 and η decays and the detection of high energy particles up to $9\,\mathrm{GeV}$ from electromagnetic and radiative processes like $e^+e^- \to e^+e^-(\gamma)$ and $e^+e^- \to \gamma\gamma$. These capabilities allow the detection of neutral particles and the identification of electrons and muons which are vital to measurements presented here as they allow for the identification of semileptonic decays and reconstruction of the neutral components associated with the semileptonic decay.

The EMC is constructed to be axially symmetric about the z-axis and has full azimuthal coverage from $15.8°$ forwards to $141.8°$ backwards as seen in Fig. 3.20, which amounts to $\sim 90\%$ of the solid angle in the CM system. The EMC is a total-absorption calorimeter made of a finely segmented array of crystals. The crystals are made from 0.1% thallium-doped cesium iodide (CsI(Tl)).

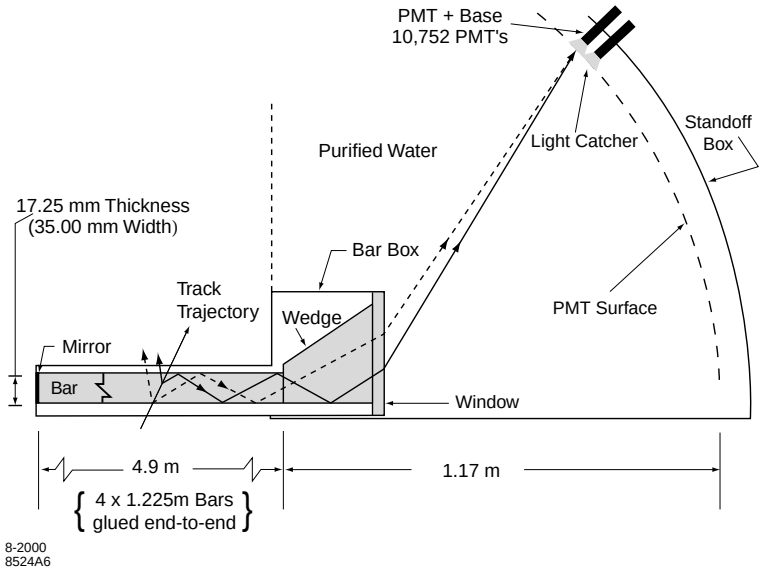

Figure 3.17: DRC schematic. The radiator bar reflects Cherenkov photons and the PMTs provide the imaging to determine the Cherenkov angle θ_C.

These crystals were chosen because they have a high light yield and small Moliere radius which provide excellent energy and angular resolution. Also, the crystals have a short radiation length, which allows containment of the highest energy showers while keeping the length of crystal to a minimum. The EMC contains 6580 total crystals which are subdivided into 56 rings. Of the 56 rings, 48 are arranged in a cylindrical barrel around the z-axis while the remaining 8 make up a forward endcap to account for the asymmetric beam conditions.

The crystals are a total absorption scintillating material. They are between $29.6\,\mathrm{cm}$ long ($16\,X_0$) in the backward end and $32.4\,\mathrm{cm}$ long ($17.5\,X_0$) in the forward end with a tapered trapezoidal cross-section. The cross section area at the front face of the crystal is $\sim 22\,\mathrm{cm}^2$ and becomes larger towards the back with an area of $\sim 36\,\mathrm{cm}^2$. Particles generate scintillation light in the crystals as they penetrate which is transported by internal reflection to two silicon photodiodes at the rear end of the crystal. A schematic of the crystal assembly is shown in Fig. 3.21.

Typically, an electromagnetic shower in the EMC will spread over several crystals, referred to as a cluster. Pattern recognition algorithms identify clusters and also separate single clusters from several overlapping clusters, referred to as merged clusters. Single clusters have one local maximum energy value whereas a merged cluster will have more, called bumps.

The energy resolution at low energies is measured with a radioactive source and yields a reso-

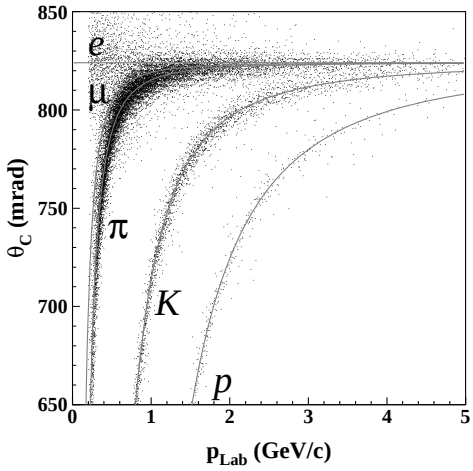

Figure 3.18: The fitted Cherenkov angle versus track momentum from a sample of multi-hadron events. The lines drawn indicate the predicted values for the various particles.

lution of $\sigma_E/E = 5.0 \pm 0.8\%$ at $6.13\,\mathrm{MeV}$. At high energies, the resolution can be deduced from Bhabha events since the shower energy can be predicted by the polar angle of the $e^{\pm}$. The energy resolution is found to be $\sigma_E/E = 1.9 \pm 0.07\%$ at $7.5\,\mathrm{GeV}$. Figure 3.22 (left) displays the energy resolution from several different decay processes as a function of energy. The energy resolution of the EMC is described by a function of a stochastic term and a constant term, added in quadrature. Fitting the data with this function results in

$$\frac{\sigma_E}{E} = \frac{(2.32 \pm 0.30)\%}{\sqrt[4]{E(\,\mathrm{GeV})}} \oplus (1.85 \pm 0.12)\%. \tag{3.4}$$

The angular resolution is determined from the decay processes $\pi^0 \to \gamma\gamma$ and $\eta \to \gamma\gamma$ where the two photons have approximately equivalent energies. The results as a function of the photon energy are shown in Fig. 3.22 (right). The angular resolution can be described by a function of a stochastic term added to a constant term. Fitting the data to this function results in

$$\sigma_\theta = \sigma_\phi = \left[\left(\frac{3.87 \pm 0.07}{\sqrt{E(\,\mathrm{GeV})}}\right) + \Big(0.00 \pm 0.04\Big)\right]\ \mathrm{mrad}. \tag{3.5}$$

Electrons are separated from charged hadrons in the EMC based on the energy of the shower, the lateral shower moments, and the momentum of the track along with a consistent determination from the DRC or DCH dE/dx measurement. The most discriminating variable is the ratio of the shower energy and track momentum E/p. The electron identification efficiency is obtained from

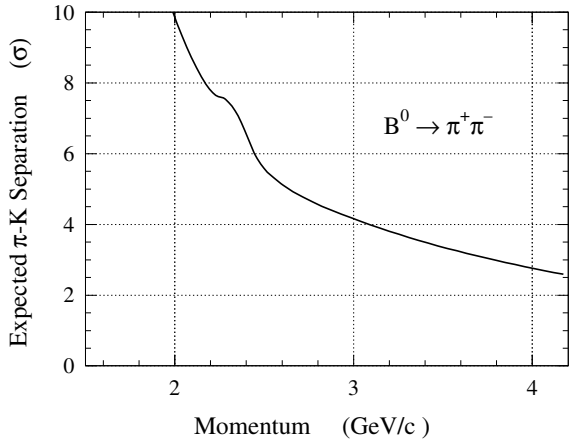

Figure 3.19: The expected π-K separation in $B^0 \to \pi^+\pi^-$ events versus the track momentum.

a sample of radiative Bhabha events and $e^+e^- \to e^+e^-e^+e^-$ events. The pion misidentification probability is obtained from from the selection of $\pi^\pm$ from the decays of K^0_S and three-prong τ decays. Figure 3.23 shows the results for the electron identification efficiency and pion misidentification probability as a function of the momentum and polar angle.

3.6 Instrumented Flux Return

The IFR is responsible for the high purity and high efficiency identification of muons and the detection of neutral hadrons over a large momentum and angular range. The proper identification of muons is crucial to the measurements presented here because they make up a significant portion of the semileptonic sample.

The IFR uses the magnet's steel flux return to absorb hadrons and filter the deeply penetrating muons through. As shown in Fig. 3.24, the IFR is separated into three parts: a barrel and two endcaps which combine to give an angular coverage down to $300\,\mathrm{mrad}$ in the forward direction and $400\,\mathrm{mrad}$ in the backward direction. The steel flux return is arranged in finely segmented layers. Single gap resistive plate chambers (RPCs) [58] are inserted in the gaps between layers to detect particles. There are 18 steel plate layers varying from $2\,\mathrm{cm}$ thick for the inner plates to $10\,\mathrm{cm}$ thick for the outer plates. The spacing between plates is $3.5\,\mathrm{cm}$ for the inner layers and $3.2\,\mathrm{cm}$ for the

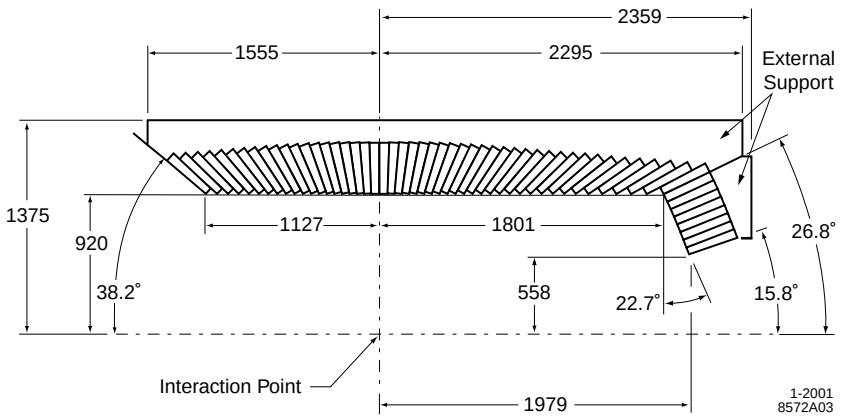

Figure 3.20: A longitudinal cutaway view of the top half of the EMC. Cross-sections of the 56 crystal rings are visible. Dimensions are listed in mm.

outer layers. The barrel has 19 RPC layers while the end caps have 18 layers. Additionally, to detect particles as they exit the EMC, there are two cylindrical RPC layers installed surrounding the magnet cryostat which is located just outside the EMC and inside the steel flux return.

The planar RPCs, as shown in Fig. 3.25, contain two $2\,\mathrm{mm}$ thick bakelite (phenolic polymer) sheets with a $2\,\mathrm{mm}$ gap between them. The gap is filled with a 56.7% argon, 38.8% freon 134a, 4.5% isobutane gas mixture. The exterior of the bakelite is coated with a resistive graphite and wrapped in an insulating mylar. One piece of graphite is connected to high voltage ($\sim 8\,\mathrm{kV}$) and the other is connected to ground creating a potential in the gap.

Particles traversing an RPC will ionize particles in the gas creating streamers which are detected by capacitive readout strips. The readout strips are located on both sides of the RPC and run lengthwise and crosswise to provide two-dimensional readout. A group of adjacent hits in one dimension in a layer are combined to form a cluster. The cluster's position is defined by the center strip of the group of hits. Two-dimensional clusters are formed by combining one-dimensional clusters from different layers and three-dimensional clusters are formed by combining two-dimensional clusters in different coordinates as long as there are no more than three of the layers not containing a cluster.

The cluster information is combined with the information from the tracking system to identify neutral hadrons, charged hadrons, and muons. Neutral hadrons are separated from charged hadrons and muons if the clusters are not associated with a charged track identified in the tracking system. This neutral cluster information is combined with EMC information and cluster information from the cylindrical RPCs located just outside the EMC and yields a K_L^0 detection angular resolution of

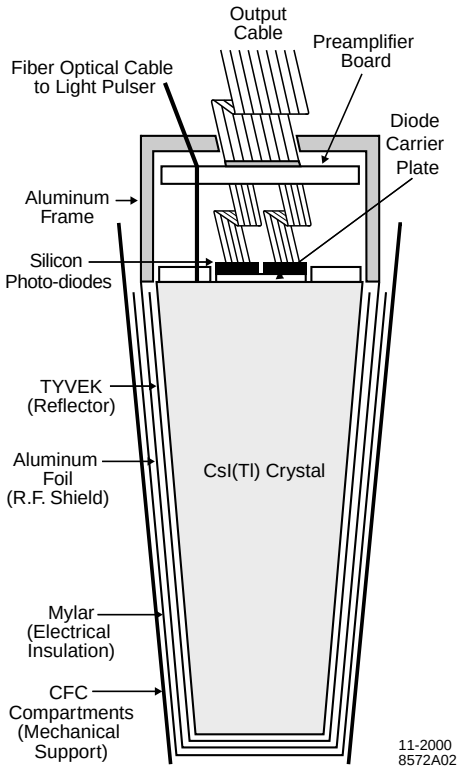

Figure 3.21: A schematic diagram of a single CsI(Tl) crystal. Please note that this figure is not to scale.

$60\,\mathrm{mrad}$.

Charged hadrons are separated from muons using several variables. The variables used are the total number of interaction lengths traversed by the particle from the IP to the last RPC (n_λ), the difference between n_λ and the predicted value of n_λ for a muon of the same vector momentum, the mean and RMS of the number of RPC hits per layer, the χ^2 for matching the geometry of the track as projected from the tracking system to the RPC clusters. The muon identification efficiency is $\sim$ 90% for momenta at $1.5 < p < 3.0\,\mathrm{GeV}/c$. The misidentification probability is $\sim$ 6-8% in this momentum range. Figure 3.26 illustrates the muon identification efficiency and the pion misidentification probability as a function of momentum and polar angle.

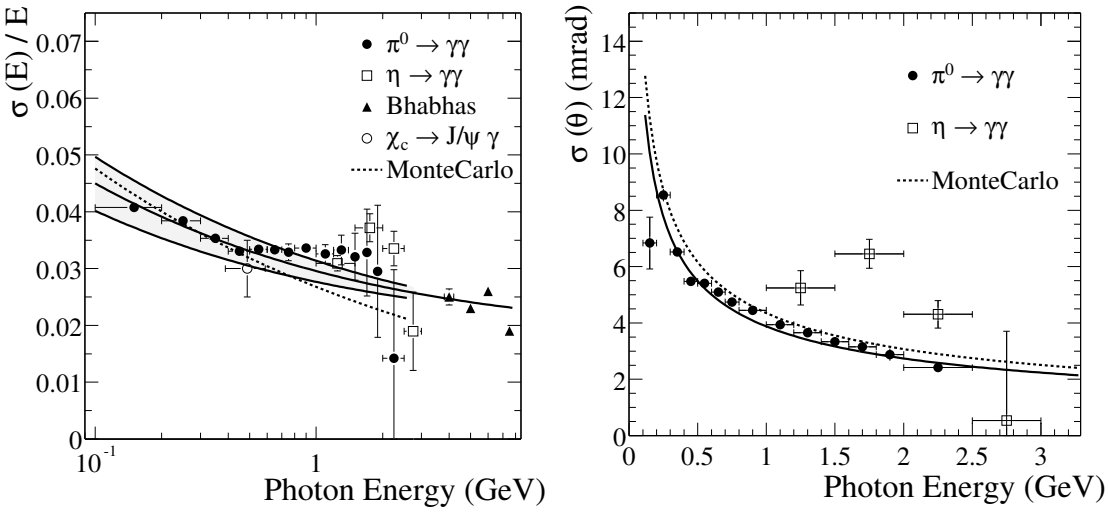

Figure 3.22: The energy resolution (left) and angular resolution (right) of the EMC. The solid lines are fits described in Eqs. 3.4 and 3.5.

3.7 Trigger System

The *BABAR* trigger system is responsible for selecting events for the data acquisition (DAQ) system to log. The trigger is designed to select $B\overline{B}$ events at $\sim 99\%$ efficiency and continuum events at $\sim 95\%$ efficiency while keeping background triggers low and thus keeping the event trigger rate at a manageable rate $\sim 150\,\mathrm{Hz}$ and keeping deadtimes on the order of a few percent. The trigger system is split into two levels: the Level 1 (L1) trigger which is executed in hardware and the Level 3 (L3) trigger which is executed in software.

3.7.1 The Level 1 Trigger System

The L1 trigger operates based on information on charged tracks from the DCH, electromagnetic showers in the EMC, and tracks detected in the IFR. The L1 trigger is made up of three independent hardware inputs. They are the drift chamber trigger (DCT), the electromagnetic calorimeter trigger (EMT), and the instrumented flux return trigger (IFT). The DCT and EMT individually meet the overall L1 trigger requirements at high efficiency which results in a large amount of redundancy. The IFT is used for providing triggers for cosmic rays passing through the detector and $e^+e^- \to \mu^+\mu^-$ decays, both of which are used for calibrations and diagnostics.

The DCT, EMT, and IFT send their information, or primitives, to the global trigger (GLT)

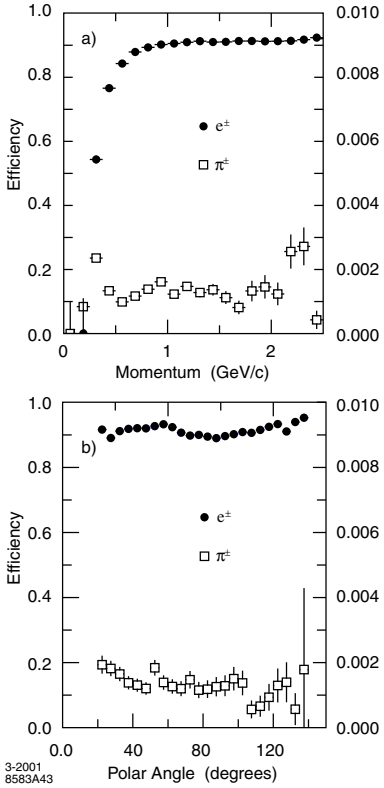

Figure 3.23: The electron identification efficiency and the pion misidentification probability as a function of the momentum (a) and the polar angle (b). The efficiency is indicated by the axis labels on the left and the misidentification probability is indicated by the axis labels on the right.

every $134\,\mathrm{ns}$. The primitives sent to the GLT summarize the position and energy read out from the corresponding detector subsystem. The GLT combines the primitives and passes them along to the Fast Control and Timing System (FCTS). The FCTS contains the trigger criteria, and if the criteria are satisfied, a L1 accept is issued for the event and the readout of the event information from all of the detectors is initiated. In normal operating mode, L1 triggers are produced at a rate of $\sim 1-2\,\mathrm{kHz}$ and occur at a fixed latency of $11-12\,\mu\mathrm{s}$ after the e^+e^- collision.

3.7.2 The Level 3 Trigger System

Trigger accepts from the L1 trigger are forwarded to the L3 trigger. The L3 trigger is executed in software and has access to the full event information that is read out from the detectors along with the L1 information. Using this full set of information, the L3 trigger is responsible for event reconstruction and classification by improving the selection provided by L1. The L3 trigger has

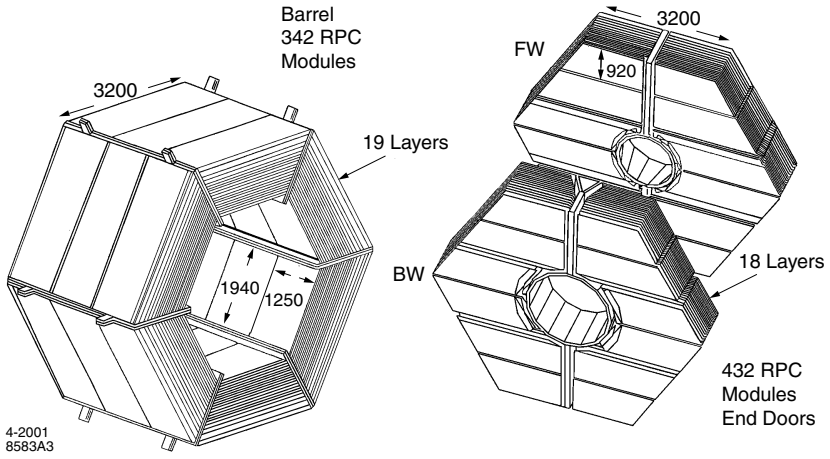

Figure 3.24: An overview of the IFR. The Barrel is pictured on the left and the end doors are pictured on the right. The dimensions listed are in mm.

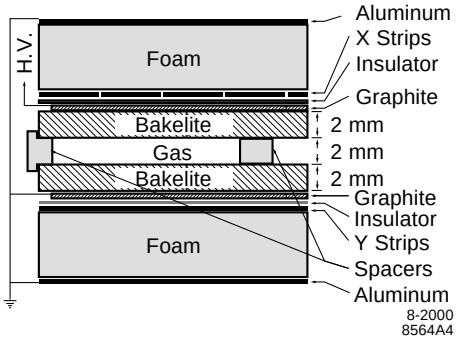

Figure 3.25: A cross sectional view of a planar RPC.

a flexible design such that different configurations can be easily loaded that permit different event selection algorithms. Events that pass the selection criteria are issued L3 accepts and the full event information is logged to disk where it can be accessed by the Online Prompt Reconstruction (OPR) system for full event reconstruction off-line. The L3 trigger reduces the L1 triggers by a factor of ~ 10 yielding an accept rate on the order of $\sim 150\,\mathrm{Hz}$.

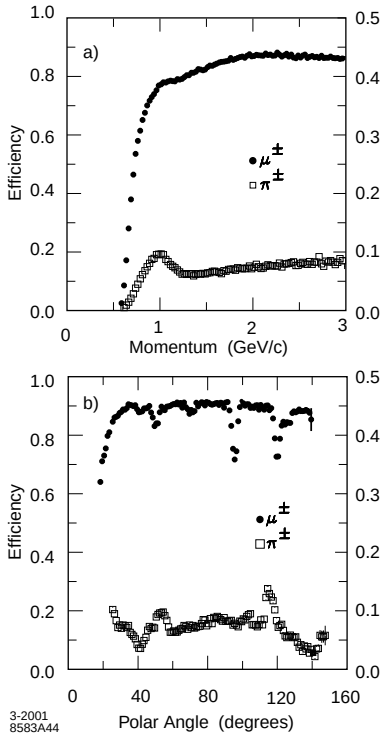

Figure 3.26: The muon identification efficiency and pion misidentification probability as a function of the momentum (a) and the polar angle (b). The efficiency is indicated by the axis labels on the left and the misidentification probability is indicated by the axis labels on the right.

3.8 Data Acquisition System

The data acquisition (DAQ) system manages the data-taking operations. The DAQ system is designed to manage logging data at L1 trigger rates of up to $2\,\mathrm{kHz}$ with an average event size of $\sim 30\,\mathrm{kbytes}$ and a L3 accept rate of $\sim 150\,\mathrm{Hz}$. The DAQ system is also designed to be reliable and user-friendly to maximize the amount of data recorded and minimize the unnecessary loss of beam collisions provided by PEP-II .

The DAQ system is comprised of a set of subsystems, each responsible for a specific task in the DAQ chain. The subsystems that comprise the DAQ system are:

- Online Dataflow (ODF). ODF is responsible for controlling the detector front-end electronics (FEEs) and transmitting information from the FEEs to the rest of the DAQ systems.

- Online Event Processing (OEP). OEP is responsible for the processing of events accepted by the trigger system. This includes the monitoring of data quality and close integration with

the L3 trigger system.

- Logging Manager (LM). The LM is responsible for writing events received from OEP to disk so they can be accessed by off-line processes.
- Online Detector Controls (ODC). ODC is responsible for controlling and monitoring the detector subsystems.
- Online Run Control (ORC). ORC provides the software interface for data-taking. ORC merges the DAQ components and controls their operations and properly sequences their operations.

The chain of events in DAQ is displayed in Fig. 3.27. The raw information from the detectors is processed and digitized in the FEEs. When a L1 accept is issued, the FEEs are read out and ODF passes the information to the Readout Modules (ROMs) in the VME dataflow crates via optical fibers. In the ROMs, the event information is assembled by detector specific software and passed along to OEP. At the OEP level, L3 event triggering is executed and events passing the L3 selection criteria are passed along to the LM. The LM combines all of the OEP information and writes it to disk. Each $\sim 1\,\mathrm{hr}$ long run corresponds to one written file in the LM.

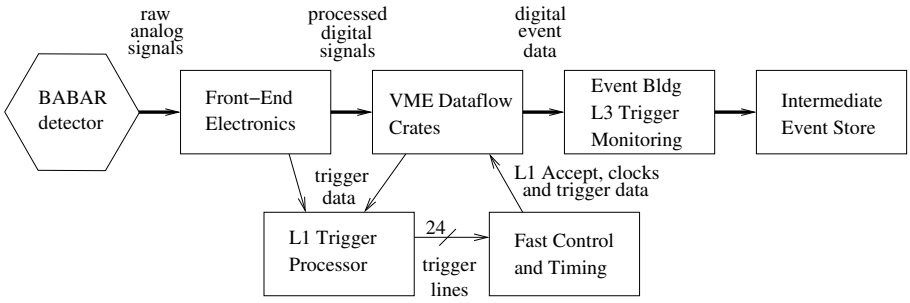

Figure 3.27: A schematic of the *BABAR* DAQ system.

Chapter 4

Particle Reconstruction

The starting point for any analysis of B meson decays at *BABAR* is the identification and reconstruction of charged and neutral particles. In this chapter, the reconstruction and identification of charged and neutral particles as it pertains to this analysis is described.

4.1 Charged Particle Reconstruction

As described in section 3.3.3, tracks are reconstructed with information from the SVT and DCH and are defined by five parameters (d_0, z_0, ϕ_0, λ, ω) and their associated error matrix. Track finding and fitting is done with a Kalman filter algorithm [59, 60]. This algorithm takes into account the magnetic field in the detector and the detailed description of the material that makes up the detector.

The primary goal of track selection is to suppress fake tracks originating in tracking reconstruction pathologies, such as loopers, and ghost tracks. In this analysis the definition of charged track is based on the following quantities:

- Distance of closest approach to the beam spot in the x-y plane ($|d_{xy}|$) and along the z axis ($|d_z|$). A restriction on those variables reduces fake tracks and background tracks not originating from the vicinity to the beam-beam interaction point. The selection criteria are $|d_{xy}| < 1.5\,\mathrm{cm}$ and $|d_z| < 10\,\mathrm{cm}$.

- Number of associated hits in the DCH. Tracks with high transverse momentum ($p_\perp > 0.2\,\mathrm{GeV}/c$) are required to have at least one associated DCH hit. This selection criterion reduces the amount of fake tracks reconstructed only from SVT segments or where the matching to the DCH has failed. This criterion is not used for low transverse momentum tracks since

slow pions (produced for instance in the $D^* \rightarrow D^0\pi$ decays) measured only in the SVT would be rejected.

- Maximum momentum. The selection criteria applied is $p_{lab} < 10\,\mathrm{GeV}/c$, where p_{lab} refers to the laboratory momentum of the track to remove tracks not compatible with the beam energies.

- The polar angle acceptance of the detector is restricted to $20^\circ < \theta_{lab} < 155^\circ$. This ensures a well-understood tracking efficiency and systematics.

For lepton and kaon candidates, the track selection criteria are modified as discussed in sections 4.2.1-4.2.3. For secondary tracks from K_S decays, no restriction on the impact parameter ($|d_{xy}|$) is imposed. In order to maximize the efficiency for low momenta tracks, which is important to an inclusive analysis, no restriction on the minimum number of hits on track is used.

Other selection criteria are used to reject pathological events that can introduce tails in the resolution of some inclusive variables, such as the reconstructed hadronic mass m_X in semileptonic decays. The problematic events and the selection criteria to identify and select them is itemized below:

- Tracks with transverse momentum $p_\perp < 0.18\,\mathrm{GeV}/c$ are not stopped in the DIRC and EMC and will spiral inside the drift chamber ("loopers"). This is illustrated in Fig. 4.1. The tracking algorithms of *BABAR* will not combine the different fragments of these tracks into a single track. Many of these loopers will fail the distance of closest approach criteria, except if they happen to have polar angle around 90°. Therefore, specific requirements have been developed to reject track fragments in the region $1.4 < \theta < 1.7\,\mathrm{rad}$ compatible with originating from a looper based on their distance from the beam spot. In order to identify looper candidates, the minimal difference in $p_\perp$, ϕ and θ (modulo π) to all other tracks in the event is determined. Tracks passing the selection criteria (different for same-sign and opposite-sign track pairs) are flagged as loopers and only the track fragment with $|d_z|$ closest to the beam spot is retained.

  These criteria remove roughly 13% of all low-momentum tracks in the central part of the detector. On average, they lower the mean charged multiplicity per B meson by less than 1%.

- The lower right quadrant of Fig. 4.1 also illustrates two tracks very closely aligned to each other ("ghosts"). These cases arise when the tracking pattern recognition divides the DCH

hits between the two track fragments. If two tracks are very close in phase space (as defined in Table 4.1), only the track with the most DCH hits is retained. This ensures that the fragment with the better momentum measurement is kept in the analysis.

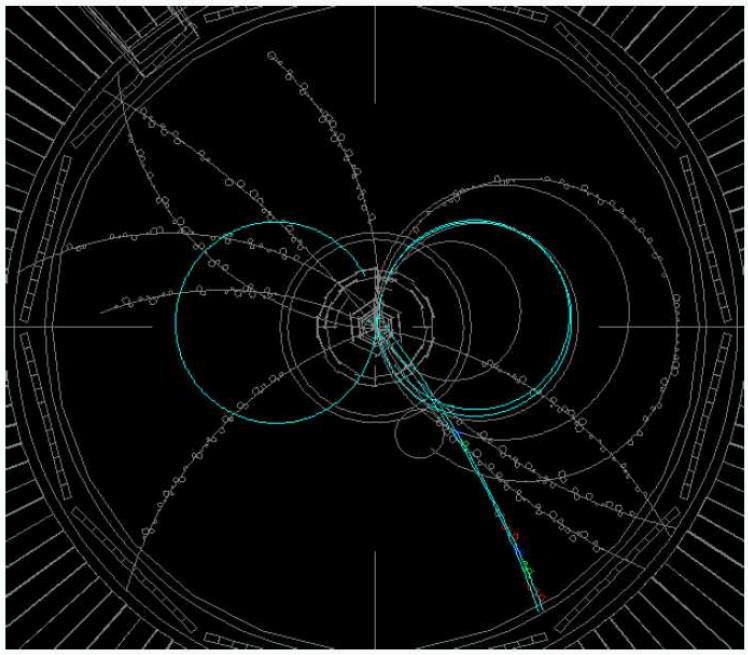

Figure 4.1: Event with looping tracks and ghost tracks. Note that this is not a common event: Loopers affect a relatively small number of events and to have the coincidence with ghost tracks (seen in the lower right quadrant) is very rare.

The track selection criteria and fake track (ghosts and loopers) criteria are summarized in Table 4.1.

4.2 Charged Particle Identification

The charged particle reconstruction described in section 4.1 does not discern between different types of charged tracks. The identification of the type of charged particle is a separate process and is described in sections 4.2.1-4.2.3. By default, a reconstructed charged particle is assumed to be a charged pion, and only if it is identified as an electron, muon, or kaon is the particle hypothesis changed. The identification process is critical to the analysis presented here because semileptonic events are identified by the presence of a high-momentum electron or muon and background $b \to c\ell\bar{\nu}$ events can be rejected by the identification of a charged kaon.

Table 4.1: Summary of track selection criteria.

Select tracks with	Selection Criteria
distance in $x-y$ plane	$\lvert d_{xy}\rvert < 1.5\,\mathrm{cm}$
distance in z axis	$\lvert d_z\rvert < 10\,\mathrm{cm}$
minimum number of DCH hits	$N_{DCH} > 0$ if $p_\perp > 0.2\,\mathrm{GeV}/c$
maximum momentum	$p_{lab} < 10\,\mathrm{GeV}/c$
geometrical acceptance	$20^\circ < \theta_{lab} < 155^\circ$
Reject track i if	**with respect to any other track j**
Loopers ($p_\perp < 0.18\,\mathrm{GeV}/c$)	
same-sign track pairs	$\Delta p_t = 100\,\mathrm{MeV}/c$ & $\lvert\Delta\phi\rvert < 200$ & $\lvert\Delta\theta\rvert < 200$ mrad
opposite-sign track pairs	$\Delta p_t = 100\,\mathrm{MeV}/c$ & $\lvert\Delta\phi\rvert < 200$ & $\pi - \theta_i - \theta_j < 200$ mrad
Parallel track pairs ($p_\perp < 0.35\,\mathrm{GeV}/c$)	$\lvert\Delta\phi\rvert < 220$ & $\lvert\Delta\theta\rvert < 215$ mrad

4.2.1 Electron Identification

Electron identification is obtained with information primarily from the EMC but also from DCH and DRC information. Different criteria are established to select electrons with different levels of purity. Electrons are primarily separated from charged hadrons on the basis of the ratio of the energy deposited in the EMC to the track momentum. This quantity should be close to unity for electrons since they deposit all of their energy in the calorimeter (Fig. 4.2). The other charged tracks should appear as MIP (minimal ionizing particles) unless they have hadronic interactions in the calorimeter crystals. To further separate hadrons a variable describing the shape of the energy deposition in the EMC (LAT) is used. In addition, the $\mathrm{d}E/\mathrm{d}x$ energy loss in the DCH and the DRC Cherenkov angle are required to be consistent with an electron which offers a good e/π separation over a wide range (for the $\mathrm{d}E/\mathrm{d}x$ distribution, please see Fig. 3.15).

The track selection criteria from section 4.1 are tightened for electron selection to suppress background and to ensure a reliable momentum measurement and identification efficiency. The transverse momentum is required to be $p_\perp > 0.1\,\mathrm{GeV}/c$, and the number of associated drift chamber hits is required to be $N_{DCH} \geq 12$. Furthermore, only tracks with a polar angle in the range $23.5^\circ < \theta_{lab} < 135.8^\circ$ and electron candidates with a laboratory momentum $p_{lab} > 0.4\,\mathrm{GeV}/c$ are considered.

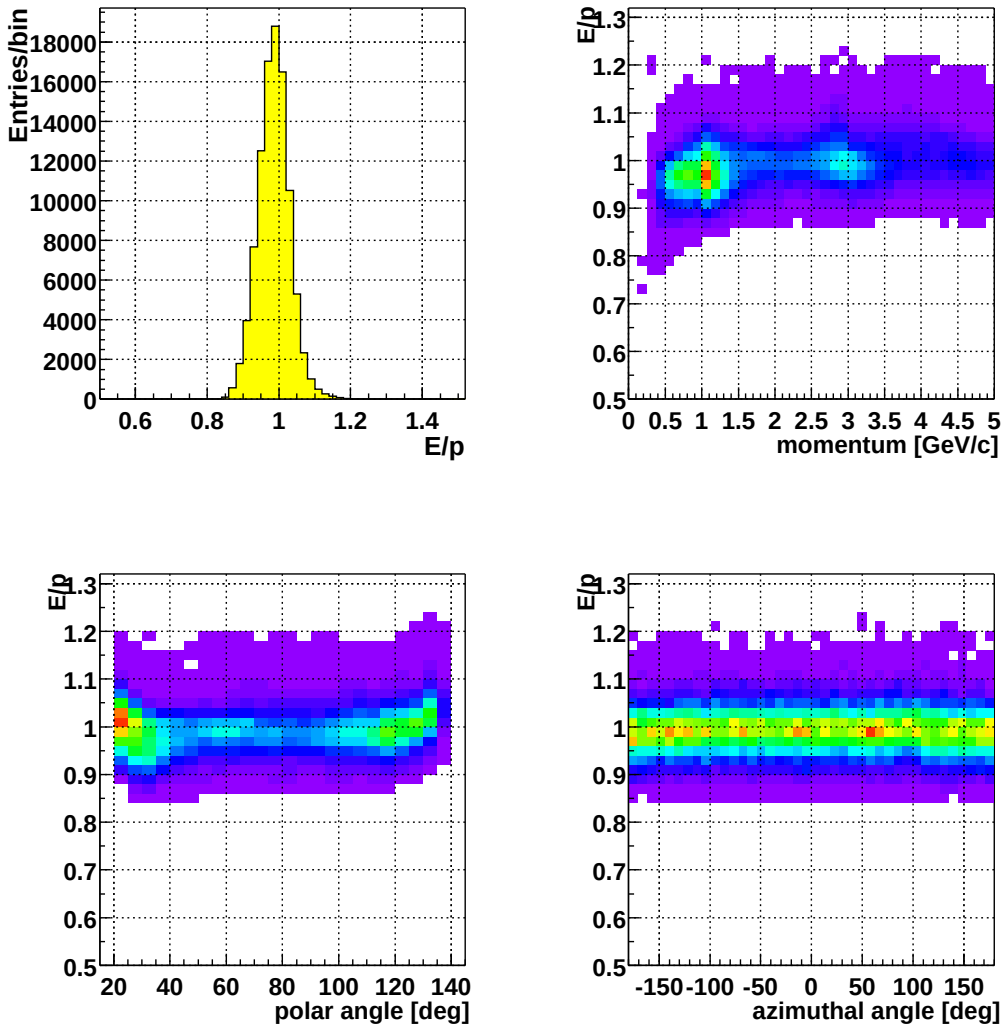

Figure 4.2: Distribution for E/p (top left) using a control sample of electrons and E/p versus momentum (top right), polar angle (bottom left) and azimuthal angle (bottom right).

Electrons are identified with a likelihood-based selector [61], which uses a number of discriminating variables:

- E_{cal}/p_{lab}, the ratio of E_{cal}, the energy deposited in the EMC, to p_{lab}, the momentum in the laboratory rest frame measured with the tracking system
- LAT, the lateral shape of the calorimeter energy deposit

- $\Delta\Phi$, the azimuthal angle between the centroid of the EMC cluster and the impact point of the track on the EMC
- N_{cry}, the number of crystals in the EMC cluster;
- dE/dx, the specific energy loss in the DCH;
- The Cherenkov angle θ_C and N_C, the number of photons measured in the DRC.

First, muons are eliminated based on dE/dx and the shower energy relative to the momentum. For the remaining tracks, likelihood functions are computed assuming the particle is an electron, pion, kaon, or proton. These likelihood functions are based on probability density functions that are derived from pure particle data control samples for each of the discriminating variables. For hadrons, we take into account the correlations between energy and shower-shapes. Using combined likelihood functions

$$\begin{aligned} L(\xi) &= P(E/p, LAT, \Delta\Phi, dE/dx, \theta_C|\xi) \\ &= P_{EMC}(E/p, LAT, \Delta\Phi|\xi)\ \ P_{DCH}(dE/dx|\xi)\ \ P_{DRC}(\theta_C|\xi) \end{aligned}$$

for the hypotheses $\xi \in \{e, \pi, K, p\}$, the fraction

$$F_{\rm e} = \frac{f_{\rm e} L({\rm e})}{\sum_\xi f_\xi L(\xi)} \, ,$$

is defined, where the relative production abundance of particles is assumed to be $f_{\rm e} : f_\pi : f_{\rm K} : f_{\rm p} = 1 : 5 : 1 : 0.1$ is assumed. A track is identified as an electron if $F_{\rm e} > 0.95$.

The electron identification efficiency has been measured with radiative Bhabha events, as a function of laboratory momentum p_{lab} and polar angle θ_{lab}. The misidentification rates for pions, kaons, and protons are extracted from selected data samples. Pure pions are obtained from kinematically selected $K^0_S \to \pi^+\pi^-$ decays and three prong $\tau^\pm$ decays. Two-body Λ and D^0 decays provide pure samples of protons and charged kaons.

The performance of the likelihood-based electron identification algorithm is summarized in Fig. 4.3, in terms of the electron identification efficiency and the per track probability that a hadron is misidentified as an electron.

The average hadron fake rates per track are determined separately for positive and negative particles, taking into account the relative abundance from Monte Carlo simulation of $B\overline{B}$ events, with

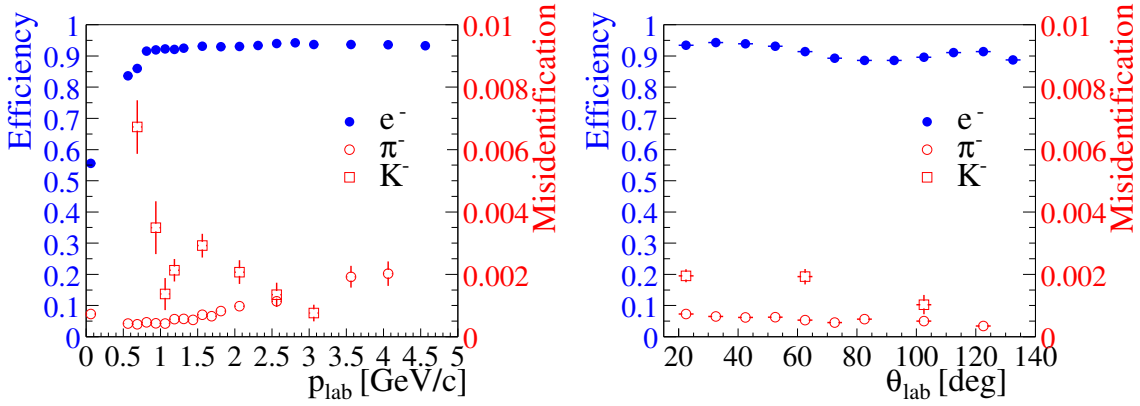

Figure 4.3: Electron identification and hadron misidentification probability for the likelihood-based electron selector as a function of momentum (left) and polar angle (right). Note the different scales for identification and misidentification on the left and right ordinates, respectively. The measurements are for luminosity-averaged rates for Run-1 and Run-2.

relative systematic uncertainties of 3.5%, 15%, and 20% for pions, kaons, and protons, respectively. The resulting average fake rate per hadron track of $p_{lab} > 1.0\,\mathrm{GeV}/c$, is of the order of 0.05% for pions and 0.2% for kaons.

4.2.2 Muon Identification

Muons are identified by measuring the number of traversed interaction lengths in the IFR and comparing it with the number of expected interaction lengths for a muon of a given momentum. Moreover, the projected intersections of a track with the IFR RPC planes are computed and, for each readout plane, all strip clusters detected within a predefined distance from the predicted intersection are associated with the track and the average number and the r.m.s. of the distribution of RPC strips per layer gives additional μ/π discriminating power. It is expected that the average number of strips per layer will be larger for pions producing an hadronic interaction than for muons. Other variables exploiting clusters distribution shapes are constructed. Selection criteria based on all these variables are applied to select muons. The performance of the muon selection has been tested on samples of kinematically identified muons from $\mu\mu ee$ and $\mu\mu\gamma$ final states and pions from three-prong τ decays and $K_S \to \pi^+\pi^-$ decays.

The muon selection procedure [62] is based on a series of requirements as follows:

- The track selection criteria from section 4.1 are tightened so: $p_\perp > 0.1\,\mathrm{GeV}/c$, $N_{DCH} \geq 12$,

$20^\circ < \theta_{lab} < 155^\circ$, and $p_{lab} > 0.4\,\mathrm{GeV}/c$

- The energy deposited in the EMC is required to be consistent with the minimum ionizing particle, $50\,\mathrm{MeV} < E_{cal} < 400\,\mathrm{MeV}$;
- The number of IFR layers associated with the track is required to be $N_L \geq 2$.
- The interaction lengths of material traversed by the track is required to be $\lambda_{meas} > 2.2$.
- The number of interaction lengths expected to be traversed by a muon of the measured momentum and angle is estimated by extrapolating the track up to the last *active* layer of the IFR. This estimate takes into account the RPC efficiencies which are routinely measured and stored. For the difference $\Delta\lambda = \lambda_{exp} - \lambda_{meas}$ we require $\Delta\lambda < 1.0$, for tracks with momentum greater than $1.2\ \mathrm{GeV}/c$. For track momenta between $0.5\,\mathrm{GeV}/c$ and $1.2\,\mathrm{GeV}/c$, a variable limit is placed: $\Delta\lambda < [(p_{lab} - 0.5)/0.7]$.
- The *continuity* of the IFR cluster is defined as $T_c = \frac{N_L}{L-F+1}$, where L and F are the last and first layers with hit. T_c is expected to be ~ 1.0 for muons penetrating the detector whereas it is expected to be much smaller for hadrons. We require $T_c > 0.3$ for tracks with $0.3 < \theta_{lab} < 1.0$ (i.e. in the forward endcap to remove beam background).
- The observed number of hit strips in each RPC layer is used to impose the conditions on the average number of hits, $\bar{m} < 8$, and the standard deviation, $\sigma_m < 4$.
- The strip clusters in the IFR layers are combined to form a track and fit to a third-degree polynomial, with the quality of the fit required to satisfy the condition $\chi^2_{fit}/DOF < 3$. In addition, the cluster centroids are compared to the extrapolated charged track, with the requirement $\chi^2_{trk}/DOF < 5$.

The muon identification efficiency has been measured using $\mu^+\mu^-(\gamma)$ events and two-photon production of $\mu^+\mu^-$ pairs. The misidentification rates for pions, kaons, and protons are extracted from selected data samples. The performance of the muon identification algorithm is summarized in Fig. 4.4, in terms of the muon identification efficiency and the per track probability that a hadron is misidentified as a muon.

4.2.3 Kaon Identification

Kaon selection is performed with variables based on information from the DRC, the DCH and the SVT [63]. Likelihood functions are computed separately for charged and neutral particles, as

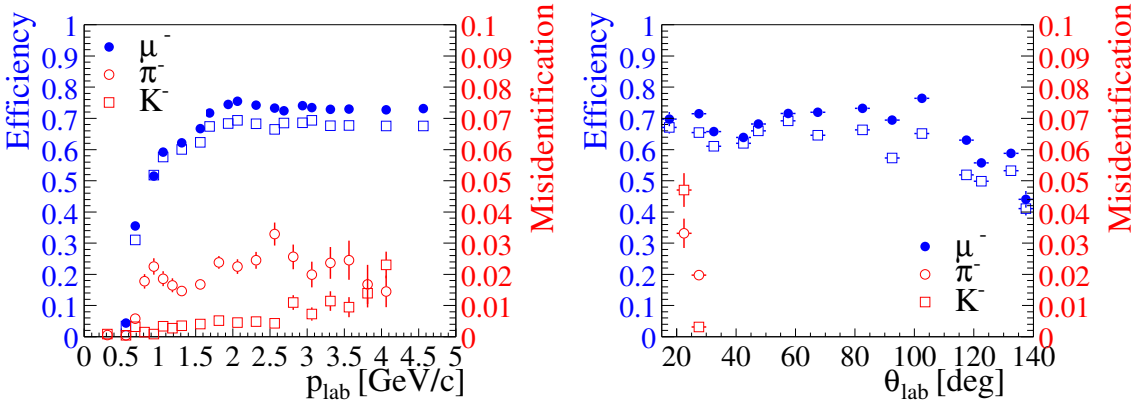

Figure 4.4: Muon identification and hadron misidentification probability for the tight muon selector as a function of momentum (left) and polar angle (right). The solid markers indicate the efficiency in 2000, the empty markers the efficiency in 2001. Note the different scales for identification and misidentification on the left and right ordinates, respectively.

products of three terms, one for each detector subsystem and then combined, similar to the electron algorithm previously described in section 4.2.1. The charged kaon efficiency is compared to the charged pion misidentification in Fig. 4.5. In the reconstruction of the invariant mass of the hadronic system, given the difference in the kaon momentum spectrum (4.5), a charged track is identified as kaon if $p_K > 300\,\mathrm{MeV}/c$ and $20^\circ < \theta_{lab} < 141^\circ$.

4.3 Neutral Particle Reconstruction

Neutral particles (photons, π^0s, neutral hadrons) are detected in the EMC as clusters of close crystals where energy has been deposited. They are required to be unmatched to any charged track extrapolated from tracking volume to EMC inner surface.

For this analysis a neutral particle is selected as a local maximum, or bump, of the energy depositions in the EMC. These energy clusters originate mostly from photons, thus momenta and angles are assigned to be consistent with photons originating from the beam-beam interactions. The list of neutrals is also used to reconstruct the π^0s, which is detailed in section 4.4.1.

A sizable background of low energy photons is due to beam-related background. To reduce the impact of these backgrounds, a restriction on the minimum energy of the neutrals has been studied. The resolution of the kinematic variables used by this analysis and the signal over background ratio have been optimized. The resulting restriction is $E_\gamma > 80\,\mathrm{MeV}$.

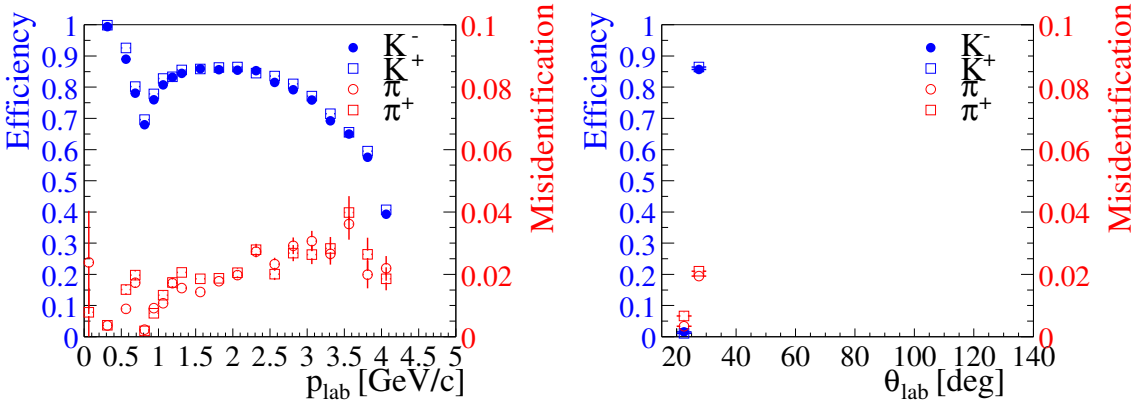

Figure 4.5: Charged kaon identification and pion misidentification probability for the tight kaon micro selector as a function of momentum (left) and polar angle (right). The solid markers indicate the efficiency for positive particles, the empty markers the efficiency for negative particles. Note the different scales for identification and misidentification on the left and right ordinates, respectively.

Some additional backgrounds are due to neutral hadronic interactions, either by K_L or neutrons. This background is removed by applying requirements on the shape of the calorimeter clusters. In order to describe the lateral energy distributions of showers, the following variables are defined: N_{cry}, the number of crystals associated with the shower, E_i, the energy deposited in the i-th crystal, numbering them such that $E_1 > E_2 > \ldots > E_N$, and r_i, φ_i, the polar coordinates in the plane perpendicular to the line pointing from the interaction point to the shower center (see Fig. 4.6).

Using these variables, one can define the lateral energy moments as

$$LAT = \frac{\sum_{i=3}^{N_{\text{cry}}} E_i r_i^2}{\sum_{i=3}^{N_{\text{cry}}} E_i r_i^2 + E_1 r_0^2 + E_2 r_0^2},$$

where r_0 is the average distance between two crystals, which is approximately $5\,\text{cm}$ for the EMC. This variable is constructed to discriminate between electromagnetic and hadronic showers based on their average properties. The summation in the numerator omits the two crystals containing the highest amounts of energy. Electrons deposit most of their energy in two or three crystals, so that the value of LAT is small for electromagnetic showers. Multiplying the energies by the squared distances enhances the effect for hadronic showers, compared with electronic showers. On the basis of control samples, a selection criterion of $LAT < 0.6$ has been chosen to separate the electron and hadron showers.

The polar angle of the bump is required to be $23.5^\circ < \theta < 145.5^\circ$ to ensure the full containment

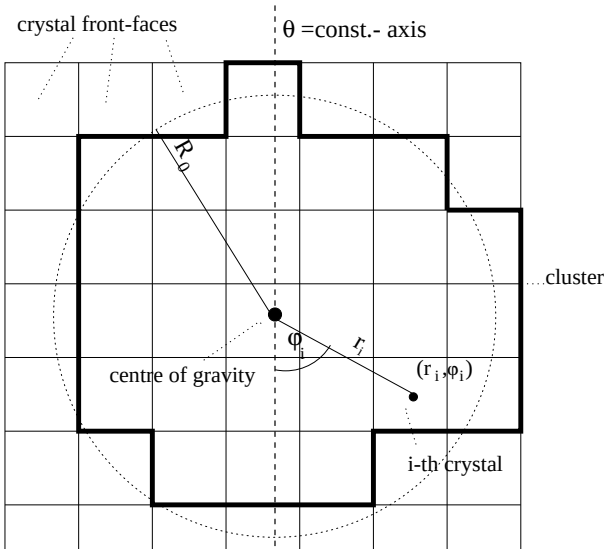

Figure 4.6: Definition of the variables r_i, φ_i and R_0

of the shower in the well-calibrated part of the EMC. Showers from split-offs are reduced by calculating the distance of closest approach of a bump to each track on the surface of the EMC requiring that the minimum distance be $d_{ca} > 20\,\mathrm{cm}$.

4.4 π^0 and K^0_S Reconstruction

The are many particles that are not directly detectable in *BABAR*, but only can be reconstructed from long-lived daughters. For example, π^0s are not directly detected but are instead reconstructed using the detectable photons it eventually decays to $\pi^0 \to \gamma\gamma$. The reconstruction of π^0 and K^0_S are discussed in sections 4.4.1 and 4.4.2.

4.4.1 π^0 Reconstruction

A wide energy spectrum of π^0s, ranging from particles almost at rest up to several GeV, is needed in this analysis. For instance, lowest energy π^0s are used to reconstruct the $D^{*0} \to D^0\pi^0$ decays while the decay products in the $B \to D\pi\pi^0$ channel have large momenta.

The π^0s are reconstructed from $\pi^0 \rightarrow \gamma\gamma$ decays using pairs of neutral clusters with a restriction on the photon minimum energy at $30\,\mathrm{MeV}$ and applying a restriction on the lateral shape of the calorimeter deposit, LAT. The resulting π^0 must have an energy above $200\,\mathrm{MeV}$. The invariant mass of the photon pair must lie between 110 and $115\,\mathrm{MeV}/c^2$, corresponding to $-4\sigma\ -\ +3\sigma$. In Fig. 4.7, invariant masses and their resolutions for simulated events and for data are shown.

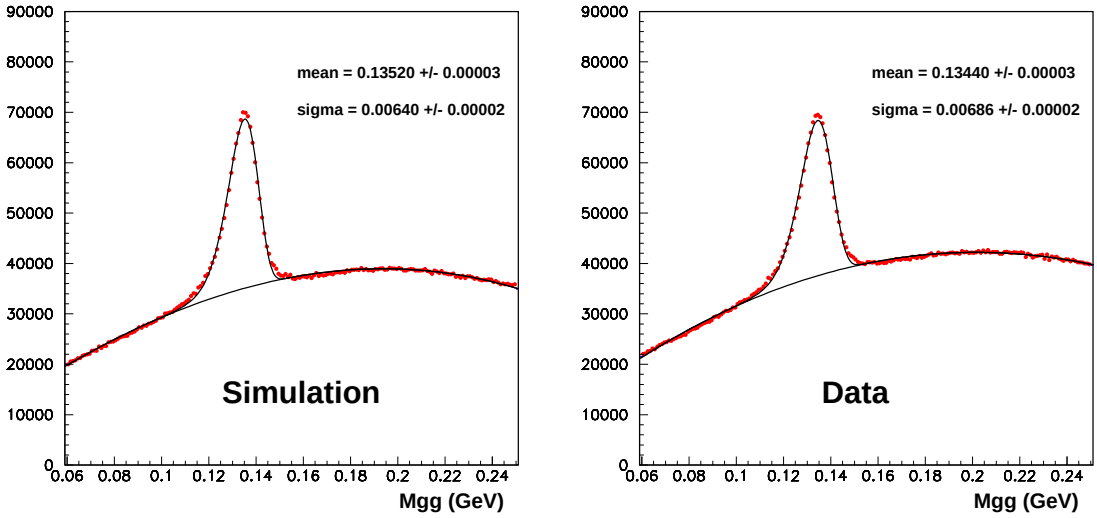

Figure 4.7: π^0 peaks for simulated events and for data.

4.4.2 K_S^0 Reconstruction

K_S^0s are reconstructed from $K_S^0 \rightarrow \pi^+\pi^-$ decays by pairing all possible tracks of opposite sign, and looking for the 3D point (vertex) which is most likely to be common to the two tracks. The algorithm is based on a χ^2 minimization and it uses the closest approach in 3D as a starting point for the vertex finding. A $\pm 3\sigma$ constraint is imposed on the invariant mass of the pion pair: $0.490 < m_{\pi^+\pi^-} < 0.505\,\mathrm{GeV}$. Figures 4.8 and 4.9 show the comparison between data and Monte Carlo simulation for the invariant mass of the $\pi^+\pi^-$ system and the K_S^0 momentum respectively. Decays of $K_S^0 \rightarrow \pi^0\pi^0$ are not used in this analysis.

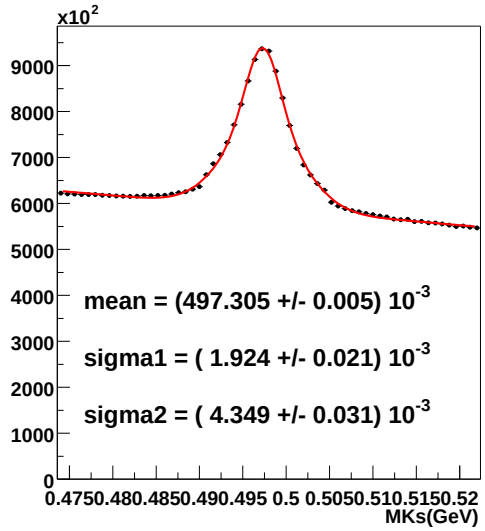

Figure 4.8: Mass distributions for $K^0_S \to \pi^+\pi^-$. The distribution is fitted with a sum of a double Gaussian and a first-order polynomial function.

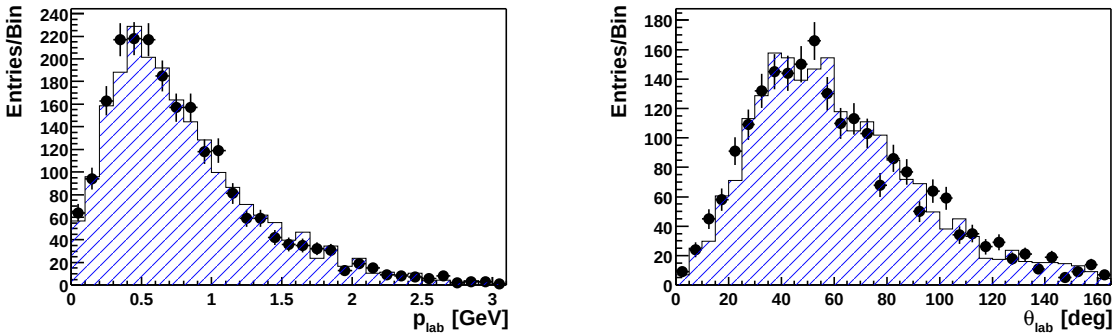

Figure 4.9: K_S momentum (left) and polar angle (right) distributions in data (solid markers) and Monte Carlo simulation (hatched histogram).

4.5 D Meson Reconstruction

Similar to π^0 and K^0_S, D mesons are not directly detected by *BABAR*, rather they are reconstructed from their decay products. The full reconstruction of B mesons in hadronic modes described in the next chapter utilizes charmed D mesons decaying in a variety of channels. The reconstruction and selection of the various types of D mesons is described in sections 4.5.1-4.5.4.

4.5.1 D^0 Meson Selection

D^0 candidates are reconstructed from the modes $D^0 \to K\pi$, $D^0 \to K\pi\pi^0$, $D^0 \to K3\pi$, and $D^0 \to K^0_S\pi\pi$. The charged tracks originating from a D meson are required to have a minimum momentum of $200\,\mathrm{MeV}/c$ for the $D^0 \to K\pi$ mode and $150\,\mathrm{MeV}/c$ for the remaining three modes. The D^0 candidates are required to lie within $\pm 3\sigma$, calculated on an event-by-event basis, of the nominal D^0 mass (Fig. 4.10). All D^0 candidates must have momentum $p^* > 1.3\,\mathrm{GeV}/c$ in the $\Upsilon(4S)$ frame. A looser constraint ($p^* > 1.0\,\mathrm{GeV}$) is applied if the D^0 is used to reconstruct a D^{*+} or D^{*0} decay. All D^0s must have a momentum in the $\Upsilon(4S)$ frame $p^* < 2.5\,\mathrm{GeV}/c$. The lower momentum constraint reduces combinatoric backgrounds while the upper momentum constraint is chosen to be at the kinematic endpoint of the D^0 coming from a $B \to D^0X$ decay or $B \to D^{*+}X$ with $D^{*+} \to D^0\pi^+$. A vertex fit is performed and a χ^2 probability greater than 0.1% is required. Table 4.2 summarizes the selection criteria for the D^0 reconstruction.

Table 4.2: Summary of selection criteria for the D^0 selection

Variable	**Selection Criteria**
Vertex Fitter χ^2	> 0.001
$p^*(D^0)$ (D^0 from D^*)	> 1.0 (> 1.3) GeV/c
	< 2.5 GeV/c
$D^0 \to K^-\pi^+$	
$m(K^-\pi^+)$	$\pm 15\,\mathrm{MeV}/c^2$
$p(K^-)$	> 200 MeV/c
$p(\pi^+)$	> 200 MeV/c
$D^0 \to K^-\pi^+\pi^0$	
$m(K^-\pi^+\pi^0)$	$\pm 25\,\mathrm{MeV}/c^2$
$p(K^-, \pi^\pm)$	> 150 MeV/c
$m(\pi^+\pi^0)$	$m(\rho) \pm 150$ MeV/c^2
$\lvert\cos\theta^*_{K\pi}\rvert$	> 0.4
$D^0 \to K^0_S\pi^+\pi^-$	
$m(K^0_S\pi^+\pi^-)$	$\pm 20\,\mathrm{MeV}/c^2$
$p(\pi^\pm)$	> 150 MeV/c
$D^0 \to K^-\pi^+\pi^+\pi^-$	
$m(K^-\pi^+\pi^+\pi^-)$	$\pm 15\,\mathrm{MeV}/c^2$
$p(K^-, \pi^\pm)$	> 150 MeV/c

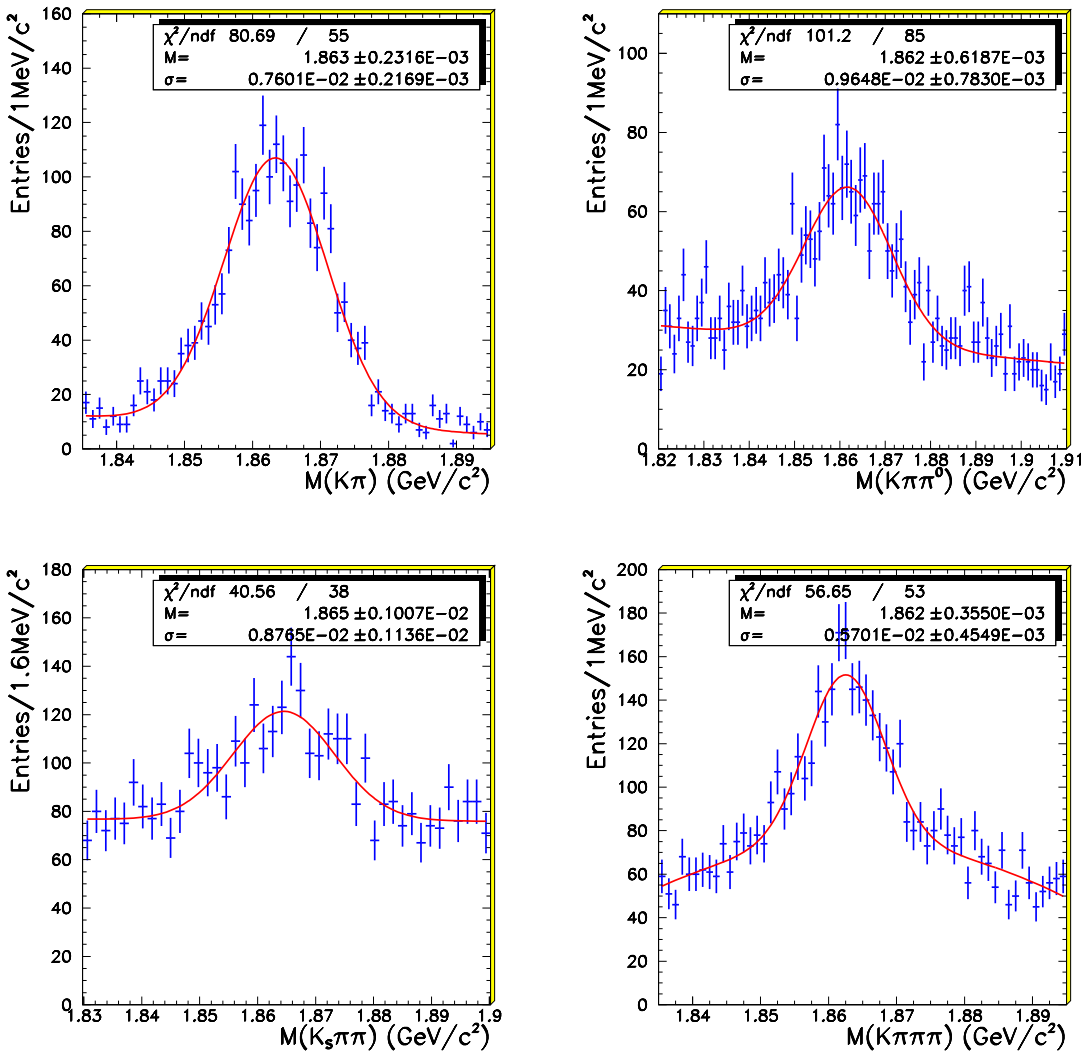

Figure 4.10: D^0 candidates selected for $D^0 \to K\pi$, $D^0 \to K\pi\pi^0$ $D^0 \to K^0_S\pi\pi$, and $D^0 \to K3\pi$ modes.

4.5.2 $D^{\pm}$ Meson Selection

D^+ candidates are reconstructed from the modes $D^+ \to K^-\pi^+\pi^+$, $D^+ \to K^-\pi^+\pi^+\pi^0$, $D^+ \to K^0_S\pi^+$, $D^+ \to K^0_S\pi^+\pi^0$, $D^+ \to K^0_S\pi^+\pi^+\pi^+$. We require that the kaon used in the $K^-\pi^+\pi^+$ and $K^-\pi^+\pi^+\pi^0$ modes have a minimum momentum of $200\,\mathrm{MeV}/c$ and that the pions have momentum greater than $150\,\mathrm{MeV}/c$. For the $K^0_S\pi^+X$ modes, the minimum charged track momentum is required to be $200\,\mathrm{MeV}/c$. D^+ candidates are required to have an invariant mass within $\pm 3\sigma$, calculated on an event-by-event basis, of the nominal D^+ mass. The D^+ candidates

must have momentum greater than $1.0\,\mathrm{GeV}/c$ in the $\Upsilon(4S)$ frame for the three cleanest modes ($D^+ \to K^-\pi^+\pi^+$, $D^+ \to K^0_S\pi^+$ and $D^+ \to K^0_S\pi^+\pi^0$) and greater than $1.6\,\mathrm{GeV}/c$ for the two remaining ones ($D^+ \to K^-\pi^+\pi^+\pi^0$ and $D^+ \to K^0_S\pi^+\pi^+\pi^+$). Moreover, all D^+ candidates must have momentum lower than $2.5\,\mathrm{GeV}/c$ in the $\Upsilon(4S)$ frame. A vertex fit is performed and a χ^2 probability greater than 0.1% is required. Table 4.3 summarizes the selection criteria for the D^+ reconstruction.

Table 4.3: Summary of selection criteria for the D^+ selection

Variable	**Selection Criteria**
Vertex Fitter χ^2	> 0.001
$p^*(D^+)$	< 2.5 GeV/c
$D^+ \to K^-\pi^+\pi^+$	
$m(K^-\pi^+\pi^+)$	± 20 MeV/c^2
$p^*(D^+)$	> 1.0 GeV/c
$p(K^-)$	> 200 MeV/c
$p(\pi^+)$	> 150 MeV/c
$D^+ \to K^-\pi^+\pi^+\pi^0$	
$m(K^-\pi^+\pi^+)$	± 30 MeV/c^2
$p^*(D^+)$	> 1.6 GeV/c
$p(K^-)$	> 200 MeV/c
$p(\pi)$	> 150 MeV/c
$D^+ \to K^0_S\pi^+$	
$p^*(D^+)$	> 1.0 GeV/c
$m(K^0_S\pi^+)$	± 20 MeV/c^2
$p(\pi^+)$	> 200 MeV/c
$D^+ \to K^0_S\pi^+\pi^0$	
$p^*(D^+)$	> 1.3 GeV/c
$m(K^0_S\pi^+)$	± 30 MeV/c^2
$p(\pi^+)$	> 200 MeV/c
$D^+ \to K^0_S\pi^+\pi^+\pi^+$	
$p^*(D^+)$	> 1.6 GeV/c
$m(K^0_S\pi^+)$	± 20 MeV/c^2
$p(\pi^+)$	> 200 MeV/c

4.5.3 $D^{*\pm}$ Meson Selection

D^{*+} candidates are formed by combining a D^0 with a pion which has momentum greater than $70\,\mathrm{MeV}/c$ (Fig. 4.11). Only the channel $D^{*+} \to D^0\pi^+$ is reconstructed since $D^{*+} \to D^+\pi^0$ events enter in the $B \to D^+X$ category as explained in chapter 5. A vertex fit for the D^{*+} is performed using a constraint on the vertical position of the beam sport to improve the angular resolution for the soft pion. A fixed resolution of $\sigma = 30\ \mu\mathrm{m}$ is used to model the beam spot spread in the vertical direction. The fit is required to converge, but no restriction is applied on the probability of χ^2. After fitting, selected D^{*+} candidates are required to have $\Delta m = m(D^0\pi^+) - m(D^0)$ within $\pm 3\sigma$ of the measured nominal value (Fig. 4.11). The Δm distribution is fitted with a double Gaussian distribution and the width is taken to be a weighted average of the core and broad Gaussian distributions. Table 4.4 summarizes the selection criteria for the D^{*+} reconstruction.

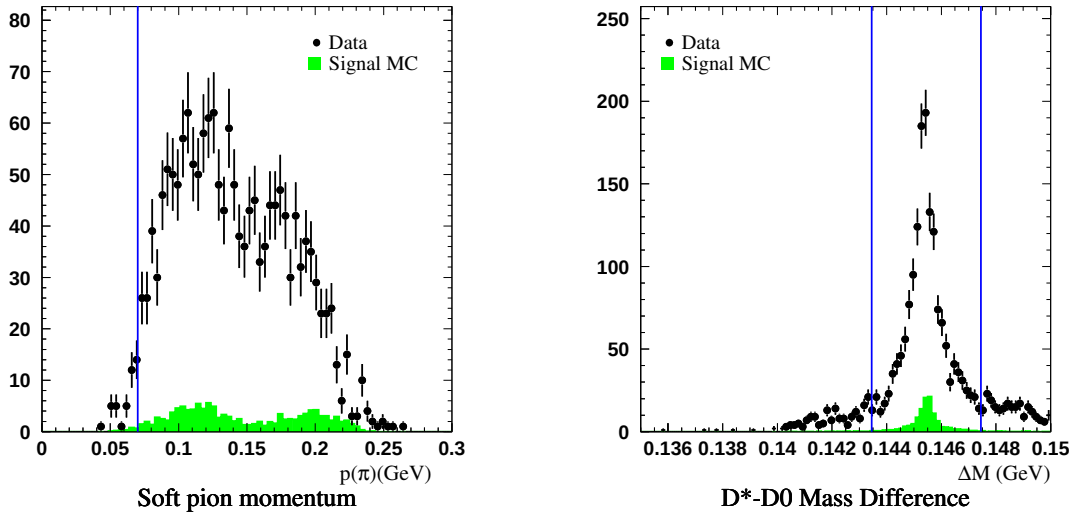

Figure 4.11: Distribution of soft pion momentum in the $\Upsilon(4S)$ frame (left) and $m(D^0\pi^+) - m(D^0)$ mass distribution for D^{*+} candidates in the $B \to D^{*+}\pi^+$, $D^0 \to K\pi$ mode. Vertical lines indicate the signal windows used in the selection.

4.5.4 D^{*0} Meson Selection

D^{*0} candidates are reconstructed by combining a previously selected D^0 candidate (see section 4.5.1) with a either a π^0 or a photon having momentum less than $450\,\mathrm{MeV}/c$ in the $\Upsilon(4S)$ frame. The minimum momentum for the π^0 is $70\,\mathrm{MeV}$ while the photons are required to have an

Table 4.4: Summary of the selection criteria for the D^{*+} selection

Variable	**Selection Criteria**
$D^{*+} \to D^0\pi^+$	
Vertexing and χ^2	beam spot constraint($\sigma_y = 30$ μm), convergence
$m(D^0\pi^+) - m(D^0)$	$\pm 3\sigma$ MeV/c^2
$p^*(\pi^+)$	[70,450] MeV/c

energy greater than $100\,\mathrm{MeV}$. For $D^{*0} \to D^0\pi^0$ decays, selected D^{*0} candidates are required to have $\Delta m = m(D^0\pi^0) - m(D^0)$ within $4\,\mathrm{MeV}/c^2$ of the nominal value while the window is wider for $D^{*0} \to D^0\gamma$ decays ($127\,\mathrm{MeV}/c^2 < \Delta m < 157\,\mathrm{MeV}/c^2$). The Δm distribution for $D^{*0} \to D^0\pi^0$, obtained from an inclusive sample of $D^0 \to K^-\pi^+$ decays, is shown in Fig. 4.12 for a $b\overline{b}$ enriched ($p^*(D^0) < 2.5$ GeV/c) sample. Table 4.5 summarizes the selection criteria for the D^{*0} reconstruction.

Table 4.5: Summary of selection criteria for the D^{*0} selection

Variable	**Selection Criteria**
$D^{*0} \to D^0\pi^0$	
$m(D^0\pi^0) - m(D^0)$	± 4 MeV/c^2
$p^*(\pi^0)$	[70,450] MeV/c
$p^*(D^{*0})$	$1.3 < p^* < 2.5$ GeV/c
$D^{*0} \to D^0\gamma$	
$m(D^0\gamma) - m(D^0)$	[127,157] MeV/c^2
$E^*(\gamma)$	[100,450] MeV
$p^*(D^{*0})$	$1.3 < p^* < 2.5$ GeV/c

4.6 B Meson Reconstruction

B meson candidates are reconstructed by combining a D meson with a linear combination of pions and kaons. The details of the B reconstruction in fully hadronic modes will be given in chapter 5. This section is intended to give a description of the two main variables used the select B candidates, to extract the yields and to define a sideband region to study the background.

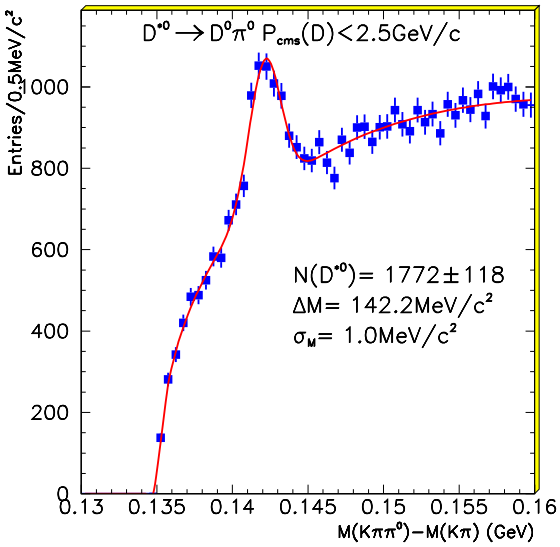

Figure 4.12: Δm distribution for $D^{*0} \to D^0\pi^0$ decays, where $p^*(D^0) < 2.5$ GeV/c

4.6.1 Energy conservation and ΔE variable

In fully reconstructing a B meson from the two-body decay of the $\Upsilon(4S)$, energy conservation can be imposed. The *energy difference* ΔE is then defined as

$$\Delta E = E_B^* - \sqrt{s}/2\,, \tag{4.1}$$

where E_B^* is the energy of the B candidate in the $\Upsilon(4S)$ rest frame (CM) and $\sqrt{s}$ is the e^+e^- CM beam energy. The resolution of this variable is affected by the detector momentum resolution and by the particle identification since a wrong mass assignment would result in a shift in ΔE . The signal event ΔE distribution, seen in Fig. 4.13, can be described by a Gaussian around a central value of zero. The continuum and $b\bar{b}$ background can be fitted with a polynomial distribution. Background due to misidentification gives shifted Gaussian peaks (visible in the left part of Fig. 4.13). The resolution of ΔE differs for various reconstructed B modes and can vary from $20\,\mathrm{MeV}$ to $40\,\mathrm{MeV}$. The source of the variation in the resolution is the charged track multiplicity and π^0 multiplicity. The higher the multiplicity, the worse the resolution because there is a higher probability of particle misidentification and poor momentum measurement. A cut on ΔE , dependent upon the B decay

mode, is then necessary as described in chapter 5.

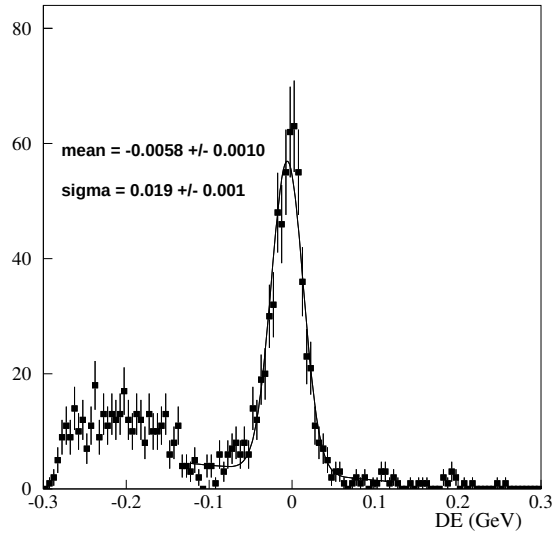

Figure 4.13: An example of ΔE distribution for $B \to D^{*+}\pi^-$ with $D^0 \to K\pi$.

4.6.2 B mass reconstruction and $m_{\rm ES}$ variable

The *beam energy-substituted mass* is defined as:

$$m_{\rm ES} = \sqrt{(\sqrt{s}/2)^2 - p_B^{*2}}\,, \tag{4.2}$$

where $\sqrt{s}$ is the total energy of the e^+e^- system in the CM rest frame and p^* is the B candidate momentum in the CM rest frame. Since $|p_B^*| \ll \sqrt{s}/2$, the experimental resolution on $m_{\rm ES}$ is dominated by beam energy fluctuations. To an excellent approximation, the shapes of the $m_{\rm ES}$ distributions for B mesons reconstructed in a final states with charged tracks only are Gaussian. The presence of neutrals in the final states, in case they are not fully contained in the EMC, can introduce tails to the distribution.

It is important to notice that $m_{\rm ES}$ and ΔE are dependent variables by their definition. However, since the sources of experimental smearing are uncorrelated (beam energy for $m_{\rm ES}$ and detector momentum resolution for ΔE), they can be treated as independent variables. See Fig. 4.14 for a

distribution of $m_{\rm ES}$ vs. ΔE .

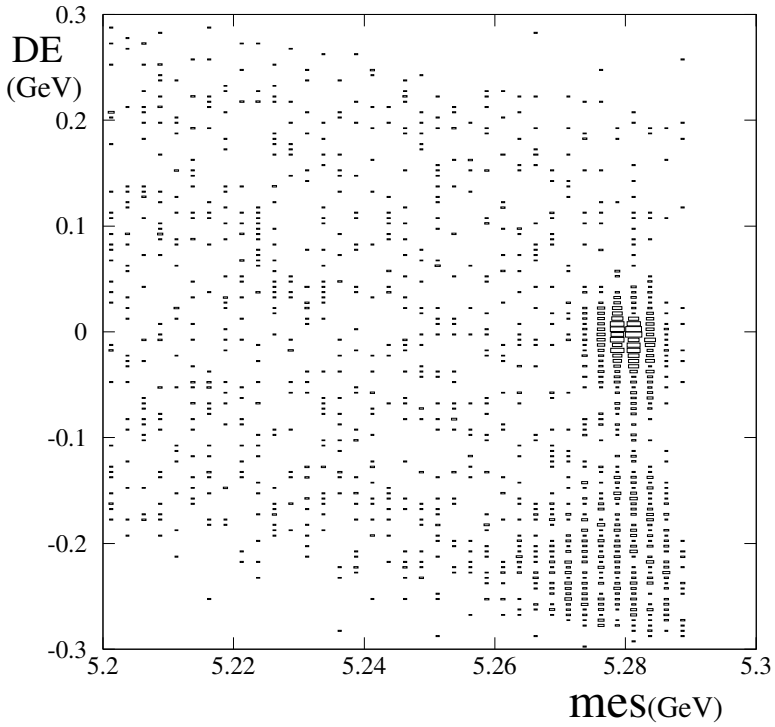

Figure 4.14: ΔE versus $m_{\rm ES}$ for the decay, $B \to D^{*+}\pi^-$ with $D^0 \to K\pi$.

Fit to the $m_{\rm ES}$ variable

The background shape in $m_{\rm ES}$ is parameterized with the ARGUS function [64]:

$$\frac{dN}{dm_{\rm ES}} = N \cdot m_{\rm ES} \cdot \sqrt{1-x^2} \cdot \exp\left(-\xi \cdot (1-x^2)\right) \tag{4.3}$$

where $x = m_{\rm ES}/m_{\rm max}$ and the parameter ξ is determined from a fit to the $m_{\rm ES}$ distribution. The value of $m_{\rm max}$, which is the endpoint of the ARGUS distribution, is fixed in the fit to $m_{\rm ES}$, since it depends only on the beam energy. ARGUS shapes describe both continuum ($c\overline{c}$ and uds) and $b\overline{b}$ background events well, as shown in Fig. 4.15.

The signal component is fitted using a Crystal Ball function [65], which is piecewise in $m_{\rm ES}$:

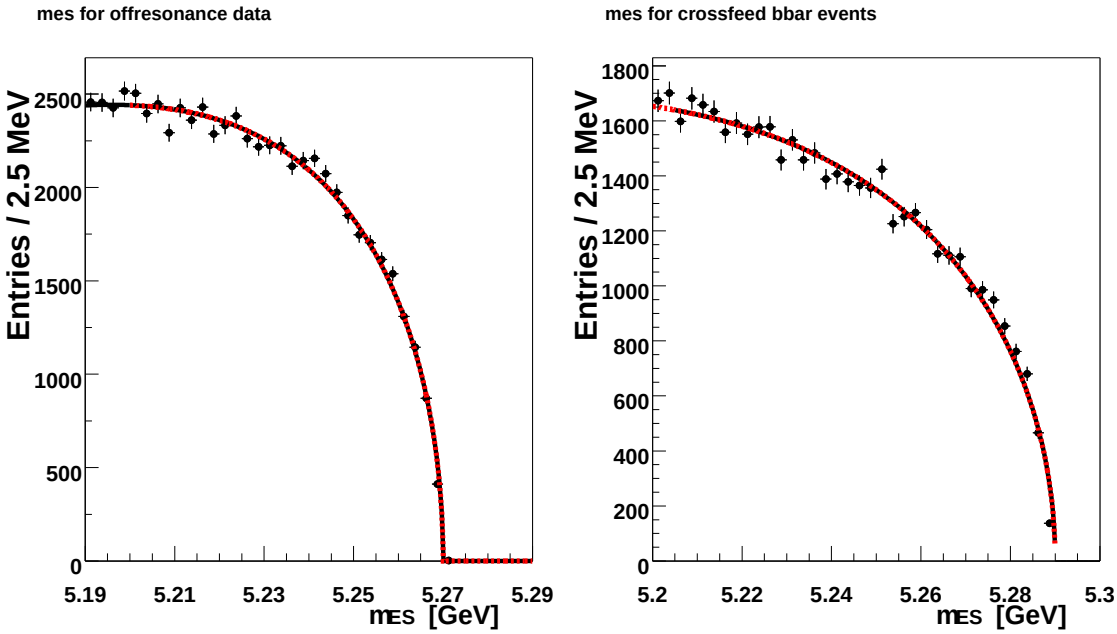

Figure 4.15: Left: $m_{\rm ES}$ distribution for candidates in the off-resonance data (40 MeV below the $\Upsilon(4S)$ mass). Right: $m_{\rm ES}$ distribution for $b\overline{b}$ background (B^0 reconstructed as B^+). ARGUS shape fit is superimposed in both cases.

- if $m_{\rm ES} > m - \sigma \cdot a$

$$\frac{dN}{dm_{\rm ES}} = N \cdot \frac{1}{\sqrt{2 \cdot \pi} \cdot \sigma} \cdot \exp\left(-\frac{1}{2} \cdot \frac{(m_{\rm ES} - m)^2}{\sigma^2}\right) \tag{4.4}$$

- and if $m_{\rm ES} < m - \sigma \cdot a$

$$\frac{dN}{dm_{\rm ES}} = N \cdot \frac{1}{\sqrt{2 \cdot \pi} \cdot \sigma} \cdot \left(\frac{n}{a}\right)^n \exp\left(-\frac{1}{2} \cdot a^2\right) \frac{1}{\left(\frac{(m_{\rm ES} - m)}{\sigma} + \frac{n}{a} - a\right)^n} \tag{4.5}$$

where m is the mean of the Gaussian peak, σ is the width of the Gaussian peak, a determines the transition point for the piecewise function, and n describes the shape of the tail.

The radiative tail of this function can account for energy losses in the showers of reconstructed π^0s. Thus, the left tail of the distribution depends on the reconstructed B mode and in particular on the number of π^0s. Figure 4.16 shows the fitted shape on the Monte Carlo for modes with no π^0s, one π^0 and two π^0s.

With these choices for background and signal forms, the maximum total number of floating parameters in fits to the $m_{\rm ES}$ distribution is 7. Two of them arise from the ARGUS function, while

the remaining five parameters are due to the Crystal Ball. The signal yield S from an $m_{\rm ES}$ fit is defined as the area of the Crystal Ball function for the region $m_{\rm ES} > 5.27$. The background B from an $m_{\rm ES}$ fit is defined as the area of the Argus function for the same region. The purity of the $m_{\rm ES}$ distribution is defined as a ratio of the signal-to-background as $P = S/(S + B)$.

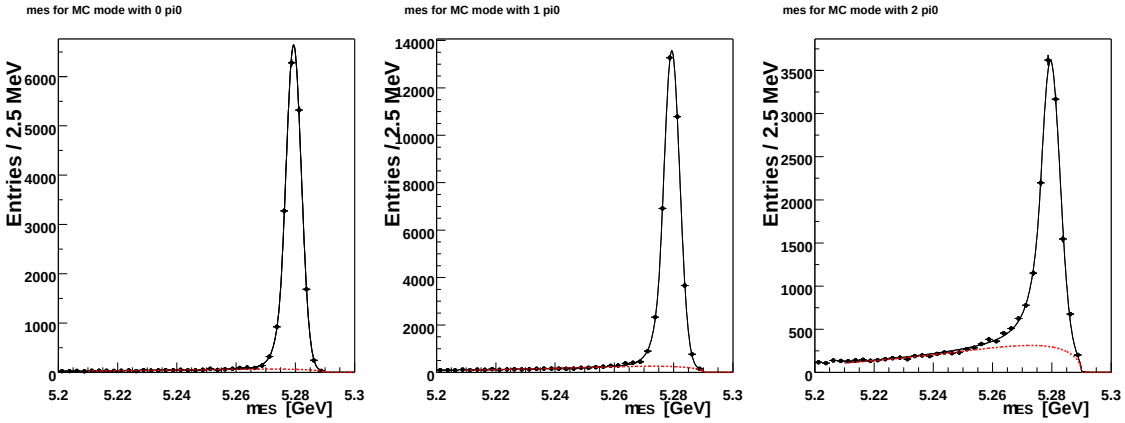

Figure 4.16: MC $m_{\rm ES}$ distributions for reconstructed B modes with (left) no π^0 in the final state, (middle) 1 π^0 in the final state and (right) 2 π^0's in the final state. The fit function is a sum of crystal ball and ARGUS function.

Chapter 5

Semi-Exclusive Reconstruction

The measurement of the partial $b \to u\ell\bar{\nu}$ decay rate $\delta\Gamma(c)$ is performed by studying the recoiling B meson from a fully reconstructed hadronically decaying B meson. The motivations for performing the study with the fully reconstructed recoil sample are explained in chapter 6. In this chapter, the methods for assembling a semi-exclusive B sample are described.

5.1 Introduction

The goal of the semi-exclusive reconstruction is to reconstruct as many B mesons in hadronic modes as is possible. The sum of a select few highly pure exclusive modes assures a very high purity sample, but the reconstruction efficiency will be low. On the other hand, a fully inclusive approach that uses modes with high track and neutral multiplicities is not feasible since the level of combinatoric background would be too high. Instead, this analysis uses a compromise between these two extremes. The reconstruction includes only favored modes by putting a limit on the maximum number of particles (multiplicity) used in the reconstruction and employing an algorithm that is as inclusive as possible in combining the particles, neglecting the intermediate states when possible.

The B meson decays predominantly into hadronic final states involving D or D^* mesons. Table 5.1 shows the relevant branching fractions for B decays that contain one of these modes. Because of these relatively large branching fractions, the semi-exclusive reconstruction will concentrate on the fully hadronic modes that involve the $D^{(*)}$, $D^{0(*)}$ mesons.

Table 5.1: Some of the inclusive and exclusive branching fractions relevant to the semi-exclusive reconstruction [6]. The reason that the branching fractions sum to a value greater than unity is that for inclusive $B \to D^{(*)}Y$ decays, there can be a significant amount of overlap as the Y can include $D^{(*)}$ mesons.

mode	branching fraction (%)
$B \to D^{*\pm}Y$	22.5 ± 1.5
$B \to D^{\pm}Y$	23.5 ± 1.9
$B \to D^{*0}/\overline{D}^{*0}Y$	26.0 ± 2.7
$B \to D^{0}/\overline{D}^{0}Y$	64.0 ± 3.0
$B \to D_s^{*\pm}Y$	7.9 ± 2.2
$B \to D_s^{\pm}Y$	10.5 ± 2.6
$B \to D_s^{*\pm}\overline{D}^{(*)}$	4.2 ± 1.2
$B \to D_s^{(*)}\overline{D}^{(*)}$	4.9 ± 1.2
$B \to D^{(*)}\overline{D}^{(*)}K$	7.1 ± 2.3

5.2 Reconstruction Method

Since high multiplicity modes are involved, techniques are applied to reduce the combinatoric background in order to obtain a sample with reasonable purity while reducing the CPU time and the size of the final sample. The strategy of the reconstruction method is as follows:

- Reconstruct all possible decay modes $B \to DY$, where D implies any D meson (D^0, D^+, D^{*0}, D^*) and the Y system is comprised of a linear combination of π^+,π^0, K^+ and K_S^0 with total charge equal to ± 1.

- Identify submodes and create subcategories according to the multiplicity and the structure of the Y system (e.g. $D\pi\pi^0$, $M_{\pi\pi^0} < 1.5\,\mathrm{GeV}/c^2$). This is meant to identify the high purity modes and to optimize the overall purity of the sample as clean modes have to be separated from the low purity ones.

- Determine a mode-by-mode ΔE cut (see 4.6.1), in order to account for different resolutions.

- Rank the submodes according to their purity and yields and study the ratio of signal-to-background $S/\sqrt{S+B}$ as a function of the number of used modes in order to maximize the statistical significance of the sample.

- Group submodes with similar purity.

- Resolve cases with multiple candidates

The reconstruction starts with the construction of D^0, D^+, D^*, D^{*0} mesons, as described in section 4.5. Pion, kaon, π^0, and K^0_S candidates are combined with the D meson to reconstruct B meson candidates. Tracks are selected using the criteria described in 4.1 with additional constraints. Overlaps from $\Lambda \to p\pi$ candidates and γ conversions ($\gamma \to e^+e^-$) are removed. Tracks satisfying the electron and muons selection criteria (4.2.1,4.2.2) are discarded. Tracks identified as kaons (4.2.3) are assigned the mass of the kaon while the others are treated as pions.

The reconstruction of π^0 candidates proceeds as described in section 4.4.1. Pairs of oppositely-charged hadrons ($V^0 = h^+h^-$) and quartets of hadrons ($W^0 = h^+h^-h^+h^-$) are created from charged tracks in the event. If both the K^0_S decay products are among the tracks used for a V^0 or a W^0, the two tracks are replaced by the K^0_S (i.e. a V^0 would become a K^0_S and a W^0 either a $K^0_S\,\pi\pi$ or a $K^0_S\,K^0_S$). The selection of K^0_S candidates is described in 4.4.2.

5.2.1 Selection of B candidates

The algorithm starts with a reconstructed D meson, which is called a pre-seed. A track is added and the combination of the D and the track form the seed *e.g.,* $B^0 \to D^-\pi^+$. This is driven by the requirement that only neutral B modes decaying into charged D mesons and charged B modes decaying into neutral D mesons will be considered. The seed is the starting point of the reconstruction. Then π^0, K^0_S, and additional track pairs are added iteratively to make up the Y system.

Each combination is classified according to the two kinematic variables ΔE and $m_{\rm ES}$ discussed in section 4.6. The plane $m_{\rm ES}$ vs. ΔE is divided in four zones that take into account the fact that the addition of a π^0 or a couple of charged tracks increases the ΔE . A B meson candidate should lie near $\Delta E = 0$ and $m_{\rm ES} = 5.279\,{\rm GeV}/c^2$. As a result, we define zones in the $m_{\rm ES} - \Delta E$ plane that guide the algorithm in the development of candidates:

- Zone A: The event has a high ΔE value and is in the $m_{\rm ES}$ signal region thus it is only considered as a B candidate and not as a seed since adding any further tracks or neutrals would inflate ΔE further.

- Zone B: The event is in the signal region in $m_{\rm ES}$ and has a ΔE that leaves room for the addition of π^0 or track pairs, thus it is considered both as a candidate and a potential seed.

- Zone C: The event is out of the signal region in $m_{\rm ES}$ so it is considered as a seed since the addition of further particles could move the event into zone A or B, resulting in a signal candidate B.

- Zone D: The event has high ΔE but is out of the $m_{\rm ES}$ signal region, so the event is discarded.

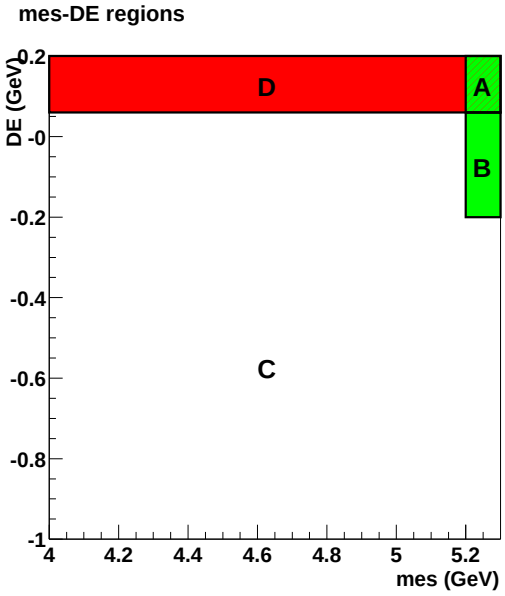

Figure 5.1: Definition of the $m_{\rm ES}$-ΔE regions. In each iteration of the semi-exclusive reconstruction a combination is used (A) only as candidate, (B) both as candidate and as seed. (C) used as seed but not as candidate and (D) discarded.

The algorithm continues to iterate, considering all possible combinations of up to 7 particles (5 charged tracks and 2 neutrals). The end result is a set of several candidates for the various D seeds.

5.3 Categorization and Summary of B Modes

The choice of the submodes is the next step in the reconstruction method. The identification of the clean modes allows us to establish an efficient and pure selection from among the multiple candidates in different modes. There are 52 B modes per seed mode (53 for the D^+ seed) which results in a total of 1097 modes, as summarized in Table 5.2.

Table 5.2: Summary of the number of semi-exclusive modes.

Channel	**pre-seed mode**	**number of B modes**
$B^+ \rightarrow D^0 Y$	$D^0 \rightarrow K^-\pi^+$	52
	$D^0 \rightarrow K^-\pi^+\pi^0$	52
	$D^0 \rightarrow K^0_S\pi^+\pi^-$	52
	$D^0 \rightarrow K^-\pi^+\pi^+\pi^-$	52
		208
$B^0 \rightarrow D^+ Y$	$D^+ \rightarrow K^-\pi^+\pi^+$	53
	$D^+ \rightarrow K^-\pi^+\pi^+\pi^0$	53
	$D^+ \rightarrow K^0_S\pi^+$	53
	$D^+ \rightarrow K^0_S\pi^+\pi^0$	53
	$D^+ \rightarrow K^0_S\pi^+$	53
		265
$B^+ \rightarrow D^{*0} Y$	$D^{*0} \rightarrow D^0\pi^0$, $D^0 \rightarrow K^-\pi^+$	52
	$D^{*0} \rightarrow D^0\pi^0$, $D^0 \rightarrow K^-\pi^+\pi^0$	52
	$D^{*0} \rightarrow D^0\pi^0$, $D^0 \rightarrow K^0_S\pi^+\pi^-$	52
	$D^{*0} \rightarrow D^0\pi^0$, $D^0 \rightarrow K^-\pi^+\pi^+\pi^-$	52
	$D^{*0} \rightarrow D^0\gamma$, $D^0 \rightarrow K^-\pi^+$	52
	$D^{*0} \rightarrow D^0\gamma$, $D^0 \rightarrow K^-\pi^+\pi^0$	52
	$D^{*0} \rightarrow D^0\gamma$, $D^0 \rightarrow K^0_S\pi^+\pi^-$	52
	$D^{*0} \rightarrow D^0\gamma$, $D^0 \rightarrow K^-\pi^+\pi^+\pi^-$	52
		416
$B^0 \rightarrow D^{*+} Y$	$D^{*+} \rightarrow D^0\pi^+$, $D^0 \rightarrow K^-\pi^+$	52
	$D^{*+} \rightarrow D^0\pi^+$, $D^0 \rightarrow K^-\pi^+\pi^0$	52
	$D^{*+} \rightarrow D^0\pi^+$, $D^0 \rightarrow K^0_S\pi^+\pi^-$	52
	$D^{*+} \rightarrow D^0\pi^+$, $D^0 \rightarrow K^-\pi^+\pi^+\pi^-$	52
		208
TOTAL		**1097**

5.4 Signal Event Selection

Once all the possible reconstruction modes are identified, a window in ΔE is defined and a criterion is established for selecting from among the multiple candidates in a given mode. The ΔE resolutions are determined from the ΔE distributions before requesting the best candidates. The resolutions depend on the number of charged tracks and above all, the number of π^0 in the Y system (since the reconstructed D meson is mass constrained).

For the modes without a π^0, a fit with a linear background and a Gaussian is performed and two

symmetric windows are taken. In the case of modes with at least one π^0, the situation is trickier. First of all, there are many candidates per event. There is no choice but to allow a maximum of 10 candidates and the candidates with the smallest $|\Delta E|$ are taken. This can create a bias in the ΔE distribution, therefore only the cleanest modes (an example for $D^*\ \pi\pi^0$ is in Fig. 5.2) are used to determine a common window for all modes including a π^0.

The chosen ΔE windows for the various types of Y systems are:

- $-45 < \Delta E\ < 30\,\mathrm{MeV}$ for $Y = 3h$
- $|\Delta E| < 45\,\mathrm{MeV}$ for $Y = h$ and $Y = K^0_S + h$
- $|\Delta E| < 48\,\mathrm{MeV}$ for $Y = 5h$ and $Y = K^0_S + 3h$
- $|\Delta E| < 50\,\mathrm{MeV}$ for $Y = K^0_S K^0_S + nh$
- $-90 < \Delta E\ < 60\,\mathrm{MeV}$ all other combinations

where h means either a charged π or K.

5.5 Selection of the Best B

Two kinds of multiple candidates are possible: multiple candidates can be reconstructed in the same submode or there can be many reconstructed submodes per event, or there can be a combination of the two situations where there are multiple candidates in a given submode with several submodes reconstructed per event. If there are multiple candidates in the same submode, the candidate with the lowest $|\Delta E|$ is taken to reduce the situation to one candidate per submode.

The selection of the best B candidate from among the different submodes cannot rely on the ΔE criterion because the modes with higher combinatoric background would be favored with respect to the clean ones, thus introducing a systematic bias. Instead, signal events are selected on the basis of the expected purity for the mode, using tables of mode-by-mode purity. The selection proceeds by taking the mode with the highest purity among those reconstructed for the event.

The purity tables are also useful to subdivide the long list of modes into an optimal set. The modes are ranked according to their purity and are added to the sample one at a time, in order of decreasing purity. Because the highest purity modes are added first, at each addition of a mode the yield increases and the purity mostly decreases. This method is very useful because the composition of the modes can be optimized for the analysis of the recoil by computing the quality factor

$S/\sqrt{S+B}$ as a function of the number of added modes. An example for the case $B^0 \to D^{*+}X$ is shown in Fig. 5.3. The optimization of the purity for the four D seeds, after applying all analysis cuts, will be described in 6.3.3.

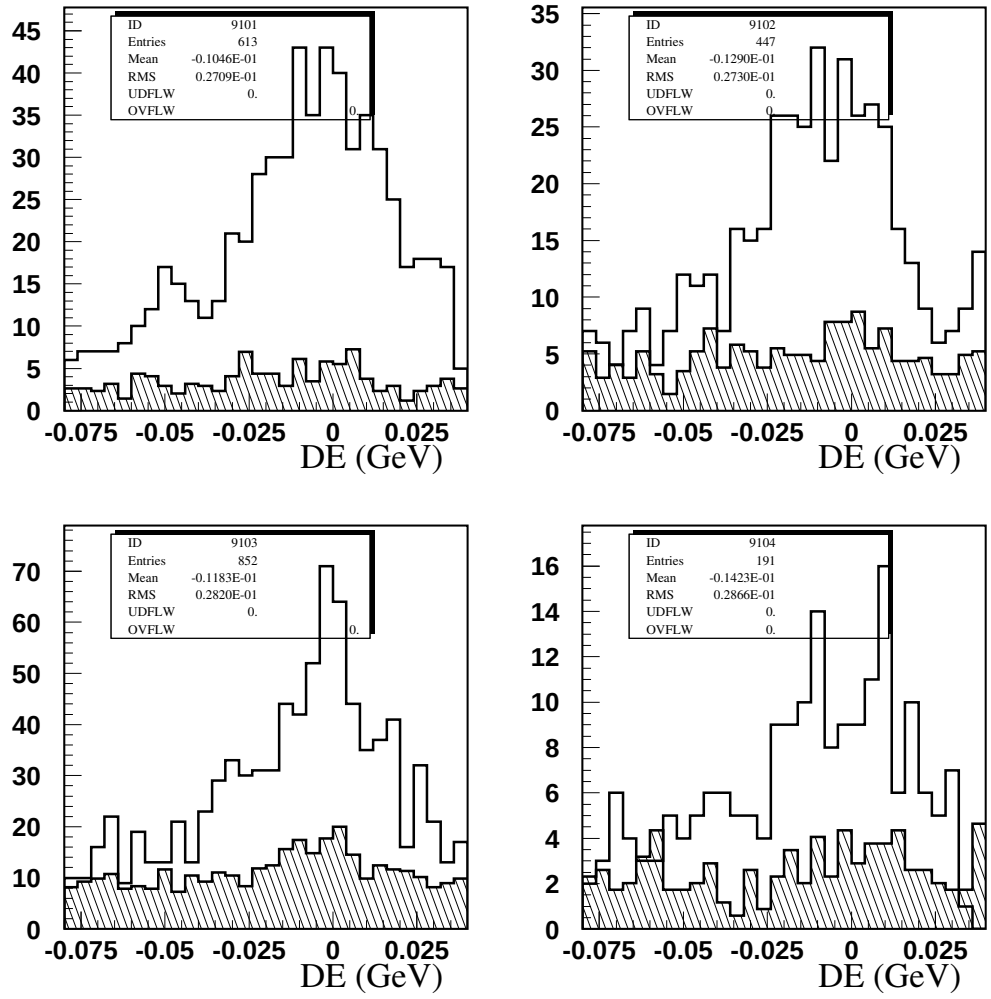

Figure 5.2: ΔE distributions for the four D^0 decay modes in $B \rightarrow D^*\pi\pi^0$, $D^* \rightarrow D^0\pi$: a) $D^0 \rightarrow K\pi$, b) $D^0 \rightarrow K\pi\pi^0$, c) $D^0 \rightarrow K3\pi$, and d) $D^0 \rightarrow K^0_S\pi\pi$

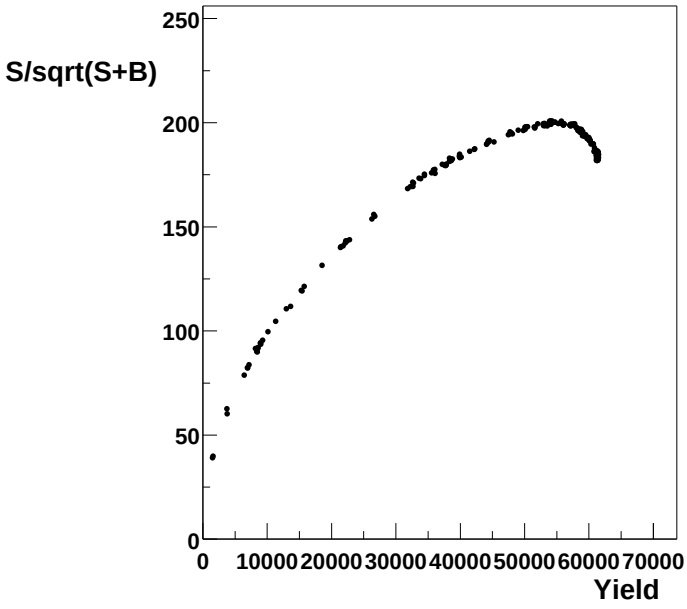

Figure 5.3: Dependence of the quality factor $S/\sqrt{S+B}$ as a function of the yield when adding modes for the $B^0 \to D^{*+}X$ case. Statistics corresponds to 80 fb^{-1}.

Chapter 6

Analysis on the Recoil

The extractions of $|V_{ub}|$ in this dissertation are made by measuring the hadronic mass spectrum of charmless semileptonic B decays. In particular, the hadronic mass spectrum yields the partial charmless semileptonic decay rate $\delta\Gamma(c)$ below a cut-off near the D mass for Eq. 2.72 and the total charmless semileptonic branching fraction $\mathcal{B}(\overline{B} \to X_u \ell \overline{\nu})$ for Eq. 2.35. This chapter describes the methods used to select $b \to u\ell\bar{\nu}$ decays and reject the dominant $b \to c\ell\bar{\nu}$ background in order to provide measurements of $\delta\Gamma(c)$ and $\mathcal{B}(\overline{B} \to X_u \ell \overline{\nu})$. The analysis is executed by examining the B mesons recoiling from the fully reconstructed B mesons that were described in chapter 5.

6.1 Introduction

The measurements of the hadronic mass spectrum of charmless semileptonic B decays are derived from studying the recoiling B meson (B_{recoil}) from the fully reconstructed B meson (B_{reco}). The strategy of the analysis is to identify semileptonic B decays ($B_{recoil} \to X\ell\bar{\nu}$) by identifying a high momentum lepton (ℓ). The hadronic X system is reconstructed from the remaining charged tracks and neutrals not belonging to the B_{reco}. Additional selection criteria are applied to select the signal $B_{recoil} \to X_u\ell\bar{\nu}$ events and reject the background $B_{recoil} \to X_c\ell\bar{\nu}$ events. Studying semileptonic decays on the recoil of a fully reconstructed B meson has many advantages, which derive from a very clean environment:

- The fully reconstructed B decays hadronically and all of the remaining particles detected belong to the recoil B. These particles are well separated from the reconstructed B. See Fig. 6.1.

- The charge of the B mesons is known.
- The momentum of the recoil B meson is known, which allows for Lorentz transformations (boosts) into the rest frame of the B meson.
- The flavor of the B mesons is known. This quantity is correlated to the charge of the lepton, which allow for rejection of cascading B decays ($B \to D \to \ell$).
- Charge conservation can be applied because the only undetected particle is a neutrino, which is neutral.
- Since the neutrino is the only undetected particle, using conservation laws, the mass of the undetected neutrino can be calculated from knowledge of the $\Upsilon(4S)$, the reconstructed B, and other particles forming the recoil B.
- Since the kinematics of the recoil system are constrained, the resolutions on signature recoil variables, such as the mass of the hadron m_X, can be improved by applying kinematic fits.

The method does have a drawback however. The full reconstruction results in a relatively small data sample since the full reconstruction described in chapter 5 has a low efficiency ($\sim 0.5\%$). The advantages far outweigh this drawback in light of the high luminosity available at *BABAR*.

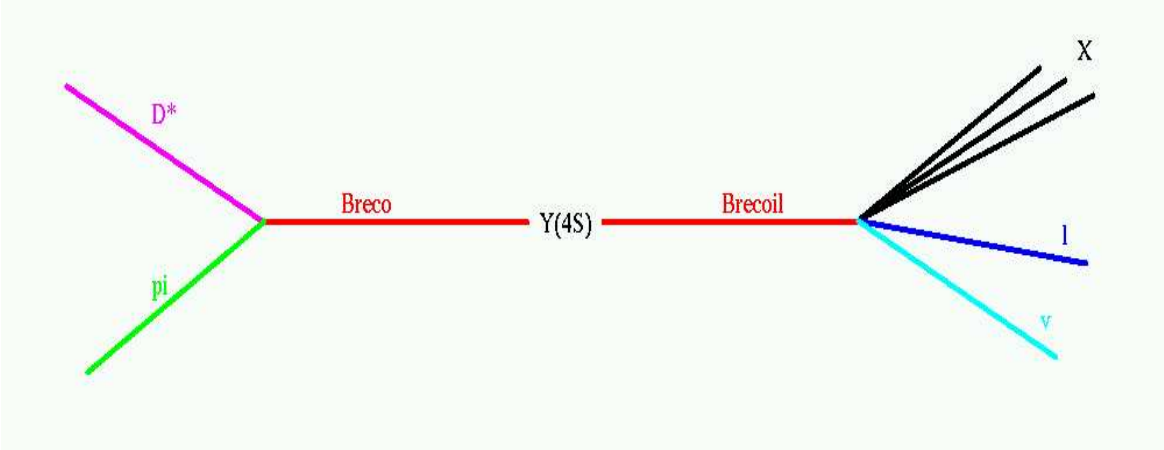

Figure 6.1: Semileptonic B_{recoil} decay recoiling from a fully reconstructed B meson.

6.2 Data and Monte Carlo Samples

This section will describe the data and Monte Carlo (MC) samples used to perform the analysis.

6.2.1 Data Sample

The analysis is based on a total integrated on-peak luminosity of $81.9\,\text{fb}^{-1}$, with $20.7\,\text{fb}^{-1}$ and $61.2\,\text{fb}^{-1}$ in Run-1 and Run-2, respectively, recorded during the years 1999-2002. They correspond to about 90 millions of pairs $B\overline{B}$. The off-peak data, corresponding to $9.6\,\text{fb}^{-1}$, is used as a control sample to check the fit to the $m_{\rm ES}$ variable for the continuum events (see section 4.6.2).

6.2.2 Monte Carlo Samples

The Monte Carlo samples used in this analysis are summarized in Table 6.1. These samples differ either in terms of the decay modes for the fully reconstructed B or the selection of semileptonic decays and their decay model. Cocktail samples contain specific hadronic decay modes for one of the B mesons, corresponding to a subset of the modes used in the semi-exclusive reconstruction. These samples have the advantage that the semi-exclusive reconstruction has high efficiency. Generic $b\overline{b}$ MC includes the full spectrum of possible decays of the B meson, so that it should represent the data and be an unbiased event sample. The cocktail MC is only used for crosscheck purposes and high statistics tests, while the generic $b\overline{b}$ samples are actually used to model the data in the fit to extract the signal.

Table 6.1: Monte Carlo event samples used in this analysis. Equivalent statistics in $|V_{ub}|$ MC assumes $\mathcal{B}(b \to u\ell\bar{\nu}) = 1.7 \times 10^{-3}$

Data Set	1' B mode	2' B mode	equiv. lumin.	recon. B s
B^0 cocktail	$cocktail$	$generic$	$250\,\text{fb}^{-1}$	326200
$B^\pm$ cocktail	$cocktail$	$generic$	$210\,\text{fb}^{-1}$	489700
B^0 generic	$generic$	$generic$	$114\,\text{fb}^{-1}$	158600
$B^\pm$ generic	$generic$	$generic$	$110\,\text{fb}^{-1}$	346600
$\|V_{ub}\|$ $hybrid$ generic	$hybrid$ signal	$generic$	$750\,\text{fb}^{-1}$	9370
$\|V_{ub}\|$ $nonres$ generic	$nonres$ signal	$generic$	$450\,\text{fb}^{-1}$	5560
$\|V_{ub}\|$ $hybrid$ cocktail	$hybrid$ signal	$cocktail$	$900\,\text{fb}^{-1}$	11300
$\|V_{ub}\|$ $nonres$ cocktail	$nonres$ signal	$cocktail$	$900\,\text{fb}^{-1}$	11600
$c\overline{c}$	-	-	$35\,\text{fb}^{-1}$	-
$u\overline{u}$, $d\overline{d}$, $s\overline{s}$	-	-	$29\,\text{fb}^{-1}$	-

Signal Monte Carlo

Three signal Monte Carlo samples are used in this analysis. The first contains only resonant exclusive $B \to X_u \ell \nu$ decays, based on the measured branching fractions and theoretical expectations. The second sample is based on a non-resonant inclusive model. The third is a combination of the two above. The size of the generated event samples and the equivalent luminosity is detailed in Table 6.1.

The ISGW2 model [66] is used to simulate exclusive charmless semileptonic decays. The branching ratios used are listed in Table 6.2 and the m_X distribution is shown in Fig. 6.2 (left).

Table 6.2: Branching ratios used in the resonant and non-resonant $\overline{B} \to X_u \ell \bar{\nu}$ signal MC (before the hybrid reweighting). The hadron masses m_X are those used in the generator.

Mode	**BR**	m_X **(** GeV/c^2**)**	**Mode**	**BR**	m_X **(** GeV/c^2**)**
$B^0 \to \pi^- \ell^+ \nu$	$180 \cdot 10^{-6}$	0.13498	$B^+ \to \pi^0 \ell^+ \nu$	$90 \cdot 10^{-6}$	0.13957
			$B^+ \to \eta \ell^+ \nu$	$30 \cdot 10^{-6}$	0.54730
$B^0 \to \rho^- \ell^+ \nu$	$260 \cdot 10^{-6}$	0.7685	$B^+ \to \rho^0 \ell^+ \nu$	$130 \cdot 10^{-6}$	0.7685
			$B^+ \to \omega \ell^+ \nu$	$130 \cdot 10^{-6}$	0.78257
			$B^+ \to \eta' \ell^+ \nu$	$60 \cdot 10^{-6}$	0.95777
$B^0 \to a_0^- \ell^+ \nu$	$14 \cdot 10^{-6}$	0.9835	$B^+ \to a_0^0 \ell^+ \nu$	$7 \cdot 10^{-6}$	0.9835
$B^0 \to a_1^- \ell^+ \nu$	$165 \cdot 10^{-6}$	1.23	$B^+ \to a_1^0 \ell^+ \nu$	$82 \cdot 10^{-6}$	1.23
$B^0 \to a_2^- \ell^+ \nu$	$14 \cdot 10^{-6}$	1.318	$B^+ \to a_2^0 \ell^+ \nu$	$7 \cdot 10^{-6}$	1.318
$B^0 \to b_1^- \ell^+ \nu$	$102 \cdot 10^{-6}$	1.231	$B^+ \to b_1^0 \ell^+ \nu$	$48 \cdot 10^{-6}$	1.231
			$B^+ \to f_0^0 \ell^+ \nu$	$4 \cdot 10^{-6}$	1.000
			$B^+ \to f_0'^0 \ell^+ \nu$	$4 \cdot 10^{-6}$	1.4
			$B^+ \to f_1^0 \ell^+ \nu$	$41 \cdot 10^{-6}$	1.2822
			$B^+ \to f_1'^0 \ell^+ \nu$	$41 \cdot 10^{-6}$	1.4268
			$B^+ \to f_2^0 \ell^+ \nu$	$4 \cdot 10^{-6}$	1.275
			$B^+ \to f_2'^0 \ell^+ \nu$	$4 \cdot 10^{-6}$	1.525
			$B^+ \to h_1^0 \ell^+ \nu$	$24 \cdot 10^{-6}$	1.17
			$B^+ \to h_1'^0 \ell^+ \nu$	$24 \cdot 10^{-6}$	1.40
Exclusive	$735 \cdot 10^{-6}$		Exclusive	$730 \cdot 10^{-6}$	
Inclusive	$616 \cdot 10^{-6}$		Inclusive	$616 \cdot 10^{-6}$	
Total	$1351 \cdot 10^{-6}$		**Total**	$1346 \cdot 10^{-6}$	

In the non-resonant model the final-state hadron is produced with a continuous invariant mass spectrum. This generator has the advantage that it allows studies of the change in the fraction of events below the hadronic mass cut as input parameters are varied. The generator simulates

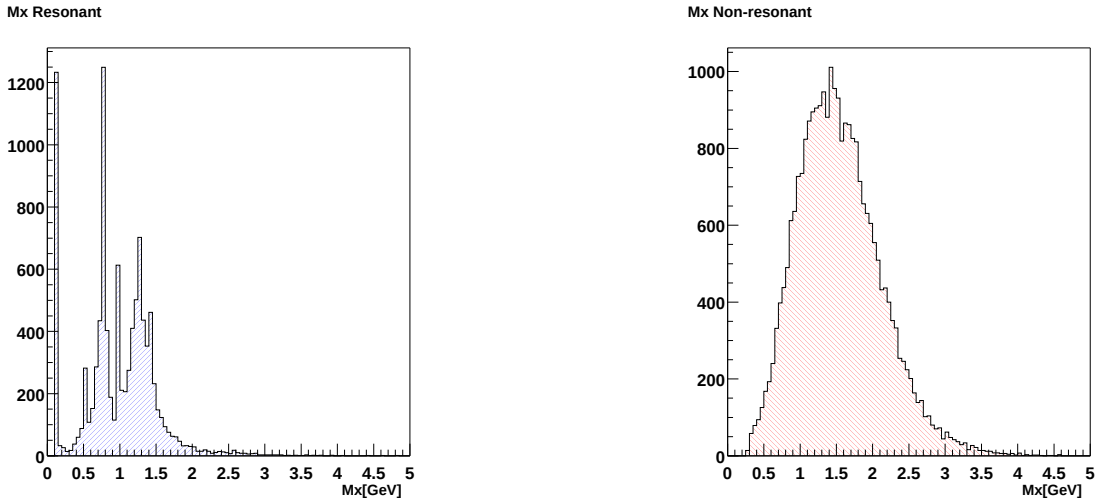

Figure 6.2: m_X distributions at generator level for pure resonant (left) and pure non-resonant $b \to u\ell\bar{\nu}$ MC simulation (right).

$B \to X_u \ell\nu$ decays and is based on the triple differential decay width as computed by Neubert and de Fazio [67] with hadronization performed with `Jetset 7.4` [68]. The three variables in the triple differential distribution are defined at the parton level as:

$$x = \frac{2E_\ell}{m_b}, \quad z = \frac{2(E_h - \overline{\Lambda})}{m_b}, \quad p^2 = \frac{m_h^2 - 2E_h\overline{\Lambda} - \overline{\Lambda}^2}{m_b^2}, \tag{6.1}$$

where E_ℓ is the energy of the charged lepton, E_h and m_h are the energy and mass of the hadronic X_u state and the parameter $\overline{\Lambda} = m_{\rm B} - m_b$. The decay width is calculated up to $\mathcal{O}(\alpha_{\rm s})$ corrections.

The parton-level generator does not include corrections for the motion of the b quark inside the B meson which is known as Fermi motion. Figure 6.3 compares the generated parton-level distributions without Fermi motion to analytical functions for various single differential decay distributions with and without QCD corrections. It is worth noting that the singularities in the analytical functions at $z = 1$ and $s_h = \overline{\Lambda}/m_b(1 + \overline{\Lambda}/m_b)$ are not present in the generator. The singularities reflect the unphysical nature of the parton-level distributions. The differences vanish once the Fermi motion is implemented and the parton-level variables are replaced with observable quantities.

The Fermi motion of the b quark inside the B meson can be incorporated in this formalism by replacing the parton-level b quark mass with $m_B - q_+$, where $q_+ = \overline{\Lambda} - k_+$ is a function of the momentum (k_+) of the b quark inside the B meson and $\overline{\Lambda}$. The functional form of the distribution of k_+ is constrained by the first three moments, which satisfy: $A_0 = 1$, $A_1 = 0$ and $A_2 = -\lambda_1/3$. The parameter $-\lambda_1$ is the average momentum squared of the b quark in the B meson. The form of

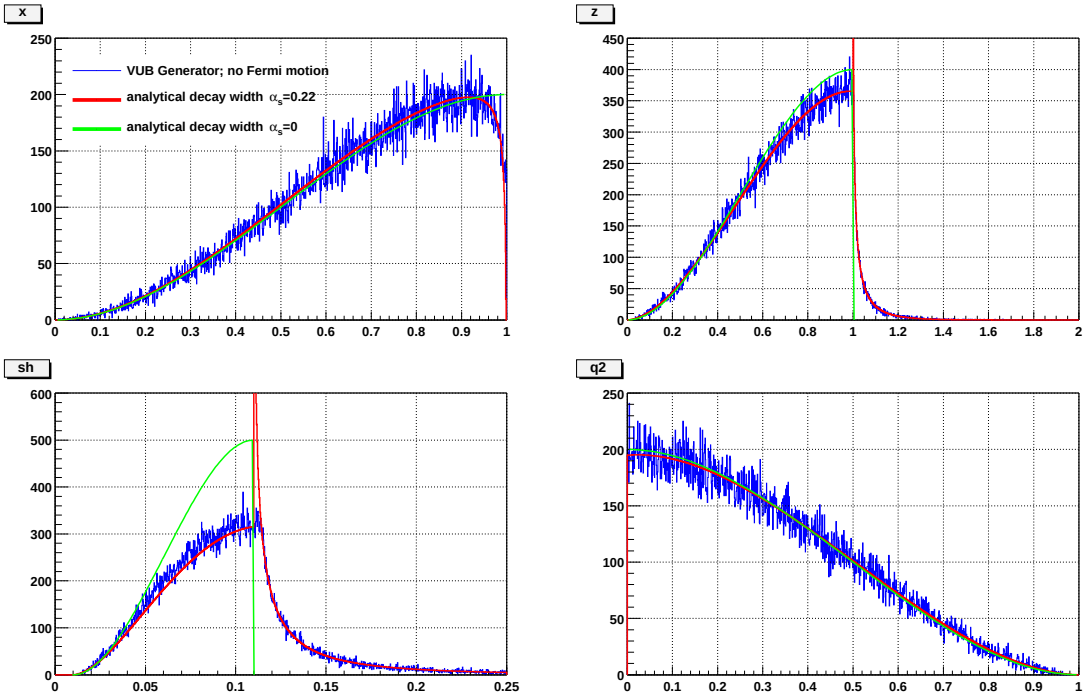

Figure 6.3: Parton-level distributions for the generator without Fermi motion. The upper left plot shows the scaled lepton energy $x = 2E_\ell/m_b$, the upper right plot the scaled hadron energy $z = 2(E_h - \overline{\Lambda})/m_b$, the lower left plot shows the scaled hadron mass squared $s_h = m_h^2/m_b^2$ and the lower right plot shows the scaled virtual W mass squared $Q^2 = q^2/m_b^2$. The red lines denote analytical single differential functions with the same input quantities and the green lines show the tree results without α_s corrections.

the Fermi motion used in the generator is

$$F(k_+) = N(1-x)^a e^{(1+a)x}; \quad x = \frac{k_+}{\overline{\Lambda}} \leq 1 \quad and \quad a = f(\overline{\Lambda}, \lambda_1), \tag{6.2}$$

which gives $A_1 = 0$ by construction. The normalization is fixed by N and the parameter a can be related to the second moment, yielding $A_2 = -\lambda_1/3 = \overline{\Lambda}^2/(1+a)$. Therefore m_b and a can be chosen as the two parameters of the function.

In practice, a reweighting of the Fermi motion parameter k_+ was used to allow variations in the choices of $\overline{\Lambda}$ and λ_1. The two parameters m_b and a of the Fermi motion are varied to estimate the uncertainty due to the Fermi motion. Figure 6.2 (right) shows the non-resonant m_X distribution after the Fermi motion is incorporated into the signal model. The values of the parameters are taken to be $m_b = 4.79\,\mathrm{GeV}/c^2$ and $a = 1.96$ [69].

The non-resonant generator cannot produce hadronic final states with masses below $2m_\pi$ and it does not produce any resonant structure in the hadronic mass distribution (e.g. from ρ, etc.). These limitations are addressed with a hybrid generator that uses the set of branching ratios to specific final-state hadrons for low-mass final states listed in Table 6.3 and supplements these decays with the non-resonant production for final states X_u with $m_X > 1.4\,\mathrm{GeV}/c^2$. The resonant and non-resonant Monte Carlo are mixed in such a way that the fraction of events below a given threshold in m_X is similar to the non-resonant case (except local discontinuity due to the resonant structure). A comparison between hybrid and non-resonant model is shown in Fig. 6.4. The total branching fractions, including the non-resonant contribution, are $\mathcal{B}(B^0 \to X_u \ell\nu) = 0.2673\%$ and $\mathcal{B}(B^+ \to X_u \ell\nu) = 0.2887\%$, as listed in Table 6.3.

Table 6.3: Branching fractions used in the $\overline{B} \to X_u \ell\bar{\nu}$ hybrid signal MC after the reweighting.

B^0 mode	$\mathcal{B} \times 10^{-4}\,(\%)$	B^+ mode	$\mathcal{B} \times 10^{-4}\,(\%)$
$B^0 \to \pi^- \ell^+ \nu$	133 ± 22	$B^+ \to \pi^0 \ell^+ \nu$	72 ± 12
		$B^+ \to \eta \ell^+ \nu$	84 ± 36
$B^0 \to \rho^- \ell^+ \nu$	$269\,^{+74}_{-77}$	$B^+ \to \rho^0 \ell^+ \nu$	$145\,^{+40}_{-41}$
		$B^+ \to \omega \ell^+ \nu$	145 ± 145
		$B^+ \to \eta' \ell^+ \nu$	84 ± 84
other resonant	0	other resonant	0
resonant	402	resonant	530
non-resonant	2271	non-resonant	2357
total	2673	total	2887

The generated exclusive branching ratios do not agree with current measurements. Thus, the exclusive modes are reweighted in the hybrid MC to agree with current measurements and obey isospin conservation. The resonant MC is also reweighted in the hybrid MC sample to have agreement between our signal MC and the measured fraction of resonant and non-resonant events. The weights for the non-resonant MC are determined as follows:

- B^0 and B^+ decays are weighted separately
- Phase space is split into eight bins for each of the variables m_X, q^2, and E_l
- In each bin, the hybrid model H can be expressed as a linear combination of resonant R and non-resonant I contributions: $H_i = R_i + w_i I_i$ where w_i is the weight applied to the non-resonant MC.

- The weights, w_i are determined by requiring that the fraction of hybrid events in each bin be equal to the fraction of non-resonant events in each bin. If w_i is found to be negative, it is reset to 0.

- Because of the possibility of negative weights being reset to 0, all of the weights w_i are globally renormalized to preserve the overall normalization.

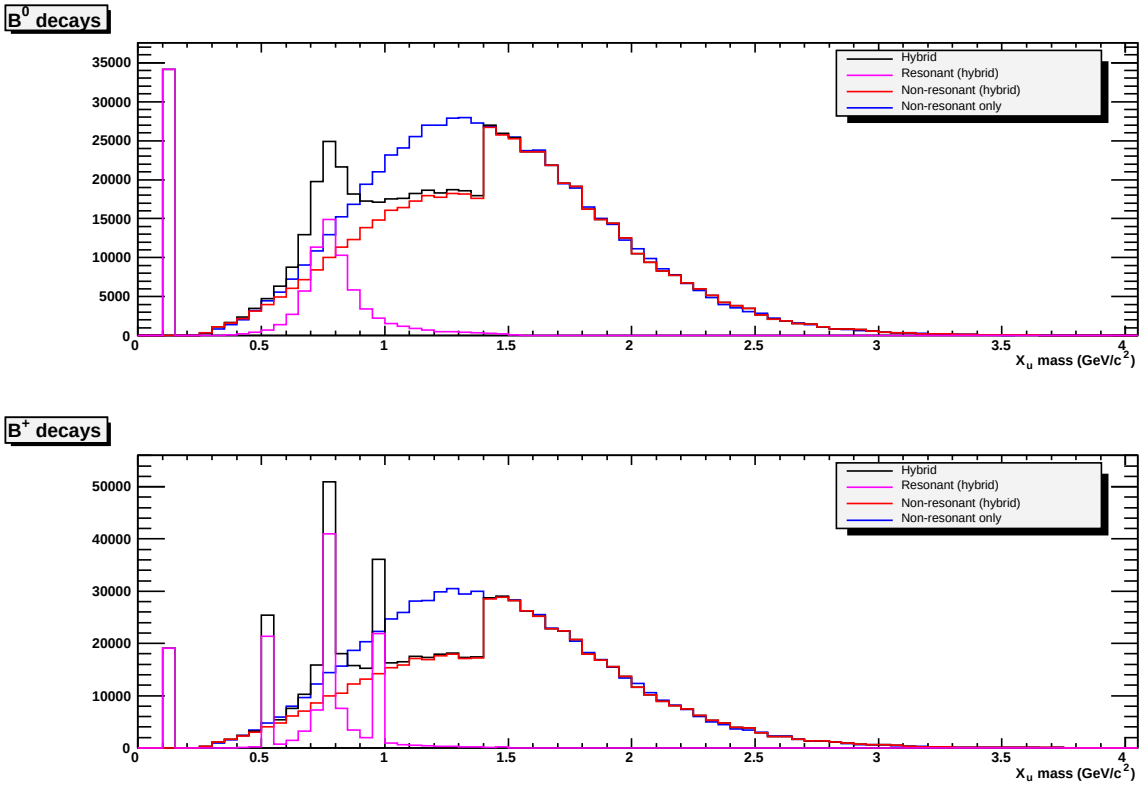

Figure 6.4: m_X distribution at the generator-level for the hybrid signal Monte Carlo for $b \to u\ell\bar{\nu}$ events. The resonant and non-resonant contributions to the hybrid are shown in magenta and red respectively along with the purely non-resonant distribution in blue.

Background $B\overline{B}$ Events

Semileptonic B decays in the generic Monte Carlo simulation have been modeled with specific decay models for the charm meson. A parameterization of HQET form factors, defined in Ref. [70], is used for $B \to D^*\ell\nu$, the model of Goity and Roberts [71] is used for the non-resonant decays $B \to D^{(*)}\pi\ell\nu$, whereas the ISGW2 model [66] is used for all other semileptonic decays. The total generated Cabibbo-favored semileptonic branching fraction is $\mathcal{B}(b \to c\ell\nu) = 10.4\%$, somewhat

lower than the recent measurement by *BABAR* [32]. These events are thus reweighted to correspond to $\mathcal{B}^0(b \to c\ell\nu) = 10.21\%$ and $\mathcal{B}^+(b \to c\ell\nu) = 11.04\%$. Also, the background $B \to D^* l\nu$ events are reweighted to use the *BABAR* measurement of the form factors [72].

Non $b\overline{b}$ Events

The non $b\overline{b}$ Monte Carlo consists of $c\overline{c}$ and $u\overline{u}$, $d\overline{d}$, $s\overline{s}$ events. These samples have been used, similar to the off-peak data, to check the $m_{\rm ES}$ shape (see 4.6.2).

6.2.3 Summary of Samples

The $m_{\rm ES}$ shapes and yields for data, Cocktail MC, generic MC, and hybrid $b \to u\ell\bar{\nu}$ MC are illustrated in Fig. 6.5 for two conditions: (1) without any event cuts and (2) after the requirement of at least one lepton with center of mass momentum greater than $1\,{\rm GeV}/c$. These plots are merely an illustration of the yields from the data and MC samples used in this analysis.

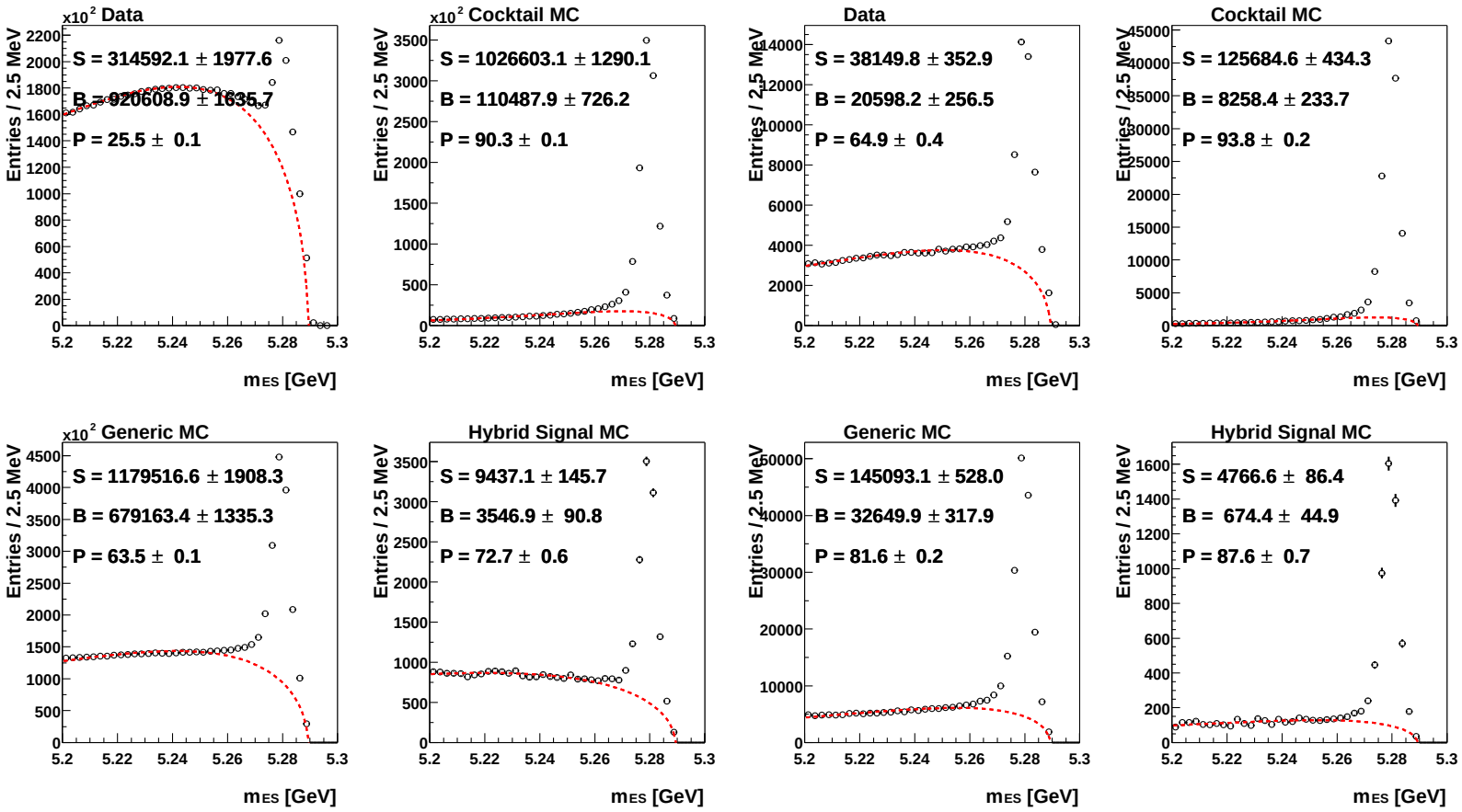

Figure 6.5: Event yields for all seeds combined without additional requirement on the recoil system (left) and after requiring a lepton with $p_{cms} > 1\,\mathrm{GeV}/c$ (right). The numbers printed on each plot indicate signal yield (S), background yield (B), and purity (P) all in the signal region defined by $m_{\mathrm{ES}} > 5.27\,\mathrm{GeV}/c^2$. Only the Argus background is fitted in these plots, with the signal yield taken as the difference between the histogram and the fitted Argus background. These plots serve as an illustration of the event yields and are not used in the analysis.

6.3 Recoil Reconstruction

To study semileptonic B decays, $B \to X\ell\nu$, the following particle selection and reconstruction techniques are employed:

- Events with a fully reconstructed B are selected by the semi-exclusive reconstruction described in chapter 5.
- Charged particles and neutral clusters in the EMC are defined to assure well known efficiencies and minimal backgrounds (see sections 4.1 and 4.3).
- Leptons (ℓ) are identified using standard *BABAR* algorithms for electrons and muons, described in sections 4.2.1 and 4.2.2. Bremsstrahlung photons are recovered before the leptons are used in the recoil as described in section 6.3.1.
- Charged and neutral kaons are used to separate $B \to X_u\ell\nu$ from the dominant $B \to X_c\ell\nu$ decays, see sections 4.2.3 and 4.4.2.
- The hadron system, X, and the undetected neutrino, ν, make up the remaining event recoiling against the B_{reco}. Their kinematic reconstruction is described in section 6.3.2.

6.3.1 Recovery of Bremsstrahlung Photons

The dominant source of energy loss in high energy electrons in the *BABAR* detector is the radiation of Bremsstrahlung photons. If a leading electron should lose energy in the form of Bremsstrahlung photons, the lepton energy will be underestimated and the emitted Bremsstrahlung photons will mistakenly enter the recoil calculation, introducing a bias in the reconstruction of the hadronic system. To recover the Bremsstrahlung photons, we select photons that are emitted within a narrow opening angle with respect to the electron. The constraint on the opening angle α_{brem} is determined from a sample of signal MC to be

$$\alpha_{\text{brem}} < 80\,\text{mrad} \tag{6.3}$$

Applying this recovery procedure results in a noticeable improvement in the p^* resolution as seen in Fig. 6.6(a). Figure 6.6(b) illustrates the improvement in the p^* resolution for electrons that are truth-matched MC events to ensure at least one Bremsstrahlung photon. Figure 6.6(c) demonstrates the effect Bremsstrahlung recovery has on the reconstruction of the hadronic system.

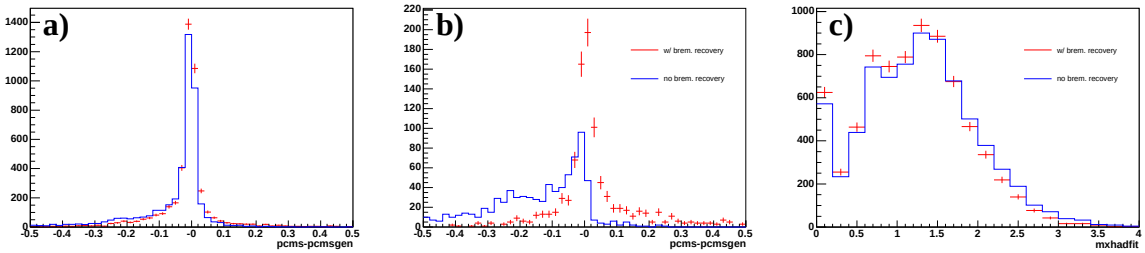

Figure 6.6: Signal MC: a) p^* resolution for all electrons, b) p^* resolution for electrons that are known through generator truth-matching to contain at least one Bremsstrahlung photon, c) m_X distribution. The blue line corresponds to no recovery and the red points correspond to recovery of photons within $\alpha_{brem} < 0.08$

The Bremsstrahlung photon recovery procedure is performed before the leading lepton is identified since the choice of the leading lepton can be affected by this process. Also, when Bremsstrahlung photons are identified and added to the corresponding electron, the photons are removed from the list of neutral particles so they won't be mistakenly included in the recoil calculation.

6.3.2 Reconstruction of the Hadronic System

The hadronic X system is comprised of charged tracks and neutrals that are not associated with the B_{reco} candidate and that are not identified as leptons. The measured four-momentum p_X^m of the X system can be written as

$$p_X^m = \sum_{i=1}^{N_{ch}} p_i^{ch} + \sum_{j=1}^{N_\gamma} p_j^\gamma \tag{6.4}$$

where p are four-momenta and the indices ch and γ refer to the the selected number of charged tracks and neutrals. K_S^0 reconstruction is only used for the kaon veto, so no mass constraint is applied.

The four-momentum of the missing particle (neutrino) is reconstructed by relating the four-momentum of the colliding beams Q_{CM} to the measured B_{reco} four-momentum p_{reco}^m, the X hadrons four-momentum p_X^m, and the lepton four-momentum p_ℓ^m,

$$p_{miss} = Q_{CM} - p_{reco}^m - p_X^m - p_\ell^m. \tag{6.5}$$

The measured invariant mass squared of the missing particle, $m_{miss}^2 = |p_{miss}|^2$, is an important

estimator of the quality of the reconstruction of the total recoil system. Any secondary particles from the decay of the hadronic X system that are undetected or poorly measured will impact the measurement of both m_X and m^2_{miss}. Likewise any sizable energy loss of the leptons via Bremsstrahlung or internal radiation will impact the measurement of these two quantities. The effect of initial-state radiation is rather small, due to the fact that the width of the $\Upsilon(4S)$ resonance is rather small.

Kinematic Fit on the Recoil

The available kinematic information for the full event is exploited by performing a 2-C kinematic fit that imposes four-momentum conservation, the equality of the masses of the two B mesons, $m(B_{recoil}) = m(B_{reco})$, and forces $m^2_{miss} = p^2_\nu = 0$. The fit is an iterative χ^2 minimization that takes into account event-by-event the measurement errors of all individual particles and the measured missing-mass squared.

The B_{reco} candidate enters with four parameters into the kinematic fit whereas the other candidates are described with only three fit parameters. The neutrino is assumed to be massless and unmeasured in the kinematic reconstruction.

The distribution of the missing-mass of the event, m^2_{miss}, before and after the kinematic fit is shown in Fig. 6.7. Due to the zero-mass hypothesis for the neutrino, the missing-mass of the event is - per definition - zero after the fit. Figure 6.7 shows also the mass resolution of the B_{reco} and the B_{recoil} candidate before and after the kinematic fit. Due to the imposed equal-mass constraint, the masses of the two B mesons are, within precision, identical after the fit.

Figure 6.8 displays the resolution for the kinematically fitted hadronic mass for signal and background events. Figure 6.9 shows the kinematically fitted mass m_X as a function of the true m_X and the measured m^2_{miss}, in terms of both the mean and the RMS width of the distributions $m_X(fit) - m_X(true)$. Forcing the semileptonic B events to fulfill the constraints of energy and momentum conservation and the equal-mass hypothesis leads not only to an improvement of the RMS width of the mass resolution for the X system but also the bias is reduced. This stability together with the overall improvements in resolution and mass bias clearly favors the fitted kinematic quantities over the reconstructed ones.

6.3.3 Event Based Selection

The event selection criteria for the analysis were determined on the basis of data/MC agreement and the optimization of the statistical uncertainty on the extraction of the number of $b \to u\ell\bar{\nu}$ signal

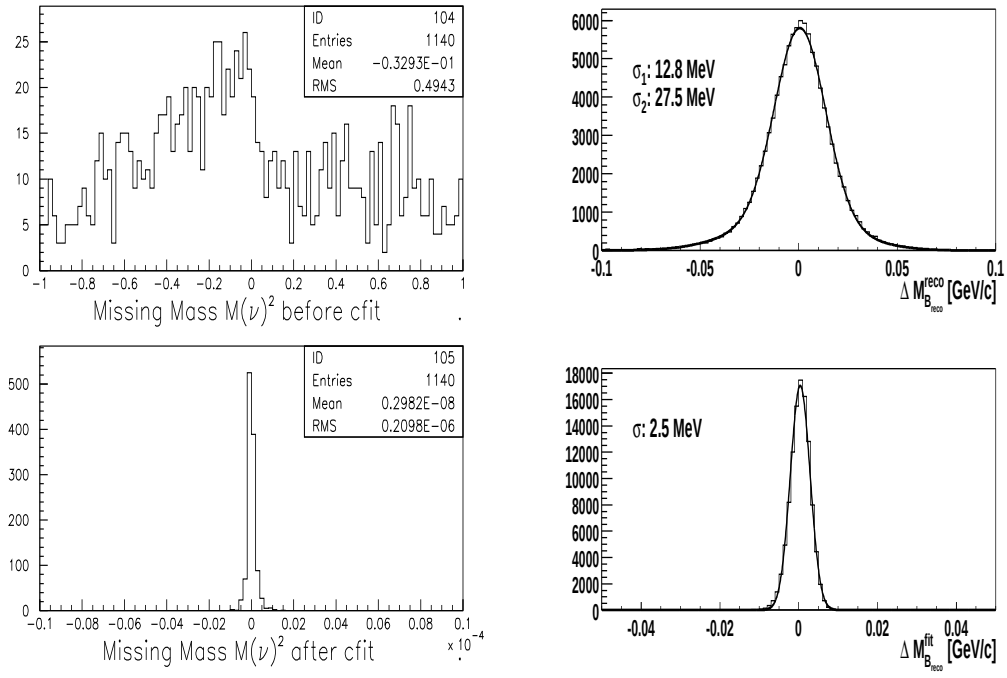

Figure 6.7: Left: Missing-mass squared of the event before (upper plot) and after (lower plot) the kinematic fit. Due to the zero-mass hypothesis for the neutrino, the missing-mass of the event after the fit is within the precision compatible with zero. Right: Mass resolution of the B_{reco} (left side) before (upper plots) and after (lower plots) the kinematic fit. Due to the imposed equal-mass constraint, the masses of the two B mesons are, within procession, identical after the fit.

events. A full data/MC comparison study was conducted for different values of each given event cut, along with a scan of the results of the signal extraction fit for different values of cut. These data/MC studies and fit scans are based on the generic MC because it is used to model the background in the fit to extract the signal yield. Due to the correlations between different event variables, the procedure was done iteratively, allowing many different combinations of event variable cuts to be observed. The event selection criteria can be loosely divided into three categories according to their purpose in this analysis. These categories are:

1. Select semileptonic decays $B_{recoil} \rightarrow X\ell\bar{\nu}$ (i.e. identification of high momentum lepton, correlated lepton charge and B flavor)

2. Select signal events $B_{recoil} \rightarrow X_u\ell\bar{\nu}$ (i.e. total charge conservation, missing system consistent with neutrino hypothesis, number of leptons)

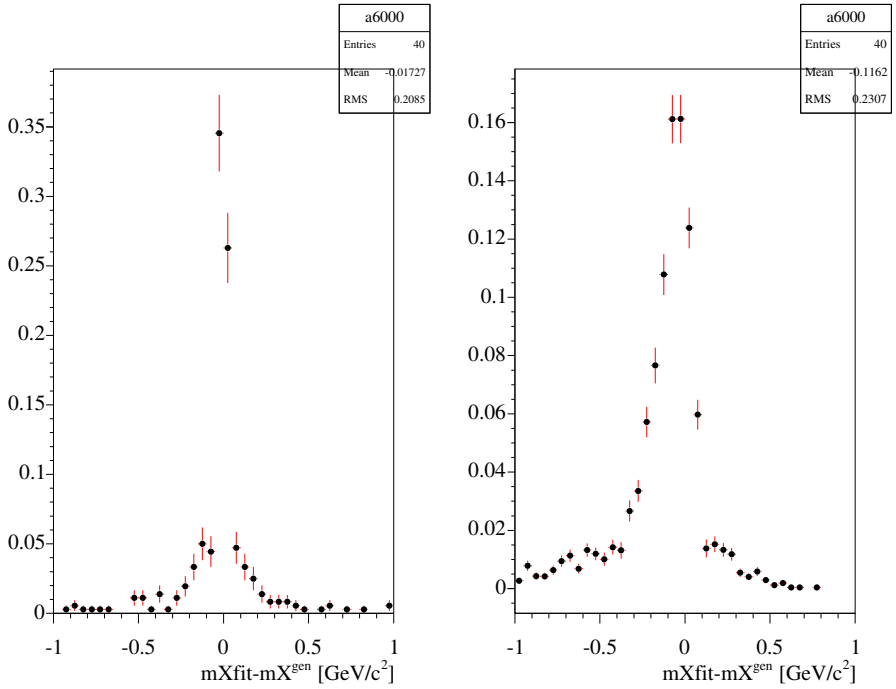

Figure 6.8: Cocktail MC: The resolution on the kinematically fitted hadronic mass with all analysis cuts applied for $b \to u\ell\bar{\nu}$ events (left) and $b \to c\ell\bar{\nu}$ events (right).

3. Reduce the amount of background events $B_{recoil} \to X_c\ell\bar{\nu}$ (kaon veto, vetoes on various partial reconstructions of $B \to D^*\ell\nu$.)

The following discussion provides a detailed discussion of the event selection criteria used in the extraction of $\delta\Gamma(c)$. The plots shown (Figs. 6.11 -6.19) are from cocktail MC (except for the purity scan) with no extra normalization and serve merely as an illustration of the shape of the event variable distribution. Plots of the background subtracted distributions of the recoil event variables for data and generic MC for the event selection can be found in section 6.3.4.

- Purity cut per seed for reconstructed B modes

  The semi-exclusive reconstruction allows for a selection of the purity of the sample. For higher purity, the total sample is smaller, while the fits to $m_{\rm ES}$ are cleaner. With a lower purity, the total sample is larger and the fits to $m_{\rm ES}$ have more combinatoric background. The impact of the purity selection on the statistical error was studied on the basis of data. In Fig. 6.10 the ratio $S/\sqrt{S+B}$ is shown for events passing all selection criteria as a function of the purity for the four charm $seeds$. Discontinuities shown by the plots are due to the addition of a single mode with quite large statistics. In Table 6.4 the optimal cuts are summarized.

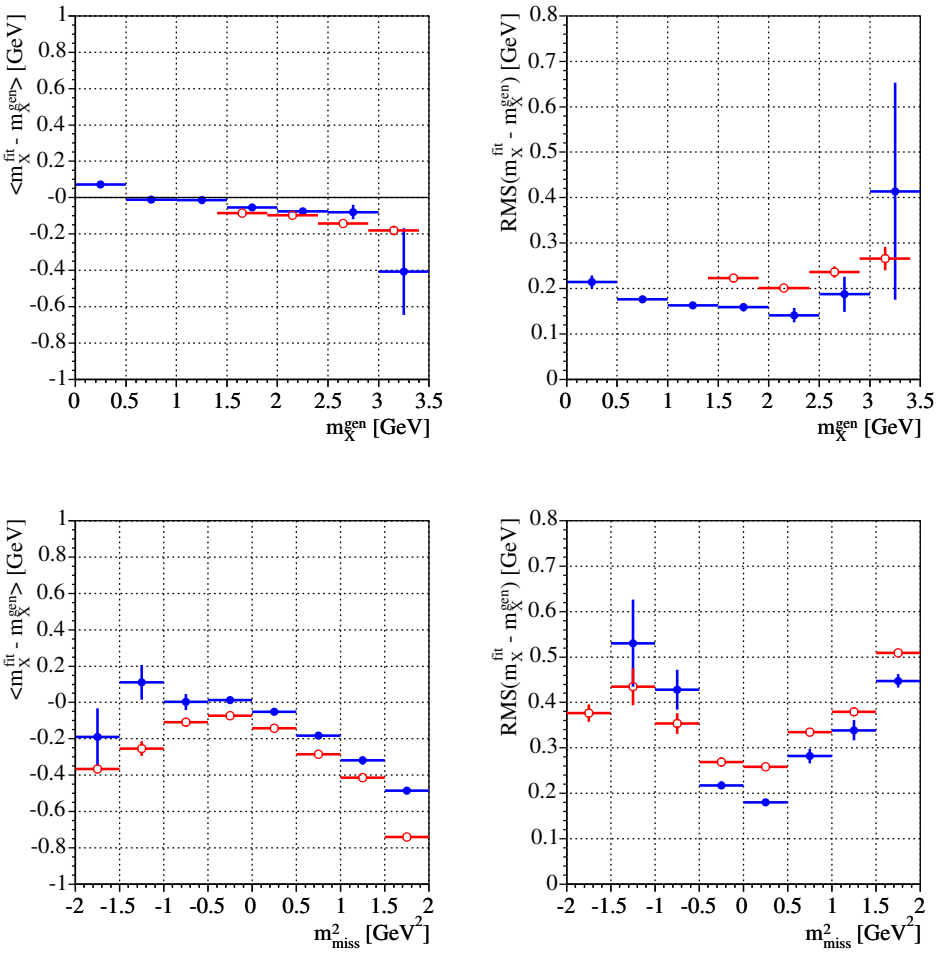

Figure 6.9: Cocktail MC: The mean (left) and RMS (right) of the resolution on the kinematically fitted hadronic mass with all analysis cuts applied in bins of true m_X (upper) and m^2_{miss} (lower). The blue points are $b \to u\ell\bar{\nu}$ events and the red points are $b \to c\ell\bar{\nu}$ events.

- Presence of a high momentum lepton, $p^*_l > 1\,\mathrm{GeV}/c$

  Semileptonic B decays are identified by the presence of a high momentum electron or muon. A requirement that $p^*_l > 1\,\mathrm{GeV}/c$ in the B rest frame is imposed to reduce backgrounds from fake leptons, secondary charm, and $\tau^\pm$ decays. Figure 6.11 shows the lepton momentum spectrum in the B rest frame separately for $b \to u\ell\bar{\nu}$ decays and $b \to c\ell\bar{\nu}$ decays.

- Number of leptons, $N_l = 1$

  The presence of a second lepton is rare in $b \to u\ell\bar{\nu}$ decays, whereas they appear more fre-

Table 6.4: Signal yield, S, and background, B, per charm seed mode of the B_{reco} candidate. The numbers are obtained from fits to the m_{ES} distributions.

Seed Mode	Purity Cut	S	B
$B \to D^* X$	24%	228 ± 18	51 ± 12
$B \to D^+ X$	9%	510 ± 31	357 ± 26
$B \to D^{*0} X$	8%	307 ± 23	172 ± 19
$B \to D^0 X$	9%	615 ± 33	470 ± 27

quently in $b \to c\ell\bar{\nu}$ decays due to the cascade decays of the charm particles. Thus, the number of leptons in the event is required to be exactly one. Of course, for the determination of the number of semileptonic decays, N_{sl}, with $p_l^* > 1\,\mathrm{GeV}/c$ the requirement is not imposed. Figure 6.12 shows the number of detected leptons per event separately for $b \to u\ell\bar{\nu}$ decays and $b \to c\ell\bar{\nu}$ decays.

- Lepton charge and B flavor correlation

  In semileptonic decays, the flavor of the decaying B meson is correlated to the charge of the primary lepton. This correlation can be written as $Q_{b(recoil)}Q_l > 0$, where $Q_{b(recoil)}$ refers to the charge of the b quark in the semileptonically decaying B_{recoil} and Q_l refers to the charge of the primary lepton. Secondary leptons from cascade D decays will have $Q_{b(recoil)}Q_l < 0$. For charged B mesons, this condition is imposed, for neutral B both combinations are retained, since in mixed events the B flavor is changed.

- Total event charge, $Q_{tot} = 0$

  Total event charge conservation, $Q_{tot} = Q_{B_{reco}} + Q_{B_{recoil}}$, is imposed to ensure proper reconstruction of the hadronic recoil system. Improper hadronic recoil reconstruction through the loss or gain of charged tracks results in an incorrect value for the hadronic mass, m_X. If an event fails the charge conservation requirement, it helps to reject these events with lost or gained tracks. Lost tracks come simply from missing particles, gained tracks come from $\gamma \to e^+e^-$ conversions, δ-rays, or tracking errors. This selection criterion rejects background because $b \to c\ell\bar{\nu}$ decays have higher charged track multiplicities. Figure 6.13 shows the total event charge separately for $b \to u\ell\bar{\nu}$ decays and $b \to c\ell\bar{\nu}$ decays.

- Missing-mass squared, $-1.0 < m^2_{miss} < 0.5\,\mathrm{GeV}^2/c^4$

  In this analysis, the only undetected particle should be a neutrino. In this hypothesis, the mass

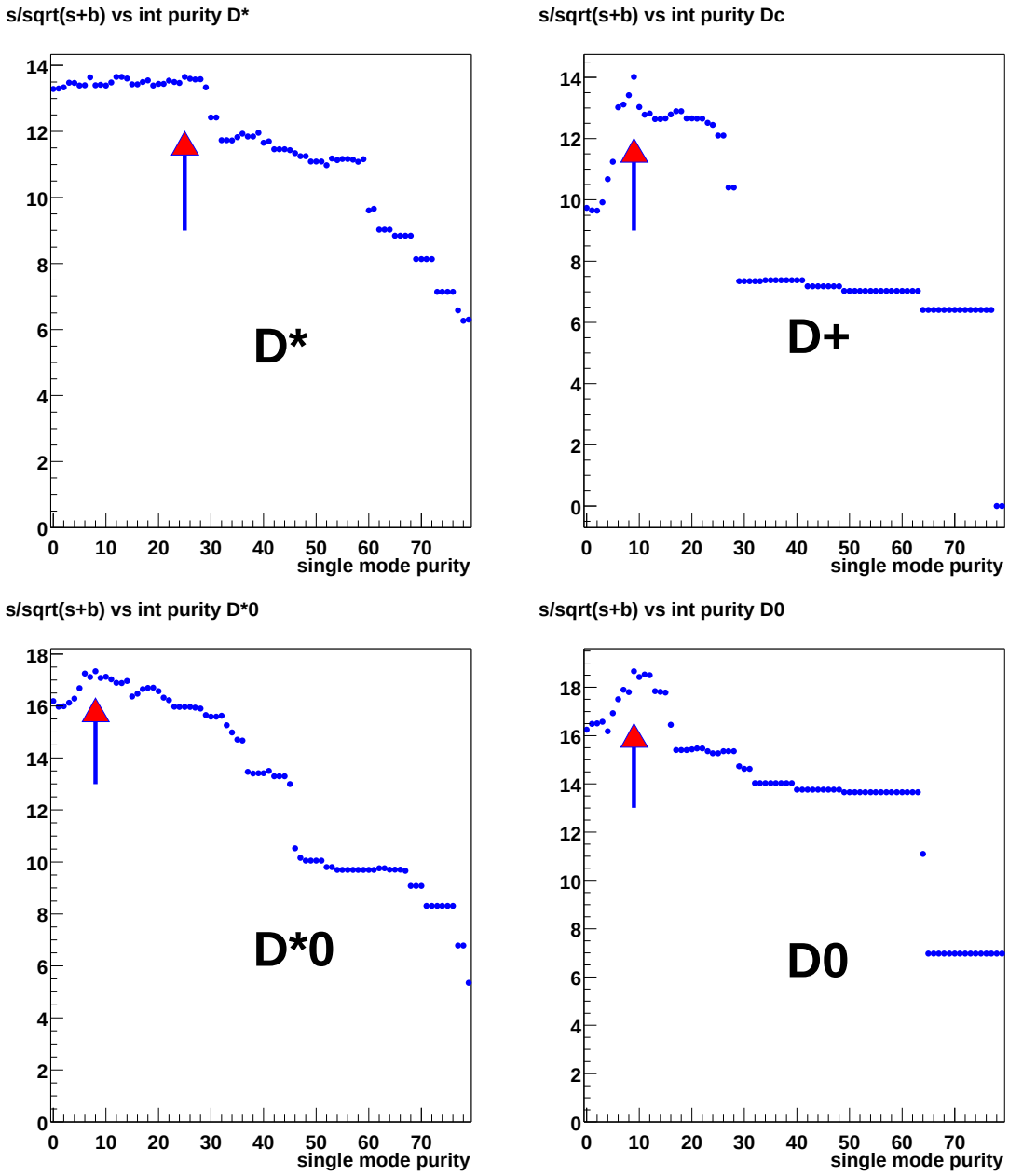

Figure 6.10: Generic MC:Statistical significance ($S/\sqrt{S+B}$) as a function of the purity of the mode of the reconstructed B sample for the four charm seeds after all cuts: clockwise (starting from the upper left plot) the seeds are $B^0 \to D^{+*}X$, $B^0 \to D^{+}X$, $B^+ \to D^{0}X$, $B^+ \to D^{*0}X$.

of the missing system should be consistent with zero. Making an event selection based on this variable makes it possible to reject events in which the recoil reconstruction is poor. This can happen if particles are poorly measured or if the recoil reconstruction falsely gains or loses

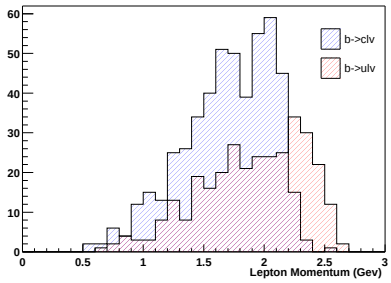

Figure 6.11: Cocktail MC: The lepton momentum spectrum with all analysis cuts applied

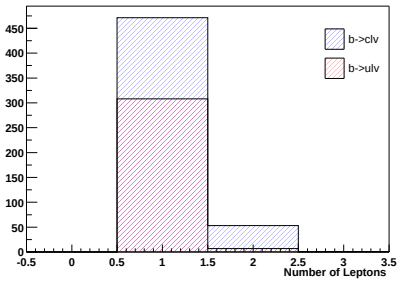

Figure 6.12: Cocktail MC: The number of leptons observed with all analysis cuts applied

particles. Background $b \to c\ell\bar{\nu}$ events are expected to have a broader m^2_{miss} distribution because they have higher particle multiplicities and possibly can contain additional neutrinos or K_L which will not be added into the recoil calculation by construction. Figure 6.14 shows the missing-mass squared separately for $b \to u\ell\bar{\nu}$ decays and $b \to c\ell\bar{\nu}$ decays.

- Number of kaons, $N_{K_\pm} = N_{K_S} = 0$

  In semileptonic B decays, a powerful way to discriminate background from signal is through the detection of kaons in the recoil system. $b \to u\ell\bar{\nu}$ decays rarely include kaons whereas $b \to c\ell\bar{\nu}$ decays most often do. Figure 6.15 demonstrates the kaon multiplicities separately for $b \to u\ell\bar{\nu}$ decays and $b \to c\ell\bar{\nu}$ decays.

- Missing momentum, $p_{miss} > 0.3\,\mathrm{GeV}/c$

  To be consistent with the hypothesis that the only undetected particle in a semileptonic B decay be a neutrino, the magnitude of the missing particle's momentum is required to have

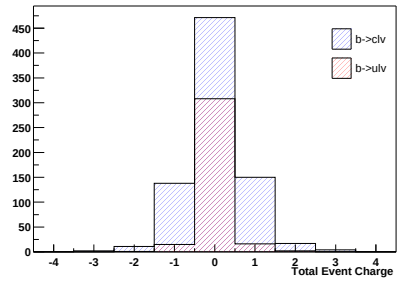

Figure 6.13: Cocktail MC: The total event charge with all analysis cuts applied

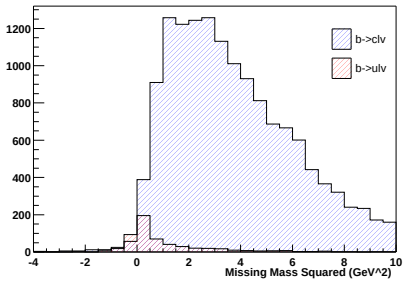

Figure 6.14: Cocktail MC: The missing-mass squared with all analysis cuts applied

a non-zero value. Figure 6.16 shows the missing momentum separately for $b \to u\ell\bar{\nu}$ decays and $b \to c\ell\bar{\nu}$ decays. It is clear that such a cut does not make an important distinction between signal and background, however it is found to contribute toward better agreement between data and MC.

- Angle of missing system, -0.95 $< \cos\theta_{miss} <$ 0.95

  Neutrinos and otherwise detectable particles that lie outside of the geometric region of acceptance in the detector are indistinguishable. Thus, we make the requirement that the cosine of the angle of the missing system be consistent with a particle not projected along the beam axis. Figure 6.17 shows the $cos\theta_{miss}$ distributions separately for $b \to u\ell\bar{\nu}$ decays and $b \to c\ell\bar{\nu}$ decays.

- Slow track killing, $p^*_{trk,low} > 0.12\,\mathrm{GeV}/c$

  Due to the relatively high particle multiplicity in D decays, the charged hadron track mo-

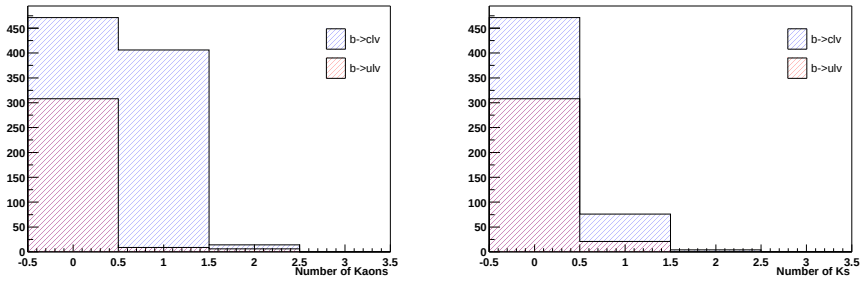

Figure 6.15: Cocktail MC: Left: the number of charged kaons with all analysis cuts applied Right: the number of K_S with all analysis cuts applied

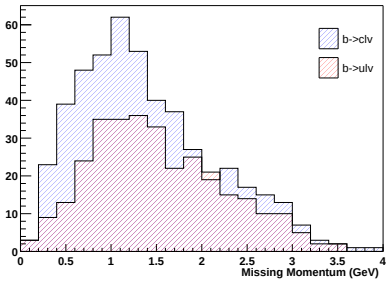

Figure 6.16: Cocktail MC: The missing momentum with all analysis cuts applied

menta will be lower for $b \to c\ell\bar{\nu}$ decays compared to $b \to u\ell\bar{\nu}$ decays. Events with $b \to u\ell\bar{\nu}$ decays have very small abundance of slow tracks (with momenta of order $p_\perp < 0.2\,\mathrm{GeV}$). Figure 6.18 shows the $p^*_{trk,low}$ distributions separately for $b \to u\ell\bar{\nu}$ decays and $b \to c\ell\bar{\nu}$ decays.

- Rejection of $B \to D^*\ell\nu$

  The decays of $B \to D^*\ell\nu$ with $D^* \to D\pi$ are a dominant source of background. These decays can be identified by exploiting the fact that the mass difference between the D^* and the D is close to the pion mass and therefore a pion produced in the D^* decay is soft and essentially collinear with the D^*. A discriminating variable that exploits these conditions can be adapted from the partial reconstruction analyses [73]: using the approximation that the direction of flight of the pion is the same as that of the D^* and taking into account that the soft pion energy in the rest frame of the D^*, E^*_π is fixed, the pion energy in the lab frame is

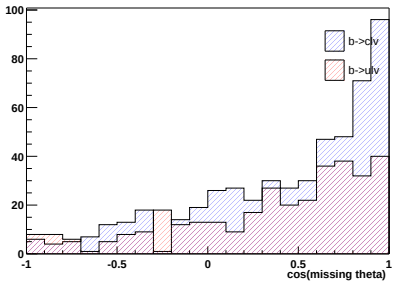

Figure 6.17: Cocktail MC: The cosine of the angle of the missing system with all analysis cuts applied

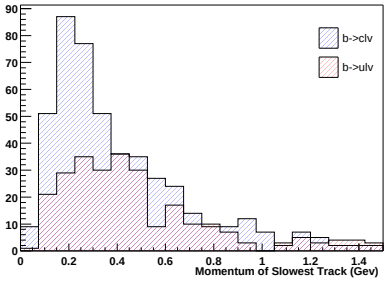

Figure 6.18: Cocktail MC: The momentum of the slowest track with all analysis cuts applied

$$E_\pi = \gamma(E^*_\pi - \beta P^*_\pi) \tag{6.6}$$

where β and γ refer to the D^* boost and P^*_π is the soft pion momentum in the D^* frame. Neglecting the second term in Eq. 6.6, the D^* energy in the LAB frame can be computed as

$$E^*_{D^*} = \gamma M_{D^*} = E_\pi \frac{M_{D^*}}{E^*_\pi} \tag{6.7}$$

Given that the 4-momentum p_{D^*} of the D^* is now known, the missing invariant mass can be computed as

$$m^2_{miss,PR} = |p_{recoil} - p_{D^*} - p_{lepton}|^2 \tag{6.8}$$

This variable peaks at zero for background and is flat for signal, and is thus used to reject background. Three decay modes are partially reconstructed:

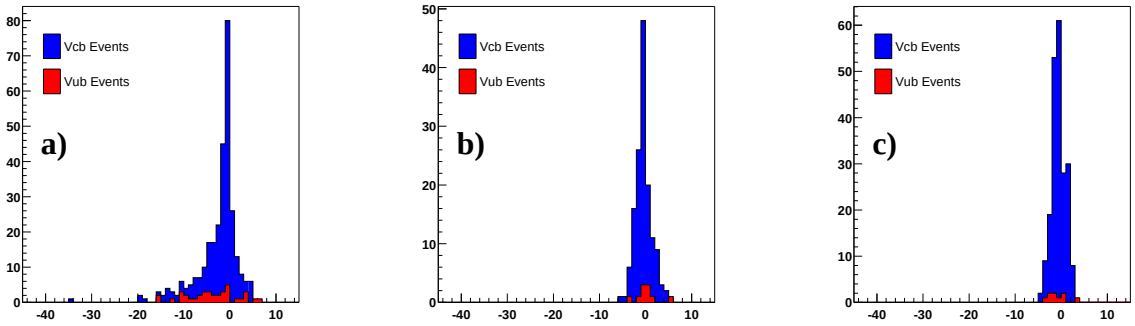

Figure 6.19: Cocktail MC: Missing-mass distribution $m^2_{miss,PR}$ for a) $D^* \to D^0\pi$, b) $D^* \to D\pi^0$, c) $D^{*0} \to D^0\pi^0$

- $D^* \to D^0\pi$: $E^*_\pi = 145\,\mathrm{MeV}$. Pions must be properly charge correlated with the leading lepton and have a momentum in the CMS frame less than $200\,\mathrm{MeV}/c$. The lowest momentum pion is selected. To optimize the signal-to-background ratio, events with $m^2_{miss,PR} > -3\,\mathrm{GeV}^2$ are rejected.
- $D^* \to D\pi^0$: $E^*_{\pi^0} = 140\,\mathrm{MeV}$. Pions must have a momentum less than $200\,\mathrm{MeV}/c$ in the CMS frame, an opening angle larger than $2.2rad$ with the leading lepton, and the event must have a neutral multiplicity greater than 4. The lowest momentum pion is selected. To optimize the signal-to-background ratio, all events which pass these criteria are rejected.
- $D^{*0} \to D^0\pi^0$: Same as above except $E^*_{\pi^0} = 142\,\mathrm{MeV}$.

As an additional check, the efficiency of the optimized cuts is calculated from the signal MC and found to reject very little signal. The signal MC efficiencies are 96% for the $D^* \to D^0\pi$, 98% for the $D^* \to D\pi^0$, and 99% $D^{*0} \to D^0\pi^0$. The efficiency from signal MC for the combination of the three cuts is 93%.

Event Based Selection Summary

On the basis of the kaon vetoes, two samples are defined:

1. signal-enhanced or signal-enriched sample where $N_{K^\pm} = N_{K^0_S} = 0$
2. signal-depleted sample where $N_{K^\pm} > 0$ or $N_{K^0_S} > 0$

The selection criteria that was previously described are summarized in Table 6.5. They are listed in two categories as a different combination of cuts is used to identify semileptonic events and charmless semileptonic events.

Table 6.5: Selection criteria for $b \to q\ell\nu$ and $b \to u\ell\nu$ events.

Selection Criteria	N_{sl}^{meas}	N_{u}^{meas}
B_{reco} Candidate	mode based	mode based
Minimum Lepton Momentum	$p^* > 1.0$ GeV/c	$p^* > 1.0$ GeV/c
Number of Charged Leptons	$N_{lepton} > 0$	$N_{lepton} = 1$
Lepton Charge-B Flavor	$Q_{b(recoil)}Q_\ell > 0$	$Q_{b(recoil)}Q_\ell > 0$
Total Charge per Event		$Q_{tot} = 0$
Missing-Mass		$-1.0 < m^2_{miss} < 0.5$ (GeV/c^2)^2
Missing Momentum		$p_{miss} > 0.3$ GeV/c
Missing Angle		$-0.95 < \cos(\theta_{miss}) < 0.95$
Kaon Veto		$N_{K^\pm} = 0$ and $N_{K_S} = 0$
Slow Track Killing		$p^*_{trk,low} > 0.12$ GeV/c
$B \to D^*\ell\nu$ Rejection		mode based

6.3.4 Comparison of Data and Monte Carlo

A good description of the relevant variables by the Monte Carlo simulation is important for this inclusive analysis. Figures 6.20–6.26 show data and MC comparisons for various variables, both for generic and cocktail MC samples. The overall agreement is between data and MC is reasonable.

All spectra in Figs. 6.20–6.26 have been background-subtracted with the appropriate $m_{\rm ES}$ sideband distribution. The event samples are divided into signal-enhanced and signal-depleted subsets based on the absence or presence of charged and neutral kaons, respectively. The histograms are normalized to equal area. Each pair of histograms is tested for compatibility with two methods. The results of both tests are printed in the upper left corner of each plot for both generic and cocktail MC: The first pair of numbers indicates the $\chi^2/{\rm d.o.f.}$ and the number in parentheses gives the Kolmogorov probability.

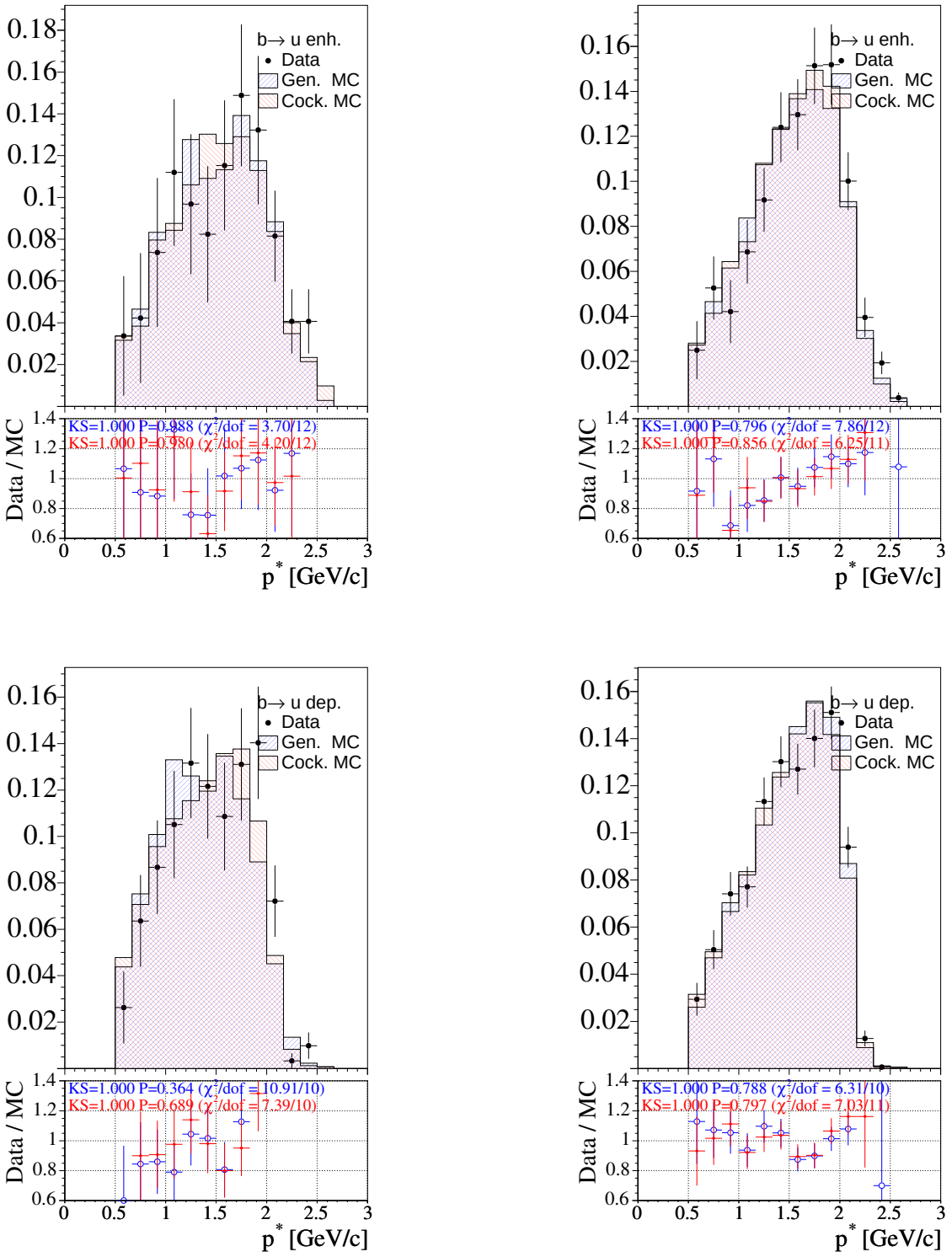

Figure 6.20: B^0 (left) and B^+ (right) lepton spectra (side-band subtracted) in generic/cocktail MC and data for $b \to u\ell\nu$ enhanced (top row) and depleted (bottom row) event samples.

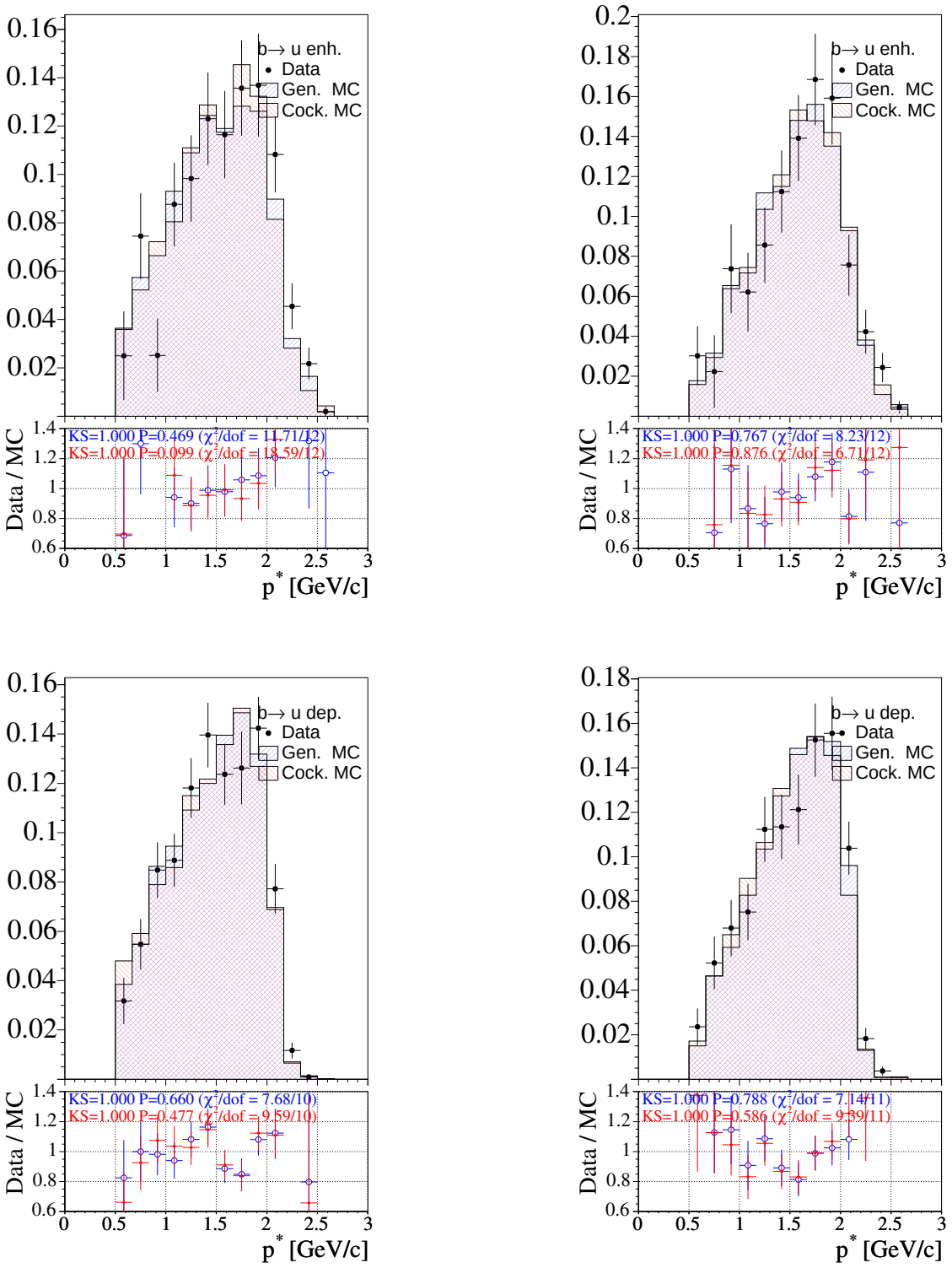

Figure 6.21: Electron (left) and muon (right) spectra (side-band subtracted) in generic/cocktail MC and data for $b \to u\ell\nu$ enhanced (top row) and depleted (bottom row) event samples.

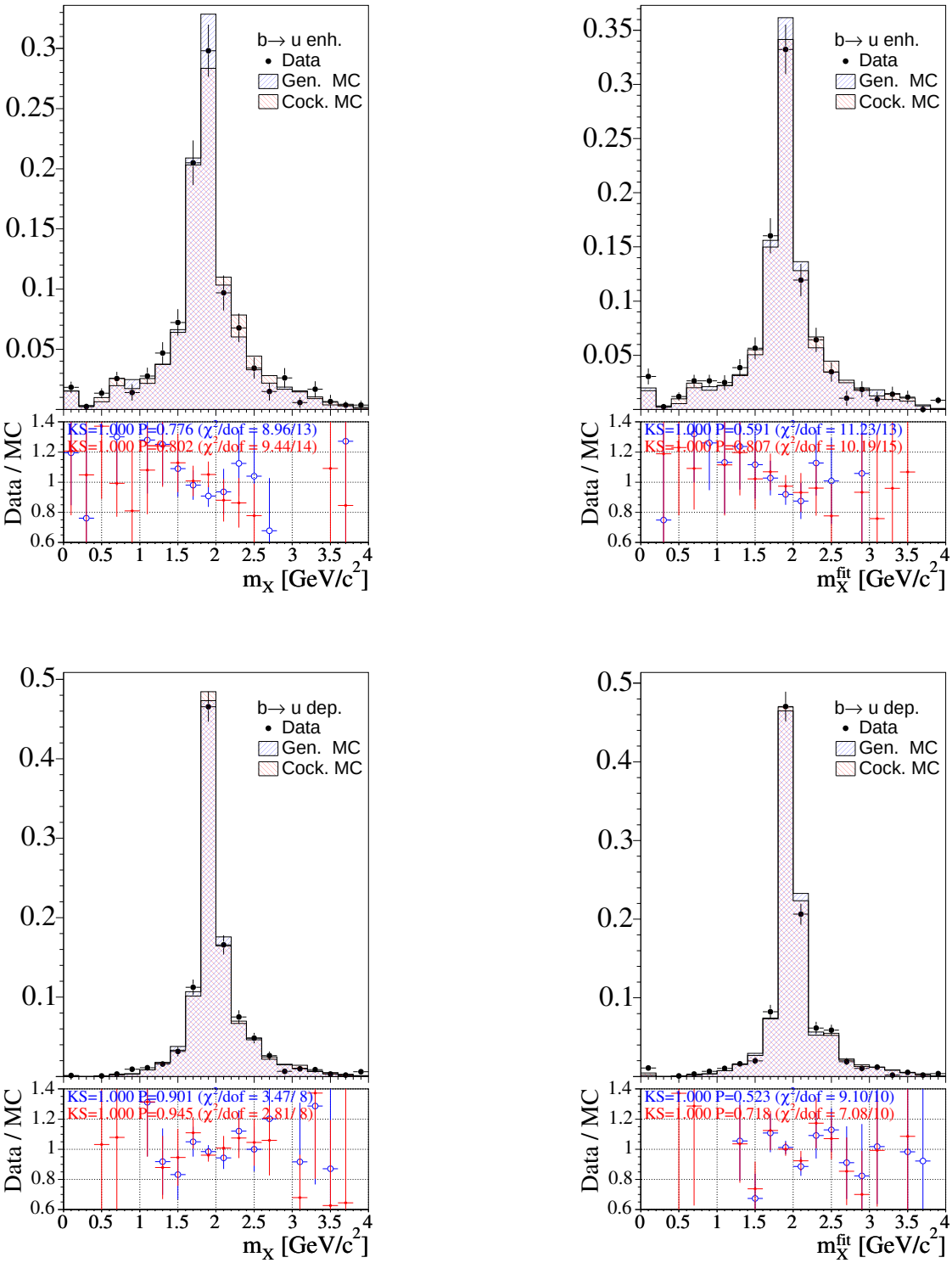

Figure 6.22: Reconstructed (left) and kinematically fitted (right) hadronic recoil invariant mass spectra (side-band subtracted) in generic/cocktail MC and data for $b \to u\ell\nu$ enhanced (top row) and depleted (bottom row) event samples.

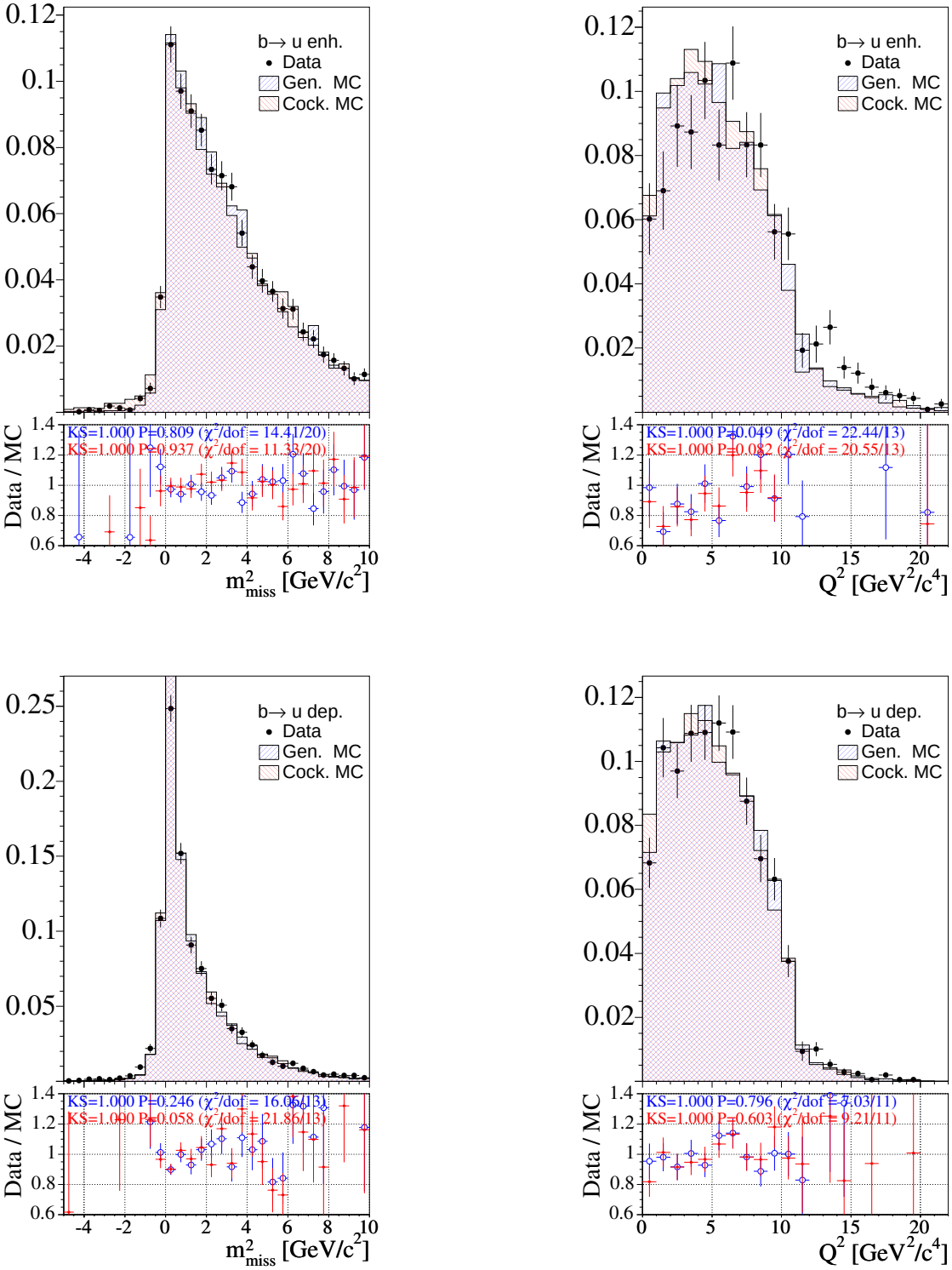

Figure 6.23: Missing-mass squared (left) and Q^2 (right) distributions (side-band subtracted) in generic/cocktail MC and data for $b \to u\ell\nu$ enhanced (top row) and depleted (bottom row) event samples.

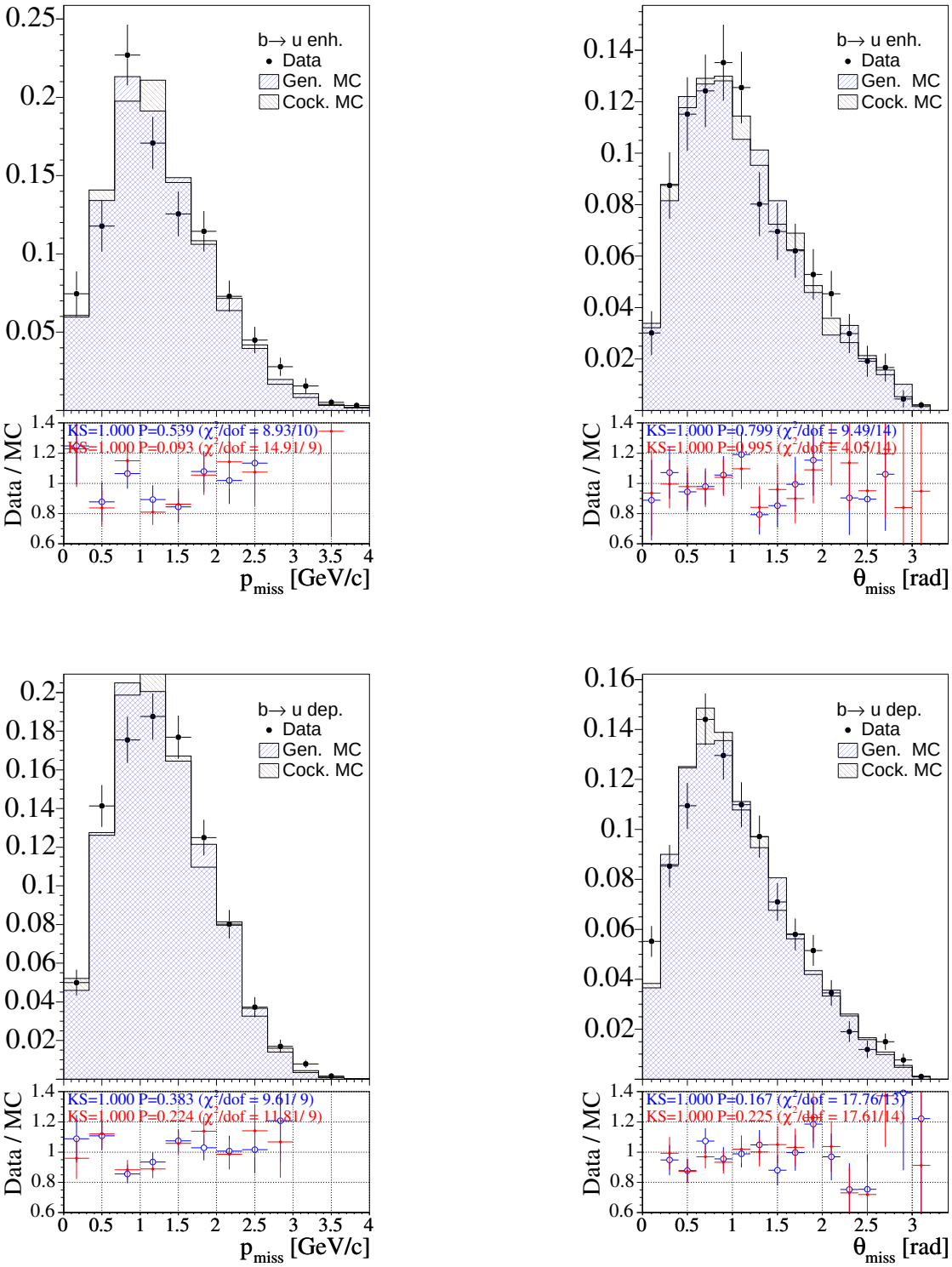

Figure 6.24: Missing momentum (left) and Θ_{miss} (right) distributions (side-band subtracted) in generic/cocktail MC and data for $b \rightarrow u\ell\nu$ enhanced (top row) and depleted (bottom row) event samples.

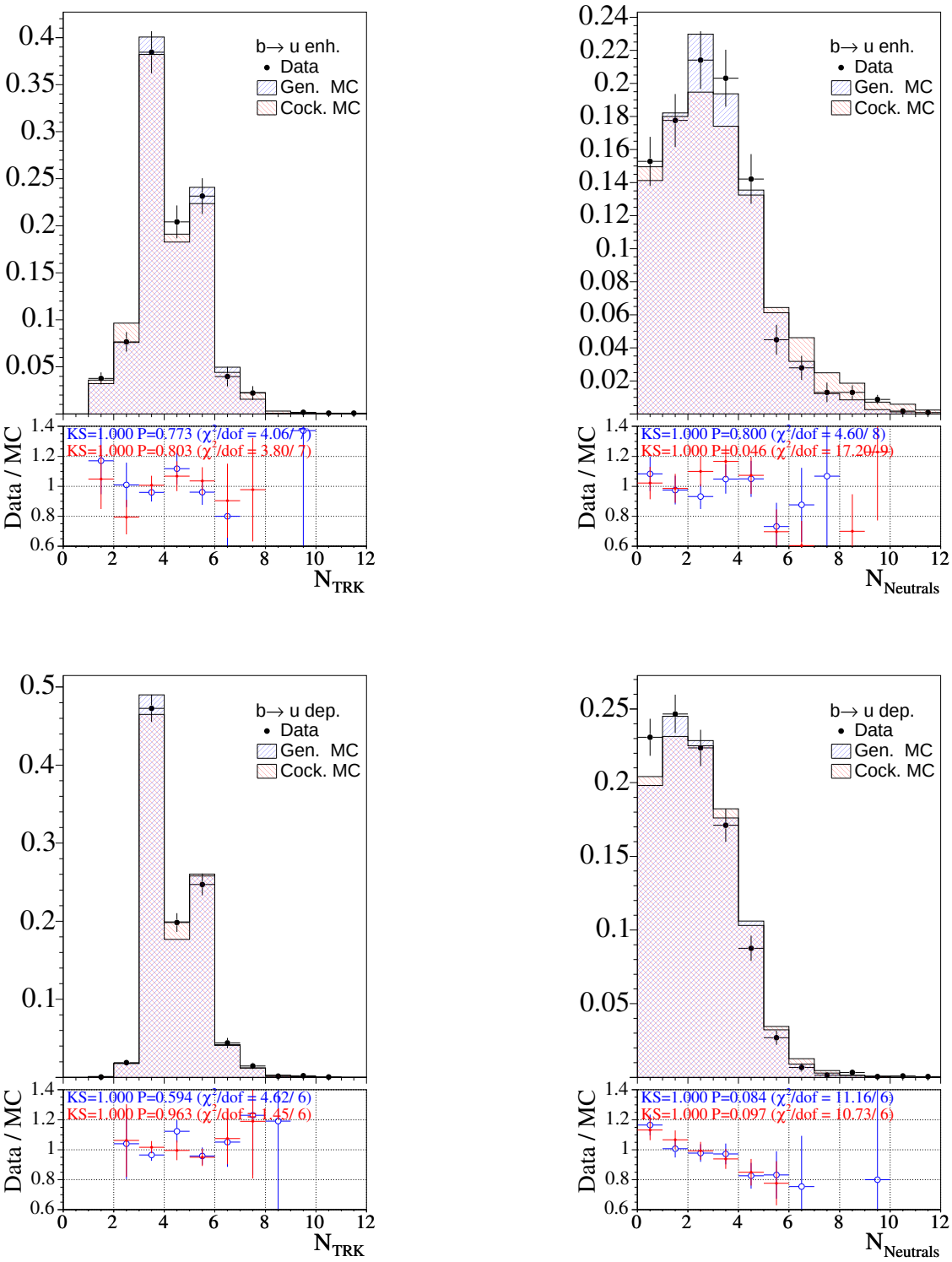

Figure 6.25: Charged (left) and neutral (right) multiplicity distributions (side-band subtracted) in generic/cocktail MC and data for $b \to u\ell\nu$ enhanced (top row) and depleted (bottom row) event samples.

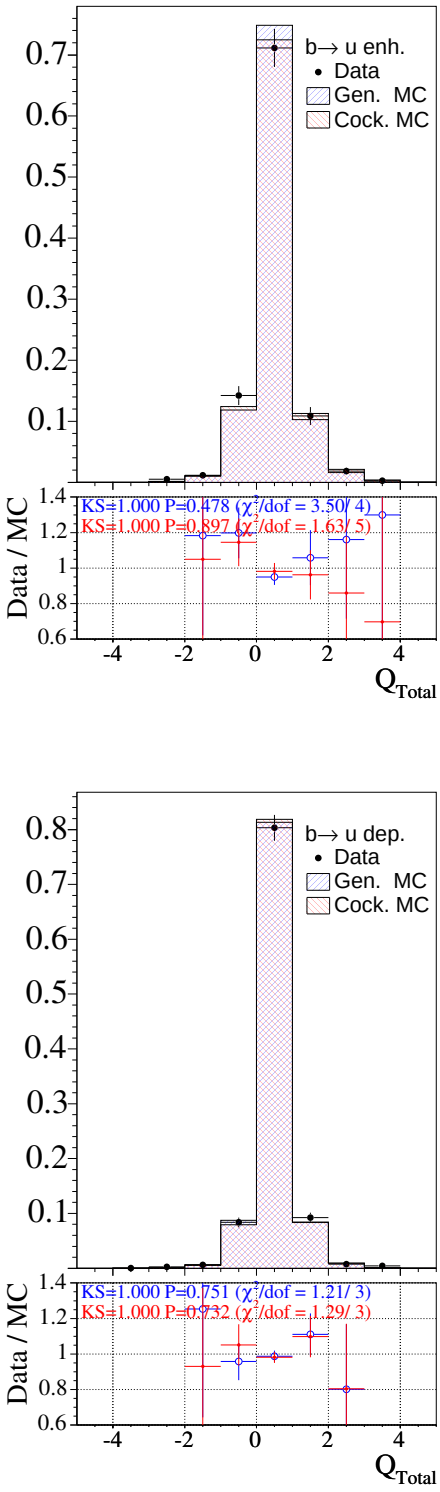

Figure 6.26: Total charge (left) distributions (side-band subtracted) in generic/cocktail MC and data for $b \to u\ell\nu$ enhanced (top row) and depleted (bottom row) event samples.

Chapter 7

Signal Extraction and Results

This chapter presents the analysis used to measure the quantities needed for the determination of $|V_{ub}|$. Section 7.1 describes the measurement of the partial rate $\delta\Gamma(c)$ determined from the number of $b \to u\ell\bar{\nu}$ events with $c < (m_X/m_B)^2$. Section 7.2 describes the determination of the weighted integrals $I_0(c)$ and $I_+(c)$, obtained from the $b \to s\gamma$ energy spectrum. Finally, section 7.3 presents the results for $|V_{ub}|$.

7.1 Extraction of $\delta\Gamma(c)$

Equation 2.72 requires the measurement of the partial $b \to u\ell\bar{\nu}$ decay rate $\delta\Gamma(c)$ below a hadronic mass cut-off $c < (m_X/m_B)^2$ from the signal events selected according to the criteria described in chapter 6. We define the cut-integrated rate as (dropping the factor of $\frac{\hbar}{\tau_B}$ since it cancels with the weighted photon spectrum integrals)

$$\delta\Gamma(c) = \frac{N_u f \mathcal{B}(\overline{B} \to X\ell\bar{\nu})}{N_{SL}\varepsilon_u} \times \frac{\varepsilon_l^{sl}}{\varepsilon_l^u} \times \frac{\varepsilon_{reco}^{sl}}{\varepsilon_{reco}^u}. \tag{7.1}$$

Equation 2.35 requires the total charmless semileptonic branching fraction (or full rate) $\mathcal{B}(\overline{B} \to X_u\ell\overline{\nu})$. We define the the total branching fraction as

$$\mathcal{B}(\overline{B} \to X_u\ell\overline{\nu}) = \frac{\delta\Gamma(c)}{\varepsilon_{m_X}} \tag{7.2}$$

The quantities in Eqs. 7.1 and 7.2 are as follows:

- N_u is the total number of signal events after all analysis cuts and after background subtraction

(see section 7.1.1).

- f corrects for difference between the true and reconstructed m_X (see section 7.1.2).
- N_{SL} is the total number of events containing at least one lepton with a momentum above the threshold of $1\,\mathrm{GeV}/c$ after a background subtraction (see section 7.1.3).
- $\mathcal{B}(\overline{B} \to X\ell\bar{\nu})$ is the inclusive semileptonic branching fraction, $\mathcal{B}(\overline{B} \to X\ell\bar{\nu}) = 0.1087 \pm 0.18(stat) \pm 0.30(syst)$ as measured by *BABAR* [32].
- ε_u is the efficiency for selecting $B_{recoil} \to X_u\ell\bar{\nu}$ decays once a $B_{recoil} \to X\ell\bar{\nu}$ has been identified with a hadronic mass below the cut-off (see section 7.1.4).
- $\frac{\varepsilon_l^{sl}}{\varepsilon_l^u}$ is the ratio of the efficiencies for selecting a semileptonic decay with a momentum above the $1\,\mathrm{GeV}/c$ threshold for $B_{recoil} \to X\ell\bar{\nu}$ and $B_{recoil} \to X_u\ell\bar{\nu}$ events (see section 7.1.4).
- $\frac{\varepsilon_{reco}^{sl}}{\varepsilon_{reco}^u}$ is the ratio of the efficiencies for successfully reconstructing a B_{reco} candidate opposite a $B_{recoil} \to X\ell\bar{\nu}$ and $B_{recoil} \to X_u\ell\bar{\nu}$ decay (see section 7.1.4).
- ε_{m_X} is the efficiency for measuring below a cut-off in the hadronic mass spectrum.

Using the ratio of the partial charmless semileptonic branching fraction $\delta\Gamma(c)$ to the total semileptonic branching fraction $\mathcal{B}(\overline{B} \to X\ell\bar{\nu})$ has three advantages. First of all, by measuring a ratio, the absolute efficiency of the semi-exclusive reconstruction is not needed. This is very important since the semi-exclusive efficiency is affected by uncertainties due to the complicated algorithm and the fact that many of the reconstructed modes are not well described in the MC. Secondly, most of the systematics due to lepton identification are removed since they are present in both numerator and denominator of the ratio. Finally the normalization to the number of semileptonic events is less affected by biases in the m_{ES} fits. As shown in Fig. 6.5, the quality of the fit and the signal over background ratio improves considerably once a cut on the lepton momentum is applied.

7.1.1 Extraction of N_u, the Number of $b \to u\ell\bar{\nu}$ Signal Events

An unbinned maximum-likelihood fit in each bin of the m_X distribution is used to determine the the number of signal events N_u. The signal component from the m_{ES} fits is parameterized by a Crystal Ball function [65] and the background is parameterized by an ARGUS function [64]. The m_{ES} fit in each bin of m_X have their signal shape parameters fixed to the fit parameters resulting

from an $m_{\rm ES}$ fit to the whole distribution. The (Crystal Ball) signal shape does not have any dependence on m_X, as verified with signal MC. The signal normalization parameter and the ARGUS parameters are allowed to float in the fits in individual bins of m_X. The bins of the m_X distribution are fit to the sum of three separate distributions: the signal N_i^u, the $\overline{B} \to X_c \ell \bar{\nu}$ background N_i^c, and the other background N_i^o. The shapes of these three contributions are determined from MC, and the normalization coefficients C_X are determined from a χ^2 fit. The sum of the three components is defined as

$$\mu_i = C_u N_i^{u,MC} + C_c N_i^{c,MC} + C_o N_i^{o,MC}, \tag{7.3}$$

and the χ^2 distribution is defined as

$$\chi^2(C_u, C_c, C_o) = -\sum_i \left(\frac{N_i^{u,meas} - \mu_i}{\sqrt{\delta(N_i^{u,meas})^2 + \delta(N_i^{u,MC})^2}} \right)^2 \tag{7.4}$$

where $N_i^{u,meas}$ is the measured number of events, $\delta(N_i^{u,meas})$ and $\delta(N_i^{u,MC})$ are the statistical errors for the $m_{\rm ES}$ fits to the data and MC respectively, and the subscript i indicates the m_X bin. The other background component is a small contribution to the fit and is not well determined. For this reason, the contribution of the other component is fixed to that of the charm background $C_o \equiv C_c$ and the sum of the two types of background is obtained from the fit, removing one degree of freedom.

For neutral B decays, the fits must properly account for $B^0 - \overline{B}^0$ mixing. Under the assumption that the neutral B sample consists solely of direct and cascade leptons, the relation of right-sign (rs) to wrong-sign (ws) neutral events can be expressed as

$$N_{rs} = (1 - \chi_d) N_B + \chi_d N_D \tag{7.5}$$

$$N_{ws} = \chi_d N_B + (1 - \chi_d) N_D \tag{7.6}$$

where χ_d is the mixing parameter [6], N_B is the number of direct decays, and N_D is the number of cascade decays. Solving,

$$N_B = \frac{1 - \chi_d}{1 - 2\chi_d} N_{rs} - \frac{\chi_d}{1 - 2\chi_d} N_{ws} \tag{7.7}$$

Of course, there can exist events with no leptons or events with two D mesons which would be

right-sign events even if it is not a direct decay. However these possibilities are not considered as the mixing correction is applied separately for the aforementioned three components of the fit.

The m_X distribution has bins with a width of $300\,\mathrm{MeV}/c^2$. To accommodate a m_X cut that is not an integer multiple of the nominal bin width, the last bin before the m_X cut is extended up to the m_X cut, so there are no bins with widths smaller than the nominal bin width of $300\,\mathrm{MeV}/c^2$. Thus the results for different m_X cuts correspond to a differently binned m_X distribution and therefore to separate fits.

Finally, the number of background-subtracted signal events N_u is defined as

$$N_u = \sum_{i=1}^{N_{bin}} \left(N_i^{u,meas} - C_c N_i^{c,MC} - C_o N_i^{o,MC} \right) \tag{7.8}$$

where N_{bin} is the number of bins in the hadronic mass distribution below the m_X cut. The fits are found to have $\chi^2/DOF \sim 1.0$, as summarized in Table 7.1. The results of the χ^2 fits to the m_X distribution can be found in Figs. 7.1 - 7.6. Also, examples of the fits to the m_{ES} distributions in each m_X bin can be found in Appendix A. The results for the fits for various hadronic mass cut-offs and subsamples are detailed in Tables 7.4-7.6.

Table 7.1: The χ^2/DOF results from the fits to the hadronic mass spectrum

m_X Cut [GeV/c^2]	χ^2	DOF	χ^2/DOF
1.55	10.373	11	0.943
1.59	11.176	11	1.016
1.67	12.947	11	1.177
1.75	11.308	11	1.028
1.83	9.493	11	0.863
2.50	10.219	11	0.929

7.1.2 Extraction of f

To obtain the true number of signal events, it is necessary to apply a correction for events generated inside (outside) the signal region and reconstructed outside (inside) the signal region. This correction factor is defined as

$$f = 1 + \frac{N_2}{N_1} - \frac{N_3}{N_1} \tag{7.9}$$

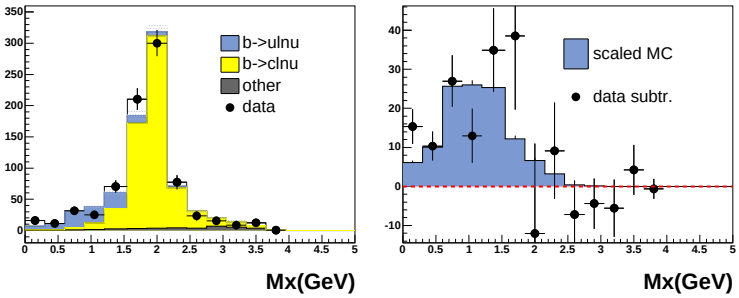

Figure 7.1: The fit results for $m_X < 1.55\,\mathrm{GeV}/c^2$.

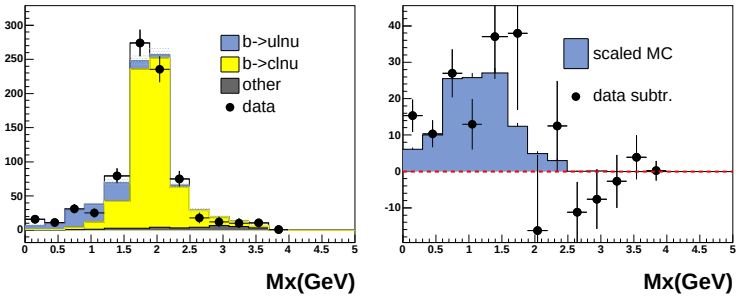

Figure 7.2: The fit results for $m_X < 1.59\,\mathrm{GeV}/c^2$.

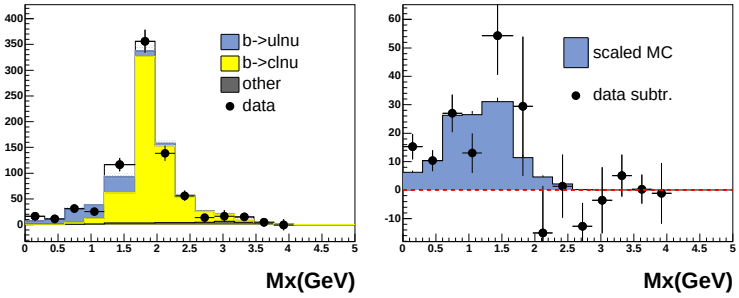

Figure 7.3: The fit results for $m_X < 1.67\,\mathrm{GeV}/c^2$.

where N_1 is the number of events observed in the signal area and N_2 (N_3) is the number of events generated inside (outside) the signal area but measured outside (inside) the signal area. The factor f is calculated on the signal MC sample. The results for the extraction of f for various hadronic mass cut-offs and subsamples are found in Tables 7.4-7.6.

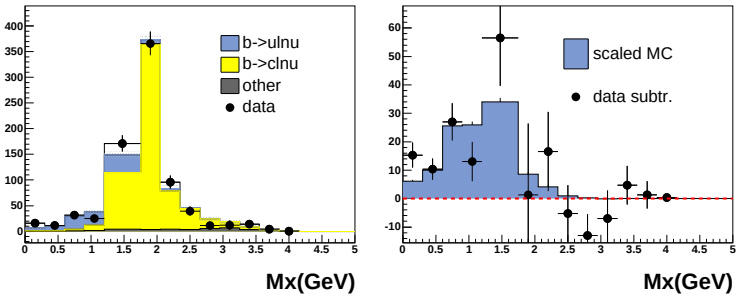

Figure 7.4: The fit results for $m_X < 1.75\,\mathrm{GeV}/c^2$.

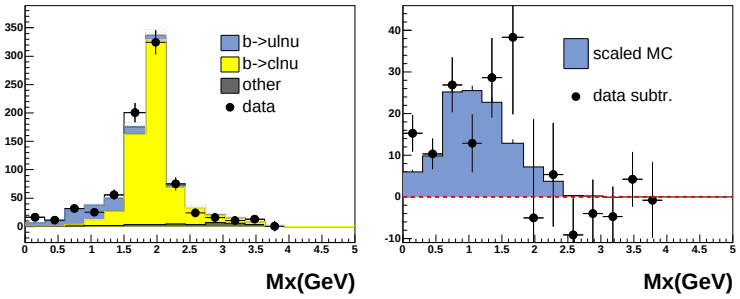

Figure 7.5: The fit results for $m_X < 1.83\,\mathrm{GeV}/c^2$.

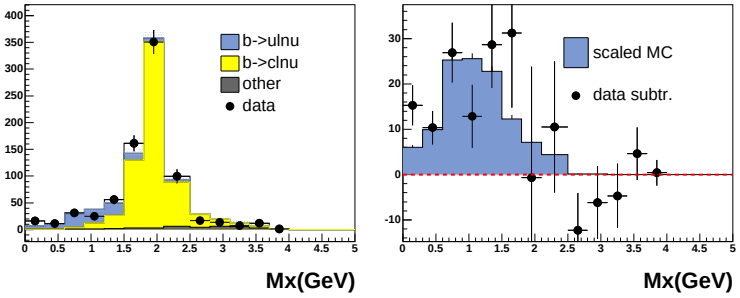

Figure 7.6: The fit results for $m_X < 2.50\,\mathrm{GeV}/c^2$.

7.1.3 Extraction of N_{SL}, the Number of Semileptonic Events

The number of semileptonic events N_{SL} is measured from a fit to the m_{ES} distribution of events with a momentum above the $1\,\mathrm{GeV}/c$ threshold. The fit allows all parameters to float and is corrected

for mixing in the neutral B mesons. The residual background in N_{SL} from semileptonic charm decays and lepton misidentification is estimated from MC and N_{SL} is corrected appropriately. As in the case of the signal extraction, a mixing correction is applied to the neutral B sample in the determination of N_{SL}. The results for the extraction of N_{SL} for various hadronic mass cut-offs and subsamples are found in Tables 7.4-7.6.

7.1.4 Efficiency Corrections

The efficiency factor $\frac{\varepsilon^{sl}_{reco}}{\varepsilon^{u}_{reco}}$ corrects for a possible bias in successfully reconstructing a B_{reco} candidate in events with a recoiling $B_{recoil} \to X\ell\bar{\nu}$ or $B_{recoil} \to X_u\ell\bar{\nu}$. From generic MC, $\frac{\varepsilon^{sl}_{reco}}{\varepsilon^{u}_{reco}} = 1.00 \pm 0.03$. We take the MC statistical error as a systematic uncertainty. This efficiency calculation is independent of of the hadronic mass cut.

The efficiency factor $\frac{\varepsilon^{sl}_{l}}{\varepsilon^{u}_{l}}$ accounts for the efficiency for detecting semileptonic decays with a momentum above the $1\,\mathrm{GeV}/c$ threshold. The efficiency is not expected to be unity because the shapes of the lepton momentum spectra are different for $\overline{B} \to X_c\ell\bar{\nu}$ and $\overline{B} \to X_u\ell\bar{\nu}$ decays. This efficiency factor is also independent of the hadronic mass cut, but will be different for electrons and muons. The results are detailed in Tables 7.4-7.6 for the various samples.

The efficiency factor ε_u is the cut efficiency after the detection of a lepton with momentum above the $1\,\mathrm{GeV}/c$ threshold and a hadronic mass below the cut-off. The efficiency is determined from hybrid signal MC and varies with the m_X cut. The results for the extraction of ε_u for various hadronic mass cut-offs and subsamples are found in Tables 7.4-7.6.

7.1.5 Fit Validation

As a cross-check of the analysis procedure, the fit is performed with the high statistics sample of cocktail MC used for all data and MC inputs. We then compare the extracted ratio of the charmless semileptonic branching ratio to the total semileptonic branching ratio R_u to the generated value, $R_u \equiv \mathcal{B}(b \to u\ell\bar{\nu})/\mathcal{B}(b \to c\ell\bar{\nu}) = 0.0116$. The results are summarized in Table 7.2 and are found to be compatible with the generated value.

Another cross-check is provided by fitting the signal depleted sample, which was defined in 6.3.3. This sample is large and contains an overwhelming amount of background, so the signal extraction will have large errors. However, this method is more useful for checking resolution effects and confirming that the shape of the m_X distribution is well understood. The fit to the depleted sample has been performed with data and is shown in Fig. 7.7. Table 7.4 contains a breakdown of the results.

Table 7.2: Analysis validation and fit results for high-statistics cocktail MC. The generated value corresponds to $R_u \equiv \mathcal{B}(b \to u\ell\bar{\nu})/\mathcal{B}(b \to c\ell\bar{\nu}) = 0.0116$.

m_X Cut [GeV/c^2]	R_u [$\times 10^{-2}$]
1.55	1.10 ± 0.09
1.59	1.14 ± 0.10
1.67	1.16 ± 0.10
1.75	1.16 ± 0.12
1.83	1.09 ± 0.14
2.50	1.06 ± 0.25

The results confirm within errors the expected result.

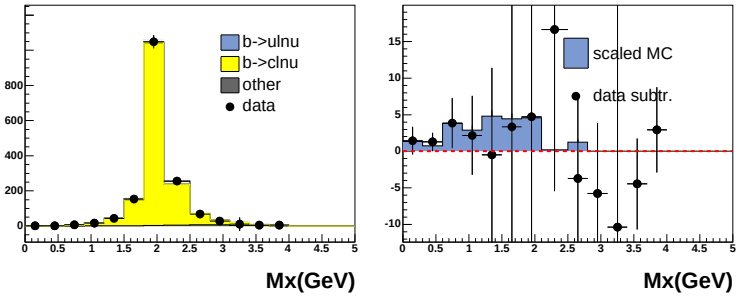

Figure 7.7: The fit results for the depleted sample.

7.1.6 Summary of $\delta\Gamma(c)$ Results

The results for the extraction of $\delta\Gamma(c)$ have been summarized in Tables 7.4-7.6 and are illustrated in Figs. 7.1–7.6. The results are shown for several m_X cuts and several different samples: charged B mesons, neutral B mesons, electrons, muons, and the depleted sample. Fit results for the sub-samples can be found in appendix B. The m_X distribution in the MC simulation describes the data well, which is consistent with the data/MC agreement study in section 6.3.4. The efficiency of the m_X cut-offs, adjusted by the correction factor f are summarized in Table 7.3.

Table 7.3: The fraction of signal events below a cut-off in the hadronic mass spectrum. The error shown is statistical. This number is only used in the extraction of the total charmless branching fraction (Eq. 7.2) for the full rate measurement.

m_X Cut [GeV/c^2]	Captured Rate (%)
1.55	77.1 ± 1.3
1.59	78.9 ± 1.3
1.67	82.9 ± 1.1
1.75	85.5 ± 1.0
1.83	88.2 ± 0.9
2.50	96.5 ± 0.4

7.2 Extraction of I_0 and I_+ from the differential $b \to s\gamma$ Photon Spectrum

We extract the differential rate of the endpoint rate from the photon energy spectrum of $b \to s\gamma$ decays provided in reference [69]; Table 7.7 summarizes the differential rate. The bin boundaries are related to the bin boundaries for the hadronic mass, with $E_\gamma^2 = (m_B^2 - m_{X_s}^2)/(2m_B)$. Reference [69] does not provide a differential rate (or, equivalently, branching fraction) in the bins of photon energy, rather the bin contents are reported in units of events$/100\,\mathrm{MeV}$. Therefore we extract the differential rate $(\Delta\mathcal{B}/\Delta E_\gamma)_i$ in bin i from the numbers in reference [69] in the following way

$$\left(\frac{\Delta\mathcal{B}}{\Delta E_\gamma}\right)_i = \frac{y_i}{0.1\,\mathrm{GeV}}$$

where y_i are the branching fraction numbers in bin i normalized to $100\,\mathrm{MeV}$ as given in table V of reference [69]. The differential branching fraction can be integrated in the range $1.8972 < E_\gamma < 2.606\,\mathrm{GeV}$ and yields the visible branching fraction

$$\begin{aligned}
\mathcal{B}(b \to s\gamma; 1.897 < E_\gamma < 2.606\,\mathrm{GeV}) &= \int_{1.897}^{2.606} \left(\frac{d\mathcal{B}}{dE_\gamma}\right) dE_\gamma \\
&= \sum_{i=0}^{18} \left(\frac{\Delta\mathcal{B}}{\Delta E_\gamma}\right)_i (\Delta E_\gamma)_i \\
&= 3.94 \times 10^{-4},
\end{aligned}$$

in accordance to the measured value quoted in reference [69].

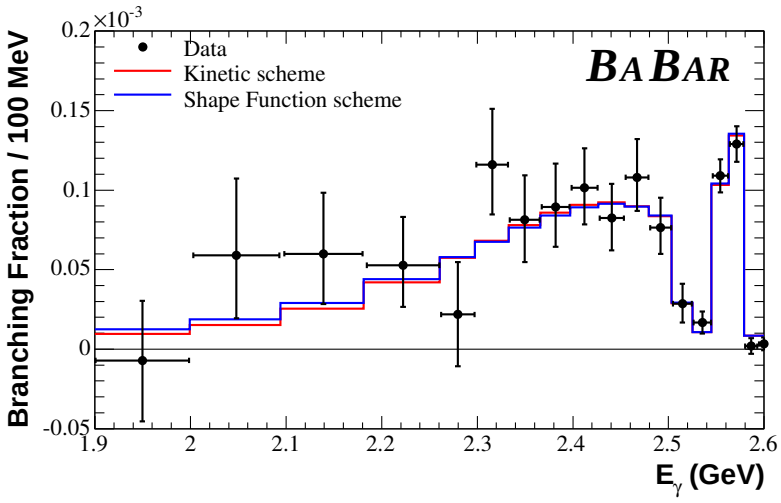

Figure 7.8: Photon energy spectrum for the decay $b \to s\gamma$ measured by *BABAR* [69]. This measurement is based on the sum of exclusive modes and results in an excellent photon energy resolution.

We extract the weighted integrals I_0 (Eq. 2.70) and I_+ (Eq. 2.71) from this photon energy spectrum with a Mathematica™ notebook. The two components to I_0 and I_+ are shown in Fig. 7.9 for a cut on the hadronic mass $m_X < 1.67\,\mathrm{GeV}/c^2$.

7.3 Determination of $|V_{ub}|$ and $\mathcal{B}(\overline{B} \to X_u \ell \bar{\nu})$

Combining the results for the partial rates $\delta\Gamma(c)$ with the weighted integrals of the photon spectrum yields results for $|V_{ub}|/|V_{ts}|$. We assume $|V_{ts}| = |V_{cb}|$ and use the measurement of $|V_{cb}|$ from *BABAR* [32] to determine $|V_{ub}|$ as listed in Table 7.8. The derivation of the error is described in detail in chapter 8. Table 7.8 presents the results for a selection of upper limits on the hadronic mass spectrum: Good consistency is observed for all cuts.

The second determination of $|V_{ub}|$ is based on the measurement of the full rate. The full rate is determined from the partial rate $\delta\Gamma(c)$ for $m_X < 2.50\,\mathrm{GeV}/c^2$, which amounts to 96.5% of the total rate. We thus scale the partial rate by this efficiency $\varepsilon_{m_X} = 0.965 \pm 0.004_{\mathrm{stat}} \pm 0.035_{\mathrm{syst}}$. The systematic error on this efficiency is taken as the full difference of the central value from unity and is added to the signal modeling error, visible in Table 7.8. The total branching fraction obtained is

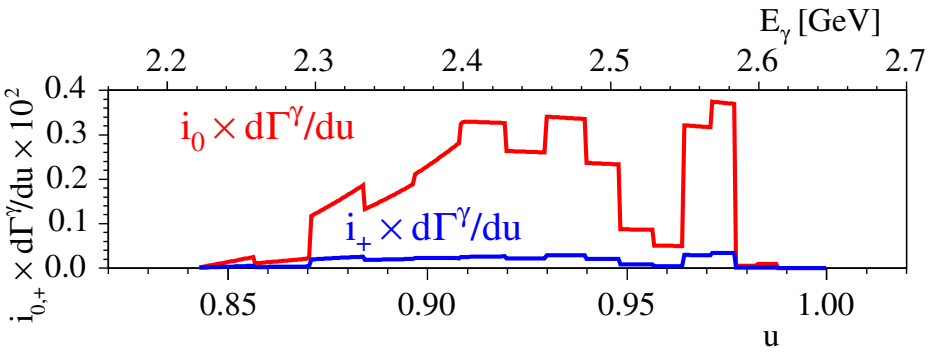

Figure 7.9: $b \to s\gamma$ photon energy spectrum as a function of $u = 2E_\gamma/\,\mathrm{m_B}$, weighted with the weight functions $i_0(u)$ and $i_+(u)$, calculated for a cut on the hadronic mass $m_X < 1.67\,\mathrm{GeV}/c^2$. The integral of these functions correspond to I_0 and I_+, respectively.

$$\mathcal{B}(\overline{B} \to X_u \ell \bar{\nu}) = (1.64 \pm 0.60_{stat} \pm 0.25_{syst}) \times 10^{-3}, \tag{7.10}$$

We use the formula of Refs. [30, 31] (Eqn. 2.35) with the B meson lifetime $\tau_B = (1.604 \pm 0.012)\,\mathrm{ps}$ [6, 74] to translate the full rate into $|V_{ub}|$:

$$|V_{ub}| = 0.00424 \sqrt{\frac{\mathcal{B}(\overline{B} \to X_u \ell \bar{\nu})}{0.002} \frac{1.61\,\mathrm{ps}}{\tau_B}} \times (1.00 \pm 0.028_{OPE} \pm 0.039_{m_b}) \tag{7.11}$$

$$= (3.84 \pm 0.70_{stat} \pm 0.15_{det} \pm 0.14_{b2c} \pm 0.22_{b2u} \pm 0.11_{OPE} \pm 0.15_{m_b}) \times 10^{-3} \tag{7.12}$$

The result is also provided in the right-most column of Table 7.8. We observe good agreement between the value obtained the OPE formula in Eq. 7.12 and the approach of Leibovich, Low, and Rothstein for cut values above $\sim 1.5\,\mathrm{GeV}/c^2$ on the mass spectrum (see Fig. 7.10). There is no evidence for large power correction effects not included in the calculation for the values quoted in Table 7.8. However, these effects may be visible when lowering the cut values to low m_X cutoffs, where a systematic rise of $|V_{ub}|$ can be observed. This departure from a stable result is expected from the breakdown of the OPE in this regime and is reflected in the very large increase of the non-perturbative error for low m_X cutoffs (see section 8.3.3).

It is interesting to observe the decrease of $|V_{ub}|$ with increasing m_X cut. This variation is

not due to the 'semi-leptonic' part of the analysis, as can be observed by the good stability of the extrapolated branching fraction at high m_X cuts, shown in Fig. 8.4. This indicates that the observed systematic decrease results either from the theoretical calculation (the weight functions in particular) or the experimental input from the $b \to s\gamma$ photon energy spectrum. At high m_X cutoffs, the theoretical errors are expected to be small. However, at high m_X cutoffs in the Leibovich, Low, and Rothstein method, the weighted integral starts lower in the measured photon energy spectrum, which is the experimentally challenging region of the photon spectrum to measure. As a result, the errors from the photon spectrum are large at high m_X cutoffs, as shown in Fig. 7.11 (compare them to the constant perturbative error, shown as the inner (yellow) error band).

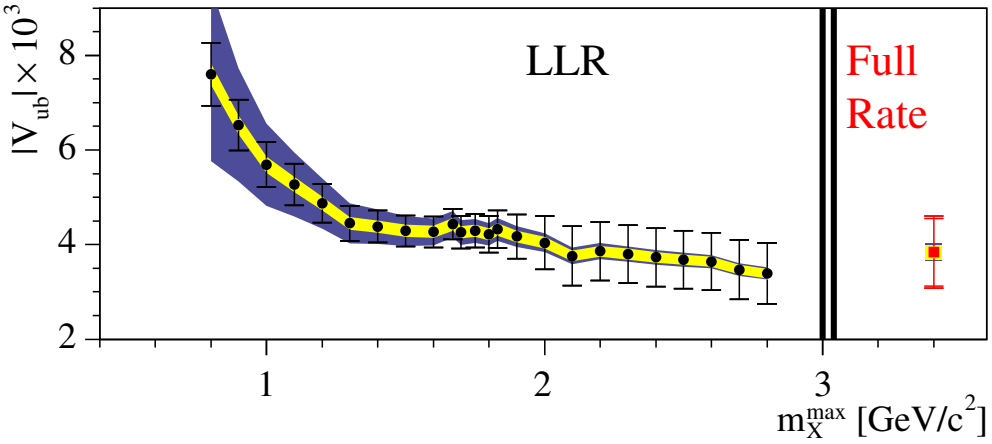

Figure 7.10: $|V_{ub}|$ vs. the upper cut on m_X. The error bars illustrate (from innermost to outermost) the experimental (statistical plus detector systematics), background and signal modeling, $b \to s\gamma$ errors. Points without the inner error bars have only the statistical error displayed. The shaded error band illustrate the perturbative error (innermost yellow band) and the total theoretical error (outermost bluish band) where the QED scale uncertainty, the perturbative and non-perturbative error have been added in quadrature.

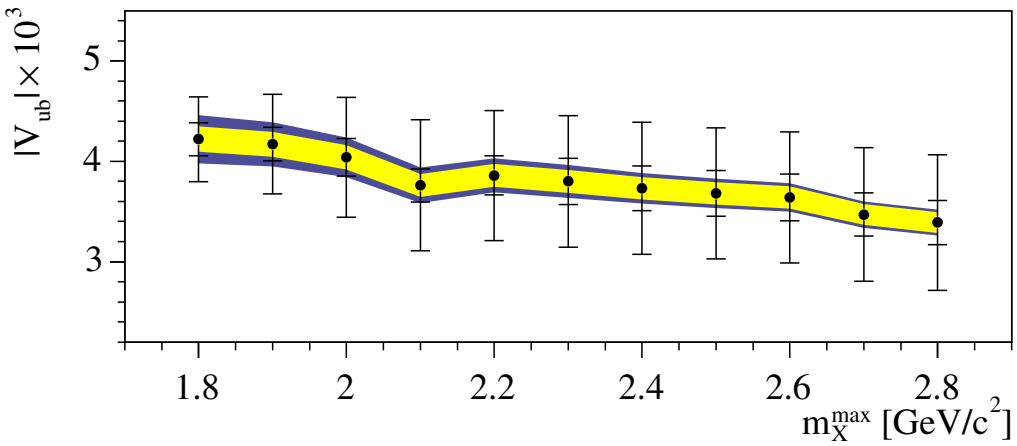

Figure 7.11: Enlarged view of $|V_{ub}|$ vs. the upper cut on m_X with special emphasis on the statistical error from the $b \rightarrow s\gamma$ photon energy spectrum. The error bars illustrate (from innermost to outermost) the statistical error from the $b \rightarrow s\gamma$ photon energy spectrum and the total error (statistical, experimental systematic, signal and background modeling). The shaded error band illustrate the perturbative error (innermost yellow band) and the total theoretical error (outermost bluish band) where the QED scale uncertainty, the perturbative and non-perturbative error have been added in quadrature.

Table 7.4: Summary of the fit parameters for data, on the full (top) and depleted (bottom) samples.

m_X cut (GeV/c^2)	N_{sl}^{meas}	$\epsilon_l^{sl}/\epsilon_l^u$	N_u	BG_u^c	BG_u^{oth}	ϵ_u	f	$\delta\Gamma(c)$ ($*10^3$)
	Full Sample							
1.55	32532 ± 242	0.82 ± 0.02	100 ± 15	48 ± 2	6 ± 0	0.235 ± 0.005	0.991 ± 0.007	1.154 ± 0.175
1.59	32532 ± 242	0.82 ± 0.02	103 ± 16	55 ± 2	6 ± 0	0.231 ± 0.005	0.994 ± 0.007	1.199 ± 0.185
1.67	32532 ± 242	0.82 ± 0.02	120 ± 17	73 ± 3	7 ± 0	0.231 ± 0.005	1.010 ± 0.005	1.426 ± 0.208
1.75	32532 ± 242	0.82 ± 0.02	122 ± 20	125 ± 7	8 ± 0	0.231 ± 0.005	1.004 ± 0.005	1.442 ± 0.241
1.83	32532 ± 242	0.82 ± 0.02	132 ± 25	199 ± 9	9 ± 0	0.231 ± 0.005	1.015 ± 0.004	1.580 ± 0.293
2.50	32532 ± 242	0.82 ± 0.02	135 ± 45	598 ± 21	18 ± 0	0.231 ± 0.004	0.998 ± 0.002	1.585 ± 0.531
	Depleted Sample							
1.55	32532 ± 242	0.82 ± 0.02	0 ± 11	69 ± 2	4 ± 0	0.022 ± 0.002	0.917 ± 0.039	-0.030 ± 1.264
1.59	32532 ± 242	0.82 ± 0.02	0 ± 14	82 ± 2	4 ± 0	0.023 ± 0.002	0.889 ± 0.036	-0.020 ± 1.492
1.67	32532 ± 242	0.82 ± 0.02	-3 ± 14	116 ± 3	4 ± 0	0.023 ± 0.002	0.930 ± 0.058	-0.303 ± 1.601
1.75	32532 ± 242	0.82 ± 0.02	-3 ± 17	161 ± 5	6 ± 0	0.022 ± 0.002	0.966 ± 0.031	-0.385 ± 2.055
1.83	32532 ± 242	0.82 ± 0.02	15 ± 22	257 ± 0	6 ± 0	0.022 ± 0.002	1.025 ± 0.028	1.885 ± 2.793
2.50	32532 ± 242	0.82 ± 0.02	17 ± 66	1494 ± 36	14 ± 0	0.023 ± 0.002	1.013 ± 0.008	2.104 ± 8.044

Table 7.5: Summary of the fit parameters for data, on the neutral B (top) and charged B (bottom) samples.

m_X cut (GeV/c^2)	N_{sl}^{meas}	$\epsilon_l^{sl}/\epsilon_l^u$	N_u	BG_u^c	BG_u^{oth}	ϵ_u	f	$\delta\Gamma(c)$ ($*10^3$)
	Neutral B Sample							
1.55	11765 ± 155	0.82 ± 0.02	34 ± 8	7 ± 1	2 ± 0	0.177 ± 0.007	0.984 ± 0.014	1.416 ± 0.352
1.59	11765 ± 155	0.82 ± 0.02	35 ± 9	8 ± 1	3 ± 0	0.175 ± 0.007	1.002 ± 0.013	1.527 ± 0.377
1.67	11765 ± 155	0.82 ± 0.02	37 ± 9	13 ± 2	3 ± 0	0.174 ± 0.007	1.020 ± 0.010	1.649 ± 0.412
1.75	11765 ± 155	0.82 ± 0.02	43 ± 11	21 ± 3	3 ± 0	0.172 ± 0.007	1.006 ± 0.008	1.878 ± 0.472
1.83	11765 ± 155	0.82 ± 0.02	51 ± 13	31 ± 4	3 ± 0	0.175 ± 0.006	1.001 ± 0.006	2.174 ± 0.548
2.50	11765 ± 155	0.82 ± 0.02	38 ± 22	108 ± 10	5 ± 0	0.173 ± 0.006	1.004 ± 0.004	1.640 ± 0.962
	Charged B Sample							
1.55	20775 ± 186	0.82 ± 0.02	67 ± 13	41 ± 2	3 ± 0	0.277 ± 0.006	0.993 ± 0.009	1.027 ± 0.193
1.59	20775 ± 186	0.82 ± 0.02	67 ± 13	47 ± 2	3 ± 0	0.272 ± 0.006	0.990 ± 0.008	1.047 ± 0.205
1.67	20775 ± 186	0.82 ± 0.02	83 ± 15	61 ± 3	4 ± 0	0.273 ± 0.006	1.006 ± 0.006	1.310 ± 0.232
1.75	20775 ± 186	0.82 ± 0.02	80 ± 17	104 ± 6	4 ± 0	0.274 ± 0.006	1.004 ± 0.006	1.254 ± 0.270
1.83	20775 ± 186	0.82 ± 0.02	84 ± 21	166 ± 8	6 ± 0	0.272 ± 0.006	1.019 ± 0.006	1.347 ± 0.334
2.50	20775 ± 186	0.82 ± 0.02	100 ± 39	488 ± 19	12 ± 0	0.273 ± 0.006	0.994 ± 0.002	1.557 ± 0.613

Table 7.6: Summary of the fit parameters for data, on the electron (top) and muon (bottom) samples.

m_X cut (GeV/c^2)	N_{sl}^{meas}	$\epsilon_l^{sl}/\epsilon_l^u$	N_u	BG_u^c	BG_u^{oth}	ϵ_u	f	$\delta\Gamma(c)$ ($*10^3$)
	Electron Sample							
1.55	18739 ± 182	0.86 ± 0.02	48 ± 12	35 ± 2	3 ± 0	0.218 ± 0.006	0.998 ± 0.010	1.094 ± 0.267
1.59	18739 ± 182	0.86 ± 0.02	54 ± 12	39 ± 2	3 ± 0	0.216 ± 0.006	0.994 ± 0.010	1.226 ± 0.276
1.67	18739 ± 182	0.86 ± 0.02	62 ± 14	48 ± 3	3 ± 0	0.215 ± 0.006	1.006 ± 0.009	1.435 ± 0.315
1.75	18739 ± 182	0.86 ± 0.02	60 ± 16	79 ± 5	4 ± 0	0.217 ± 0.006	1.001 ± 0.008	1.361 ± 0.360
1.83	18739 ± 182	0.86 ± 0.02	71 ± 18	116 ± 7	4 ± 0	0.217 ± 0.006	1.022 ± 0.007	1.646 ± 0.433
2.50	18739 ± 182	0.86 ± 0.02	84 ± 34	339 ± 16	7 ± 0	0.222 ± 0.006	0.997 ± 0.003	1.874 ± 0.760
	Muon Sample							
1.55	13737 ± 159	0.76 ± 0.02	50 ± 10	21 ± 1	6 ± 0	0.261 ± 0.008	0.982 ± 0.009	1.124 ± 0.236
1.59	13737 ± 159	0.76 ± 0.02	50 ± 11	24 ± 1	6 ± 0	0.256 ± 0.007	0.993 ± 0.008	1.170 ± 0.253
1.67	13737 ± 159	0.76 ± 0.02	56 ± 12	36 ± 2	7 ± 0	0.256 ± 0.007	1.012 ± 0.006	1.320 ± 0.285
1.75	13737 ± 159	0.76 ± 0.02	62 ± 14	59 ± 4	7 ± 0	0.254 ± 0.007	1.011 ± 0.006	1.471 ± 0.340
1.83	13737 ± 159	0.76 ± 0.02	59 ± 17	101 ± 7	8 ± 0	0.255 ± 0.007	1.016 ± 0.006	1.406 ± 0.411
2.50	13737 ± 159	0.76 ± 0.02	57 ± 32	290 ± 15	16 ± 1	0.252 ± 0.007	0.996 ± 0.002	1.348 ± 0.752

Table 7.7: Differential $b \to s\gamma$ branching fraction in bins of photon energy E_γ. Note that these numbers are normalized to the bin width and not to $100\,\mathrm{MeV}$ as in Fig. 7.8. The systematic error has been symmetrized.

Bin	$E_\gamma^{min}\,[\,\mathrm{GeV}]$	$E_\gamma^{max}\,[\,\mathrm{GeV}]$	$\Delta E_\gamma\,[\,\mathrm{GeV}]$	$\frac{\Delta\mathcal{B}}{\Delta E_\gamma}\,[\,\mathrm{GeV}^{-1}]$	σ_{stat}	σ_{syst}
1	1.897	2.000	0.103	-0.000072	0.000366	0.000092
2	2.000	2.094	0.094	+0.000590	0.000339	0.000273
3	2.094	2.181	0.087	+0.000600	0.000278	0.000195
4	2.181	2.261	0.080	+0.000528	0.000243	0.000122
5	2.261	2.298	0.037	+0.000218	0.000316	0.000077
6	2.298	2.333	0.035	+0.001160	0.000281	0.000156
7	2.333	2.366	0.033	+0.000812	0.000249	0.000096
8	2.366	2.397	0.031	+0.000895	0.000233	0.000103
9	2.397	2.427	0.030	+0.001020	0.000208	0.000103
10	2.427	2.454	0.027	+0.000824	0.000184	0.000090
11	2.454	2.480	0.026	+0.001080	0.000184	0.000107
12	2.480	2.503	0.023	+0.000763	0.000147	0.000080
13	2.503	2.525	0.022	+0.000286	0.000112	0.000041
14	2.525	2.545	0.020	+0.000168	0.000062	0.000031
15	2.545	2.563	0.018	+0.001090	0.000077	0.000070
16	2.563	2.579	0.016	+0.001290	0.000073	0.000085
17	2.579	2.593	0.014	+0.000019	0.000049	0.000007
18	2.593	2.606	0.013	+0.000033	0.000040	0.000008

Table 7.8: The results for the determination of $|V_{ub}|$ and summary of the relative uncertainties. The first part of the table shows the results obtained in the framework of Leibovich, Low, and Rothstein and the right-most column provides the results based on the full rate.

m_X Cut (GeV/c^2)	Units	1.55	1.59	1.67	1.75	1.83	2.50	2.50
$\|V_{ub}\|$	$[\times 10^{-3}]$	**4.31**	**4.26**	**4.43**	**4.29**	**4.32**	**3.68**	**3.84**
$\sigma(stat)$	%	7.9	8.1	7.7	8.9	9.9	18.2	18.2
$\sigma(det.)$	%	2.7	2.9	3.4	3.4	3.7	3.8	3.8
$\sigma(\text{bg model})$	%	1.0	1.0	1.0	1.3	1.1	3.8	3.8
$\sigma(\text{signal model})$	%	3.7	3.7	3.9	3.9	4.6	5.4	5.6
σ_{stat} $(b \to s\gamma)$	%	3.4	3.4	3.5	3.4	3.8	6.2	n/a
σ_{syst} $(b \to s\gamma)$	%	2.3	2.3	2.3	2.3	2.4	3.1	n/a
$\sigma_{exp}(\|V_{cb}\|)$	%	1.0	1.0	1.0	1.0	1.0	1.0	n/a
$\sigma(\alpha)$	%	1.0	1.0	1.0	1.0	1.0	1.0	n/a
$\sigma(\text{pert.})$	%	3.0	3.0	2.9	2.9	3.0	2.9	2.8
$\sigma(\text{nonpert.})$	%	6.3	6.0	5.4	5.0	4.5	2.4	3.9
$\sigma_{theo}(\|V_{cb}\|)$	%	1.7	1.7	1.7	1.7	1.7	1.7	n/a

Chapter 8

Systematic Uncertainties

This chapter discusses at length the systematic uncertainties associated with the extraction of $|V_{ub}|$. The first section describes the systematic uncertainties on the extraction of the partial rate $\delta\Gamma(c)$. The second section describes the errors from the $b \to s\gamma$ photon energy spectrum and their propagation to $|V_{ub}|$. The final section discusses the theoretical errors.

8.1 $\delta\Gamma(c)$ Systematics

Table 8.6 summarizes the systematic uncertainties on the measurement of $\delta\Gamma(c)$ discussed in this section, for various m_X cut-offs. Because $|V_{ub}| \propto \sqrt{\delta\Gamma(c)}$, the errors on $|V_{ub}|$ (see Table 7.8) are smaller by a factor of two.

8.1.1 B_{reco} Reconstruction

The semi-exclusive reconstruction is a possible source of uncertainty in the measurement of $\delta\Gamma(c)$. One possible source is a mismatch of data and MC in the composition of the B_{reco} sample. This effect can have an impact on the analysis in several ways. First of all, the individual decay modes, depending on the multiplicity, may have different resolution in the kinematic quantities so that a difference in the B_{reco} composition might also result in a different resolution. Similarly, the ratio of efficiencies $\epsilon_t^{sl}/\epsilon_t^u$ could be mode dependent and a data/MC composition mismatch could give a different ratio. Finally the cross-feed among the reconstructed modes and between B^0 and B^+ could be different in data and in Monte Carlo samples.

In order to minimize the impact of this effect the generic MC was used to model the data since

the cocktail MC reproduces only a few very clean modes, as previously described. The measured quantities have been compared for full generic and cocktail MC simulation and the observed differences have been found to be negligible.

Figure 8.1 shows the difference between data and generic MC for the integrated purity variable. The analysis was also repeated with a re-weighting that enforced an identical distribution of purity for the modes. The change in the result is less than 1%.

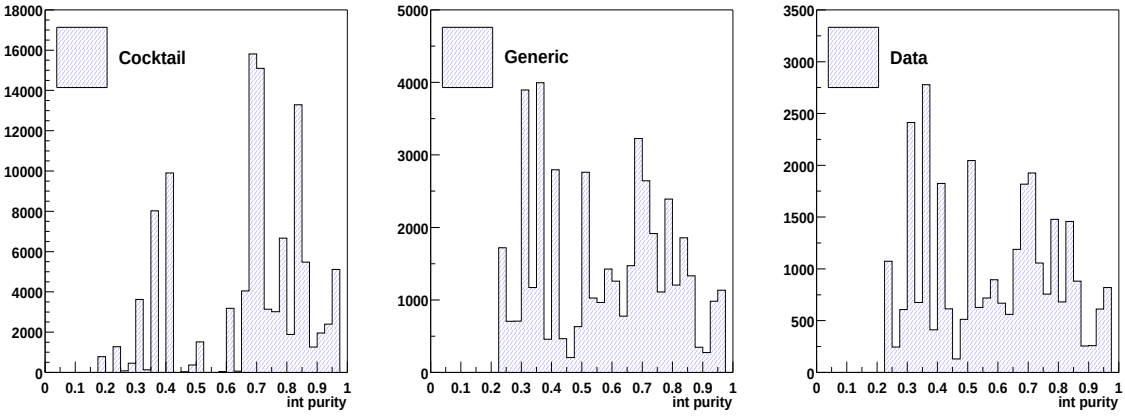

Figure 8.1: Integrated purity for cocktail MC (left), generic MC (middle) and data (right), as an indicator of the sample composition.

Another effect could be introduced by B^0-B^+ cross-feed. In Fig. 8.2 the fitted m_X shapes for the cross-feed events is shown. The fractions of these events corresponds to $3.0 \pm 0.6\%$ for B^+s and $1.8 \pm 0.5\%$ for B^0's. In order to determine the impact of this effect, the data events were fitted using a Monte Carlo model with and without cross-feed. The results are consistent.

Since all the effects are negligible, as expected, no systematic uncertainty is assigned to the B_{reco} composition.

8.1.2 Fit to the $m_{\rm ES}$ Distributions

The signal extraction uses a Crystal Ball function to model the signal shape. Alternatively, a Gaussian model was also used and the difference between the results is taken as a systematic error. Also, in the signal extraction, the $m_{\rm ES}$ fits are unbinned. Binning the fits was also explored and the difference in results is taken as a systematic error. Finally, the parameters that enter the $m_{\rm ES}$ fits were varied within their errors to measure the systematic uncertainty.

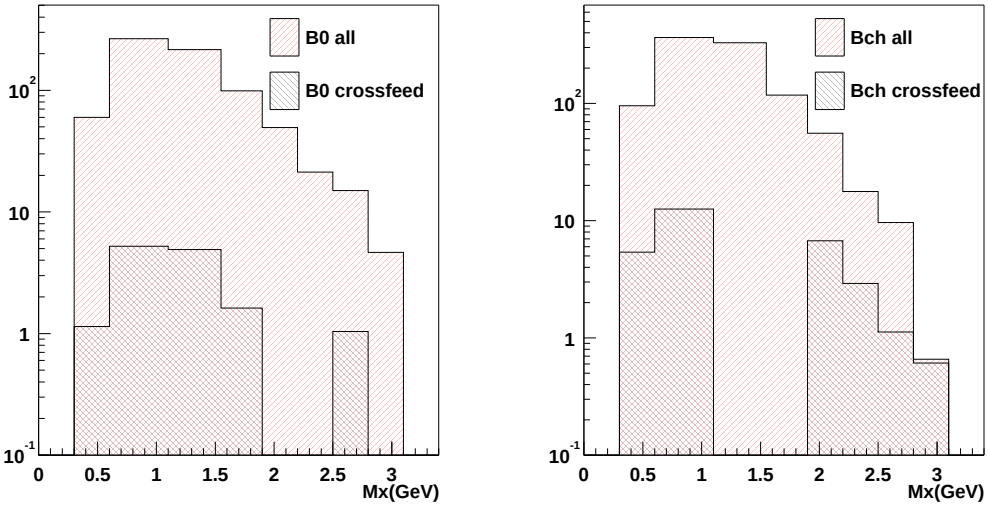

Figure 8.2: The $b \to c\ell\bar{\nu}\, m_X$ distribution (all cuts applied) for cross-feed events compared with the total sample. Left plot corresponds to B^0s, right to B^+ s.

8.1.3 Floating the Other Component

The signal extraction fixes the relative contribution of the other background distribution to that of the charm background. These are the factors $C_{c,o}$ in Eq. 7.3. The alternative method of letting this contribution float in the fit was explored and the difference in results taken as a systematic uncertainty.

8.1.4 B_{reco} Tagging Efficiency ($\epsilon_t^{sl}/\epsilon_t^u$)

The uncertainty on the ratio of B_{reco} tagging efficiencies $\epsilon_t^{sl}/\epsilon_t^u$ is estimated to be 3.0% (see section 7.1.4).

8.1.5 Binning of the m_X Distribution

The hadronic mass spectrum is binned in $300\,\mathrm{MeV}/c^2$ bins, approximately equivalent to the m_X resolution. The fit result varies based on choice of binning, so the binning was varied at $100\,\mathrm{MeV}/c^2$ intervals from $200\,\mathrm{MeV}/c^2$ to $600\,\mathrm{MeV}/c^2$ and the difference the extracted value of $\delta\Gamma(c)$ is taken as a systematic uncertainty.

8.1.6 Tracking

Differences in the tracking efficiency and track resolution can impact the m_X, m^2_{miss} and Q_{tot} distributions. In addition, there is a small fraction of tracks that are duplicated such that a single particle results in two measured tracks, and any differences between data and Monte Carlo simulation may lead to a distortion of the m_X distribution.

To study tracking efficiencies, control samples are used. For high momentum tracks, a control sample of high momentum tracks from $e^+e^- \rightarrow \tau^+\tau^-$ decays are used because of the high cross-section. The efficiencies from data and MC are found to be in good agreement. The difference is estimated at 1.3% per track. For low momentum tracks $D^{*+} \rightarrow D^0\pi^+$, $D^0 \rightarrow K^-\pi^+$ events are selected as a control sample. The pion in these decays are low momentum particles and are consequently used for the low momentum efficiency. The agreement of data/MC is good and a difference in efficiency of 0.9% per track is observed (see Fig. 8.3).

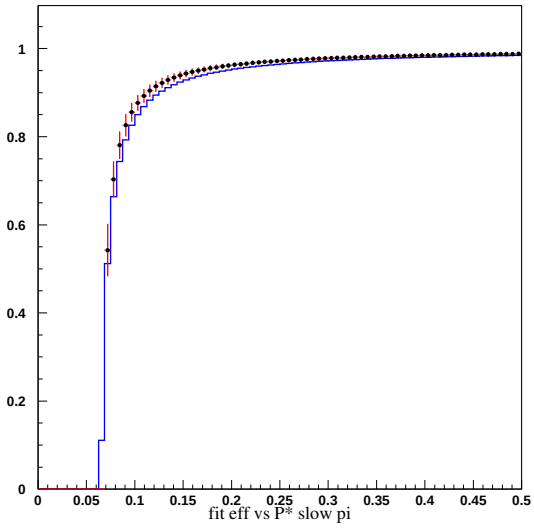

Figure 8.3: Relative efficiency for Monte Carlo (histogram) and for data (dots) for the soft pions from $D^{*+} \rightarrow D^0\pi^+$, $D^0 \rightarrow K^-\pi^+$ decays, as a function of the momentum.

In general, the tracking efficiencies are modeled well in the MC and found to be in good agreement with data, as shown in our data/MC comparison from Fig. 6.25, and no efficiency corrections need to be applied.

To estimate the systematic error from the tracking, tracks are randomly removed from the recoil

B meson with a probability of 1.3% for $p_\perp > 200\,\mathrm{MeV}/c$ and a probability of 2.5% if $p_\perp < 200\,\mathrm{MeV}/c$. The resulting shift in the value of $\delta\Gamma(c)$ is taken as a systematic error.

8.1.7 Lepton Identification

As described in section 4.2, lepton identification efficiencies and misidentification probabilities are derived from control samples. For electron efficiency, radiative Bhabha events are used. For pions, the decay products of $K^0_S \to \pi^+\pi^-$ are used. Muons with a momentum spectrum covering the range of interest are extracted from the $e^+e^- \to \mu^+\mu^-\gamma$ channel and $e^+e^- \to e^+e^-\mu^+\mu^-$ channel.

The results from data are shown in Fig. 4.3 (electrons) and 4.4 (muons). The statistical and systematic errors from the data/MC comparison are used to compute the systematic uncertainties. For the efficiency, each bin in momentum and polar angle is shifted by $\pm 2\%$ for electrons and $\pm 3\%$ for muons. For the misidentification probability, each bin in momentum and polar angle is shifted by $\pm 15\%$. The difference in the fitted $\delta\Gamma(c)$ is taken as a systematic uncertainty.

8.1.8 Charged Kaon Identification

The systematics uncertainties from kaon identification efficiency and misidentification probabilities are obtained with the same technique used for lepton identification. A control sample of kaons and pions is obtained taking kaons from the process $D^* \to D^0\pi$, $D^0 \to K\pi$. The results for the efficiency and misidentification probabilities are shown in Fig. 4.5.

For the efficiency, each bin in momentum and polar angle is shifted by $\pm 2\%$. For the misidentification probability, each bin in momentum and polar angle is shifted by $\pm 15\%$. The difference in the fitted $\delta\Gamma(c)$ is taken as a systematic uncertainty.

8.1.9 Neutral Reconstruction

Differences between data and MC simulation in the photon detection efficiency and resolution, as well as additional energy depositions in the EMC, can impact the m_X and m^2_{miss} distributions.

Control samples are used to study the efficiency and resolution. The efficiency study is performed with hadronic τ decays that represent an abundant source of π^0s. $e^+e^- \to \tau^+\tau^-$ events are selected by identifying the decay $\tau \to e\nu\bar{\nu}$. The recoiling τ is then studied. The ratio $R = N(\tau \to h^\pm\pi^0)/N(\tau \to h^\pm\pi^0\pi^0)$ is computed both for data and MC as a function of the

π^0 energy in order to evaluate possible differences in efficiency. The agreement has been found to be good and the ratio is compatible with the unity over the full range. This is reflected in the good data/MC agreement seen in Fig. 6.25.

The resolution has been studied by examining π^0s from both $\tau \rightarrow h^{\pm}\pi^0$ and $\tau \rightarrow h^{\pm}\pi^0\pi^0$ decays. The π^0 mass is fitted in energy bins and the resolution (σ using a Gaussian fit) is then compared for data and MC. The MC resolution is found to have some modest disagreement with data, and a smearing factor is applied to improve the level of agreement between data and MC. The resulting smearing factors are shown in Table 8.1.

Table 8.1: Smearing factor in different neutral energy bins.

Energy range	Smearing factor
30–100 MeV	3%
100–300 MeV	2.6%
300–600 MeV	1.6%
>600 MeV	0%

To estimate the systematic uncertainty for the neutral resolution, the smearing is turned off and the resulting shift in $\delta\Gamma(c)$ is taken as a systematic uncertainty. The systematic uncertainty for the neutral efficiency is estimated by randomly removing 2.5% of neutrals from the recoil calculation and the resulting shift in $\delta\Gamma(c)$ is also taken as a systematic error.

8.1.10 K_L^0 Reconstruction

Although we do not perform K_L^0 identification since the calorimeter and IFR information do not allow for it with a sufficient purity, a possible systematic effect exists from the proper detection of the neutral energy deposited in the EMC. For the most part, the neutral selection eliminates neutral clusters from K_L^0 interactions. To assess the systematic error, all neutrals resulting from a K_L^0 are removed from the reconstruction of the hadronic X system and the resulting difference in the extracted result is taken as the uncertainty.

8.1.11 Semileptonic B Branching Fractions

The exclusive semileptonic branching fractions for $B \rightarrow X_c\ell\nu$ decays and the corresponding hadronic mass spectrum is crucial for the determination of the $b \rightarrow c$ background. Two systematic effects are considered:

- The individual branching fractions in the Monte Carlo simulations are known to differ from the current world averages [6]. This difference is corrected by re-weighting all events to match the world averages (see Table 8.2). Here D^{**} refers to either non-resonant or broad D^{**} states and the corresponding branching fraction is taken as the difference between the total semileptonic rate and the other measured branching fractions.
- The uncertainties in the measured branching fractions and the decay model introduce systematic errors. This effect has been estimated by determining $\delta\Gamma(c)$ for branching fractions that are varied within one standard deviation around the current measured value. The spread in the $\delta\Gamma(c)$ results from the full fit based on the variation of these branching fractions is taken as the systematic error.

Table 8.2: The current best measurements for the branching fractions for $B \to X_c \ell \nu$ decays and values used in MC simulation. The non resonant $B \to Dl\nu X$ is obtained by difference of the inclusive rate and the other 4 components.

B Decay mode	best measurement (%)	MC (%)
$B^0 \to D^- l\nu$	2.07 $\pm$0.15[6]	2.10
$B^0 \to D^{*-} l\nu$	5.70+0.53−1.02 [6]	5.6
$B^0 \to D_1^- l\nu$	0.52$\pm$0.15[75]	0.56
$B^0 \to D_2^{*-} l\nu$	0.23$\pm$0.23 [75]	0.37
$B^0 \to X_c l\nu$	10.21$\pm$0.17 [6]	10.4
$B^+ \to D^0 l\nu$	2.24$\pm$0.16[6]	2.10
$B^+ \to D^{*0} l\nu$	6.17 + 0.83 − 1.13 [6]	5.60
$B^+ \to D_1^0 l\nu$	0.56$\pm$0.16[75]	0.56
$B^+ \to D_2^{*0} l\nu$	0.30$\pm$ 0.30 [75]	0.37
$B^+ \to X_c l\nu$	11.04$\pm$0.18 [6]	10.4

8.1.12 $B \to D^* l\nu$ Form Factors

Another source of uncertainty in our modeling of the charm background is the uncertainty in the knowledge of the form factors that describe the $B \to D^* l\nu$ decays. As previously mentioned in section 6.2.2, the generic MC is reweighted to use the *BABAR* measured form factors [72]. To study the uncertainty, the three form factors, $R1$, $R2$ and ρ^2, are each varied $\pm 1\sigma$. We observe a small difference in our result based on the form factor parameters and take this as a systematic uncertainty.

8.1.13 Charm Decay Branching Fractions

Analogous to the semileptonic B branching fractions, the branching fractions and decay models for hadronic and semileptonic charm decays will affect the measurement. This effect will be different for neutral and charged Bs since B^0 decay mostly into charged Ds while $B^{\pm}$ decay mostly into D^0.

Tables 8.3 and 8.4 list the $D^{\pm}$ and D^0 (respectively) current average measurements for the exclusive and inclusive branching fractions and the values used in the MC simulation. The most important decay modes are the ones involving neutral and charged kaons. Charm baryon and D_s decay modes are not included. The same reweighting procedure as for semileptonic B decays in section 8.1.11 has been followed to adjust the charm branching fractions used in the MC simulation to the current best measurements.

The uncertainty in the inclusive D branching fractions is considered separately. They are particularly relevant because they affect the amount of K_L and K^+ in the sample. Similar to the semileptonic B branching fractions, the values of the branching fractions are varied within their errors and the spread in the fit results for $\delta\Gamma(c)$ is taken as a systematic uncertainty.

8.1.14 Signal Model and Parameterization

The extraction of $\delta\Gamma(c)$ is dependent on the underlying model used for the signal MC. The default choice, as previously mentioned in section 6.2.2, is the exponential model of de Fazio and Neubert [67] (see Eq. 6.2). Also explored is a Gaussian [76] model whose form is

$$F(k_+) = N(1-x)^a e^{-b^2(1+x)^2}; \quad b = \Gamma(\frac{a+2}{2})/\Gamma(\frac{a+1}{2}), \tag{8.1}$$

and the Roman model [36] whose form is

$$F(k_+) = N\frac{\kappa}{\pi} e^{-\frac{1}{4}(\frac{a}{\kappa(1-x)} - \kappa(1-x))^2}; \quad \kappa = \frac{a}{\pi} e^{\frac{a}{2}} K_1(a/2) \tag{8.2}$$

where K_1 is a modified Bessel function of the first kind. The differences between the models is taken as a systematic uncertainty. Table 8.5 contains results for the extracted value of $\delta\Gamma(c)$ using these alternate models for the same nominal central value of the shape function parameters as is used in the exponential model described in 6.2.2.

Table 8.3: D^+ branching fractions, current best measurements and values used in the MC.

	$\mathcal{B}R$	
D^+ Decay mode	PDG	MC
$D^+ \to K^+X$	0.275 ± 0.024	0.34
$D^+ \to K^0X$	0.61 ± 0.08	0.62
$D^+ \to K^0\pi$	0.0271±0.0020	0.0294
$D^+ \to K\pi\pi$	0.088 ±0.006	0.0896
$D^+ \to K^0\pi\pi^0$	0.098 ±0.030	0.107
$D^+ \to K\pi\pi\pi^0$	0.063 ±0.010	0.0658
$D^+ \to K^0\pi\pi\pi$	0.069 ±0.009	0.0784
$D^+ \to K\pi\pi\pi\pi$	0.0071±0.0010	0.0127
$D^+ \to K\pi\pi\pi^0\pi^0$	0.020 ±0.007	0.0053
$D^+ \to K^0\pi\pi\pi\pi^0$	0.054 ±0.030	0.0551
$D^+ \to K^0\pi\pi\pi\pi\pi$	0.0008±0.0007	0.0008
$D^+ \to K\pi\pi\pi\pi\pi^0$	0.0020±0.0018	0.0043
$D^+ \to K^0K^0K$	0.018 ±0.008	0.0187
$D^+ \to \pi\pi^0$	0.0025±0.0007	0.0024
$D^+ \to \pi\pi\pi$	0.0030±0.00045	0.0048
$D^+ \to \pi\pi\pi\pi^0$	0.019 ±0.015	0.0227
$D^+ \to \pi\pi\pi\pi\pi$	0.002±0.0004	0.0006
$D^+ \to \pi\pi\pi\pi\pi\pi^0$	0.0029±0.0029	0.0009
$D^+ \to \mu\nu$	0.0008±0.0017	0.0038
$D^+ \to K^0l\nu$	0.068 ±0.008	0.1334
$D^+ \to K\pi l\nu$	0.085±0.0096	0.0644
$D^+ \to K^0\pi\pi l\nu$	<0.009	0.0003
$D^+ \to K\pi\pi^0 l\nu$	<0.0017	0.0054
$D^+ \to \pi^0 l\nu$	0.0031±0.0015	0.0099

8.1.15 Fermi Motion

Along with being dependent on the model, the extraction of $\delta\Gamma(c)$ is dependent on the choices for the model parameters used in the signal MC. To estimate this uncertainty, the parameters of the Fermi motion model, m_b and a, are varied within the $\Delta\chi^2 = 1$ error ellipse [69] in our signal model. Table 8.5 displays the results for this study. The systematic error is conservatively determined as half of the full difference between the largest and smallest deviation with respect to the nominal value.

Table 8.4: D^0 branching fractions, current best measurements and values used in the MC.

	$\mathcal{B}R$	
D^0 Decay mode	PDG	MC
$D^0 \to K^+X$	0.53 ± 0.04	0.54
$D^0 \to K^0X$	0.42 ± 0.05	0.39
$D^0 \to K\pi$	0.0380±0.0009	0.0387
$D^0 \to K^0\pi^0$	0.0230±0.0022	0.0210
$D^0 \to K^0\pi\pi$	0.0597±0.0035	0.0552
$D^0 \to K\pi\pi^0$	0.130 ±0.008	0.1380
$D^0 \to K^0\pi^0\pi^0$	0.0178±0.0026	0.0164
$D^0 \to K\pi\pi\pi$	0.0746±0.0031	0.0897
$D^0 \to K^0\pi\pi\pi^0$	0.109 ±0.013	0.0976
$D^0 \to K\pi\pi^0\pi^0$	0.15 ±0.05	0.0844
$D^0 \to K\pi\pi\pi\pi^0$	0.040 ±0.004	0.0435
$D^0 \to \pi\pi$	0.00143±0.00007	0.0015
$D^0 \to \pi^0\pi^0$	0.00084±0.00022	0.00083
$D^0 \to \pi\pi\pi^0$	0.011 ±0.004	0.0257
$D^0 \to \pi\pi\pi\pi$	0.0073±0.0005	0.00725
$D^0 \to \pi\pi\pi\pi\pi^0$	0.019 ±0.004	0.0177
$D^0 \to \pi\pi\pi\pi\pi\pi$	0.0004±0.0003	0.0004
$D^0 \to Kl\nu$	0.0343±0.0014	0.0670
$D^0 \to K\pi^0l\nu$	0.011 ±0.007	0.0133
$D^0 \to K^0\pi l\nu$	0.018 ±0.008	0.0260
$D^0 \to K\pi\pi l\nu$	<0.0012	0.0015
$D^0 \to \pi l\nu$	0.0036±0.0006	0.0000

8.1.16 Modeling of $\overline{B} \to X_u\ell\bar{\nu}$ Decays

As previously stated, the efficiencies are obtained from our signal MC sample. The contributions to the exclusive modes that make up our hybrid signal MC are varied conservatively within known errors and the differences in $\delta\Gamma(c)$ are taken as systematic uncertainties. Also, the inclusive $\overline{B} \to X_u\ell\bar{\nu}$ branching fraction assumed in the hybrid signal MC is varied and the difference is also taken as a systematic uncertainty. Table 8.5 summarizes the results of the study on the exclusive modes. The systematic error is determined by adding the error from each of the individual modes in quadrature. The error on an individual mode is obtained by averaging the magnitude of the difference of each the positive and negative variation from the default value of $\delta\Gamma(c)$.

8.1.17 Hadronization Uncertainties

The fragmentation of light quarks in the non-resonant MC generator is handled by `Jetset 7.4`, whereas the resonant MC is implemented in terms of ISGW2. To estimate the systematic uncertainty, the fits to extract $\delta\Gamma(c)$ are performed with the pure-nonresonant MC for the signal MC. The full difference of this result with respect to the default result with the hybrid signal MC is taken as the systematic error for the uncertainties in the hadronization model. See Table 8.5 for the results.

Table 8.5: $\delta\Gamma(c) \times 10^3$ results and errors for various m_X cuts for the signal modeling studies in sections 8.1.14–8.1.17. The error is determined from the largest deviations to the nominal value.

m_X cut-off (GeV/c^2) :	1.55	1.59	1.67	1.75	1.83	2.50
	$\delta\Gamma(c) \times 10^3$					
Nominal, $(m_b, a) = (4.79, 1.96)$	1.154	1.199	1.426	1.442	1.580	1.585
Roman SF	1.160	1.211	1.439	1.456	1.586	1.601
Gaussian SF	1.168	1.219	1.449	1.468	1.599	1.622
$(m_b, a) = (4.69649, 1.43862)$	1.239	1.288	1.543	1.564	1.743	1.780
$(m_b, a) = (4.85544, 2.49430)$	1.096	1.138	1.344	1.359	1.474	1.449
$(m_b, a) = (4.80151, 1.65665)$	1.142	1.186	1.408	1.424	1.560	1.558
$(m_b, a) = (4.78365, 2.25499)$	1.163	1.211	1.441	1.458	1.598	1.611
$(m_b, a) = (4.76026, 1.45243)$	1.178	1.224	1.458	1.475	1.627	1.640
$(m_b, a) = (4.74458, 1.90944)$	1.200	1.248	1.490	1.509	1.666	1.694
$(m_b, a) = (4.82514, 1.80233)$	1.122	1.165	1.380	1.395	1.522	1.510
$(m_b, a) = (4.81757, 2.47456)$	1.132	1.178	1.396	1.411	1.539	1.533
Error [%]	6.2	6.3	7.0	7.1	8.5	10.4
$\pi(-30\%)$	1.167	1.213	1.442	1.457	1.596	1.593
$\pi(+30\%)$	1.141	1.186	1.410	1.428	1.566	1.576
$\rho(-30\%)$	1.167	1.213	1.441	1.459	1.598	1.605
$\rho(+30\%)$	1.141	1.186	1.411	1.426	1.563	1.565
$\omega(-40\%)$	1.149	1.194	1.418	1.435	1.572	1.576
$\omega(+40\%)$	1.166	1.213	1.441	1.457	1.597	1.600
$\eta, \eta'(-100\%)$	1.142	1.187	1.411	1.430	1.566	1.582
$\eta, \eta'(+100\%)$	1.161	1.206	1.434	1.447	1.585	1.574
Error [%]	1.9	1.9	1.9	1.8	1.7	1.5
Non-Resonant	1.181	1.223	1.446	1.459	1.593	1.570
Error [%]	2.3	2.0	1.4	1.2	0.8	0.9

8.1.18 $s\overline{s}$ Popping

Our signal MC contains $s\overline{s}$ popping events (i.e. decays of the heavy X_u states into $K\overline{K}$ pairs) both in the resonant and the non-resonant contributions. In the hybrid model the fractions of $s\overline{s}$ popping events for B^+ (B^0) are 10.7% (0.1%) for the resonant component and 12.0% (11.3%) for the non-resonant one. The resonant contribution is almost entirely due to the $f_1^{'}$ and $h_1^{'}$ decays that produce only $K\overline{K}$ pairs. The non-resonant contribution is modeled using `Jetset 7.4`. The $s\overline{s}$ popping parameter in jetset74 is also known as γ_s and it is set to $\gamma_s = 0.30$ in our MC. This parameter has been measured by two experiments at center of mass energies between 12 and 36 GeV as $\gamma_s = 0.35 \pm 0.05$[77], $\gamma_s = 0.27 \pm 0.06$[78]. Reference [78] shows how the scaling to lower energies (to 3 GeV, equivalent to the energies involved in the X_u decays for $m_X < m_D$) works fine compared to reference [79].

In order to calculate the systematic uncertainty we varied the fraction of $s\overline{s}$ popping events by $\pm 100\%$ for the resonant contribution and by $\pm 30\%$ for the non-resonant one (taking as 1 σ interval the sum of the intervals from the two experiment).

8.1.19 Monte Carlo Statistics

The finite available MC statistics affects the measurement in that it introduces an uncertainty in the shape of the background model. In order to separate this uncertainty from the purely statistical one, the measurement is repeated setting this term to zero. The statistical error obtained in this way is considered as statistical error (although the quoted central value is the one obtained with the default fit) and the difference in quadrature between the errors obtained with this fit and the default one is assigned to the systematic error as "MC statistics".

8.1.20 Stability Checks

The stability of the extracted partial hadronic $\overline{B} \to X_u \ell \bar{\nu}$ rate, $\delta\Gamma(c)$, has been tested by varying various event selection criteria. Clearly, one cannot expect the partial rate to stay stable as the hadronic mass cut is varied because more of the total rate will be captured. Thus, to examine the stability, we observe the total ratio of branching fractions, R_u, instead of the partial rate. The following selection criteria are examined:

- m_X **cut**: The B^0 scan shows a slope as a function of the m_X cut as seen in Fig. 8.4. The B^+ scan is very stable which is also seen in Fig. 8.4.

- m^2_{miss} **cut**: the results are stable, as seen in Fig. 8.5, over a large range in the cut ($0.9 > m^2_{miss} > 0.1\,(\,\mathrm{GeV}/c^2)^2$). This implies that the background shape is well estimated in this interval since the signal over background ratio varies widely. Plots show some disagreement when the cut becomes very tight ($m^2_{miss} < 0.1\,(\,\mathrm{GeV}/c^2)^2$). In this region the result is dominated by the uncertainties in the m^2_{miss} resolution and the systematic effects are very large. Also, there is some disagreement when the cut becomes large. In this region, there is an overwhelming amount of background because m^2_{miss} is a very powerful one for discriminating signal and background. Hence, the fit result has very large systematic uncertainties associated.

- **lepton momentum cut**: the result is very stable below $1.5\,\mathrm{GeV}/c$. For $p^* > 1.5\,\mathrm{GeV}/c$ the result tends to shift to small values (Fig. 8.6). This effect is due to a lower fraction of signal events close to the $b \to c\ell\bar{\nu}$ endpoint. It cannot be explained as an underestimation of the background contribution, since the subtracted shape does not match the background one. Since the cut on p^* is quite loose for this analysis, the result is not affected by this discrepancy (the dependency is quite flat around the cut region).

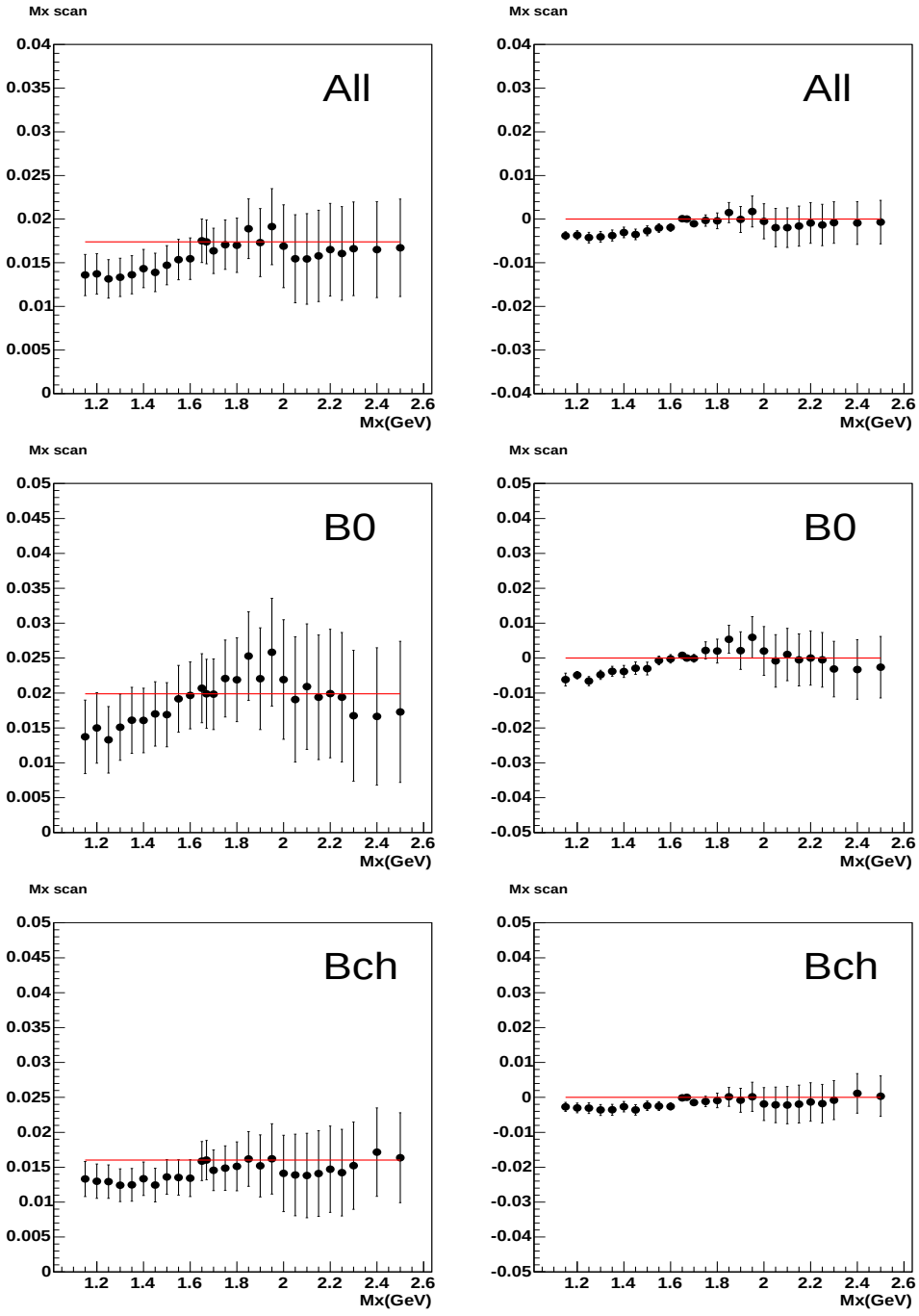

Figure 8.4: Measurement of $R_{u/sl}$ as a function of the m_X cut applied. The left column displays the results with correlated errors. The right column shows the difference to the default analysis working point with uncorrelated errors shown. The errors are statistical only.

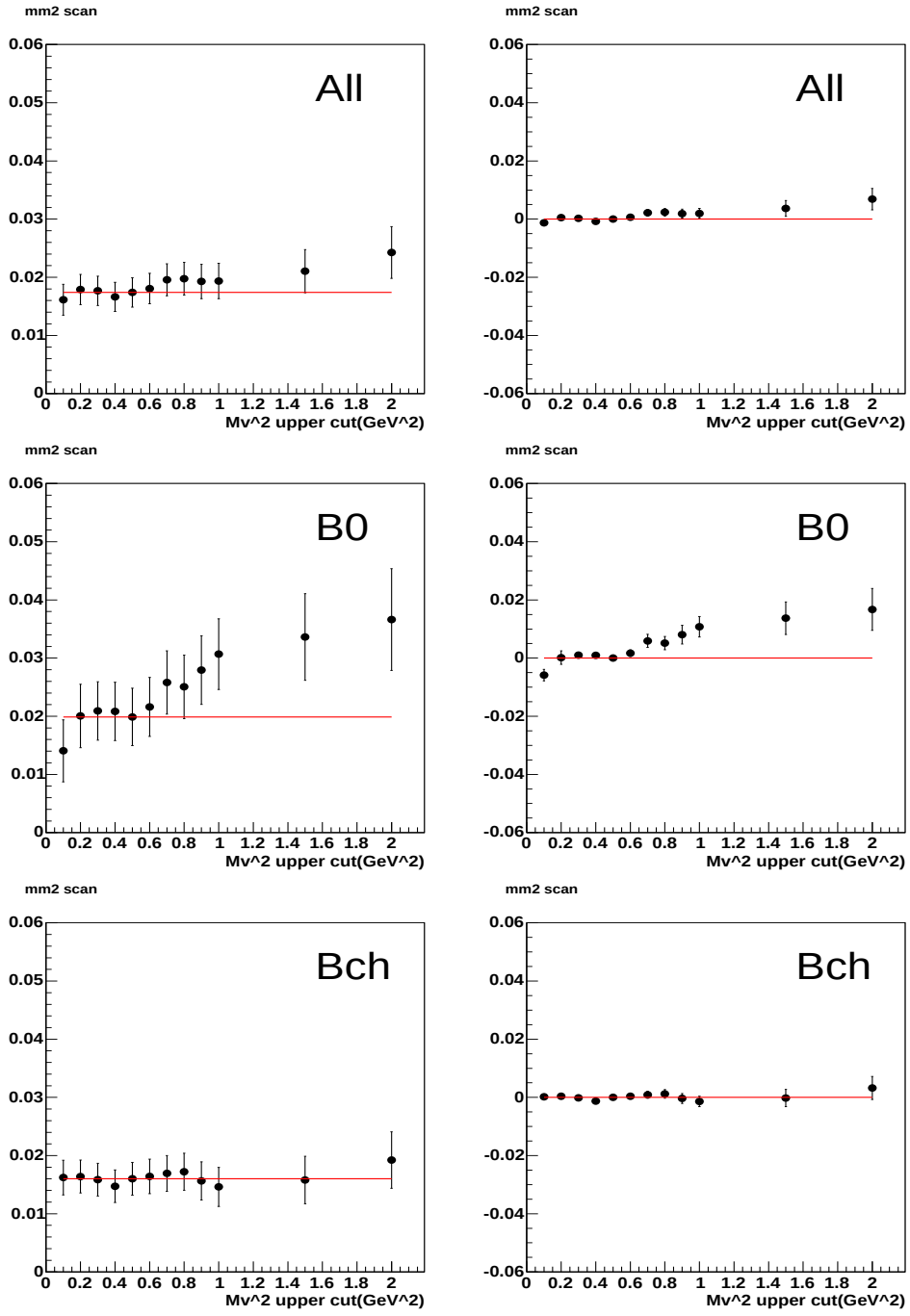

Figure 8.5: Measurement of $R_{u/sl}$ as a function of the m^2_{miss} cut applied. The left column displays the results with correlated errors. The right column shows the difference to the default analysis working point with uncorrelated errors shown. The errors are statistical only.

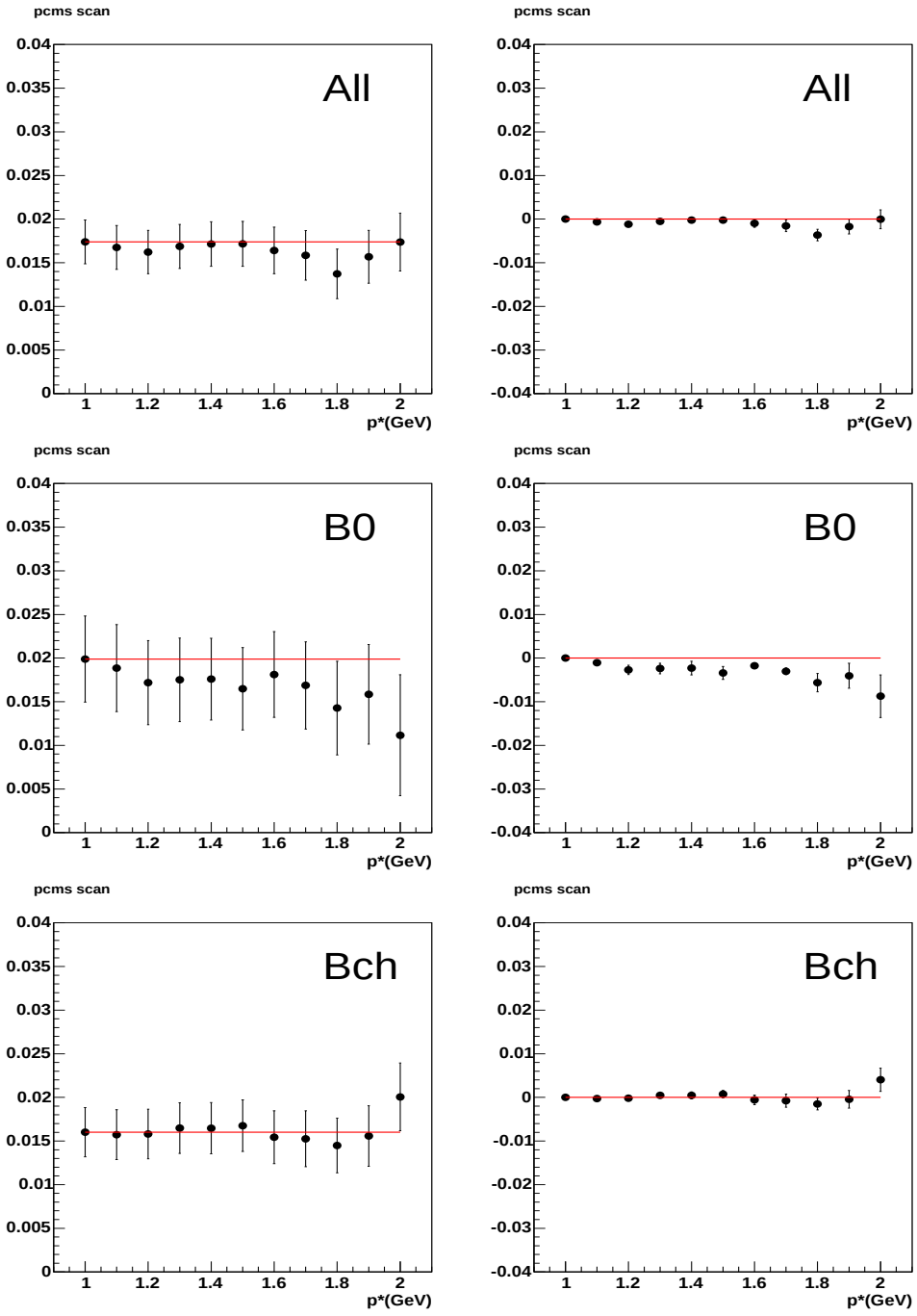

Figure 8.6: Measurement of $R_{u/sl}$ as a function the cut on the lepton momentum applied. The left column displays the results with correlated errors. The right column shows the difference to the default analysis working point with uncorrelated errors shown. The errors are statistical only.

Table 8.6: Summary of errors on the partial $b \to u\ell\bar{\nu}$ rate $\delta\Gamma(c)$. The errors are listed in units of % of $\delta\Gamma(c)$.

Source	$1.55\,\mathrm{GeV}/c^2$	$1.59\,\mathrm{GeV}/c^2$	$1.67\,\mathrm{GeV}/c^2$	$1.75\,\mathrm{GeV}/c^2$	$1.83\,\mathrm{GeV}/c^2$	$2.50\,\mathrm{GeV}/c^2$
Data Statistics	15.1	15.4	14.6	16.7	18.5	33.5
MC Statistics	4.5	5.2	5.2	6.2	7.2	14.2
Total Statistics	**15.8**	**16.2**	**15.5**	**17.8**	**19.9**	**36.4**
Electron ID	1.0	1.0	1.0	1.0	1.0	1.0
Muon ID	1.0	1.0	1.0	1.0	1.0	1.0
$K^{\pm}$ ID	1.5	1.5	1.5	1.5	1.5	1.5
Tracking Efficiency	1.1	1.1	1.4	1.5	3.7	1.0
Neutral Efficiency	1.1	1.1	1.1	1.1	2.1	3.1
Neutral Resolution	1.1	1.1	1.1	1.1	1.1	2.1
K_L interactions	1.0	1.5	1.8	2.1	1.9	0.8
m_{ES} fits	2.5	2.5	4.4	3.8	4.1	4.7
Other Bkgd Component	2.0	2.7	1.6	1.5	0.8	0.7
m_X binning	1.0	1.0	1.4	2.6	1.0	2.4
$\varepsilon_t^{sl}/\varepsilon_t^u$	3.0	3.0	3.0	3.0	3.0	3.0
Total Experimental	**5.4**	**5.8**	**6.7**	**6.8**	**7.4**	**7.6**
$B \to D^{(*,**)} l\bar{\nu} X$ branching fractions	0.9	0.9	1.4	2.4	2.1	7.5
$B \to D^* l\bar{\nu}$ form factors	0.4	0.5	0.6	0.7	0.8	0.6
D branching fractions	0.4	0.4	0.4	0.5	0.6	0.6
Total background modeling	**1.0**	**1.0**	**1.5**	**2.5**	**2.2**	**7.5**
Excl. $b \to u\ell\bar{\nu}$ branching fractions	1.9	1.9	1.9	1.8	1.7	1.5
Incl. $b \to u\ell\bar{\nu}$ branching fraction	1.0	1.0	1.0	1.0	1.0	1.0
Hadronization error	2.3	2.0	1.4	1.2	0.8	0.9
$s\bar{s}$ popping	2.6	2.6	2.6	2.5	2.5	2.5
Fermi motion	6.2	6.3	7.0	7.1	8.5	10.4
Total signal modeling	**7.4**	**7.4**	**7.9**	**7.9**	**9.1**	**10.9**

8.2 Statistical and Systematic Uncertainties from the $b \to s\gamma$ Photon Energy Spectrum

We consider three different uncertainties from the $b \to s\gamma$ spectrum affecting the determination of $|V_{ub}|$: (1) statistical errors not correlated among different E_γ bins, (2) systematic errors not correlated among different E_γ bins, and (3) correlated systematic errors. The uncorrelated errors are dominated by statistical uncertainties and the estimation of the missing fraction. In the region of interest, i.e., for $c < 0.21$ the photon spectrum is restricted to $E_\gamma > 2.2\,\mathrm{GeV}$, the statistical error is (substantially) larger than the systematic error. The correlated errors arise from (for example) uncertainties in B counting, etc.

We determine the uncorrelated error on $|V_{ub}|$ from the $b \to s\gamma$ spectrum by generating 100 toy spectra, where the central value in each bin has been varied according to a Gaussian distribution with a width given by the statistical and systematic error, respectively, of the bin (see Table 7.7). The results are illustrated in Fig. 8.7 and amount to an error of $\Delta(|V_{ub}|)/|V_{ub}| = 4.1\%$ for the analysis with $m_X < 1.67\,\mathrm{GeV}$. This error depends on c, the upper cut on the m_X spectrum: The higher the m_X cut, the lower the photon energy spectrum is sampled, where its statistical error is huge. This is the reason why this error component increases with increasing m_X-cut (see Table 7.8).

The effect of the correlated systematic error of 3.1%, arising from B counting and the initial photon selection [69], correlated among all bins of the $b \to s\gamma$ photon spectrum results in a total error of $\Delta(|V_{ub}|)/|V_{ub}| = 1.6\%$.

8.3 Theoretical Uncertainties on the Extraction of $|V_{ub}|$

We consider as theoretical uncertainties the scale uncertainty of α, higher-order terms of the perturbative expansion, and non-perturbative effects (e.g. from power corrections). The estimation of the non-perturbative error is based on the prescription by Leibovich, Low, and Rothstein in reference [39]. We study the uncertainties of neglecting higher-order terms by varying the relevant scales within reasonable and common ranges. For this study, we use an equation obtained from Leibovich and Rothstein [80] that explicitly spells out the different scales and allows the proper variation, in particular of the renormalization scale μ:

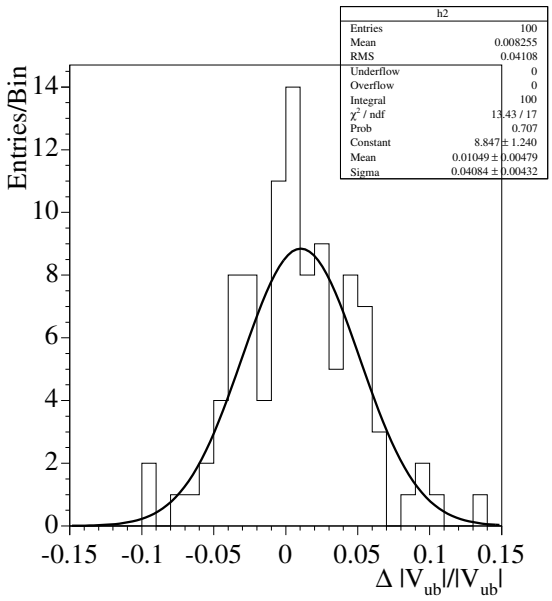

Figure 8.7: Relative error estimation for $|V_{ub}|$ due to the combined statistical and systematic error in the $b \to s\gamma$ photon energy spectrum.

$$\frac{|V_{ub}|}{|V_{ts}|} = \left\{ \frac{6\,\alpha(\mu_{QED}) \times [1 + H^{\gamma}_{mix}(\mu_b)] \times [C_7(\mu_b)^2 - f(\mu, m_b, C^0_i(m_W))]\,\delta\Gamma(c)}{\pi[I_0(c, \alpha_S(\mu)) + I_+(c, \alpha_S(\mu))]} \right\}^{\frac{1}{2}}, \quad (8.3)$$

$$f(\mu, m_b, C^0_i(m_W)) = \alpha_S(\mu_b)\beta_0 \log\left(\frac{\mu}{m_b}\right)\left[\frac{8}{23\pi}C^0_7(m_W) - \frac{8}{69\pi}C^0_8(m_W) + 0.053C^0_2(m_W)\right]. \quad (8.4)$$

8.3.1 Scale Uncertainty of α

In the calculation of the Wilson coefficients, entering in the calculation of H^{γ}_{mix} and $C_7(m_b)^2$, QED corrections have not been included. It is therefore not clear whether the electromagnetic coupling constant α should be renormalized at $\mu \sim m_b$ or at $\mu \sim m_W$. We follow the prescription in reference [47]. We allow α to vary between $\alpha(m_b)$ and $\alpha(m_W)$, i.e. $\alpha^{-1} = 130.3 \pm 2.3$. The resulting uncertainty on $|V_{ub}|$ is small ($< 1\%$) and independent of the cut c.

8.3.2 Perturbative Error

The calculation of Leibovich, Low, and Rothstein is at order α_S and does not include higher order terms (BLM terms, as an estimate of α_S^2 corrections, are also not included). The dominant perturbative error therefore comes from neglecting terms of order α_S^2. An estimate of the size of the subleading corrections is obtained by varying the renormalization scale μ from $\mu = m_b/2$ to $\mu = 2m_b$. In the master formula the default is at $\mu = m_b$. The choice to vary the renormalization scale in this range is conventional, but a conservative approach. Equation 8.3 explicitly spells out which scale is relevant in the computation of the Wilson coefficients and the strong coupling constant $\alpha_S = \alpha_S(\mu)$. It is via the strong coupling constant that the weighted integrals are subject to the variation. The asymmetric variation of the renormalization scale leads to an asymmetric error, which we quote in a symmetrized (linearly) form in Table 7.8.

8.3.3 Non-perturbative Error

The non-perturbative error covers (the absence of) higher-order terms in the $1/m_B$ expansion, power corrections (or their absence), etc. We estimate this uncertainty with the formula

$$\Delta(|V_{ub}|^2)/|V_{ub}|^2 \sim \Lambda^2/cm_b^2, \tag{8.5}$$

where $\Lambda \sim 500\,\mathrm{MeV}$, as provided in reference [39]. The resulting error on $|V_{ub}|$ is half of this uncertainty and given in Table 7.8. There is a strong dependence on the cut c, the prime reason why the m_X spectrum has to be measured to higher values in this analysis than before [81].

The error due to the uncertainty of the b quark mass $m_b = 4.79 \pm 0.2\,\mathrm{GeV}$ is found to be negligible.

Chapter 9

Conclusions

Two new methods to determine $|V_{ub}|$ are presented in this dissertation with substantially smaller theoretical errors than previously achieved. The results are summarized in Table 7.8. In the first method, based on the calculations of Leibovich, Low, and Rothstein, the cut-integrated hadronic mass spectrum (partial rate) and the weighted photon energy spectrum from $b \to s\gamma$ decays are used to avoid any explicit dependence on structure functions. At the default working point, $|V_{ub}|$ is determined from the cut-integrated hadronic mass spectrum for $m_X < 1.67\,\mathrm{GeV}/c^2$. This point was chosen to optimize the total error on $|V_{ub}|$. The result is

$$\begin{aligned} |V_{ub}| &= (4.43 \pm 0.34^{stat}_{\delta\Gamma(c)} \pm 0.15^{syst}_{\delta\Gamma(c)} \pm 0.04_{b2c} \pm 0.17_{b2u} \\ &\quad \pm 0.16^{stat}_{bsg} \pm 0.10^{syst}_{bsg} \pm 0.04^{exp}_{|V_{cb}|} \pm 0.29_{theo}) \times 10^{-3} \qquad (9.1) \\ &= (4.43 \pm 0.38_{stat} \pm 0.25_{syst} \pm 0.29_{theo}) \times 10^{-3} \qquad (9.2) \end{aligned}$$

where the first line of 9.1 are the errors associated with the measurement of the cut-integrated rate $\delta\Gamma(c)$ from the hadronic mass spectrum and the second line are the errors from the $b \to s\gamma$ photon energy spectrum, the experimental errors from $|V_{cb}|$, and the theoretical errors. The theoretical error is the sum in quadrature of the theoretical errors from the LLR determination and the theoretical error from $|V_{cb}|$, as shown in the bottom portion of Table 7.8. The subscript "b2u" indicates systematic error from the modeling of $b \to u\ell\bar{\nu}$ decays and Fermi motion, while the subscript "b2c" indicates systematic error associated with the modeling of $b \to c\ell\bar{\nu}$ background as taken from Table 8.6 and summarized further in Table 7.8.

The statistical error in 9.2 is taken as the sum in quadrature of the $b \to u\ell\bar{\nu}$, $b \to s\gamma$, and $|V_{cb}|$

statistical errors. The theoretical error remains unchanged, and the systematic uncertainty in 9.2 is comprised of the remaining errors added in quadrature ($\delta\Gamma(c)$ systematic, $b \to s\gamma$ systematic, background modeling, signal modeling, $|V_{cb}|$ systematic).

In the second method it is demonstrated that, contrary to previous experience, it is possible to measure more than 95% of the full $b \to u\ell\bar{\nu}$ rate by extending the signal range up to $m_X < 2.50\,\mathrm{GeV}/c^2$. In this approach the standard OPE formula to translate the branching fraction to $|V_{ub}|$ is used, which was described in section 7.3. The result is:

$$|V_{ub}| = (3.84 \pm 0.70_{stat} \pm 0.15_{syst} \pm 0.14_{b2c} \pm 0.22_{b2u} \pm 0.19_{theo}) \times 10^{-3} \quad (9.3)$$

$$= (3.84 \pm 0.70_{stat} \pm 0.30_{syst} \pm 0.19_{theo}) \times 10^{-3} \quad (9.4)$$

Good agreement is observed between the two methods, which is illustrated in Fig. 7.10. Also, these extracted values are consistent with other determinations of $|V_{ub}|$ and current world averages, as shown in Fig. 9.1. The inclusive $|V_{ub}|$ determinations in Fig. 9.1 are based on shape function parameters taken from a fit to the Belle $b \to s\gamma$ photon spectrum [82] and are sensitive to the values of these parameters. As mentioned in 6.2.2, the measurements presented in this dissertation, while not as sensitive to these parameters, are based on shape function parameters obtained from a fit to the *BABAR* photon spectrum [69], so a rigorous comparison is not able to be made.

The results from the method of Leibovich, Low, and Rothstein are stable for m_X cutoffs above $\sim 1.4\,\mathrm{GeV}/c^2$ and below $\sim 2.0\,\mathrm{GeV}/c^2$. The LLR results are also consistent with the result based on the full rate. At low m_X cutoffs, the breakdown of the OPE calculation can be observed, consistent with the very large increase of the non-perturbative error in this regime. At high m_X cutoffs in the LLR method, the weighted integral starts lower in the measured photon energy spectrum, which is the experimentally challenging region of the photon spectrum to measure. As a result, the errors from the photon spectrum are large at high m_X cutoffs.

It is important to emphasize that the calculations used in the analyses in this dissertation (both LLR and the connection between the full rate and $|V_{ub}|$) are independent of the other calculations normally employed in the context of $|V_{ub}|$ determinations and therefore provide an essential and independent approach and cross-check. The $|V_{ub}|$ determination based on the LLR method has a total error competitive with other measurements but the amount of error due to the dependence on theoretical models is much reduced. However, the experimental errors are increased from the propagation of the errors from the $b \to s\gamma$ photon spectrum.

With the promise of a $1\,\mathrm{ab}^{-1}$ data sample available at *BABAR* in the near future, this analysis could see several improvements. With a reduction of the uncertainties due to theoretical models, the experimental errors represent a large fraction of the total error. The measurement of the partial rate $\delta\Gamma(c)$ and the $b \to s\gamma$ photon spectrum could be made more precise which would improve the precision on the determination of $|V_{ub}|$.

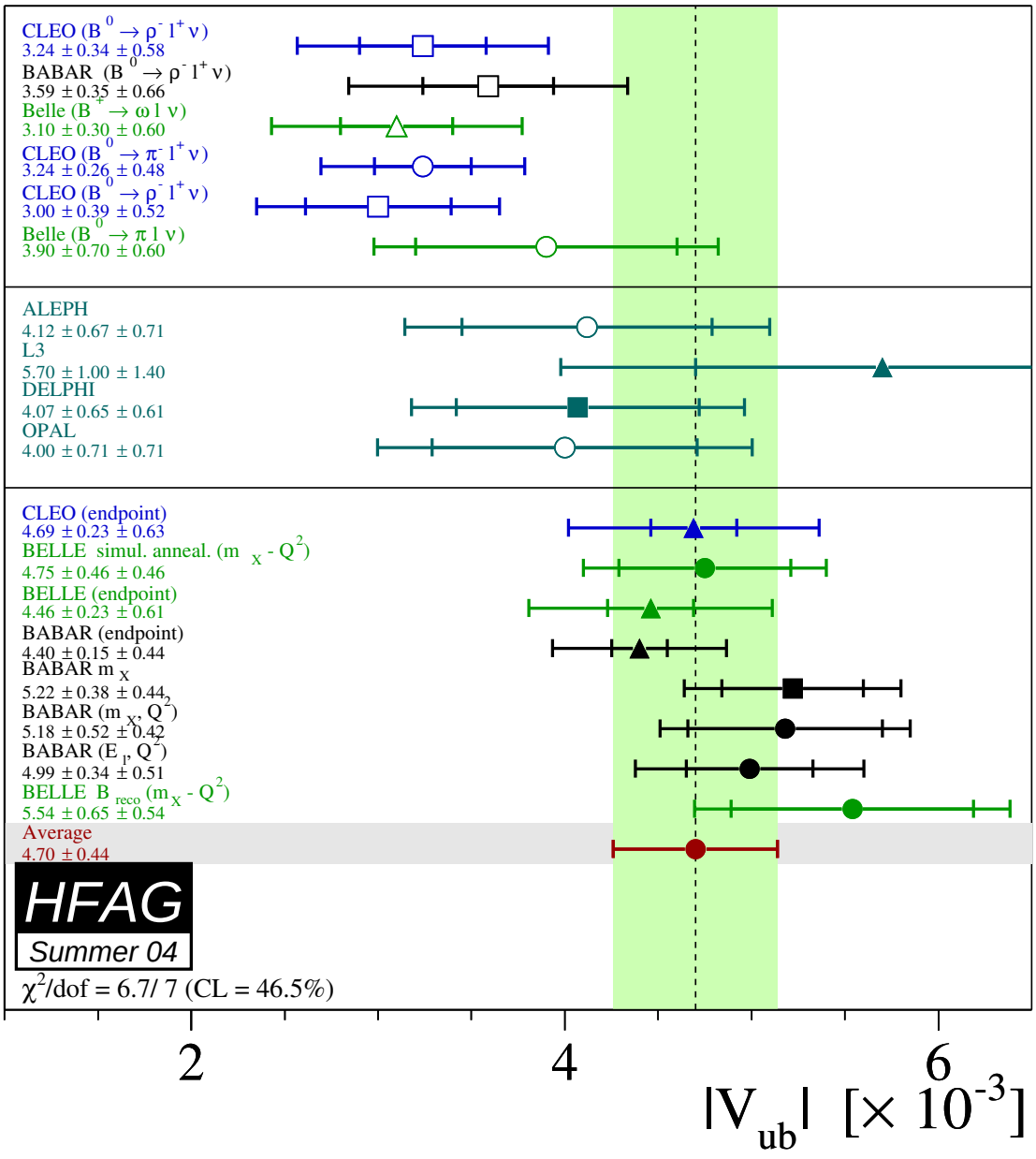

Figure 9.1: Results for $|V_{ub}|$ extractions from other experiments. The world average is calculated by HFAG [83]. The inclusive results are obtained with shape function parameters obtained from fits to the Belle $b \to s\gamma$ photon spectrum [82].

Appendix A

Fits to the $m_{\rm ES}$ Distribution

The signal extraction technique is explained in section 7.1.1. To extract the signal contriubtion, the $m_{\rm ES}$ distributions in each bin of m_X of the hadronic mass spectrum must be fitted. The following plots (A.1-A.12) are examples of the fits with $m_X < 1.67\,{\rm GeV}/c^2$ for data, $b \to c\ell\bar{\nu}$ background from generic MC, other background from generic MC, and signal MC. The fits are applied separately for $B^{\pm}$, mixed B^0, and unmixed B^0 because the neutral B sample must have a mixing correction applied to it, as explained in section 7.1.1.

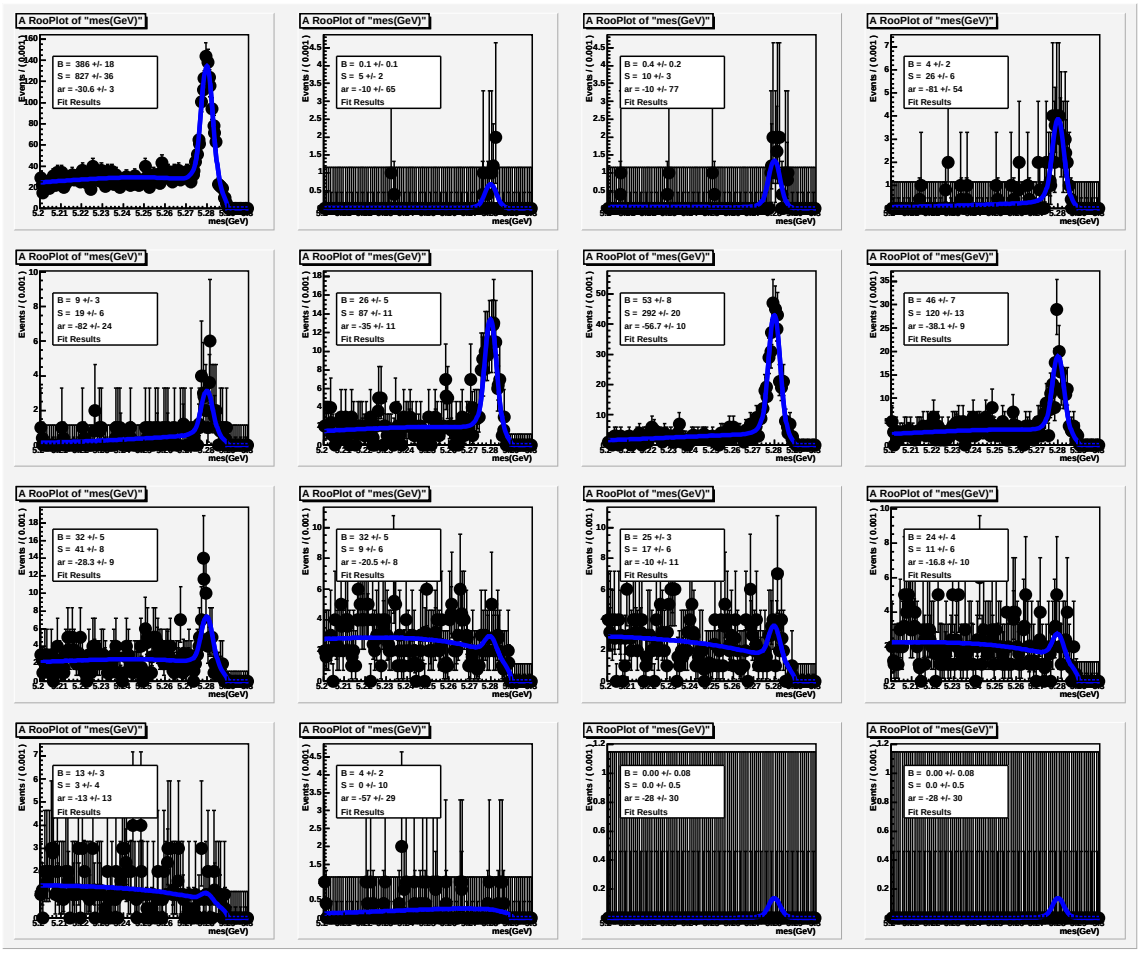

Figure A.1: DATA: The total $m_{\rm ES}$ distribution (top left) and the individual $m_{\rm ES}$ distributions in each bin of m_X for $B^{\pm}$s.

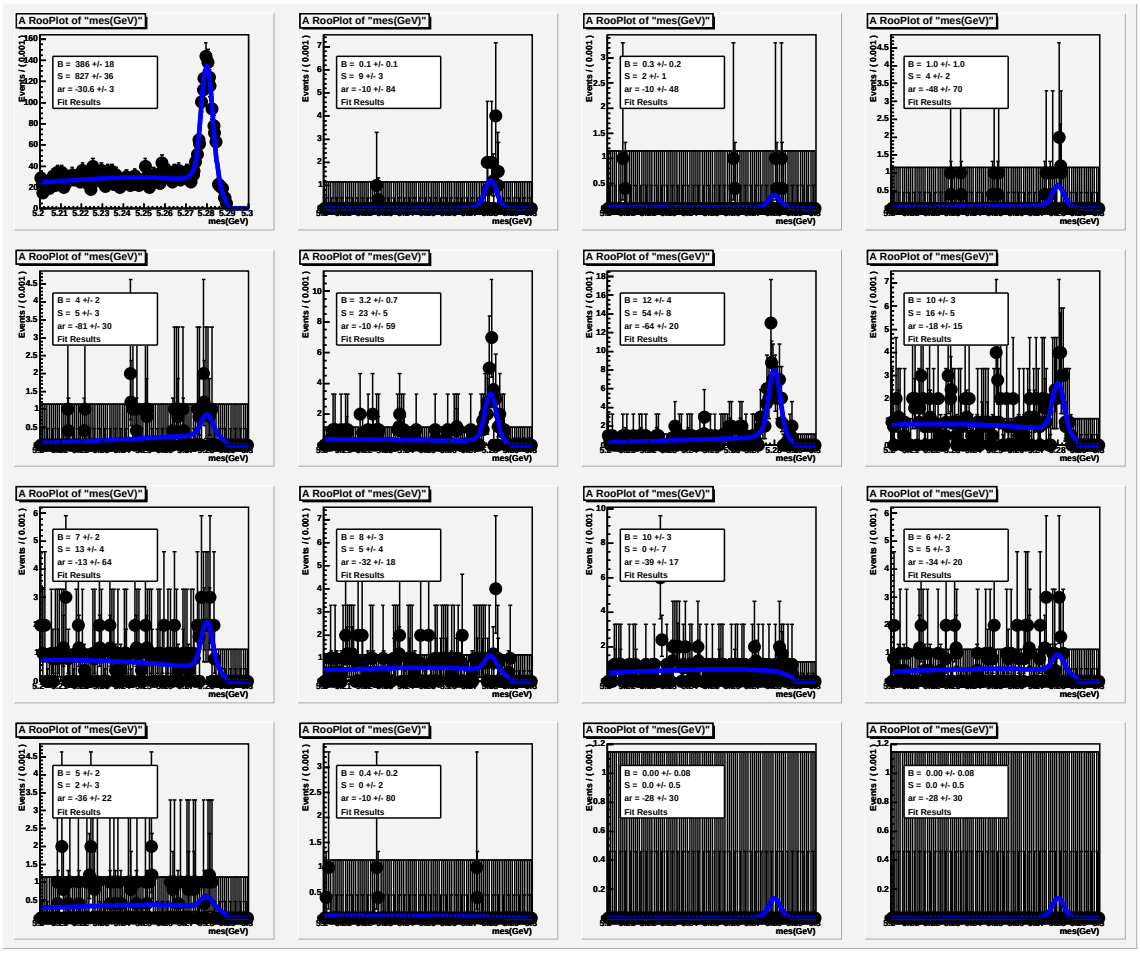

Figure A.2: DATA: The total $m_{\rm ES}$ distribution (top left) and the individual $m_{\rm ES}$ distributions in each bin of m_X for right sign B^0s.

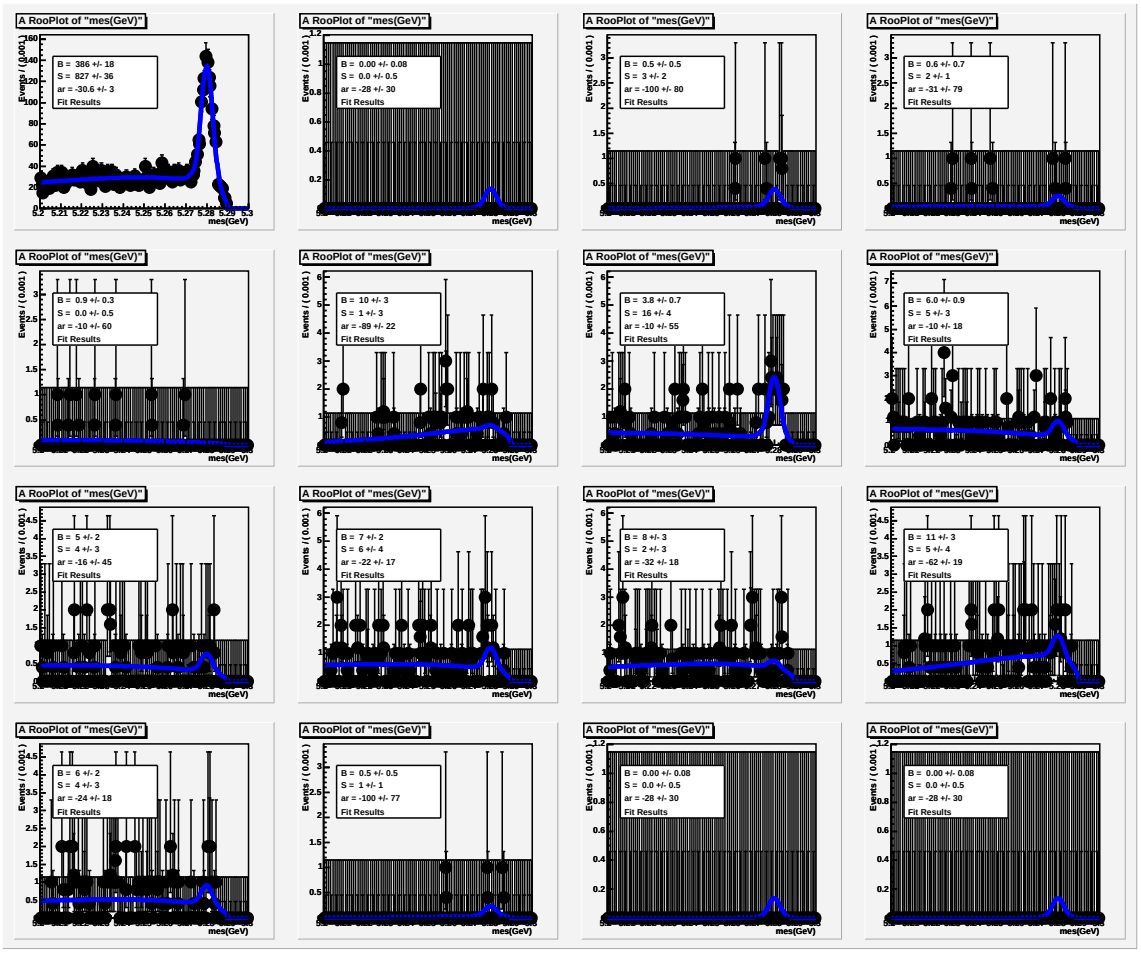

Figure A.3: DATA: The total $m_{\rm ES}$ distribution (top left) and the individual $m_{\rm ES}$ distributions in each bin of m_X for wrong sign B^0s.

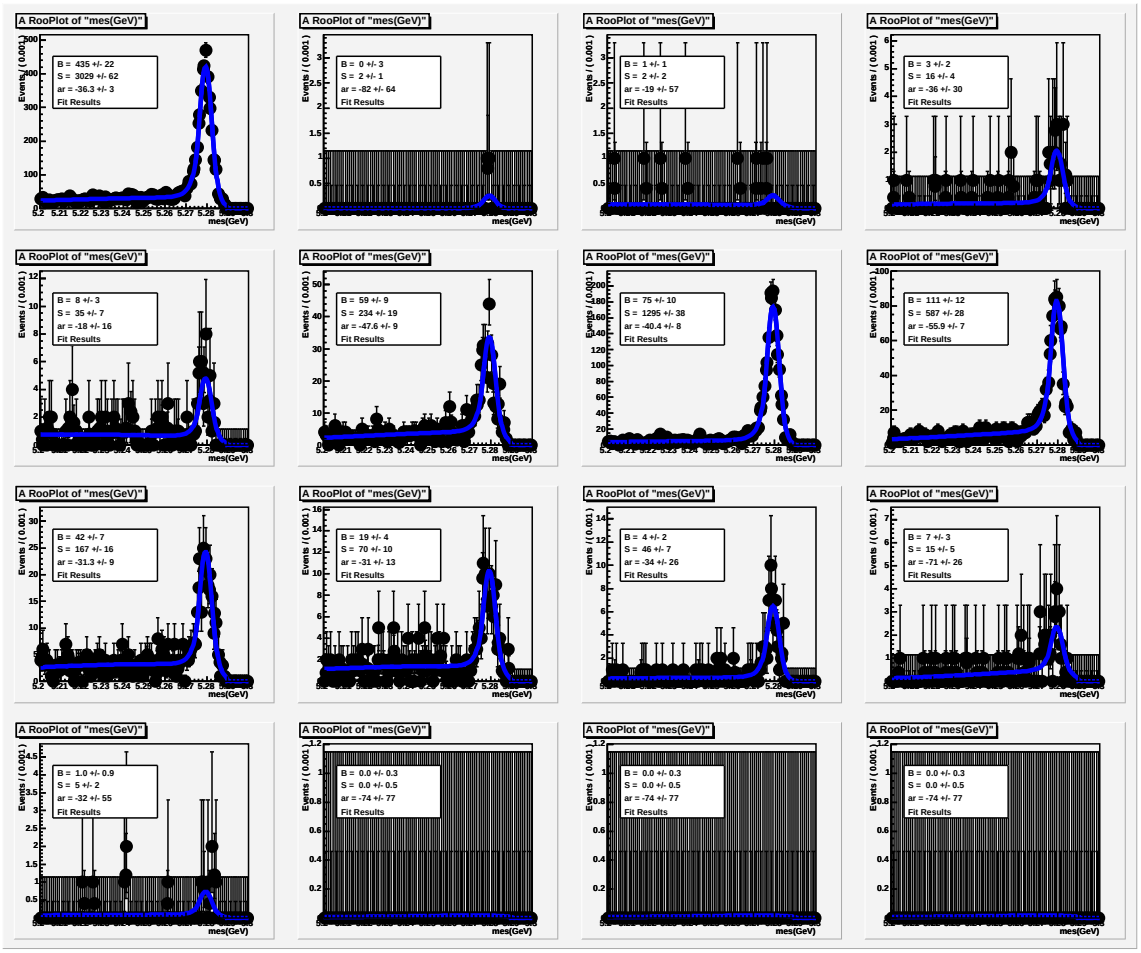

Figure A.4: GENERIC MC, $b \to c\ell\bar{\nu}$: The total $m_{\rm ES}$ distribution (top left) and the individual $m_{\rm ES}$ distributions in each bin of m_X for $B^{\pm}$s.

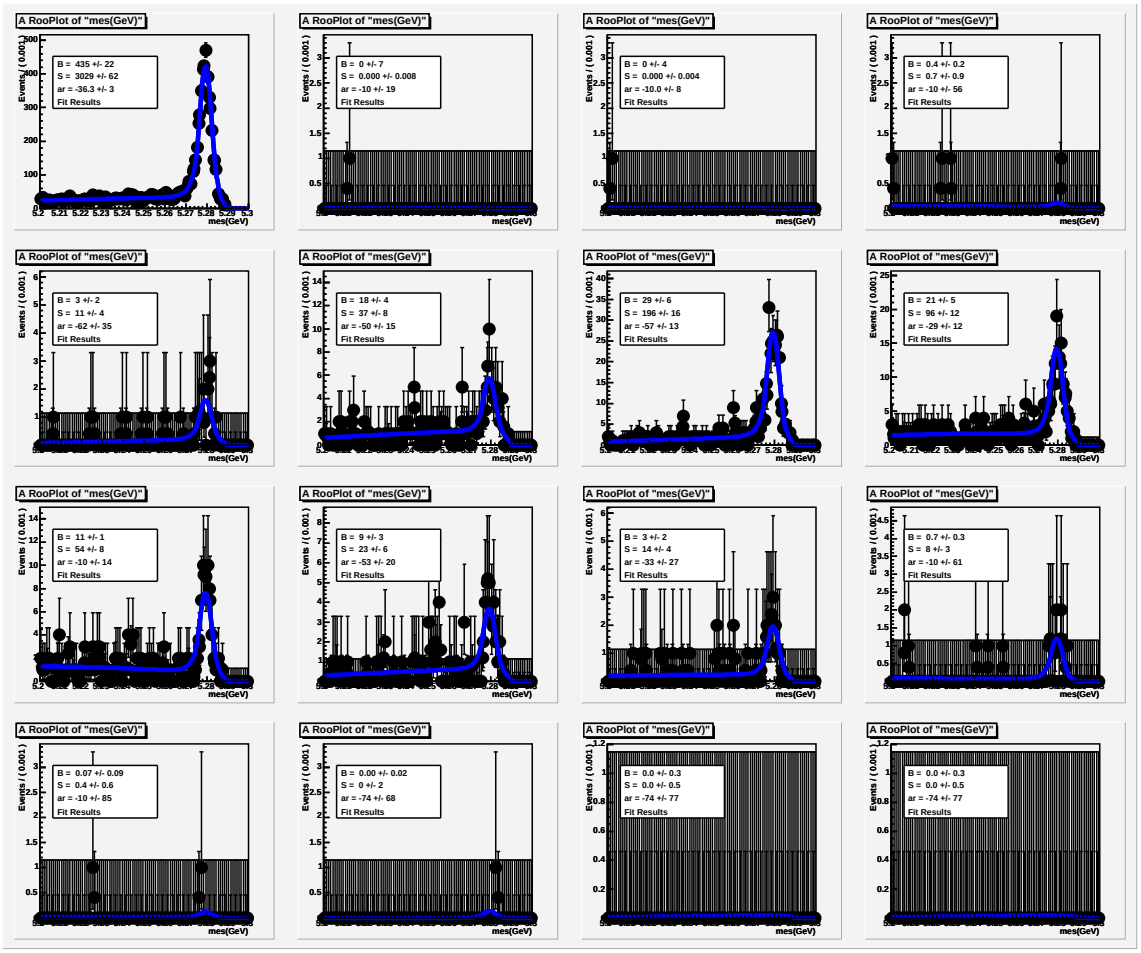

Figure A.5: GENERIC MC, $b \to c\ell\bar{\nu}$: The total $m_{\rm ES}$ distribution (top left) and the individual $m_{\rm ES}$ distributions in each bin of m_X for right sign B^0s.

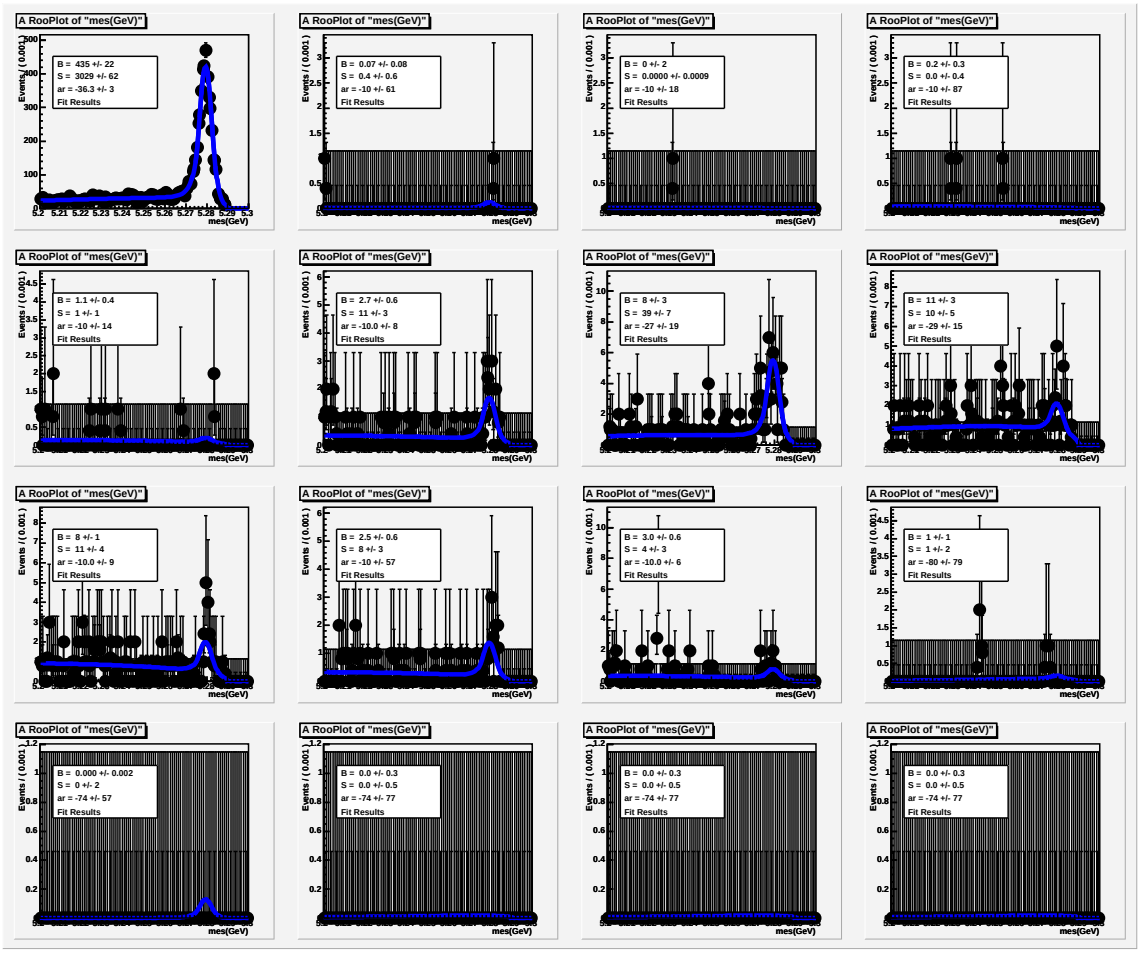

Figure A.6: GENERIC MC, $b \to c\ell\bar{\nu}$: The total $m_{\rm ES}$ distribution (top left) and the individual $m_{\rm ES}$ distributions in each bin of m_X for wrong sign B^0s.

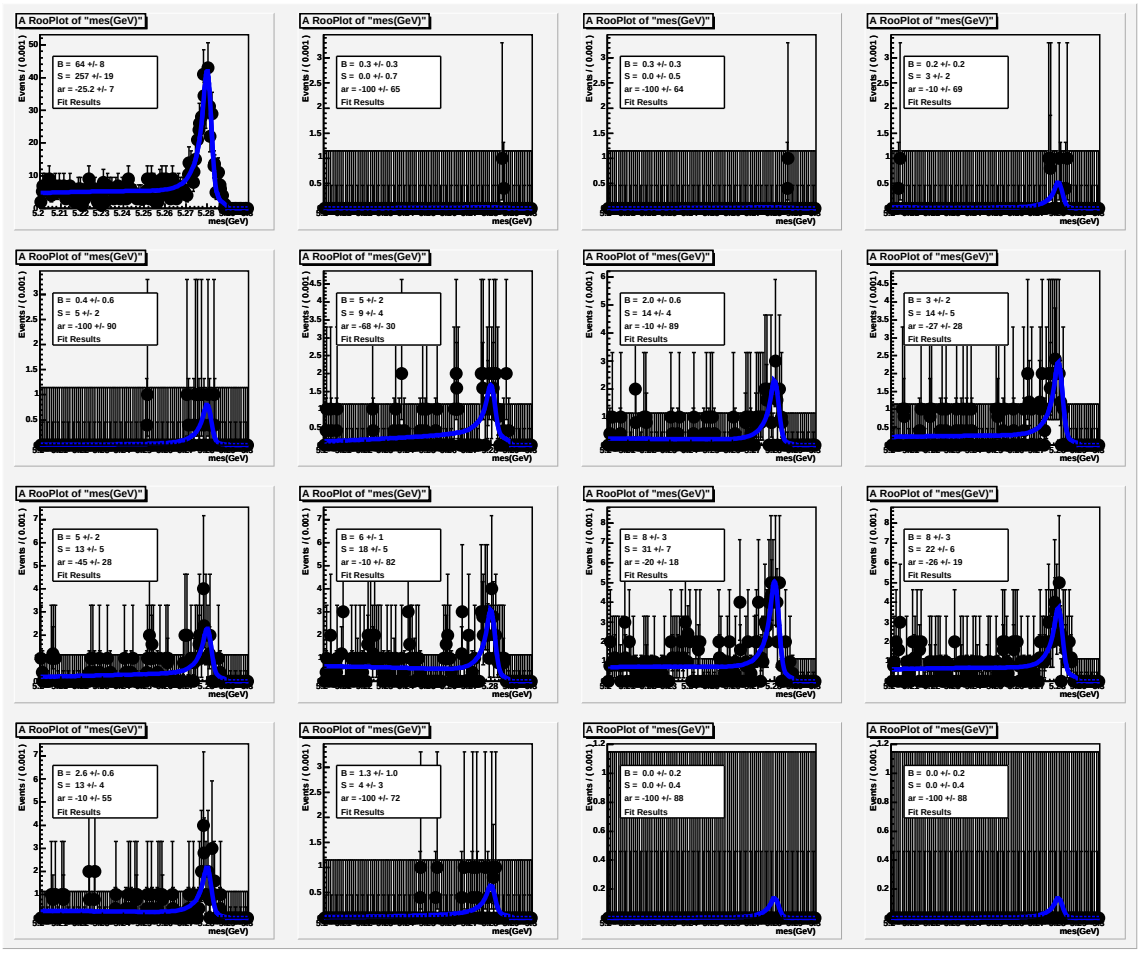

Figure A.7: GENERIC MC, other: The total $m_{\rm ES}$ distribution (top left) and the individual $m_{\rm ES}$ distributions in each bin of m_X for $B^{\pm}$s.

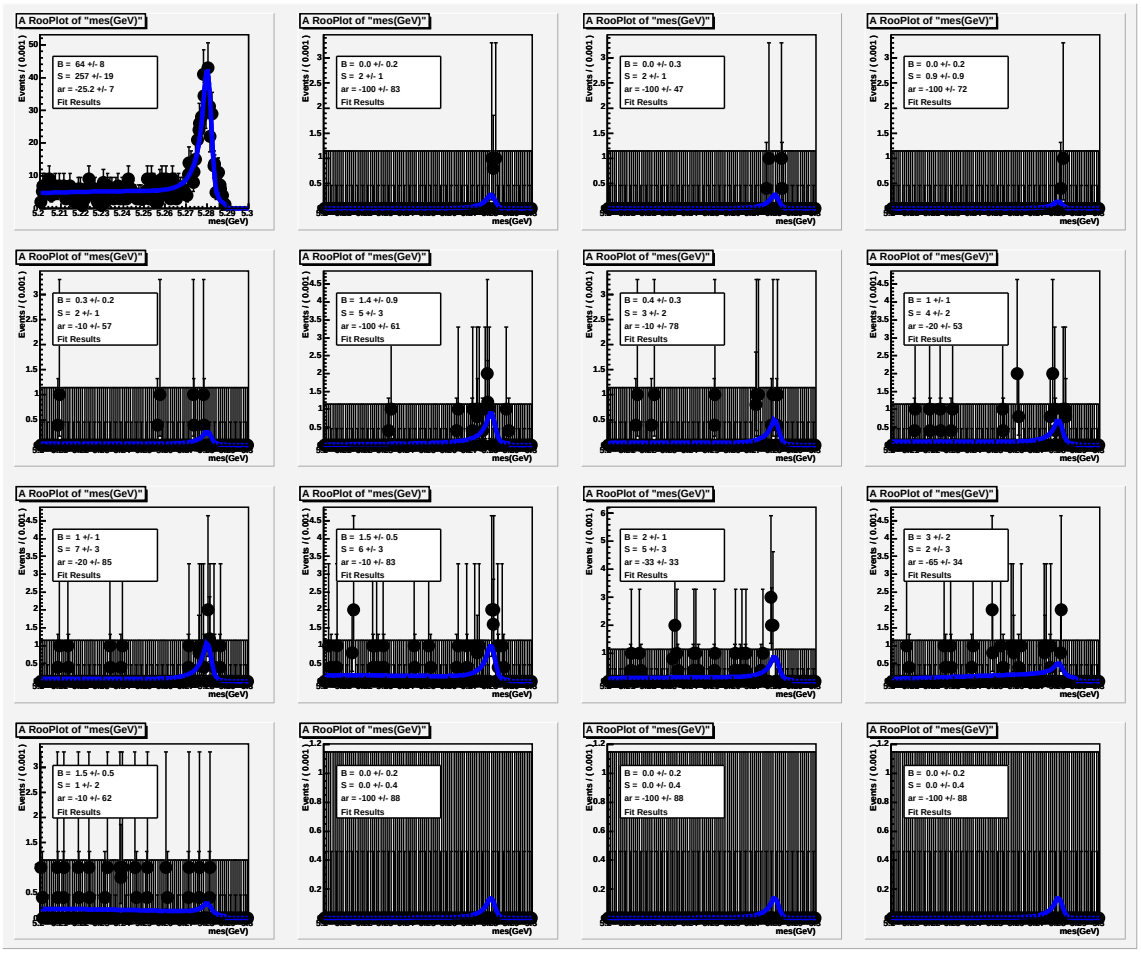

Figure A.8: GENERIC MC, other: The total $m_{\rm ES}$ distribution (top left) and the individual $m_{\rm ES}$ distributions in each bin of m_X for right sign B^0s.

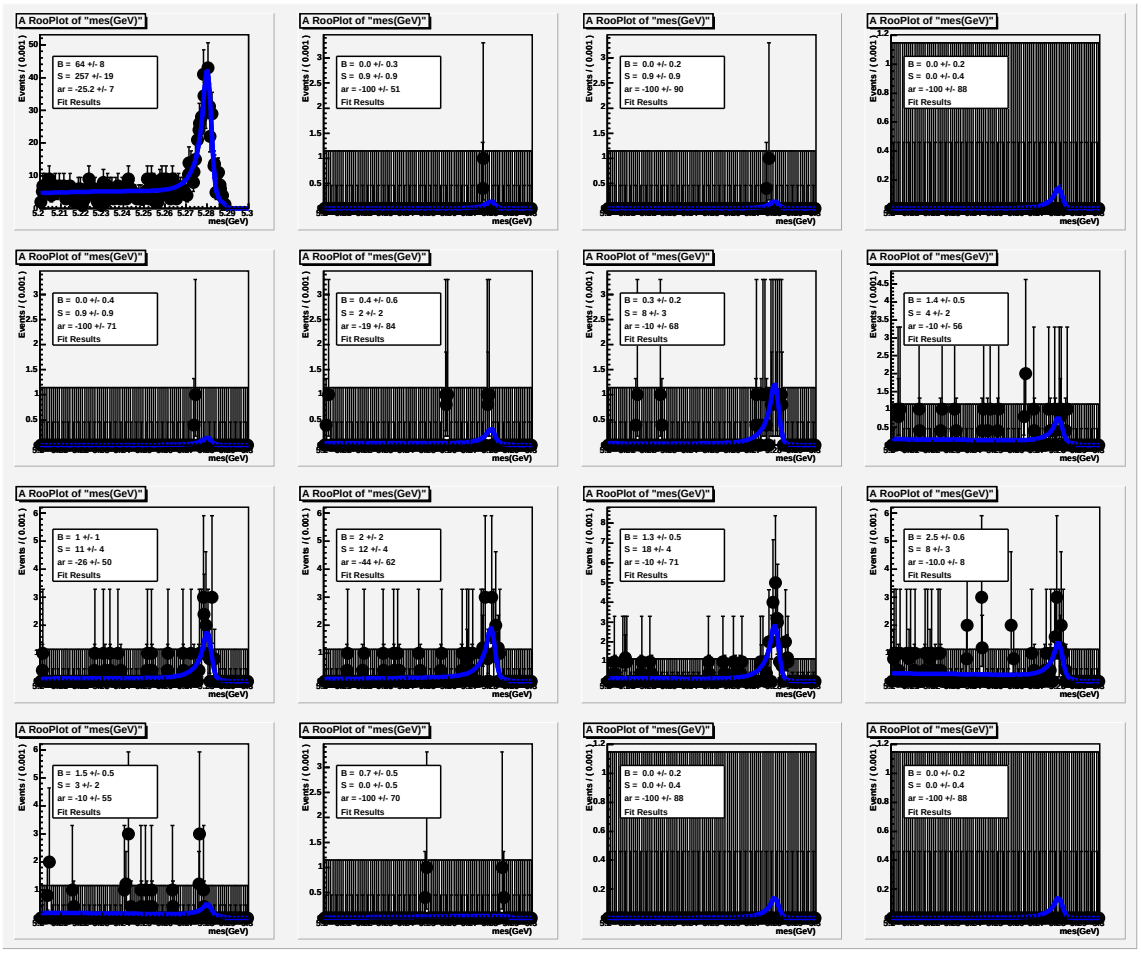

Figure A.9: GENERIC MC, other: The total $m_{\rm ES}$ distribution (top left) and the individual $m_{\rm ES}$ distributions in each bin of m_X for wrong sign B^0s.

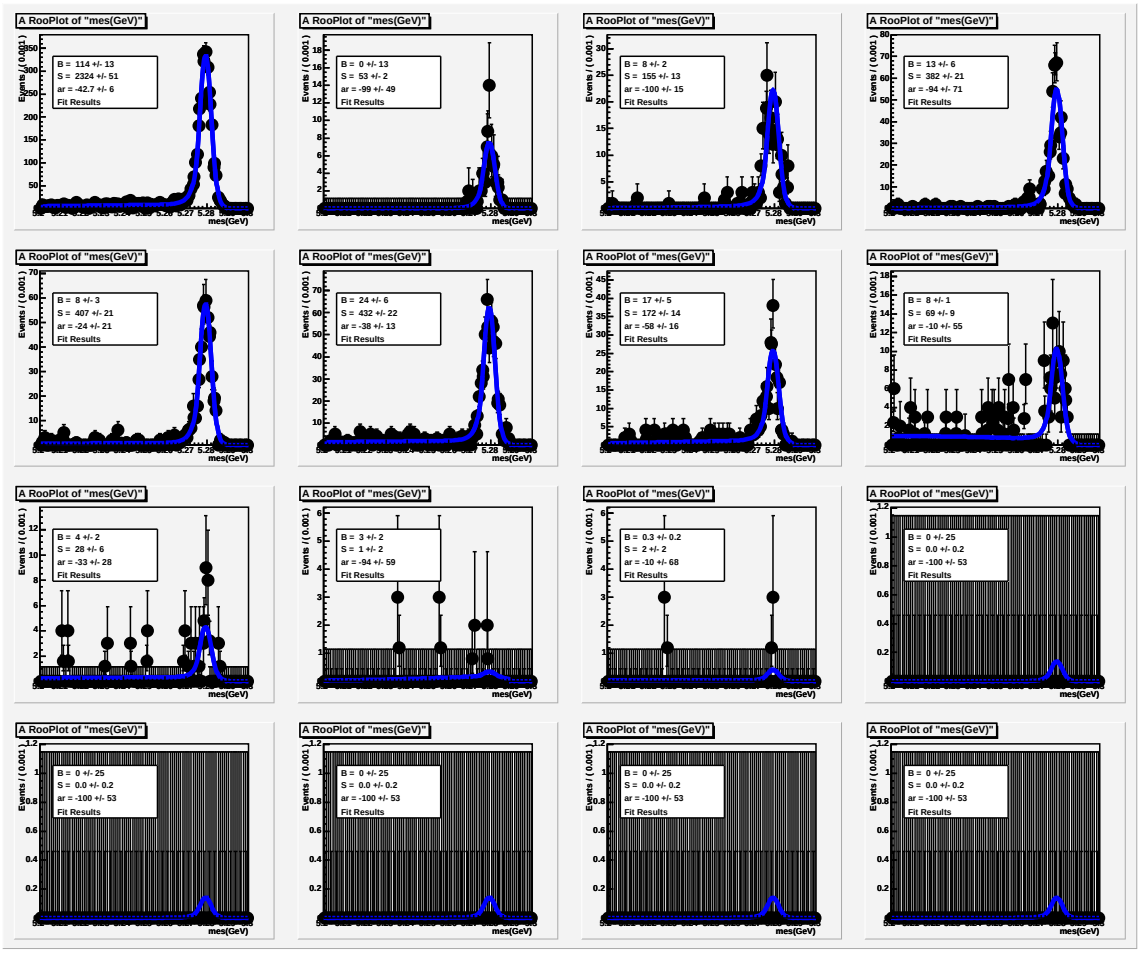

Figure A.10: SIGNAL MC: The total $m_{\rm ES}$ distribution (top left) and the individual $m_{\rm ES}$ distributions in each bin of m_X for $B^{\pm}$s.

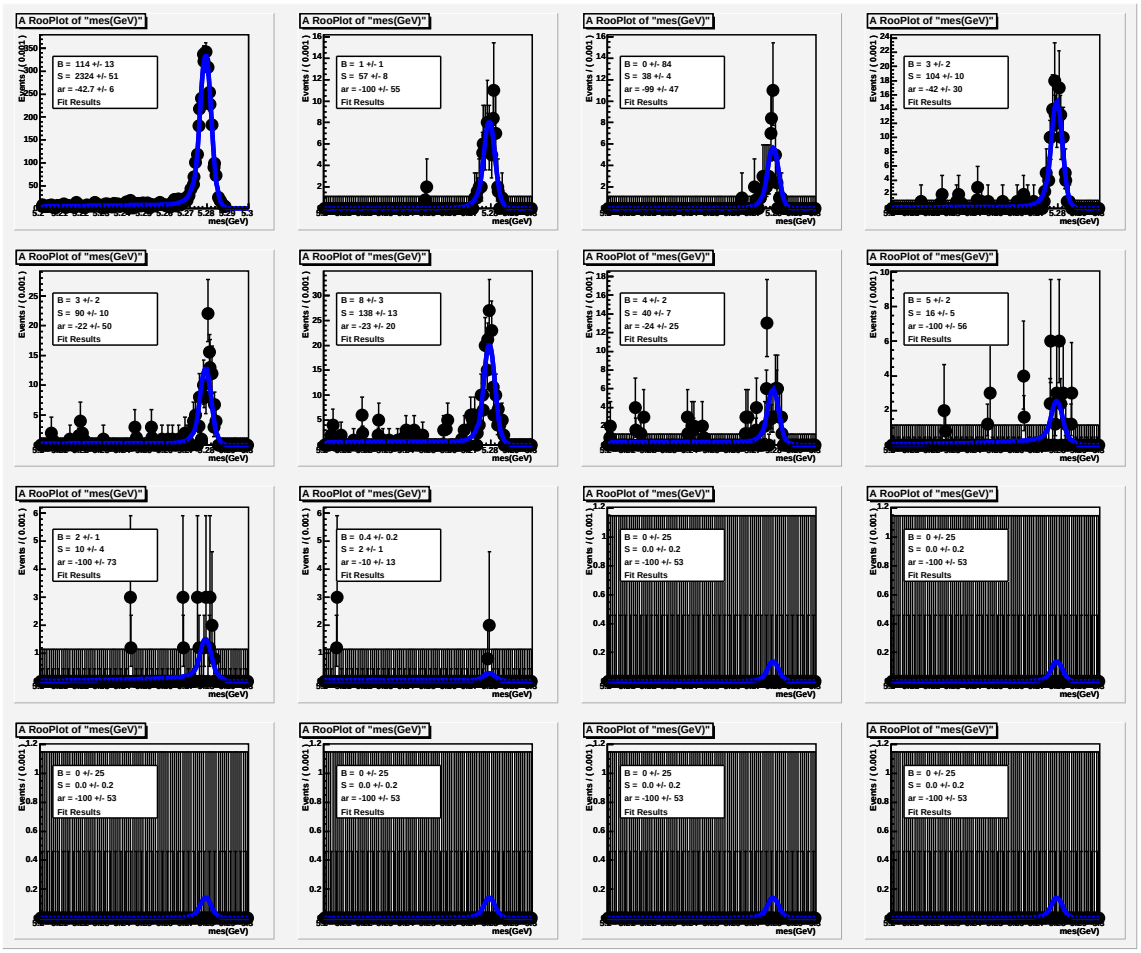

Figure A.11: SIGNAL MC: The total $m_{\rm ES}$ distribution (top left) and the individual $m_{\rm ES}$ distributions in each bin of m_X for right sign B^0s.

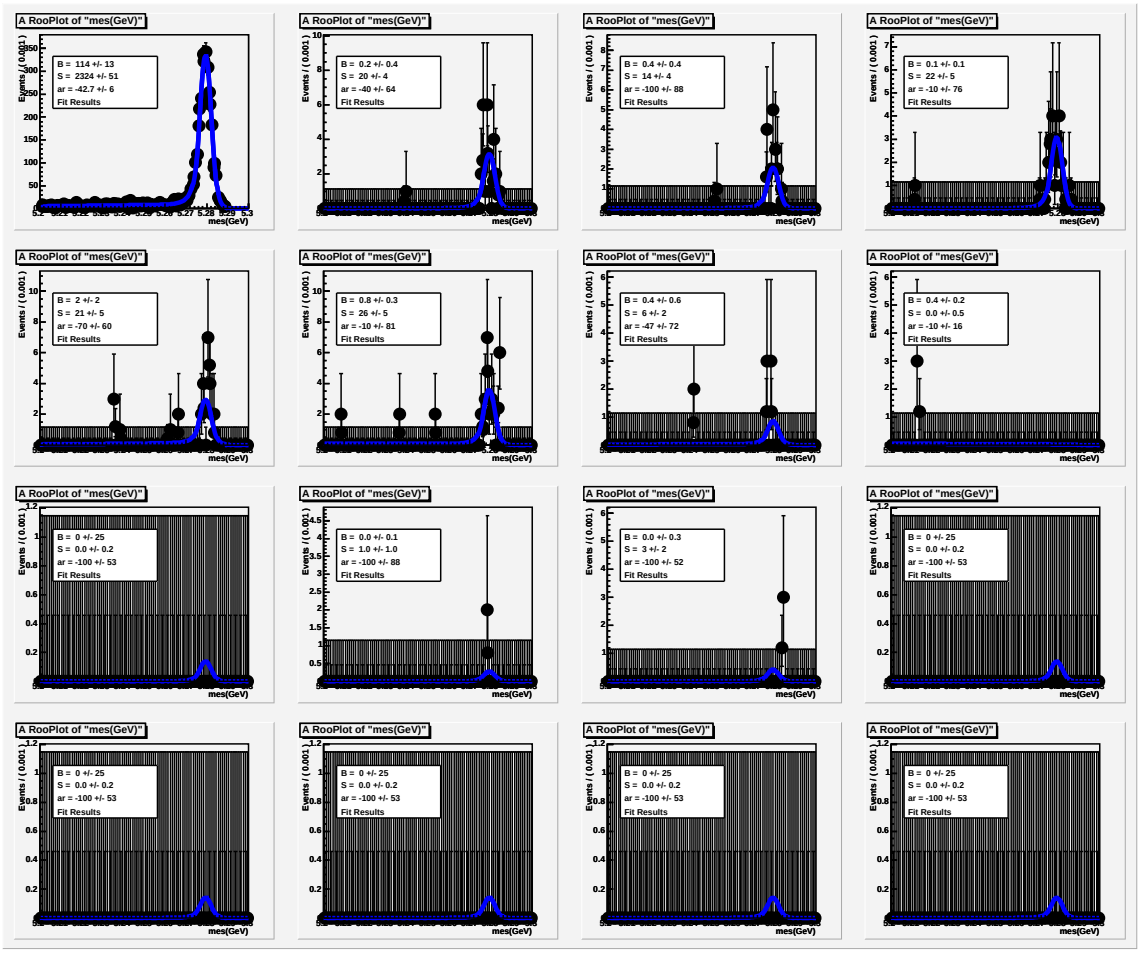

Figure A.12: SIGNAL MC: The total $m_{\rm ES}$ distribution (top left) and the individual $m_{\rm ES}$ distributions in each bin of m_X for wrong sign B^0s.

Appendix B

Fit Results on Various Subsamples

In section 7.1.6, fit results for various subsamples were presented in Tables 7.4-7.6. The fit results to the hadronic mass spectrum for these various subsamples are shown here in Figs. B.1-B.12.

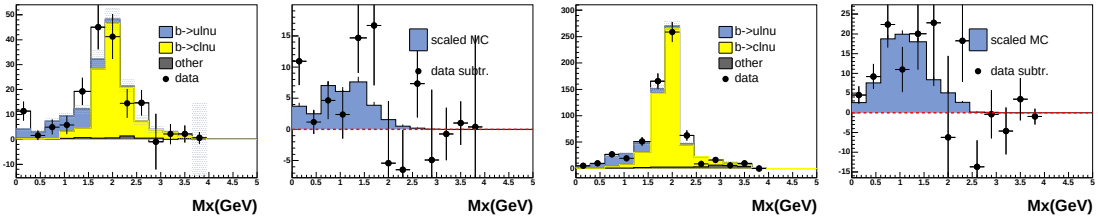

Figure B.1: Fit results for $m_X < 1.55\,\mathrm{GeV}/c^2$: The left plot is neutral B and the right plot is charged B.

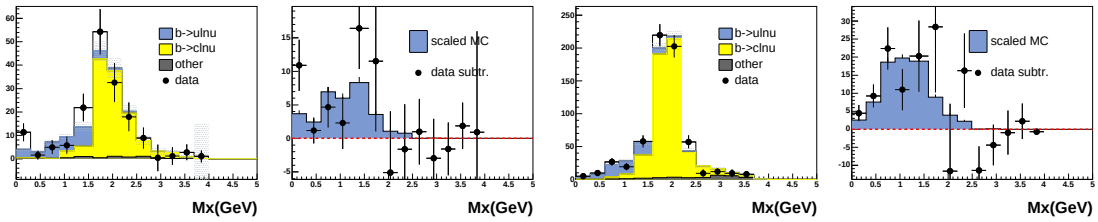

Figure B.2: Fit results for $m_X < 1.59\,\mathrm{GeV}/c^2$: The left plot is neutral B and the right plot is charged B.

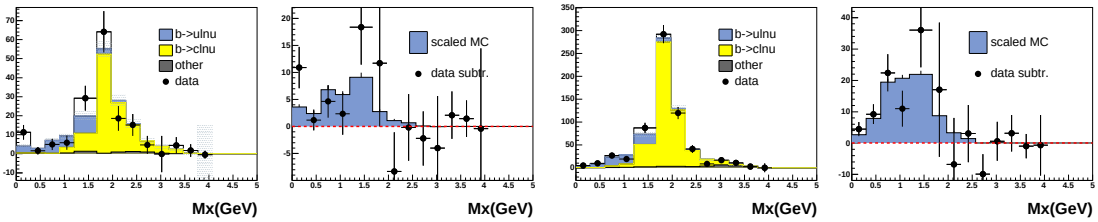

Figure B.3: Fit results for $m_X < 1.67\,\mathrm{GeV}/c^2$: The left plot is neutral B and the right plot is charged B.

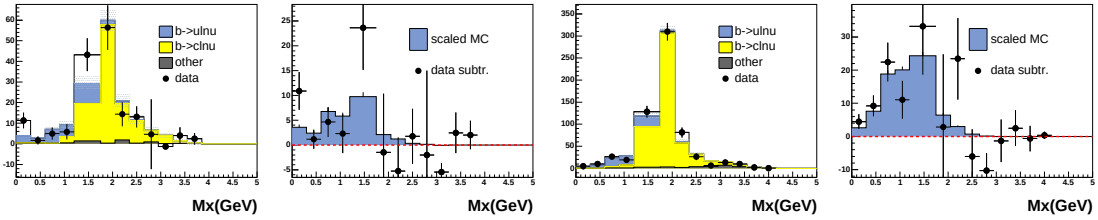

Figure B.4: Fit results for $m_X < 1.75\,\mathrm{GeV}/c^2$: The left plot is neutral B and the right plot is charged B.

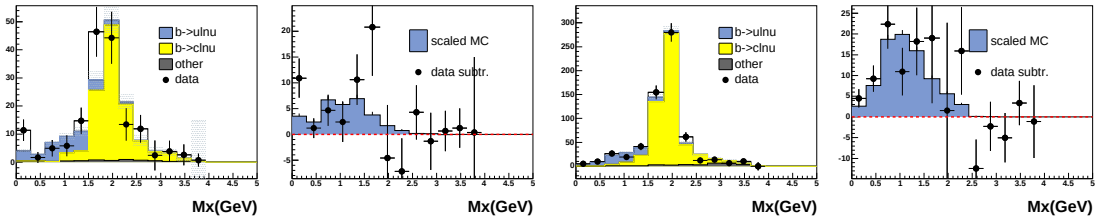

Figure B.5: Fit results for $m_X < 1.83\,\mathrm{GeV}/c^2$: The left plot is neutral B and the right plot is charged B.

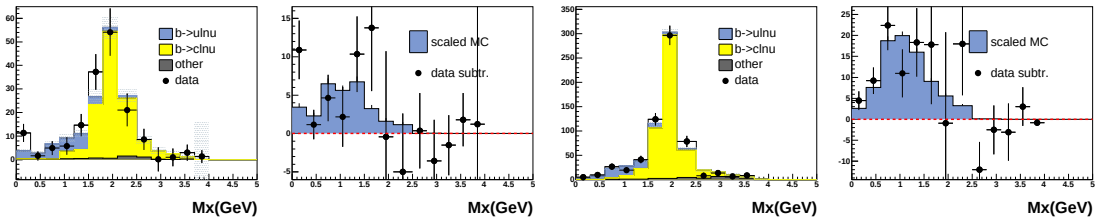

Figure B.6: Fit results for $m_X < 2.50\,\mathrm{GeV}/c^2$: The left plot is neutral B and the right plot is charged B.

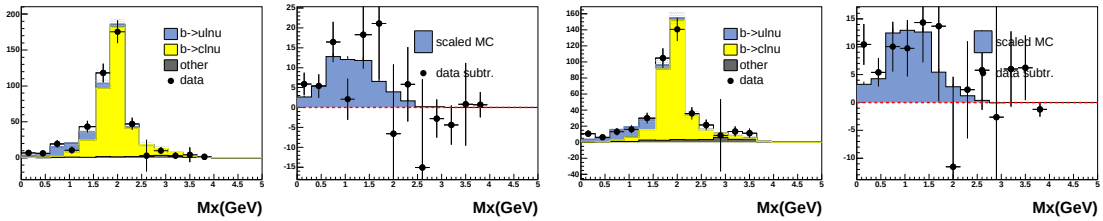

Figure B.7: Fit results for $m_X < 1.55\,\mathrm{GeV}/c^2$: The left plot is electrons and the right plot is muons.

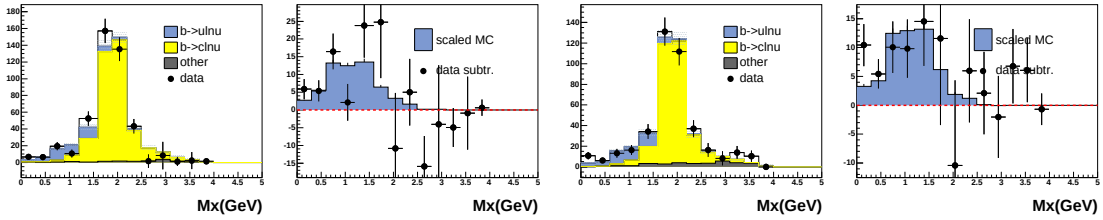

Figure B.8: Fit results for $m_X < 1.59\,\mathrm{GeV}/c^2$: The left plot is electrons and the right plot is muons.

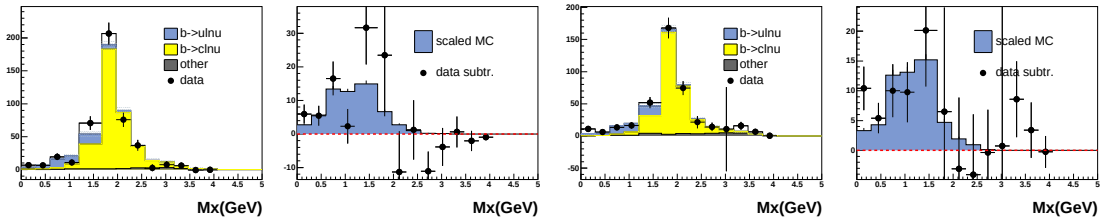

Figure B.9: Fit results for $m_X < 1.67\,\mathrm{GeV}/c^2$: The left plot is electrons and the right plot is muons.

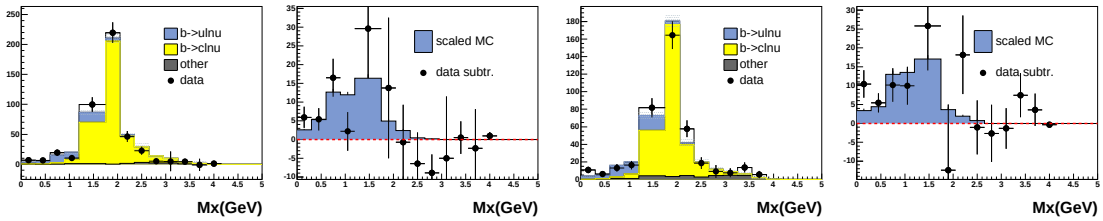

Figure B.10: Fit results for $m_X < 1.75\,\mathrm{GeV}/c^2$: The left plot is electrons and the right plot is muons.

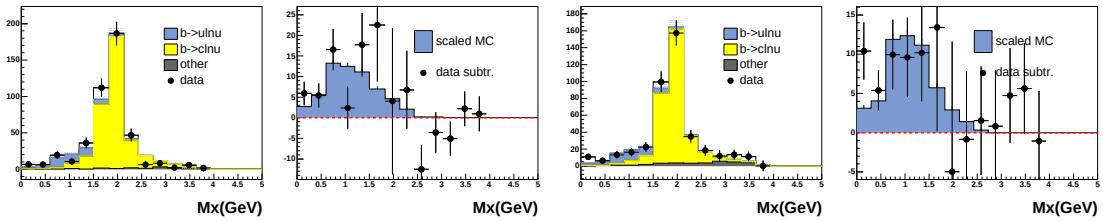

Figure B.11: Fit results for $m_X < 1.83\,\mathrm{GeV}/c^2$: The left plot is electrons and the right plot is muons.

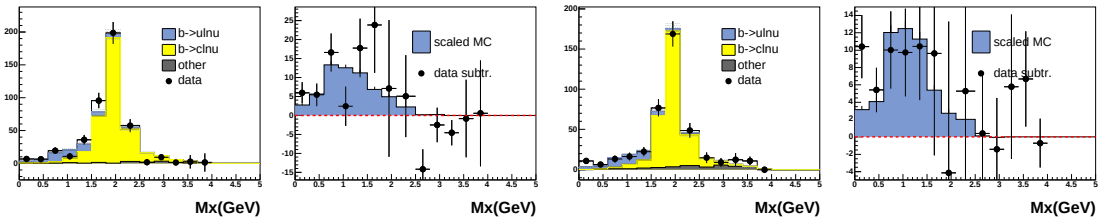

Figure B.12: Fit results for $m_X < 2.50\,\mathrm{GeV}/c^2$: The left plot is electrons and the right plot is muons.

References

[1] N. Cabibbo, "Unitary Symmetry And Leptonic Decays," Phys. Rev. Lett. **10**, 531 (1963).

[2] M. Kobayashi and T. Maskawa, "CP Violation In The Renormalizable Theory Of Weak Interaction," Prog. Theor. Phys. **49**, 652 (1973).

[3] A. J. Buras and R. Fleischer, "Quark mixing, CP violation and rare decays after the top quark discovery," Adv. Ser. Direct. High Energy Phys. **15**, 65 (1998)

[4] L. Wolfenstein, "Parametrization Of The Kobayashi-Maskawa Matrix," Phys. Rev. Lett. **51**, 1945 (1983).

[5] C. Dib, I. Dunietz, F. J. Gilman and Y. Nir, "Standard Model Predictions For CP Violation In B0 Meson Decay," Phys. Rev. D **41**, 1522 (1990).

[6] S. Eidelman *et al.*, the Particle Data Group, Phys. Lett. B **592**, 1 (2004)

[7] CKMfitter Group (J. Charles et al.), Eur. Phys. J. C **41**, 1-131 (2005), updated results and plots available at: http://ckmfitter.in2p3.fr

[8] N. Isgur and M. B. Wise, "Weak Decays Of Heavy Mesons In The Static Quark Approximation," Phys. Lett. B **232**, 113 (1989).

[9] N. Isgur and M. B. Wise, "Weak Transition Form-Factors Between Heavy Mesons," Phys. Lett. B **237**, 527 (1990).

[10] E. Eichten and B. Hill, Phys. Lett. B **234**, 511 (1990).

[11] E. Eichten and B. Hill, Phys. Lett. B **243**, 427 (1990).

[12] H. Georgi, Phys. Lett. B **240**, 447 (1990).

[13] M. Neubert, Phys. Rept. **245**, 259 (1994)

[14] K. G. Wilson, "Nonlagrangian Models Of Current Algebra," Phys. Rev. **179**, 1499 (1969).

[15] I. I. Y. Bigi, N. G. Uraltsev and A. I. Vainshtein, "Nonperturbative corrections to inclusive beauty and charm decays: QCD versus phenomenological models," Phys. Lett. B **293**, 430 (1992) [Erratum-ibid. B **297**, 477 (1993)]

[16] I. I. Y. Bigi, M. A. Shifman, N. G. Uraltsev and A. I. Vainshtein, "QCD predictions for lepton spectra in inclusive heavy flavor decays," Phys. Rev. Lett. **71**, 496 (1993)

[17] I. I. Y. Bigi *et al.*, *in Procedings of the Annual Meeting of the Division of Particles and Fields of the APS*, Batavia, Illinois, (1992), edited by C. Albright *et al.*, World Scientific, Singapore (1993), p. 610

[18] B. Blok and M. A. Shifman, "The Rule of discarding 1/N(c) in inclusive weak decays. 1," Nucl. Phys. B **399**, 441 (1993)

[19] A. V. Manohar and M. B. Wise, "Inclusive semileptonic B and polarized Lambda(b) decays from QCD," Phys. Rev. D **49**, 1310 (1994)

[20] B. Blok, L. Koyrakh, M. A. Shifman and A. I. Vainshtein, "Differential distributions in semileptonic decays of the heavy flavors in QCD," Phys. Rev. D **49**, 3356 (1994) [Erratum-ibid. D **50**, 3572 (1994)]

[21] A. F. Falk and M. Neubert, "Second order power corrections in the heavy quark effective theory. 1. Formalism and meson form-factors," Phys. Rev. D **47**, 2965 (1993)

[22] A. F. Falk and M. Neubert, "Second order power corrections in the heavy quark effective theory. 2. Baryon form-factors," Phys. Rev. D **47**, 2982 (1993)

[23] M. A. Shifman and M. B. Voloshin, "Preasymptotic Effects In Inclusive Weak Decays Of Charmed Particles," Sov. J. Nucl. Phys. **41**, 120 (1985) [Yad. Fiz. **41**, 187 (1985)].

[24] M. A. Shifman and M. B. Voloshin, "Hierarchy Of Lifetimes Of Charmed And Beautiful Hadrons," Sov. Phys. JETP **64**, 698 (1986) [Zh. Eksp. Teor. Fiz. **91**, 1180 (1986)].

[25] A. Ali and E. Pietarinen, "Semileptonic Decays Of Heavy Quarks In Quantum Chromodynamics," Nucl. Phys. B **154**, 519 (1979).

[26] G. Altarelli, N. Cabibbo, G. Corbo, L. Maiani and G. Martinelli, "Leptonic Decay Of Heavy Flavors: A Theoretical Update," Nucl. Phys. B **208**, 365 (1982).

[27] C. H. Jin, W. F. Palmer and E. A. Paschos, "A Parton model for inclusive semileptonic B meson decays," Phys. Lett. B **329**, 364 (1994)

[28] A. Bareiss and E. A. Paschos, "Semileptonic B Meson Decays In The Parton Model," Nucl. Phys. B **327**, 353 (1989).

[29] Y. Nir, "The Mass Ratio M (C) / M (B) In Semileptonic B Decays," Phys. Lett. B **221**, 184 (1989).

[30] N. Uraltsev, "Theoretical uncertainties in Gamma(sl)(b $\to$ u)," Int. J. Mod. Phys. A **14**, 4641 (1999), and private communication (2004).

[31] A. H. Hoang, Z. Ligeti and A. V. Manohar, "B decays in the Upsilon expansion," Phys. Rev. D **59**, 074017 (1999)

[32] B. Aubert *et al.* [BABAR Collaboration], "Determination of the branching fraction for B → X/c l nu decays and of |V(cb)| from hadronic mass and lepton energy moments," Phys. Rev. Lett. **93**, 011803 (2004)

[33] M. Neubert, "QCD based interpretation of the lepton spectrum in inclusive anti-B → X(u) lepton anti-neutrino decays," Phys. Rev. D **49**, 3392 (1994)

[34] M. Neubert, "Analysis of the photon spectrum in inclusive B → X(s) gamma decays," Phys. Rev. D **49**, 4623 (1994)

[35] I. I. Y. Bigi, M. A. Shifman, N. G. Uraltsev and A. I. Vainshtein, "On the motion of heavy quarks inside hadrons: Universal distributions and inclusive decays," Int. J. Mod. Phys. A **9**, 2467 (1994)

[36] I. I. Y. Bigi, M. A. Shifman, N. Uraltsev and A. I. Vainshtein, "Heavy quark distribution function in QCD and the AC**2M**2 model," Phys. Lett. B **328**, 431 (1994)

[37] T. Mannel and M. Neubert, "Resummation of nonperturbative corrections to the lepton spectrum in inclusive B → X lepton anti-neutrino decays," Phys. Rev. D **50**, 2037 (1994)

[38] A. K. Leibovich, I. Low and I. Z. Rothstein, "Extracting V(ub) without recourse to structure functions," Phys. Rev. D **61**, 053006 (2000)

[39] A. K. Leibovich, I. Low and I. Z. Rothstein, "Extracting |V(ub)| from the hadronic mass spectrum of inclusive B decays," Phys. Lett. B **486**, 86 (2000)

[40] A. K. Leibovich, I. Low and I. Z. Rothstein, "A comment on the extractions of V(ub) from radiative decays," Phys. Lett. B **513**, 83 (2001)

[41] G. P. Korchemsky and G. Sterman, "Infrared factorization in inclusive B meson decays," Phys. Lett. B **340**, 96 (1994)

[42] C. Greub, T. Hurth and D. Wyler, "Virtual corrections to the decay $b \to s\gamma$," Phys. Lett. B **380**, 385 (1996)

[43] C. Greub, T. Hurth and D. Wyler, "Virtual $O(\alpha_s)$ corrections to the inclusive decay $b \to s\gamma$," Phys. Rev. D **54**, 3350 (1996)

[44] A. Ali and C. Greub, "Inclusive Photon Energy Spectrum In Rare B Decays," Z. Phys. C **49**, 431 (1991).

[45] A. Ali and C. Greub, "A Profile Of The Final States In B → X(S) Gamma And An Estimate Of The Branching Ratio Br (B → K* Gamma)," Phys. Lett. B **259**, 182 (1991).

[46] A. Ali and C. Greub, "Rare decays B → X(d) gamma in the standard model," Phys. Lett. B **287**, 191 (1992).

[47] K. G. Chetyrkin, M. Misiak and M. Munz, "Weak radiative B-meson decay beyond leading logarithms," Phys. Lett. B **400**, 206 (1997) [Erratum-ibid. B **425**, 414 (1998)]

[48] R. Akhoury and I. Z. Rothstein, "The Extraction of V_{ub} from Inclusive B Decays and the Resummation of End Point Logs," Phys. Rev. D **54**, 2349 (1996)

[49] PEP-II - An Asymmetric B Factory, Conceptual Design Report, SLAC-418, LBL-5379 (1993).

[50] P.Oddone, in *Proceedings of the UCLA Workshop: Linear Collider $B\overline{B}$ Factory Conceptual Design*, edited by D. Stork, World Scientific (1987), p. 243.

[51] B. Aubert *et al.* [BABAR Collaboration], "Measurement of the B+/B0 production ratio from the Upsilon(4S) meson using B+ → J/psi K+ and B0 → J/psi K0(S) decays," Phys. Rev. D **69**, 071101 (2004)

[52] B. Aubert *et al.* [BABAR Collaboration], "The BaBar detector," Nucl. Instrum. Meth. A **479**, 1 (2002)

[53] D. Barbieri *et al.*, "Silicon sensors for the BaBar vertex tracker: Design, electrical tests and production quality control," Nuovo Cim. A **112**, 113 (1999).

[54] B. N. Ratcliff, "The DIRC Counter: A Particle Identification Device for the B Factory," SLAC-PUB-5946(1992), and "The DIRC Counter: A New Type of Particle Identification Device for B Factories," SLAC-PUB-6047(1993).

[55] P. Coyle *et al.*, "The DIRC counter: A New type of particle identification device for B factories," Nucl. Instrum. Meth. A **343**, 292 (1994).

[56] B. N. Ratcliff, "Imaging rings in ring imaging Cherenkov counters," Nucl. Instrum. Meth. A **502**, 211 (2003).

[57] M. Benkebil, R. Cizeron, S. Plaszczynski, M. H. Schune and G. Wormser, "Water resistant rhodium plated reflectors for use in the DIRC BaBar Cherenkov detector," Nucl. Instrum. Meth. A **442**, 364 (2000).

[58] R. Santonico and R. Cardarelli, "Development Of Resistive Plate Counters," Nucl. Instrum. Meth. **187**, 377 (1981).

[59] P. Billoir, "Track Fitting With Multiple Scattering: A New Method," Nucl. Instrum. Meth. A **225**, 352 (1984).

[60] D.N. Brown, E.A. Charles, D.A. Roberts, "The *BABAR* Track Fitting Algorithm," *Proceedings of CHEP 2000*, Padova, Italy (2000).

[61] T. Brandt, "Likelihood Based Electron Identification," *BABAR* Analysis Documents #396 (2002).

[62] F. Fabozzi and L. Lista, "Muon Identification in the *BABAR* Experiment," *BABAR* Analysis Document #60 (2000).

[63] S. M. Spanier, "Kaon Selection at *BABAR*," *BABAR* Analysis Document #116 (2001).

[64] H. Albrecht *et al.* [ARGUS Collaboration], "Exclusive Hadronic Decays Of B Mesons," Z. Phys. C **48**, 543 (1990).

[65] T. Skwarnicki [Crystal Ball Collaboration], "A Study Of The Radiative Cascade Transitions Between The Upsilon-Prime And Upsilon Resonances," DESY-F31-86-02

[66] D. Scora and N. Isgur, "Semileptonic meson decays in the quark model: An update," Phys. Rev. D **52**, 2783 (1995)

[67] F. De Fazio and M. Neubert, "B → X/u l anti-nu/l decay distributions to order alpha(s)," JHEP **9906**, 017 (1999)

[68] T. Sjostrand, "High-energy physics event generation with PYTHIA 5.7 and JETSET 7.4," Comput. Phys. Commun. **82**, 74 (1994).

[69] B. Aubert *et al.* [BABAR Collaboration], "Measurements of the B → X/s gamma branching fraction and photon spectrum from a sum of exclusive final states," Phys. Rev. D **72**, 052004 (2005)

[70] J. E. Duboscq *et al.* [CLEO Collaboration], "Measurement of the form-factors for anti-B0 → D*+ lepton- anti-neutrino," Phys. Rev. Lett. **76**, 3898 (1996).

[71] J. L. Goity and W. Roberts, "Soft Pion Emission In Semileptonic B Meson Decays," Phys. Rev. D **51**, 3459 (1995)

[72] M. Gill, *et al.*, "Measurement of B to D^* Form Factors in the Semileptonic Decay B to Dstar e ν", *BABAR* Analysis Documents #1224 (2005).

[73] B. Aubert *et al.* [BABAR Collaboration], "Measurement of the anti-B0 lifetime and of the B0 anti-B0 oscillation frequency using partially reconstructed anti-B0 → D*+ l- anti-nu/l decays,"

[74] The impact of the uncertainty of the fraction of neutral and charged B mesons is negligible.

[75] D. Abbaneo *et al.* [ALEPH Collaboration], "Combined results on b-hadron production rates and decay properties,"

[76] A. L. Kagan and M. Neubert, "QCD anatomy of B → X/s gamma decays," Eur. Phys. J. C **7**, 5 (1999)

[77] M. Althoff *et al.* [TASSO Collaboration], "A Detailed Study Of Strange Particle Production In E+ E- Annihilation At High-Energy," Z. Phys. C **27**, 27 (1985).

[78] W. Bartel *et al.* [JADE Collaboration], "Charged Particle And Neutral Kaon Production In E+ E- Annihilation At Petra," Z. Phys. C **20**, 187 (1983).

[79] V. Luth *et al.*, "K0 Production In E+ E- Annihilation," Phys. Lett. B **70**, 120 (1977).

[80] Adam Leibovich and Ira Rothstein, private communication.

[81] B. Aubert *et al.* [BABAR Collaboration], "Measurement of the inclusive charmless semileptonic branching ratio of B mesons and determination of |V(ub)|," Phys. Rev. Lett. **92**, 071802 (2004)

[82] A. Limosani and T. Nozaki [Heavy Flavor Averaging Group], "Extraction of the b-quark shape function parameters using the Belle B $\rightarrow$ X/s gamma photon energy spectrum,"

[83] J. Alexander *et al.* [Heavy Flavor Averaging Group (HFAG)], "Averages of b-hadron properties as of summer 2004,"